Georgia State University
ScholarWorks @ Georgia State University

Physics and Astronomy Dissertations | Department of Physics and Astronomy

7-17-2009

A Multi-Wavelength Investigation of Seyfert 1.8 and 1.9 Galaxies

Margaret Trippe

Follow this and additional works at: https://scholarworks.gsu.edu/phy_astr_diss

Part of the Astrophysics and Astronomy Commons, and the Physics Commons

Recommended Citation

Trippe, Margaret, "A Multi-Wavelength Investigation of Seyfert 1.8 and 1.9 Galaxies." Dissertation, Georgia State University, 2009.
https://scholarworks.gsu.edu/phy_astr_diss/35

This Dissertation is brought to you for free and open access by the Department of Physics and Astronomy at ScholarWorks @ Georgia State University. It has been accepted for inclusion in Physics and Astronomy Dissertations by an authorized administrator of ScholarWorks @ Georgia State University. For more information, please contact scholarworks@gsu.edu.

A MULTI-WAVELENGTH INVESTIGATION OF SEYFERT 1.8 AND 1.9 GALAXIES

by

MARGARET L. TRIPPE

Under the Direction of D. Michael Crenshaw

ABSTRACT

We focus on determining the underlying physical cause of a Seyfert galaxy's appearance as type a 1.8 or 1.9. Are these "intermediate" Seyfert types typical Seyfert 1 nuclei reddened by central dusty tori or by nuclear dust lanes/spirals in the narrow-line region? Or, are they similar to NGC 2992, objects that have intrinsically weak continua and weak broad emission lines? Our study compares measurements of the reddenings of the narrow and broad-line regions with each other and with the X-ray column derived from *XMM Newton* $0.5 - 10$ keV spectra to determine the presence and location of dust in the line of sight for a sample of 35 Seyfert 1.8s and 1.9s. From this, we find that Seyfert 1.9s are an almost equal mix of low-flux objects with unreddened broad line regions, and objects with broad line regions reddened by an internal dust source, either the torus or dust structures on the same size scale as the narrow line region. The 1.9s that recieved this designation due to a low continuum flux state showed variable type classifications. All three of the Seyfert 1.8s in our study are probably in low continuum states. Many objects have been misclassified as Seyfert 1.8/1.9s in the past, probably due to improper [N II]/Hα deconvolution leading to a false detection of weak broad Hα.

INDEX WORDS: Active galaxies, Seyfert galaxies, Optical spectroscopy, X-ray spectroscopy, Astronomical dust

A MULTI-WAVELENGTH INVESTIGATION OF SEYFERT 1.8 AND 1.9 GALAXIES

by

MARGARET L. TRIPPE

A Dissertation Submitted in Partial Fulfillment of Requirements for the Degree of

Doctor of Philosophy

in the College of Arts and Sciences

Georgia State University

2009

Copyright by
Margaret L. Trippe
2009

A MULTI-WAVELENGTH INVESTIGATION OF SEYFERT 1.8 AND 1.9 GALAXIES

by

MARGARET L. TRIPPE

Committee Chair:	D. Michael Crenshaw
Committee:	Matthias Dietrich Xiaochun He H. Richard Miller Paul Wiita

Electronic Version Approved:

Office of Graduate Studies
College of Arts & Sciences
Georgia State University
August 2009

TABLE OF CONTENTS

LIST OF TABLES

LIST OF FIGURES

LIST OF ABBREVIATIONS

ADU	Analog Digital Unit
AGN	Active Galactic Nuclei
BLR	broad line region
CCD	Charged Coupled Device
CTIO	Cerro Tololo Inter-American Observatory
EPIC	European Photon Imaging Counter
ESO	European Southern Observatory
FWHM	full-width at half-maximum
HST	*Hubble Space Telescope*
IDL	Interactive Data Language
IR	infrared
IRAF	Image Reduction and Analysis Facility
IRS	Infrared Spectrograph
ISM	interstellar medium
KPNO	Kitt Peak National Observatory
LINERs	low ionization emission-line regions
LOS	line-of-sight
MAST	Multimission Archive at Space Telescope
NASA	National Aeronautic and Space Administration
NED	NASA Extragalactic Database

NGC	New General Catalog
NLR	narrow line region
NTT	New Technology Telescope
P.A.	Position Angle
PAH	polycyclic aromatic hydrocarbons
pc	parsecs
PI	Principal Investigator
PSF	point spread function
QSO	quasi-stellar object
quasars	quasi-stellar radio sources
RXTE	*Rossi X-ray Timing Explorer*
SDSS	Sloan Digital Sky Survey
SED	spectral energy distribution
SMBH	supermassive black hole
STIS	Space Telescope Imaging Spectrograph
UGC	Uppsala General Catalogue
UV	ultraviolet
WFPC2	Wide Field Planetary Camera 2
XMM	*X-ray Multi-Mirror Mission*
***XMM*-SAS**	XMM Science Analysis Software

– 1 –

Introduction to AGN

1.1 The Discovery of AGN

An active galactic nucleus, or AGN, is a bright point source in the center of an otherwise normal galaxy (see Fig. 1.1). In fact, many AGN have luminosities that rival or exceed those of all the hundreds of billions of stars in the host galaxies in which they reside. The light from these bright galactic centers cannot be attributed to stars; unlike stars, which emit most of their light at optical or near-optical wavelengths, AGN emit powerfully across a much larger swath of the electromagnetic spectrum, from high energy X-rays to low-energy radio waves. As a consequence of this broad-spectrum emission, AGN were discovered and classified separately at different wavelengths as technological advances in the observation of each part of the spectrum were made.

AGN were first discovered in optical light. Edward Fath, in his dissertation work on "spiral nebulae", was the first to describe the optical spectrum of an AGN: a normal galaxy spectrum with absorption features from stars, that also showed six strong emission lines, identifiable with the lines observed in gaseous nebulae (Fath 1909). Edwin Hubble noted two more galaxies with similar emission lines in his famous study of "extragalactic nebulae" in 1926, but it was not until almost two decades later that the first systematic study of these objects was done by Carl Seyfert, who obtained spectra of a sample of galaxies with high central surface brightnesses (Seyfert 1943). He found that the spectra of several of these galaxies were dominated by high-excitation, broad (relative to stellar absorption lines) nuclear emission lines, similar to those seen by Fath and Hubble (Peterson 1997). Many more

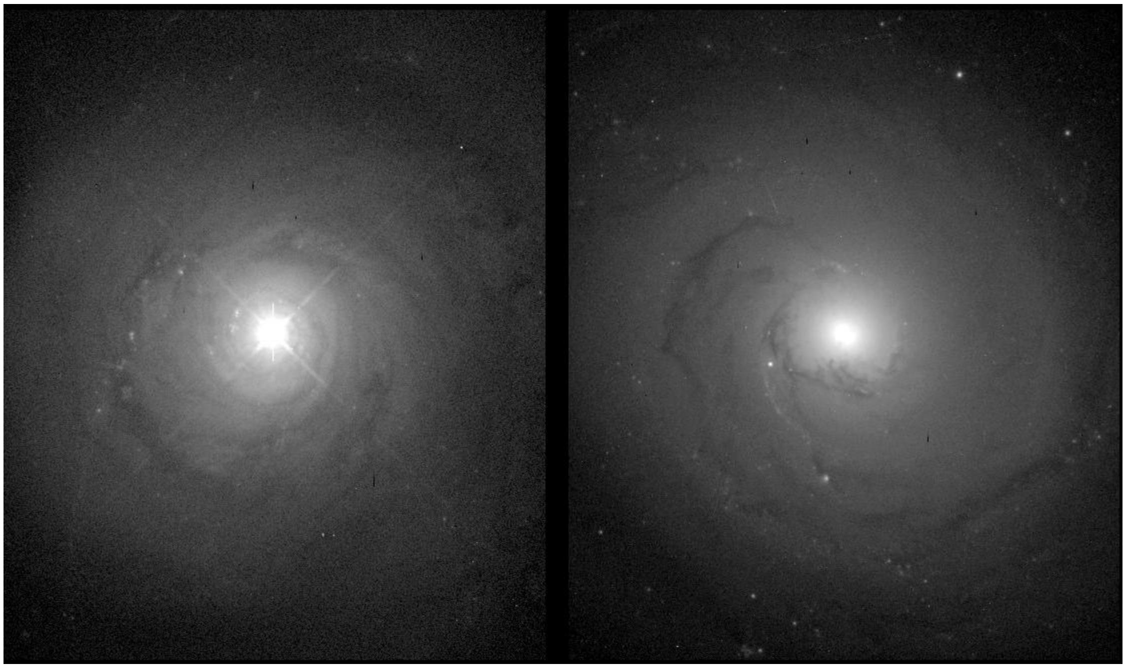

Figure 1.1 Images of the active galaxy NGC 5548 (left panel) and the quiescent galaxy NGC 3277 (right panel), from http://www.astr.ua.edu.

Seyfert galaxies, as we call objects with similar properties today, were discovered in a similar way as larger systematic spectroscopic searches were made of high central surface brightness galaxies. Schmidt camera objective prism surveys, most notably by Benik Markarian in the 1960s, identified galaxies with a strong UV excess (Markarian 1967, 1969a,b) and led to the spectroscopic identification of even more Seyferts. Seyfert galaxies are still being discovered today, as large surveys such as the Sloan Digital Sky Survey (SDSS) obtain spectra of large swaths of the sky.

AGN were re-discovered in the radio as the result of the radio surveys that began in the 1950s. The positions of some of these radio sources were found to be coincident with objects that appeared to be stars on normal photographs (for example, see Baade & Minkowski 1954). However, the spectra of these sources were puzzling. While unambiguously non-stellar, they showed strong broad emission lines that could not be matched with the emission lines known to come from gaseous nebulae. Maarten Schmidt solved the riddle of these so-called quasi-stellar radio sources (or quasars) in 1963, realizing that the emission lines seen in the spectrum of the radio source 3C 273 were actually the hydrogen Balmer series at the (then) extravagant redshift of $z = 0.158$ (Schmidt 1963). It was eventually realized that these quasars are high-luminosity analogs of the nearby Seyfert galaxies, observed from a such a great distance that the host galaxy cannot be detected. It was not long until many radio-quiet objects with similar properties were found when searches for quasars using optical selection techniques were begun.

The classes we use today to describe AGN with similar characteristics are relics of their separate discovery and study in the optical and radio regimes. For instance, AGN are sometimes classified based on the appearance of their optical spectra, sometimes by their optical luminosity, and sometimes by their radio luminosity/morphology. It is therefore common for an AGN to have more than one classification, and this classification may differ depending upon the method of its detection. The main classes of AGN generally recognized today are quasars (high luminosity radio loud AGN), quasi-stellar objects or QSOs (high luminosity radio quiet AGN), blazars (highly variable radio loud AGN), radio galaxies (radio loud AGN), Seyferts (low luminosity radio quiet AGN), and Low Ionization Nuclear Emission-line Regions or LINERS (very low luminosity AGN). My dissertation work focuses on Seyferts.

1.2 Optical Classification of Seyferts

Seyfert galaxies are relatively nearby, low-luminosity AGN; $M_B > -21.5$ is the standard criterion used to distinguish them from quasars (Schmidt & Green 1983). Their apparent closeness is a selection effect due to their low luminosity, and although most "classic" Seyferts have $z \leq 0.1$, many are known to exist at larger redshifts from recent surveys such as SDSS. While Seyferts were originally found as galaxies with high surface brightness nuclei that emit strong line emission, the meaning of this label has evolved to imply the presence of high-ionization emission lines in their optical spectra, a characteristic which distinguishes them from non-AGN galaxies with nuclear star forming regions. These AGN tend to be found in gas-rich early Hubble type (Sa, SBa, SBb) disk galaxies (Heckman 1978). It has been suggested (Simkin et al. 1980) that structures induced by mergers or other gravitational interactions with nearby galaxies feed the nuclear activity from gas in the disk. About 1% of all spiral galaxies host Seyfert nuclei (Osterbrock & Ferland 2006), thus making them the second most common type of AGN in the local universe after LINERs.

Astronomers seem unable to resist separating the objects they find into two basic types (e.g., supernovae, stellar populations), and Seyferts too are customarily divided into two types, following the scheme of Khachikian & Weedman (1971), based on their emission-line spectra. All Seyferts have optical spectra that show narrow permitted and forbidden emission lines. Those Seyferts whose spectra show additional broad permitted emission lines are classified as type 1. Those whose spectra manifest only the narrow emission lines are classified as type 2. Furthermore, the spectra of type 2 contrast sharply with type 1 in that they exhibit only weak, mostly stellar continua, while the spectra of type 1 Seyferts are characterized by strong non-stellar continua. Figure 1.2 shows examples of the spectra of each.

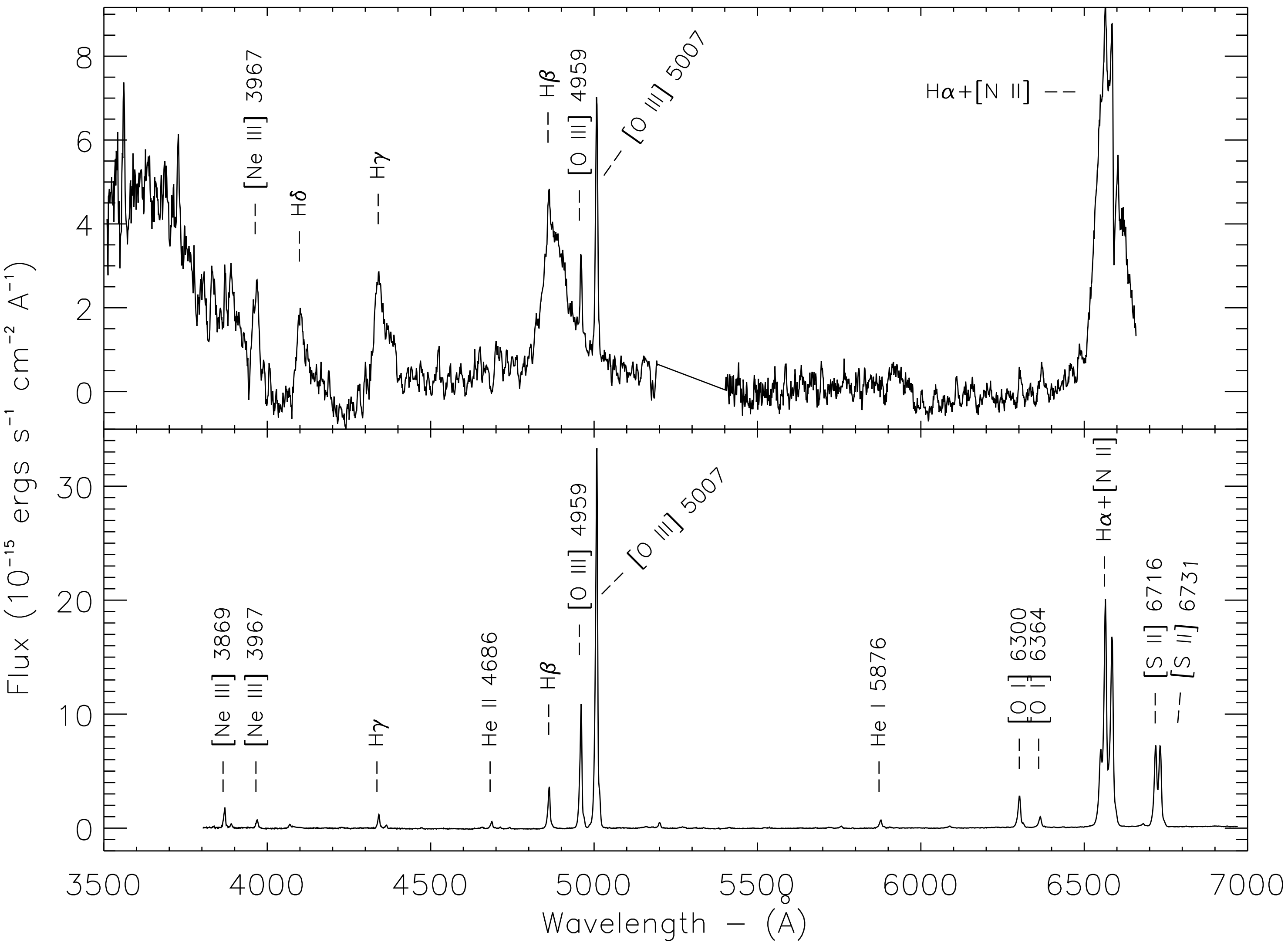

Figure 1.2 Sample spectrum of a type 1 Seyfert, Mrk 1018 (top panel), and of a type 2 Seyfert, NGC 4388 (bottom panel).

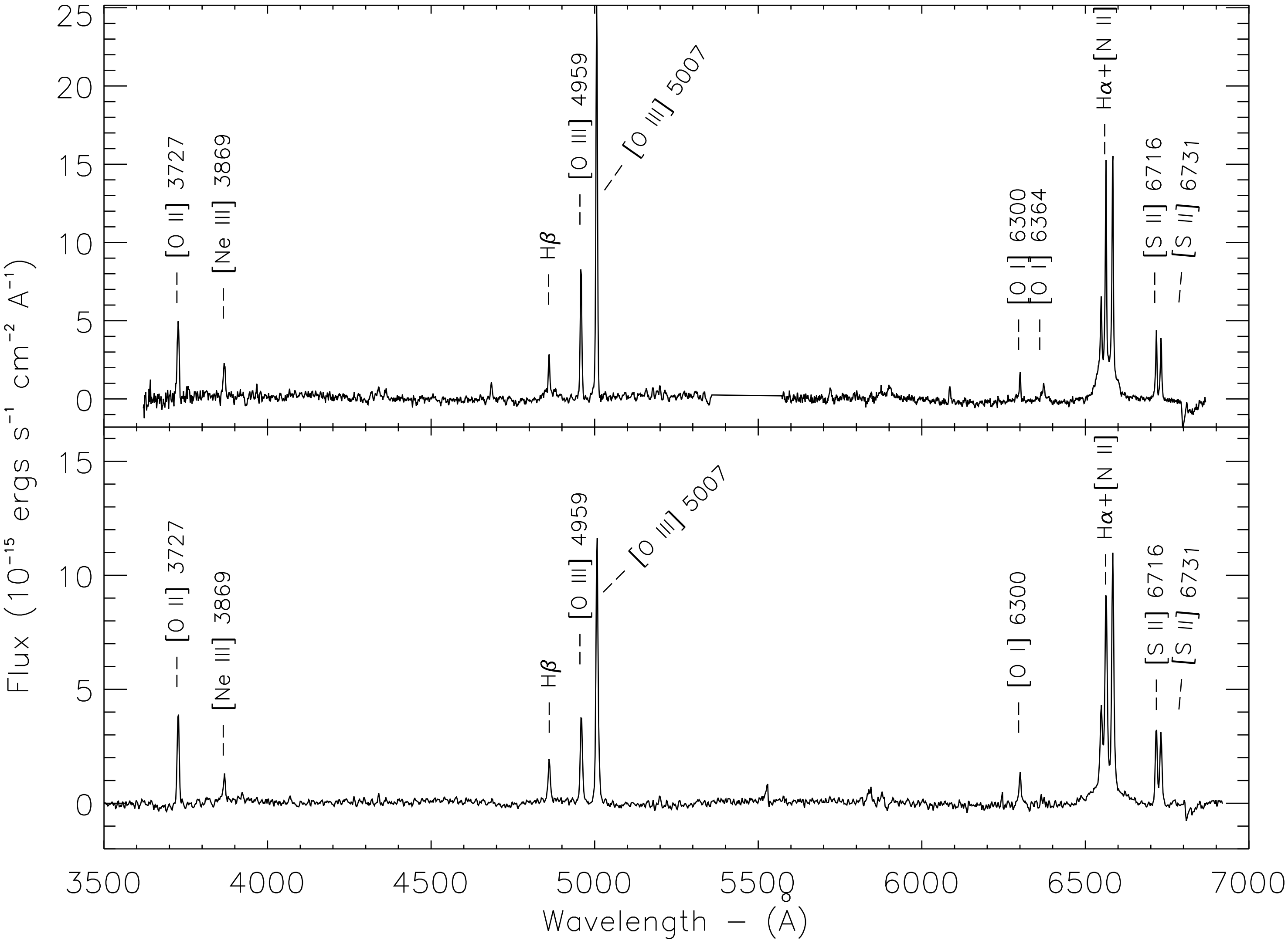

Figure 1.3 Sample spectrum of type 1.8 Seyfert, Mrk 1126 (top panel), and of a type 1.9 Seyfert, NGC 3786 (bottom panel).

Some Seyferts, however, have characteristics that fall in between these two types. Osterbrock (1977) added several intermediate types to our classification system to describe these galaxies with composite spectral features: Seyfert 1.2, 1.5, 1.8, and 1.9. The larger the numerical value of the class, the weaker the featureless continuum and broad components of the permitted lines. Maiolino & Rieke (1995) set quantitative bounds on the classes proposed by Osterbrock, and these are used to define each class throughout the rest of this dissertation (note that [O III] refers to the [O III] $\lambda5007$ emission line in these definitions):

- Seyfert 1: Objects showing a broad Hβ emission line with [O III]/Hβ < 0.3
- Seyfert 1.2: Objects showing a broad Hβ with $0.3 <$ [O III]/Hβ < 1
- Seyfert 1.5: Objects showing a broad Hβ with $1 <$ [O III]/Hβ < 4
- Seyfert 1.8: Objects showing a broad Hβ with $4 <$ [O III]/Hβ (see Fig. 1.3)
- Seyfert 1.9: Objects not showing broad Hβ, but having broad Hα (see Fig. 1.3)

Line ratios are also used as criteria to distinguish Seyferts from other objects with similar spectra, such as LINERs and starburst (H II) galaxies (Baldwin et al. 1981; Kewley et al. 2006). Figure 1.4 shows a diagram of diagnostic line ratios from Veilleux & Osterbrock (1987) used to separate these classes. The abscissa on this diagram is the ratio of the flux of the [O I] $\lambda6300$ line to the flux of narrow Hα, a measure of the extent of the "partially-ionized zone" created by high-energy photons. The ordinate is the ratio of the flux of the [O III] $\lambda5007$ line to the flux of narrow Hβ, a proxy for the level of ionization. Seyfert galaxies fall into the upper-right side of this diagram, indicating they have high levels of ionization and large partially-ionized zones. LINERs, with their weaker continua and thus lower ionizations, fall below the Seyferts on the right. Starburst galaxies fall to the left of both of these classes;

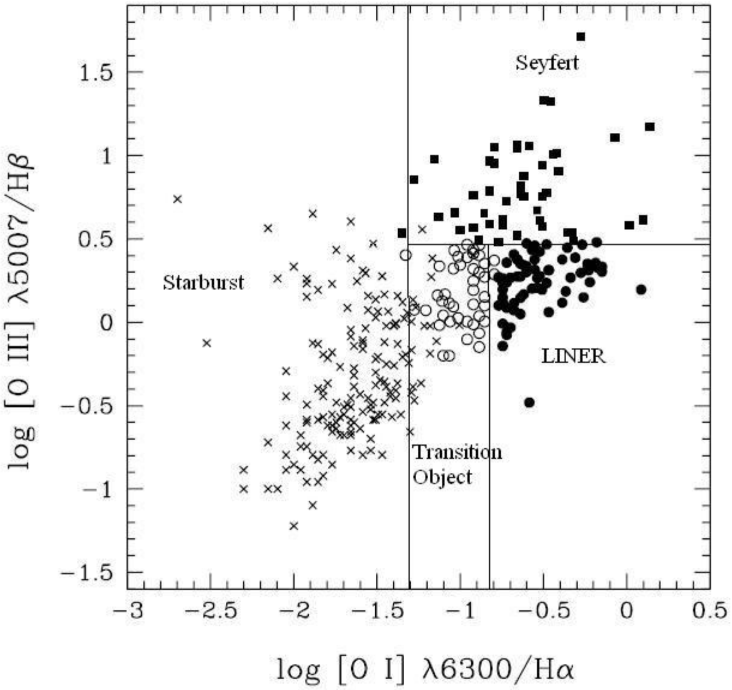

Figure 1.4 An example of an emission line ratio diagnostic diagram used to help classify galaxies, from Ho et al. (1997a).

the thermal continua of even the hottest stars contain very few high-energy photons relative to the continua of AGN. The objects whose [O I]/Hα ratios fall between the LINER and starburst regions, and whose [O III]/Hβ ratios fall below the Seyfert region, are classified as “transition objects”; these are objects whose spectra are apparently a combination of LINER and starburst.

1.3 General Structure of an AGN

The different types of AGN are all believed to be powered by the gravitational energy released as material in an accretion disk of hot gas spirals into the supermassive black hole (SMBH), usually between 10^6 - 10^9 $M_\odot$, at the center of the host galaxy. As the gas spirals inward, it is heated to high temperatures by friction and dissipative forces within the disk and emits large amounts of radiation. The structure of an accretion disk depends upon many parameters: magnetic field strength, accretion rate, and the presence/absence of a disk corona or jets (Peterson 1997), but in general they are thought to be thermal structures emitting radiation that peaks in intensity in the UV, but also includes X-ray and optical wavelengths. Hovering around the disk, a hot coronal gas is expected to be present, and it is the up-scattering of the UV photons from the disk by these hot coronal electrons that is expected to produce the hard X-rays observed in radio quiet AGN (e.g., Wang & Netzer 2003).

The accretion disk-black hole system is surrounded by a number of dense ($n_H = 10^8 - 10^{11}$ cm^{-3}) clouds of gas within a few light-days to a few light-weeks, inferred from the optical spectra of Seyfert 1 galaxies and quasars. These clouds are photoionized by the continuum produced by the accretion disk, and emit line radiation by the recombination of electrons with ions, as well as the collisional excitation of bound electrons, and the electrons' subsequent downward energy-level transitions. No forbidden emission is produced by these clouds; their high densities lead to collisional de-excitation of the energy levels in ions which give rise to such emission. The emission lines of these clouds are Doppler-broadened by their movement in the gravitational field of the black hole to have full widths at half-maxima (FWHM) in the range of $\sim 800 - 8,000$ km s^{-1}, and thus these clouds are said to exist in the "broad-line region" (BLR).

Beyond the BLR, the AGN photoionizes the surrounding low-density ($n_H = 10^3 - 10^6$ cm^{-3}) clouds of gas within several hundreds of parsecs, a large enough spatial scale for these clouds/knots to be resolved in *HST* optical images. These ionized regions are usually seen to take the shape of a bicone with its apex centered on the central engine (Tadhunter & Tsvetanov 1989; Das et al. 2005). The emission lines from this region are not broadened by the influence of the central supermassive black hole. They have FWHM of only $\sim 200-500$ km s^{-1}, and thus this area is termed the "narrow-line region" (NLR). Both permitted and forbidden line emission is produced by the rarefied gas in the NLR. While much of the line emission is similar to that observed in other types of photoionized nebulae, such as planetary nebulae or H II regions, the range in ionization species in the NLR of Seyferts is greater than in these other sources, due to the relative hardness of the ionizing continuum. For example, although [O II], [O III], [N II] and [Ne III] are observed, [O I], [N I], [Ne V], [Fe VII], and [Fe X] are also consistently present (Osterbrock & Ferland 2006).

1.4 Unified Models of Seyfert Galaxies

An orientation-dependent scheme to explain the differences in the properties of type 1 and type 2 AGN was first hinted at by Rowan-Robinson (1977), who suggested Seyfert 1 and Seyfert 2 galaxies to be intrinsically similar objects, but Seyfert 2s suffer from greater extinction than Seyfert 1s. Later X-ray studies, such as Lawrence & Elvis (1982), supported this idea by revealing the central X-ray sources in Seyfert 2s are attenuated by significantly larger gas column densities than Seyfert 1s. The first indication of the geometry of the obscuring regions was discovered by Antonucci (1984) using optical spectropolarimetric observations of radio galaxies. They found the polarization of $\vec{E}$ in narrow-line radio galaxies to be aligned approximately perpendicular to their radio jets, while in broad-line radio galaxies the polarization tended to be closer to parallel to the radio jets (Tadhunter 2008). They realized that these properties could be explained in terms of scattered AGN light, with parallel alignments due to equatorial scattering by a disk viewed obliquely and perpendicular alignments due to polar scattering by material in the opening of an optically thick torus-like structure (Tadhunter 2008). The paper presenting these results (Antonucci 1984) contains the first sketch of the central obscuring torus which is now the centerpiece of unified schemes. Antonucci & Miller (1985) later used spectropolarimetric observations to show broad permitted line components in the polarized spectrum of the nearby bright Seyfert 2 galaxy NGC 1068, thought to be due to the scattering of the nuclear light into our line of sight by dust or electrons, confirming the idea that it is a Seyfert 1 nucleus hidden behind optically thick material.

The sketch of Urry & Padovani (1995) shown in Fig. 1.5 summarizes the main ideas of the orientation-dependent unified model. The toroidal obscuration in this picture is now thought to be a parsec-scale (Nenkova et al. 2008) configuration of individual optically-thick clouds (Krolik & Begelman 1988; Nenkova et al. 2002), as opposed to the smooth distribution portrayed in Fig. 1.5. However, the dust and gas properties of this material are not yet well known.

1.5 Enter Seyfert 1.8s and 1.9s

Seyfert 1.8s and 1.9s were originally discovered and labeled by Donald Osterbrock. Working on a spectral survey of Seyferts at Lick Observatory, he noted five AGN with spectra that fell in between type 1 and type 2 in appearance: Mrk 423, Mrk 516, Mrk 609, Mrk 1018, and V Zw 317 (Osterbrock 1981). Those with weak broad Hα and Hβ lines he called type 1.8, and those with only weak broad Hα he called type 1.9. He noted

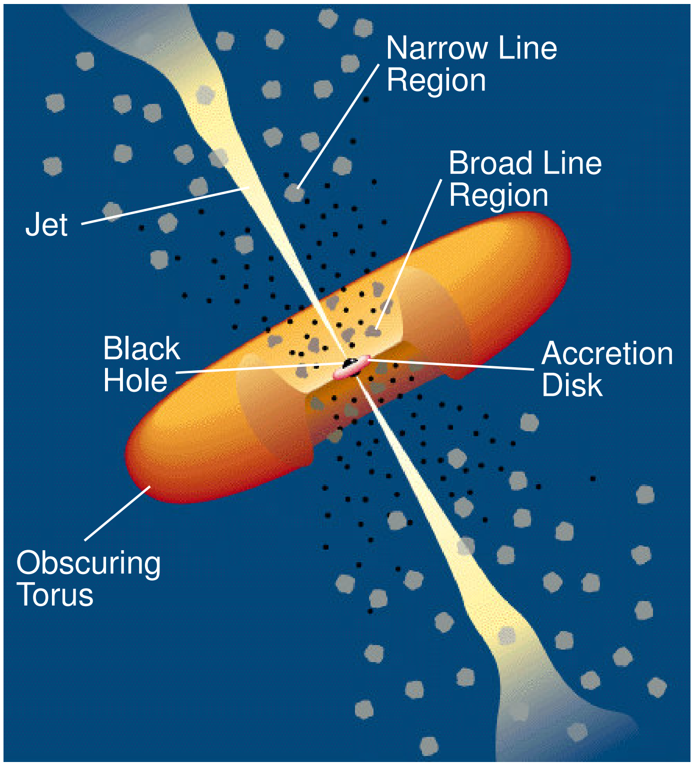

Figure 1.5 A highly schematic but fairly complete picture of the unified model of AGN. According to this model, type 1 AGN are seen along a line of sight that allows a clear view of the central region of the AGN, while in type 2's our view of this central region is blocked by the "obscuring torus" (credit: Urry & Padovani 1995).

that these AGN appeared to have large broad Balmer decrements, i.e., that the ratios of the broad Hα/Hβ emission lines were greater than observed in Seyfert 1 galaxies, and suggested this to be due to the extinction of the BLR by dust. In terms of the unified model, this would indicate a line of sight that grazes the outer edge of the obscuring dusty torus.

However, Rudy & Willner (1983) later questioned this explanation for the appearance of 1.8/1.9s, when they produced theoretical models showing that large Balmer decrements could alternatively be produced if the broad-line clouds themselves have fairly low optical depths and ionization parameters, negating the need for dusty material external to the broad-line clouds (Rudy & Willner 1983). This became known as the "(τ, U)" theory (Goodrich 1995), and was supported by observations of broad Lyα lines in a couple of 1.9s (Rudy et al. 1988).

Since these initial studies, there have been several attempts to verify which of these theories is predominantly true. R. Goodrich obtained spectropolarimetric observations of NGC 2622, NGC 7603, and Mrk 1018. He found "the changes in flux of the broad lines and the continuum near H-alpha and H-beta are consistent with changes in the extinction in all cases" (Goodrich 1989), indicating that the appearance of these objects was probably dependent on dust in the torus. Goodrich continued his investigation by measuring the Paα flux of a sample of 1.8/1.9s; this study showed some 1.8/1.9s have Paα fluxes consistent with dust reddening, but others are consistent with the (τ, U) theory (Goodrich 1990). Another study (Goodrich 1995) of variability of the broad-line components of Seyfert 1.8/1.9s again gave mixed results. NGC 7603, Mrk 993, and Mrk 1018 all seemed to show variability in their Hα lines consistent with the same change in reddening of their Hβ lines, and thus their spectral variability was attributed to the motions of clouds of dust (presumably in the torus) in front of the nucleus. On the other hand, NGC 2622, Mrk 883 and UGC 7064 underwent changes inconsistent with a simple change in reddening. Further support for the reddening of the BLR by dust came from the X-ray regime, with Risaliti et al. (1999) finding that the gas columns in Seyfert 1.8 and 1.9 galaxies are significantly lower than in Seyfert 2s, though still larger than in Seyfert 1s.

Thus, the issue of whether Seyfert 1.8s and 1.9s have high broad Balmer decrements due to extinction by dust has remained unresolved. Seyfert 1.8 and 1.9 galaxies are nearby and relatively bright. If they are indeed being affected by a modest, and therefore measurable, amount of extinction by the torus, they would provide excellent testbeds to study the dust properties of the torus, which are crucial to understanding the true spectral energy distributions of AGN and environments in the immediate vicinity of SMBHs.

Our study to resolve this issue began with NGC 2992.

– 2 –

Extreme Long-term Optical Variability in NGC 2992

2.1 Introduction to NGC 2992

NGC 2992 is a nearby galaxy with redshift $z = 0.00771$ (Keel 1996) that has been well studied in all wavelength regimes. Optical spectra of the nucleus show it to be a Seyfert galaxy, but its type classification has been observed to vary conspicuously in the past, leading to classifications ranging from Seyfert 1 to Seyfert 2. Early spectra published by Shuder (1980), Veron et al. (1980), and Ward et al. (1980) all show the presence of a weak broad Hα component but no detectable corresponding broad Hβ component, leading to its original classification as a Seyfert 1.9. When it was observed in 1994 by Allen et al. (1999), however, it had apparently lost its broad Hα component and was classified as a Seyfert 2. A 1999 spectrum taken by Gilli et al. at the ESO NTT showed it to have regained its broad Hα emission (Gilli et al. 2000). Gilli et al. also correlated the presence of broad Hα with the galaxy's X-ray flux; they found NGC 2992 to have been in a high X-ray state when it was initially observed in the late 1970s and early 1980s, but that the X-ray flux had been slowly decreasing over time and was at a minimum when Allen et al. observed its optical spectrum in 1994. At the time of Gilli et al.'s observation of broad Hα in 1999, they used BeppoSAX data to show that NGC 2992 had returned again to its previous active X-ray state, and postulated these variations were due to different phases of rebuilding of the central accretion disk. The interesting history of variation of this object, as well as its intermediate type classification, induced us to choose it as the subject of an optical monitoring campaign.

2.2 Observations of NGC 2992 and Data Reduction

We monitored NGC 2992 for about a year and a half, from 2006 January to 2007 June, using the R-C spectrograph on the Cerro Tololo Inter-American Observatory (CTIO) 1.5-m telescope in Chile. We obtained observations on a monthly basis, except for the period when the galaxy was too close to the Sun to be observed. Spectra were observed using two different settings: one with a grating with a resolution of 4.3 Å (giving a dispersion of ∼1.47 Å /pixel) to take blue spectra from approximately $3660 - 5440$ Å to include Hβ, and the other with a resolution of 3.1 Å (∼1.10 Å /pixel dispersion) and a Schott GG 495 filter to take red spectra from approximately $5650 - 6970$ Å to include the Hα line. We used a slit at a 90° P.A. centered on the galaxy's nucleus to obtain accurate absolute fluxes on photometric nights. The majority of the spectra were taken using a $2''$ slit width, but observations were also taken on nights when other slit widths were in use. Table 2.1 chronicles the dates and settings of our observations. To eliminate cosmic ray hits, we took three exposures each time the galaxy was observed. The stars LTT 4364 and Feige 110 were also observed with these settings for the purpose of flux calibration. The spectra were then reduced and flux calibrated using standard IRAF reduction packages for long-slit spectroscopy. Since the spectra were seen to have remained essentially constant with time, we averaged them to obtain a higher S/N ratio in our final resulting spectrum. As shown in Fig. 2.1, the final spectrum looks like that of a Seyfert 2, in that only narrow emission lines are present and it exhibits strong stellar absorption features.

In order to assess the impact of using slits of different sizes, we compared the integrated fluxes of the [S II] λ6716 and λ6731 lines in a spectrum taken with the $2''$ slit width with the

Table 2.1. Log of Observations

Date (U.T.)	Wavelength Coverage (Å)	Exposure Time (s)	Slit Width (arcsec)
2006 Jan. 9	3660-5440	1,200	2.0
2006 Jan. 11	5650-6970	900	2.0
2006 Feb. 2	5650-6970	900	1.5
2006 Feb. 3	3660-5440	1,200	2.0
2006 Mar. 9	5650-6970	900	3.3
2006 Mar. 10	3660-5440	1,200	3.3
2006 Apr. 6	3660-5440	1,200	2.0
2006 May 8	3660-5440	1,200	1.5
2006 May 9	5650-6970	900	4.0
2006 Jun. 4	5650-6970	900	4.0
2006 Jun. 7	3660-5440	1,200	2.0
2006 Nov. 29	3660-5440	1,200	2.0
2006 Dec. 17	5650-6970	900	2.0
2006 Dec. 18	3660-5440	1,200	2.0
2007 Jan. 16	5650-6970	900	2.0
2007 Jan. 17	3660-5440	1,200	2.0
2007 Feb. 9	5650-6970	900	4.0
2007 Feb. 8	3660-5440	1,200	4.0
2007 Apr. 3	5650-6970	900	2.0
2007 Mar. 30	3660-5440	1,200	2.0
2007 Jun. 21	3660-5440	1,200	4.0
2007 Jun. 26	5650-6970	900	2.0

integrated fluxes of the lines in a spectrum taken with the 4″ slit width. We found there to be only about a 20% difference between the two. The final spectrum we present is an average of all 10 observations, only 4 of which were made with slits larger than 2″. We therefore estimate the fluxes of these narrow lines to be increased by only $(4/10) \times 22\% \approx 9\%$ over what they would be if a 2″ slit width had been used exclusively throughout the observations.

To obtain a spectrum suitable for measurement of nuclear emission lines, the light from the nucleus must be isolated from that of the host galaxy. We removed the host galaxy spectrum from the CTIO data by subtracting off a normal galaxy spectrum (from Kinney et al. 1996) scaled to give the optimum fit to the observed average spectrum's continuum

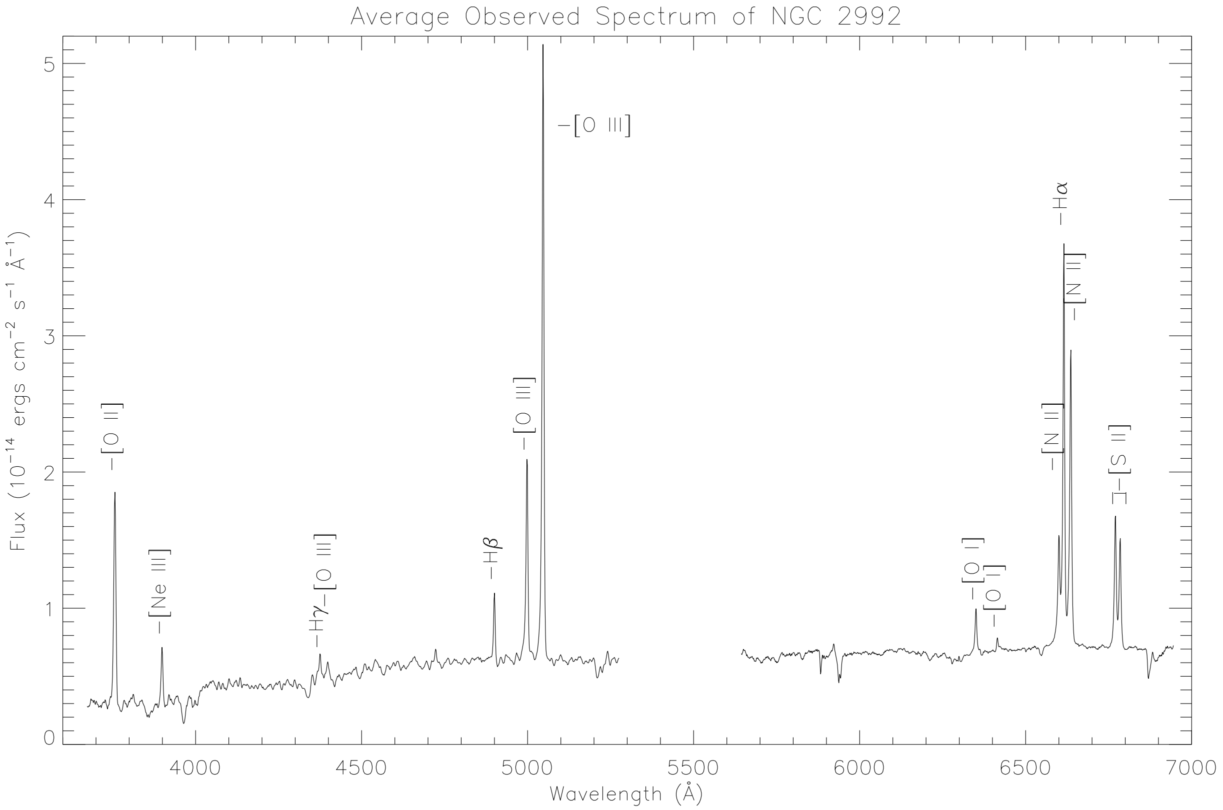
Average Observed Spectrum of NGC 2992

Figure 2.1 The average observed spectrum of NGC 2992.

and absorption line features. The remaining continuum was fit by a power-law ($F_\nu \propto \nu^\alpha$) with $\alpha = -1.83$ and subtracted off, but with little effect, as this component was very weak, consistent with the rest of the evidence that NGC 2992 was a Type 2 Seyfert at the time of the CTIO observations. Figure 2.2 shows the resulting spectrum after these subtractions.

2.3 Data Analysis

We determined the reddening of the narrow-line region from the narrow components of Hα and Hβ, assuming their intrinsic ratio to be equal to the Case B recombination value of $H\alpha/H\beta = 2.9$ (Osterbrock & Ferland 2006), and further assuming the standard Galactic

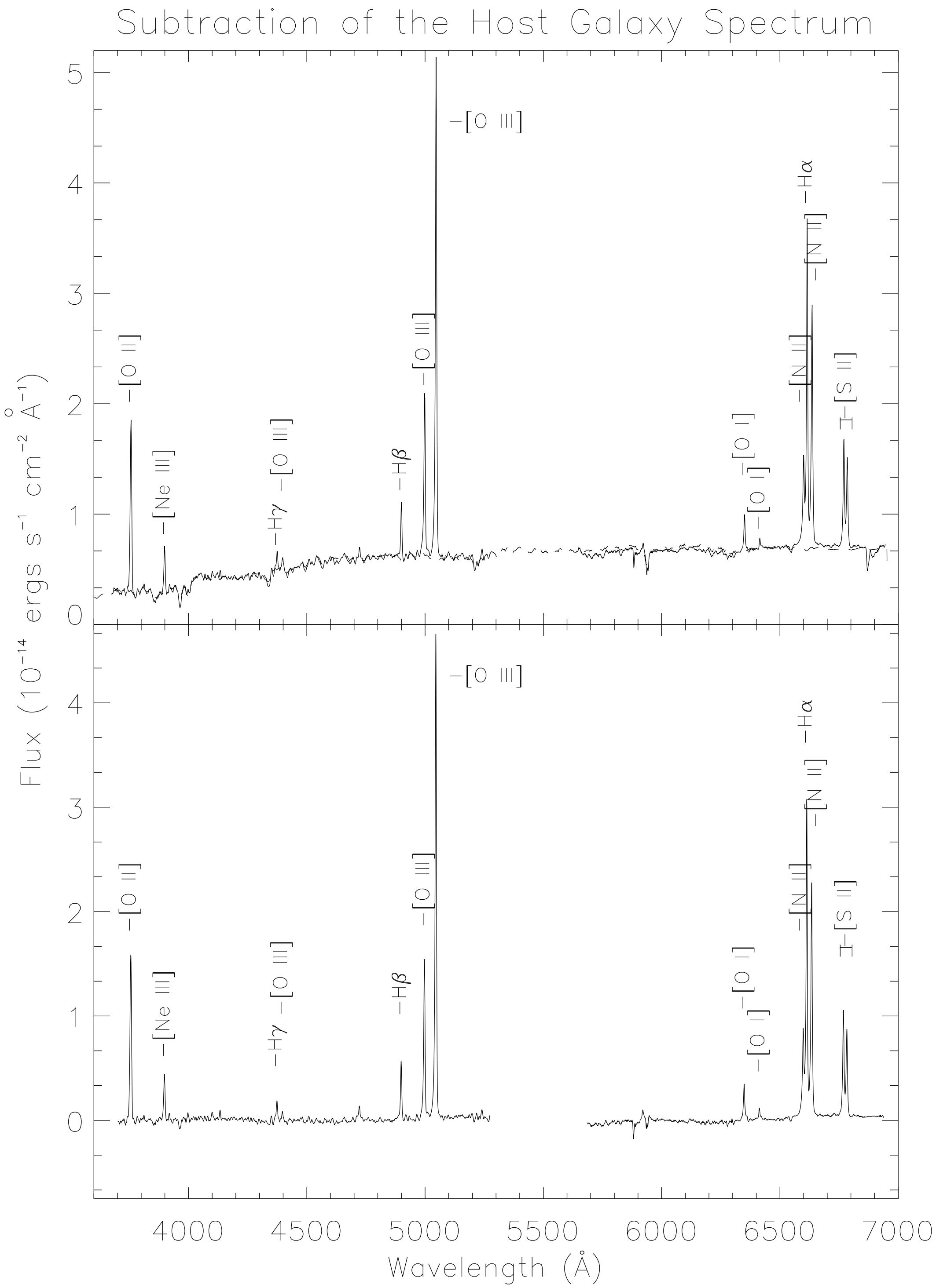

Figure 2.2 The top panel shows the average observed spectrum of NGC 2992 with overplot of host galaxy fit (dashed line); the bottom panel displays the observed spectrum after subtraction of the host galaxy fit.

Table 2.2. Narrow-line ratios for NGC 2992

Line	Observed Ratios to Hβ	Dereddened Ratios[a]
[O II] 3727	3.86±0.48	7.09±0.17
[Ne III] 3869	0.93±0.13	1.58±0.80
Hγ 4340	0.85±0.17	1.16±0.17
[O III] 4363	0.67±0.19	0.89±0.20
Hβ 4861[b]	1.00±0.17	1.00±0.17
[O III] 4959	3.68±0.54	3.51±0.54
[O III] 5007	10.27±1.27	9.53±1.30
[O I] 6300	0.77±0.17	0.39±0.15
[O I] 6374	0.18±0.04	0.09±0.03
[N II] 6548	2.21±0.29	1.03±0.28
Hα 6563	6.28±0.79	2.90±0.78
[N II] 6583	5.24±0.65	2.40±0.64
[S II] 6716	2.44±0.30	1.07±0.29
[S II] 6731	1.93±0.24	0.84±0.23

[a] For $E(B-V) = 0.71 \pm 0.11$ mag

[b] The integrated absolute flux of the Hβ line in this spectrum is $33.7\pm4.2 \times10^{-15}$ ergs cm^{-2} s^{-1}

reddening curve of Savage & Mathis (1979) to be applicable. By this method we found $E(B-V) = 0.71 \pm 0.11$ mag, and de-reddened the spectrum accordingly. We give measured values of NGC 2992's observed and de-reddened line ratios relative to Hβ in Table 2.2.

To study the Hα profile, we deblended the narrow [N II] $\lambda\lambda$6548, 6583 Å lines flanking each side of Hα by using the distinctly narrow component of the Hα line as a template for each of the doublet lines in an iterative process. The template was moved to the position of each [N II] line, scaled in width and height to match it, and subtracted off. The height of the line at 6583 Å was set to three times that of the line at 6548 Å based on the ratio of their transition probabilities (Osterbrock & Ferland 2006). The profile before and after

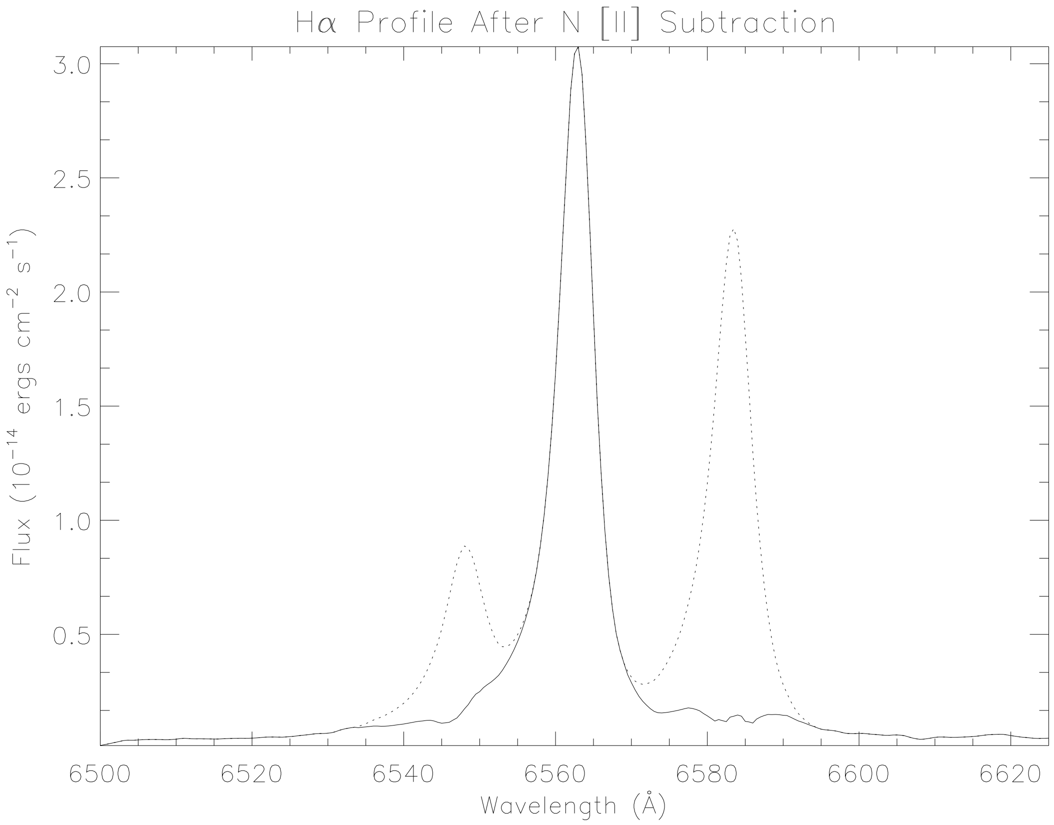

Figure 2.3 NGC 2992's Hα profile before (dotted line) and after (solid line) subtraction of the [N II] doublet.

subtraction of the [N II] lines is shown in Fig. 2.3. If there is a broad component, it is certainly very faint, no more than 30% of the flux of the narrow component.

2.4 Results from NGC 2992

Given its history of extreme variability, NGC 2992 has remained at a remarkably constant low state over the year and a half of our observations. As can be seen from Fig. 2.4 where three representative spectra (from the beginning, middle and end of the campaign) are plotted, NGC 2992 showed no evidence for variation over the observation period. The Hα profile showed no sign of change in any broad component. Furthermore, the continuum did not change over this time period, in line with our conclusion that it was dominated by stellar light.

The observations, when compared with the historical spectra mentioned in the introduction, do at least prove that this Seyfert has undergone yet another dramatic change, from the high flux state it was in when last observed by Gilli et al. in 1999, back to the low state observed by Allen et al. in 1994. Figure 2.5 plots the data from Fig. 8 in Gilli et al. (2000), three spectra all observed with $2''$ slit widths taken over the course of 31 years, along with our new average spectrum around Hα. It can be seen that NGC 2992 lost its broad Hα in 1994, recouped it again by 1999 (as noted by Gilli et al. 2000), but has now lost it again in our spectra.

By using the observed reddening of the narrow-line region, $E(B-V) = 0.71$ mag, and the relation $N_H = 5.2 \times 10^{21} E(B-V)$ cm^{-2} derived by Shull & van Steenberg (1985) for the local ISM, we estimate the column density absorbing the narrow-line region to be $N_H = 3.7 \pm 0.6 \times 10^{21}$ cm^{-2}. This is equivalent, within the error estimates, to the value derived by Gilli et al. from the ratio of narrow $Pa\beta/H\alpha$ of $E(B-V)$ of 0.65±0.19 mag ($N_H = 3.4 \pm 1.0 \times 10^{21}$ cm^{-2}). Gilli et al. also found $E(B-V) = 0.71$±0.19 mag ($N_H = 3.7 \pm 1.0 \times 10^{21}$ cm^{-2}) for the BLR in 1999, using a near IR spectrum exhibiting broad Brγ and Paβ lines. The nearly identical reddenings of the BLR and NLR indicate a dust screen external to the NLR, as suggested by Gilli et al. (2000).

X-ray observations have found absorption values similar to those observed in the optical. Yaqoob et al. (2007) found N_H to be $7.99 \pm 0.60 \times 10^{21}$ cm^{-2} from Suzaku observations in November and December of 2005, only a month before we began our optical monitoring at CTIO. This value is similar to Gilli et al.'s measurement with BeppoSAX of $N_H = 9.0 \pm 0.3 \times 10^{21}$ cm^{-2}, from when the galaxy was in a high X-ray and optical

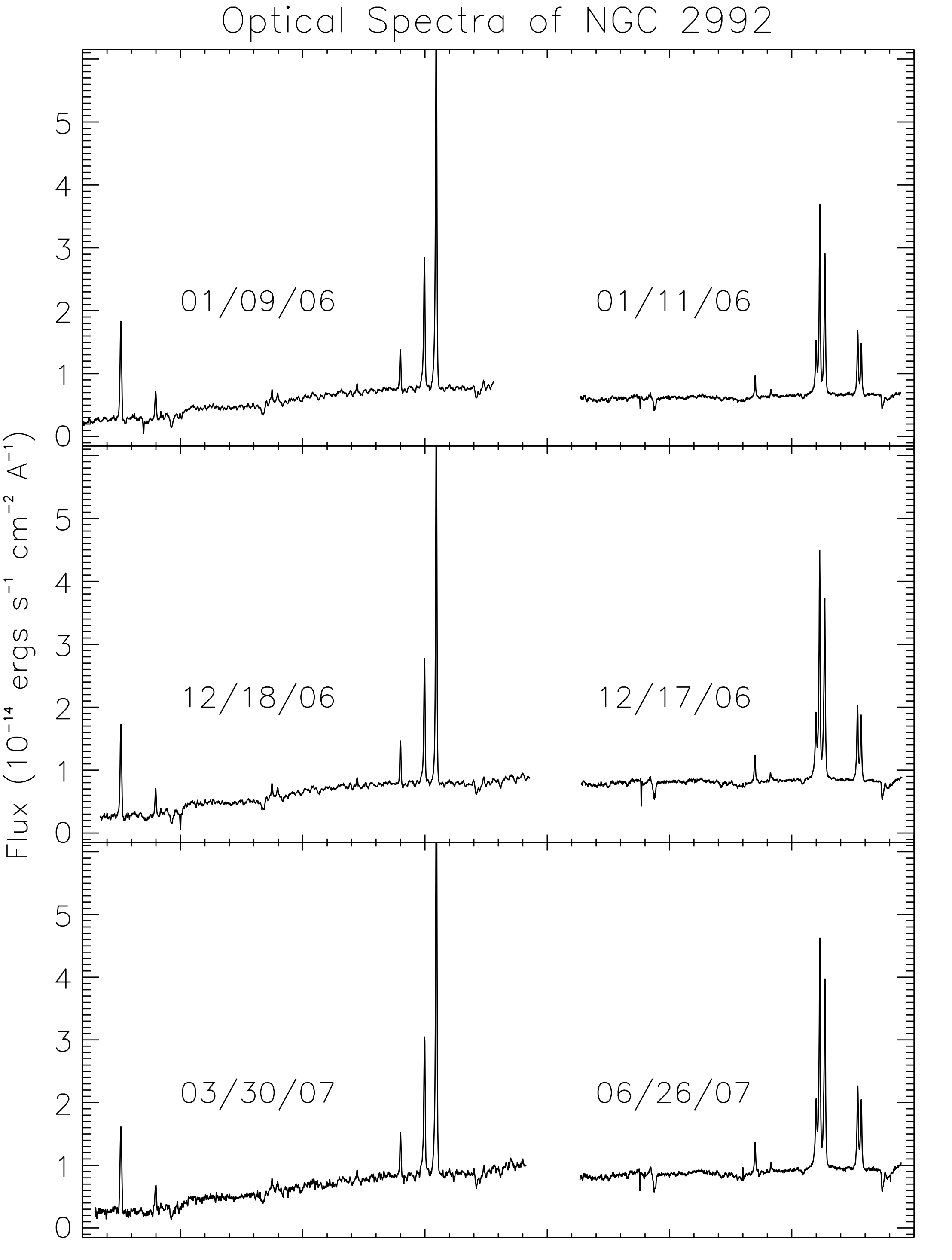

Figure 2.4 Three representative blue and red spectra from the beginning, middle, and end of our monitoring campaign of NGC 2992. The slight differences in absolute flux are likely due to seeing and/or non-photometric conditions, as noted in the text.

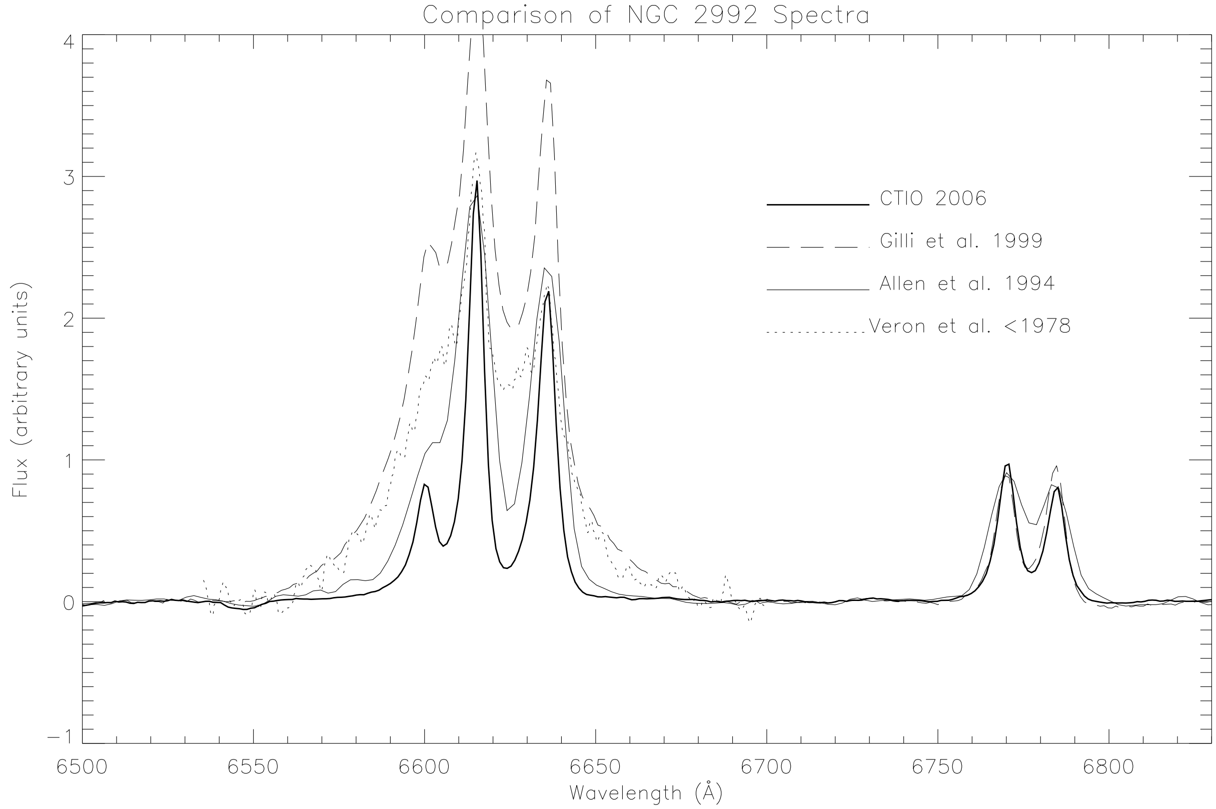

Figure 2.5 The variation of NGC 2992's broad Hα with time. For comparison purposes, we have subtracted the continuum and scaled the spectra in such a way that the narrow [S II] lines, which are expected to remain constant, match. NGC 2992 has dropped back into a low optical flux state, similar to that observed by Allen et al. in 1994, since it was last observed by Gilli et al. in 1999. Many thanks to Roberto Maiolino for providing the optical spectra previous to 2006. (see Gilli et al. 2000).

state. Throughout the history of NGC 2992's observations, the X-ray flux has been seen to vary dramatically, from $f_{2-10keV} = 0.63 \times 10^{-11}$ ergs cm^{-2} s^{-1} observed by Gilli et al. with BeppoSAX in 1997 (Gilli et al. 2000) to $f_{2-10keV} = 8.88 \times 10^{-11}$ ergs cm^{-2} s^{-1} observed by Murphy et al. with RXTE in 2005 (Murphy et al. 2007), but the X-ray column has remained virtually constant at $\sim 10^{22}$ cm^{-2} (Gilli et al. 2000; Colbert et al. 2005; Yaqoob et al. 2007). The observed X-ray columns are two to three times higher than those estimated by the reddening values. This may be due to a lower dust-to-gas ratio than that of our Galaxy, or to a separate dust-free X-ray absorber close to the nucleus.

To investigate the mid-IR properties of NGC 2992, we retrieved and processed its low-resolution Spitzer IRS spectrum from the Spitzer archives (see Deo et al. 2007 for details). As shown in Fig. 2.6, the spectrum exhibits PAH emission features typical of a strong starburst contribution as well as highly ionized narrow lines, such as [O IV] $\lambda 25.89$ μm and [Ne V] $\lambda 14.31$ μm, attributable to the hard ionizing continuum of the central AGN. The spectrum also exhibits a strong silicate 9.7 μm absorption feature, which is typically found in Seyfert galaxies with highly inclined ($b/a < 0.5$) host galaxy disks (Deo et al. 2007). Indeed, the galactic disk of NGC 2992 is highly inclined, with $b/a = 0.31$, according to NED (the NASA/IPAC Extragalactic Database, http://nedwww.ipac.caltech.edu). From the Spitzer spectrum, the trough of the silicate 9.7 μm feature is at an optical depth of $\tau = 0.35$, which corresponds to a reddening of $E(B-V) = 2.1$ based on the relationship for diffuse ISM clouds ($A_V = 18.5\tau_{9.7\mu m}$) given by Roche & Aitken (1984). There are a couple of explanations for this reddening being a factor of $\sim$ 3 higher than the direct values from the BLR and NLR. One possibility is a strong contaminating contribution to the silicate feature from a starburst heavily enshrouded in dust. Another possibility is that the dust may be richer in silicates than Galactic dust, as suggested for the damped Lyα absorber toward AO 0235+164 (Kulkarni et al. 2007).

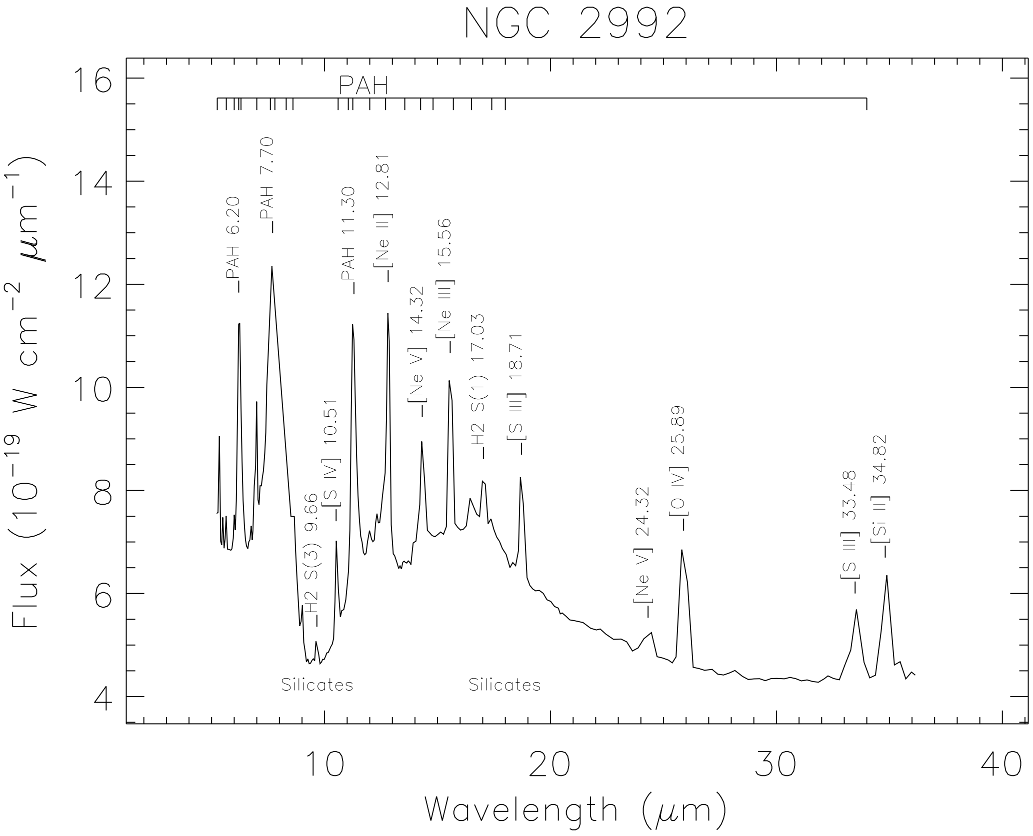

Figure 2.6 Spitzer IRS spectrum of NGC 2992.

2.5 Discussion and Conclusions

In Table 2.3, we give a summary of determinations of reddening and/or hydrogen column densities in the line of sight to different components of the AGN. It is important to keep in mind that the uncertainties quoted in Table 2.3 reflect only measurement errors; systematic uncertainties such as different measurement techniques and instruments are not included. The fact that these column densities derived from different regions all fall within about a factor of three of each other suggests that they are all being reddened by the same source, likely a large-scale dust lane in the host galaxy. An optical Hubble WFPC2 image of the nucleus of NGC 2992 obtained with the F606W filter substantiates this explanation, as it

Table 2.3. Summary of Absorption Determinations

Region	$E(B-V)$	N_H (10^{21}cm^{-2})	Date of Obs.	Reference
X-ray emission region	–	7.99±0.6	2005	Yaqoob et al. (2007)
X-ray emission region	–	9.0±0.3	1998	Gilli et al. (2000)
X-ray emission region	–	14.0±5.0	1997	Gilli et al. (2000)
BLR	0.71±0.19	3.7±0.99	1999	Gilli et al. (2000)
NLR	0.71±0.11	3.7±0.57	2006-2007	This work.
NLR	0.65±0.19	3.4±0.99	1999	Gilli et al. (2000)
External galaxy	2.1±0.20	11.0±1.0	2005	This work.

clearly shows a pronounced hundred-pc scale lane of dust passing across the point-source nucleus (see Fig. 2.7).

Variable reddening due to dust in this lane is unlikely to be the cause of NGC 2992's history of broad-line variation. A simple calculation of the timescale of variation due to dust in the host galaxy moving at 300 km s^{-1} across a BLR 10 light-days in size gives a timescale $\tau \approx 30$ years, much too long to be the cause of variations observed to occur in only a few years. The strong correlation between the flux of the broad component of Hα and the $2-10$ keV X-ray flux shown by Gilli et al. (2000), as well as the fact that the line of sight column density has remained virtually constant despite these variations, are further indications of an intrinsic origin of NGC 2992's variability.

We conclude that NGC 2992 was identified as a Seyfert 1.9 based on its discovery in a low continuum state. It is clear that it is not a case of an oblique line of sight through the atmosphere of a dusty torus; the observed reddening is explained by an external dust lane.

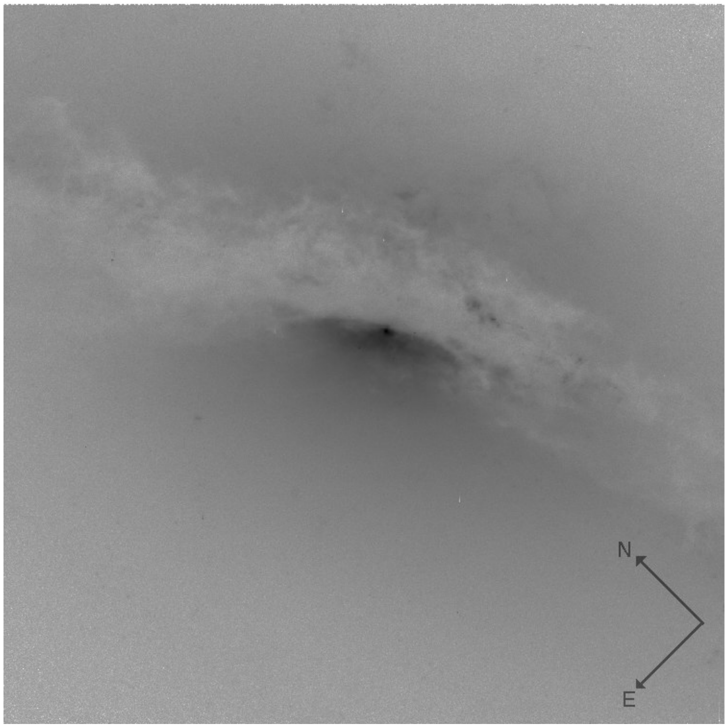

Figure 2.7 Hubble WFPC2 image of NGC 2992 taken with the F606W filter, showing a large lane of dust crossing directly over the nucleus, inverted so emission is dark and absorption is light. This image is from the Space Telescope Science Institute's Multimission Archive (MAST).

2.6 Motivation

These findings from NGC 2992 brought our attention to the fact that extinction typically attributed to the torus may in some cases be due to the host galaxy, and calls into question the nature of Seyfert 1.8/1.9 galaxies. Are most Seyfert 1.8/1.9s AGN with reddened BLRs? Or are they instead similar to NGC 2992, with intrinsically weak continua?

This work is an attempt to answer these questions by combining new optical spectra with archival data from other wavelength regimes to understand the physical reason behind the 1.8/1.9 designation of a sample of Seyferts. In doing so, we want to isolate those Seyferts whose broad lines are likely reddened by the torus, which are suitable for use in a study of the dust and gas in the torus, from those 1.8/1.9s in which the optical extinction, if present, is unrelated to the torus.

We postulate two main physical situations could cause an AGN's appearance as a 1.8/1.9. In one case, which we refer to as the "internally reddened" case throughout the remainder of this thesis, a type 1 Seyfert appears to be a 1.8/1.9 because we are observing it along a line of sight that passes through a dusty absorber which obscures most of the BLR flux in the optical except the strongest line, Hα, and perhaps the next strongest, Hβ. In the other case, the continuum source has at least temporarily diminished, leaving only weak broad lines. These weak components may be further diminished or totally extinguished by extinction from dust in the host galaxy, or they may be indiscernible in optical spectra due to noise and contamination by the underlying stellar absorption spectrum of the host galaxy. We refer to this as the "low-flux" case. Though there is not a single definitive method to discern between these possibilities, there are several observational clues that can help determine which cause is the most likely.

The internal reddening case is indicated by observational signs of a large reddening source between the BLR and NLR (i.e. $E(B-V)_{BLR} > E(B-V)_{NLR}$). In general, this could be due to either 1) dust between the BLR and NLR, such as the torus, or 2) dust on the same scale as the NLR, such as the nuclear dust spirals found by Pogge & Martini (2002). For Seyfert 1.8s, whose spectra contain both broad Hα and Hβ, this is easily checked by a comparison of the BLR and NLR Balmer decrements; a heavily reddened BLR and less reddened NLR is convincing evidence for internal reddening. For 1.9s, only a lower limit to the reddening of the BLR can be found from an optical spectrum, from an upper limit to the Hβ flux. However, X-ray spectra give information about the total line-of-sight gas column (N_H) to the very center of AGN, and can therefore be useful to determine the location of a reddening source in 1.9s. For example, if the reddening of the NLR corresponds to a column density similar to the column derived from the the X-ray spectrum (assuming a Galactic dust/gas ratio), then it is unlikely that the central source is being reddened by a torus. Furthermore, for either type 1.8 or 1.9 a study of optical spectral variability can provide useful information; if variations of the continuum shape or the strengths of broad Hα and Hβ are consistent with the same change in reddening, and occur more quickly than would be expected from dust moving in the external galaxy, we can again infer the presence of a source of internal reddening (see Goodrich 1995).

On the other hand, observed broad-line variations inconsistent with variable reddening indicate an intrinsically variable ionizing continuum, and could mean that the 1.8/1.9 is a low-flux state of an object that would normally appear as a Seyfert 1. Such an object could have a completely unreddened BLR. Or, if $E(B-V)_{BLR} \approx E(B-V)_{NLR}$, the reddening of the BLR is most likely due to dust in the host galaxy, and not the torus. We refer to this as "external reddening". Other clues that the BLR may be heavily reddened by the dust in the host galaxy are a strong silicate 9.7 μm absorption feature in the mid-IR (Deo et al. 2007), or a high inclination of the host galaxy itself, indicated by a small ratio of minor axis length to major axis length (b/a).

2.6.1 Sample

In this study, we consider a sample of 35 Seyferts classified as 1.8 or 1.9 by at least one of several sources: Sandage & Tammann (1987), Osterbrock (1989), Osterbrock & Martel

(1993), Goodrich (1995), Maiolino & Rieke (1995), Ho et al. (1995), Risaliti et al. (1999), or Quillen et al. (2001). The Seyferts in these publications are bright and relatively well-known, allowing us to establish the classification history of each based on previously published spectra in the literature.

Chapter 3 gives the details of our optical observations and data reduction processes, and describes our type classification requirements and method for measuring $E(B-V)_{NLR}$ and $E(B-V)_{BLR}$. Chapter 4 describes our X-ray data and spectral analysis. Chapter 5 outlines data from other resources we found helpful: optical WFPC2 images of the nuclei, and mid-IR Spitzer IRS spectra. Chapter 6 gives brief notes on the spectra of the Seyferts in our sample, and our classification of each object into one of the above categories (low flux or internally reddened), based on the evidence from our own data and from previously published sources. Chapter 7 is a discussion of the findings and summary of the results.

– 3 –

Optical Spectroscopy

3.1 Introduction to Optical Spectroscopy of Seyferts

The optical emission-line spectrum of a Seyfert galaxy is produced by gas photoionized by the central continuum source over a large range of distances. The line intensities, widths, and shapes are thus powerful tools for learning about the physical conditions in the different regions of the AGN.

3.1.1 NLR Lines

The most prominent optical emission lines from the NLR are the so-called "forbidden" lines, due to collisional excitation by thermal electrons of the low-lying energy levels of heavy elements, and subsequent downward radiative transitions. The most dominant lines are usually the green [O III] $\lambda\lambda$4959, 5007 lines. [O II] λ3727 and lines from [Ne III] are often prominent in the blue part of the spectrum, and in the red there are [N II] $\lambda\lambda$6548, 6583 and [S II] $\lambda\lambda$6716, 6731. The range in ionization species in the NLR of Seyferts is very great, with ionization potentials ranging from 0 eV (e.g., neutral elements such as [O I]) up to 361 eV (e.g., [Fe X IV]). Permitted lines are also present, from the re-capture of thermal electrons to excited levels, and ensuing radiative transitions to lower levels. In addition to permitted lines from the H I Balmer series (Hα at 6563 Å, Hβ at 4861 Å, and Hγ at 4340 Å), there are lines from He I and He II as well.

The profiles of these lines often have Gaussian cores, but their bases often show extended asymmetric wings (Whittle 1985a,b). Most often, the blue wing shows relatively more flux, an effect thought to be due to an outflowing component to the emission coming from the near (and most often less obscured) side of the AGN (Osterbrock & Ferland 2006). Measurement of the narrow line widths in a single object shows that the widths correlate with both ionization potential and critical density (De Robertis & Osterbrock 1984; Moore et al. 1996; Erkens et al. 1997), implying that the NLR has a radially stratified density structure (Kraemer et al. 2000; Kraemer & Crenshaw 2000).

It is important to note that variability of the narrow lines is not expected. The NLR extends to distances up to a kiloparsec, and therefore the light-travel time across the NLR means only long-term continuum changes will be visible in the narrow lines. Additionally, the time it takes to absorb the incident photons and reprocess them into emission lines (the hydrogen recombination timescale τ_{rec}, approximately 150 years for $n_H = 10^3$ cm^{-3}) will further damp out line variability (Peterson 1997).

3.1.2 BLR Lines

Seyfert 1, 1.2, and 1.5 galaxies are characterized by their broad permitted H I emission, but lines due to He I (λ5876), He II (λ4686), and Fe II ($\lambda\lambda$4570, 5250) are also present. In fact, all of the broad lines in the optical are permitted recombination lines; no forbidden lines show profiles characteristic of the BLR. This indicates that the BLR is a relatively high density region, in which the levels of abundant ions which might otherwise give rise to forbidden emission are collisionally de-excited.

Broad lines have widths that vary greatly from object to object, as well as diverse profile shapes. The widths range from ∼500 to 10,000 km s^{-1}, and in many cases this leads to blending between line profiles. The profiles are often described as logarithmic (Capriotti et al. 1980, 1981), at least in the wings, but in many cases they are irregularly shaped, and both blueward and redward asymmetries are observed in the broad lines of different objects. To further complicate matters, the line structure often differs from line to line in the same spectrum.

The fluxes of the broad lines vary strongly in response to changes in continuum flux. Extensive monitoring campaigns have been carried out to measure the time lag between continuum variation and the response of the broad lines (see, e.g., Peterson et al. 2004). The interpretation of the findings of these campaigns depends on the assumed geometry, but they do give an indication of the light travel time between the central object and the BLR clouds, which for Seyfert galaxies is usually $\sim 2 - 20$ days (Peterson & Wandel 1999). This technique also shows that BLR radius is correlated with the luminosity of the AGN (Kaspi et al. 2005). The observed range of lags shows that the BLR is also highly stratified; higher ionization species have shorter lags, and therefore are thought to reside closer to the central source than lower ionization species (Peterson 1993).

3.1.3 Continuum

The continua of type 2 Seyferts are mostly due to starlight from the host galaxy; the continuum emitted by the central engine is weak and difficult to discern in these types. In type 1s the stellar continuum is present, but diluted by the strong "featureless" blue continuum thought to arise from the accretion disk, often modeled by a power-law in the optical regime.

Furthermore, there is often a sharp rise to short optical wavelengths visible in the continua of type 1s, termed the "small blue bump", a combination of blended iron emission lines and Balmer continuum emission.

3.1.4 Effects of Dust

Optical spectroscopy gives important information about the amount of dust along the line of sight to the line-emitting regions in AGN. Dust grains are effective absorbers of light with wavelengths similar to, or smaller than, the diameter of the grains, which span a wide range in size but include many of ∼1000 Å in diameter. Because of this, a beam of light passing through a region of interstellar dust is reddened; the UV and blue optical wavelengths are preferentially absorbed/scattered by the grains, while the red light that passes through is less affected. Observationalists commonly use a quantity called the "color excess", or "reddening", denoted by $E(B-V)$, to measure the severity of this effect on an observed spectrum. $E(B-V)$ is the difference between the number of magnitudes of extinction in Johnson B filter (centered at 4400 Å) and the number of magnitudes of extinction in the Johnson V filter (centered at 5500 Å). The greater the amount of dust in the line of sight, the greater the value of $E(B-V)$. The relative extinction R in a certain waveband λ is defined to be the ratio of the number of magnitudes of extinction ($A_\lambda = -2.5log(f_{\lambda,observed}/f_{\lambda,intrinsic})$) in that band to the reddening, i.e. $R_\lambda = A_\lambda/E(B-V)$. As the ratio of two quantities that scale with the amount of dust, R_λ is not a measure of the amount of dust, but rather of the dust properties, such as grain composition, size, and shape. For the local Galactic ISM, R_λ has been empirically determined to high accuracy by measuring the fluxes of reddened and

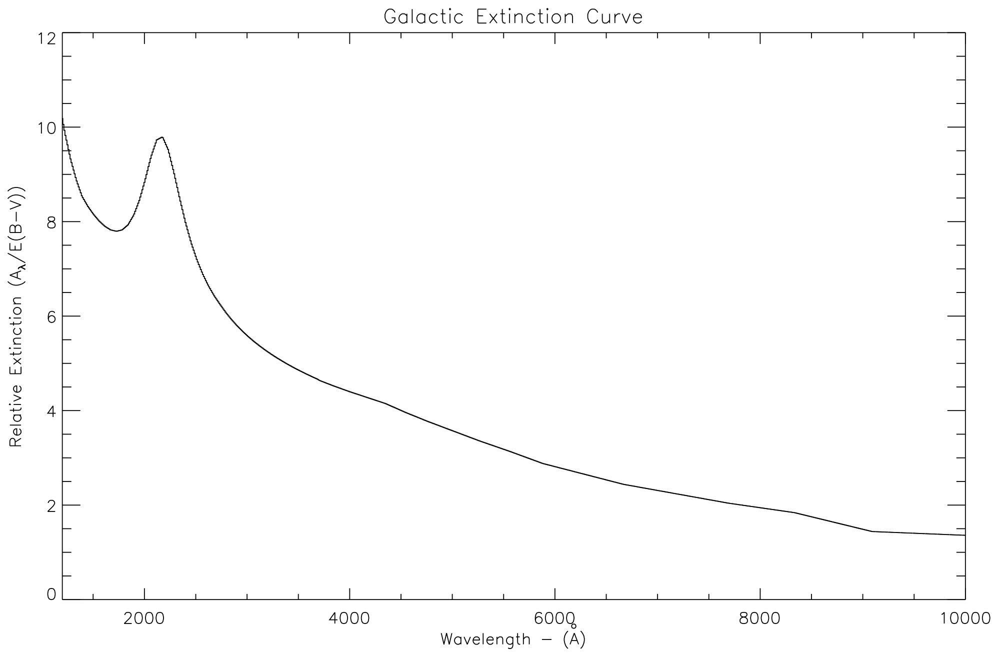

Figure 3.1 The standard Galactic relative extinction curve of Savage & Mathis (1979). The bump at 2200 Å is thought to be due to carbonate grains.

unreddened stars of the same spectral type (see Fig. 3.1).

In this study, we assume the dust in our Seyferts has the same properties as Galactic dust (i.e., that the reddening curve of Fig. 3.1 is valid), simply because we do not have data to determine R_λ by any other method. However, on the basis that extragalactic reddening curves determined by other methods are very similar to the Galactic curve longwards of 4000 Å (Crenshaw et al. 2001), this assumption should not detract from the quality of our results.

By assuming the standard Galactic reddening curve, one need only measure the integrated fluxes of two lines with a known intrinsic intensity ratio to determine the amount of dust in the line of sight to the line-emitting region using the equation

$$E(B-V) = \frac{2.5}{R_{\lambda 1} - R_{\lambda 2}} \log \frac{\left(\frac{f_{\lambda 1}}{f_{\lambda 2}}\right)_{intrinsic}}{\left(\frac{f_{\lambda 1}}{f_{\lambda 2}}\right)_{observed}} \tag{3.1}$$

.

Recombination lines are well-suited for use as reddening indicators; their intrinsic ratios are approximately constant over a wide range in temperatures (Osterbrock & Ferland 2006). Naturally, the best lines are the strongest, and we therefore use Hα and Hβ. In this way, measurement of the Balmer decrement measures the amount of dust in the line of sight.

The intrinsic value of the Balmer decrement of the narrow lines is well-determined; a value of $(f_{H\alpha}/f_{H\beta})_{intrinsic,\ NLR} = 2.9$, is often used, based on radiative transfer calculations assuming Case B recombination conditions (optically thick to Lyman photons, a good assumption for the tenuous NLR gas). For the BLR, the situation becomes more complicated, as collisional excitation begins to affect the line ratios in this high-density region, and there has been debate about the accuracy of presuming a single number for the BLR Balmer decrement in different objects. Photoionization models predict the ratio to vary widely depending upon the conditions of the BLR (Netzer 1975; Kwan & Krolik 1981; Korista & Goad 2004), and Rudy et al. (1988) showed that the steep Balmer decrement of Mrk 609 (at least during its "high" optical state observed in 1984) is not due to reddening, based upon the strength of the broad Lyα line in a simultaneous IUE spectrum. However, a recent study by Dong et al. (2008) finds the broad Balmer decrements of a large homogeneous sample of blue (i.e. unreddened) Seyfert 1s/QSOs from SDSS to have a log-Gaussian distribution that peaks at 3.06, with a standard deviation of only 0.03 dex. Additionally, they find no correlation between Balmer decrement and luminosity, accretion rate, or continuum slope. We therefore assume the standard value of $(f_{H\alpha}/f_{H\beta})_{intrinsic,\ BLR} = 3.1$.

A key assumption of this method is that the extinction arises from a uniform foreground screen of dust. For the BLR, only a few light-days across and well inside the dust sublimation radius, this is quite realistic. For the NLR, where dust lanes/spirals in the host galaxy may cause some regions to be more heavily reddened than others, and which may itself contain dust, using just one number to characterize the reddening is obviously an oversimplification. However, this method remains the only practical solution for finding at least an estimate of the amount of dust obscuring the NLR.

3.2 Observations and Data Reduction

The first step of our study was to obtain new optical spectra of each of the 1.8/1.9s in our sample to check their classification, analyze their Balmer line ratios, and look for variability in their broad lines. Several of the AGN in our sample were observed by the Sloan Digital Sky Survey (SDSS); we retrieved these spectra and included them in our study. Most of the other galaxies were observed between 2007 June and 2009 January at the R-C spectrograph on the Cerro Tololo Inter-American Observatory (CTIO) 1.5-m telescope in Chile, or at the DeVeny spectrograph on the 72″ Perkins telescope at Lowell Observatory in Arizona. Table 3.1 gives the observing log of these optical observations.

Spectra from CTIO were observed using two different settings. The first used a grating with a resolution of 4.3 Å (giving a dispersion of ∼1.47 Å/pixel) to take blue spectra from approximately 3660 – 5440 Å to include the Hβ line. The second used a grating with a resolution of 3.1 Å (∼1.10 Å/pixel dispersion) and a Schott GG 495 filter to take red spectra from approximately 5650 – 6970 Å, to include the Hα line. We used a slit at a 90° P.A. centered on the galaxy's nucleus to minimize the effects of differential atmospheric refraction and obtain accurate fluxes on photometric nights. The majority of the spectra were taken using a $2''$ slit width, but observations were also taken on nights when other slit widths were in use, as noted in Table 3.1. To eliminate cosmic ray hits, we took three exposures each time each AGN was observed. The stars LTT 4364 and Feige 110 were also observed with these settings for the purpose of flux calibration. The spectra were then reduced and flux calibrated using standard IRAF reduction packages for long-slit spectroscopy.

The same observing procedure was used during the observing runs at Lowell. There, most of the objects were observed with a grating with a resolution of 4.5 Å (∼2.18 Å/pixel dispersion) and a $2''$ slit aperture each night. A slight modification to the grating tilt was made after the first night of the observing run, and therefore several of the spectra have a wavelength range of 3185 – 6715 Å, while the others range from 3255 – 6785 Å. Mrk 1320 was additionally observed with a red setup, as its relatively high redshift meant Hα was shifted off the spectrum taken with the first setup. The red setup used to observe Mrk 1320 used a grating with a resolution of 3.4 Å (∼1.67 Å/pixel dispersion), and a Schott OG 570 filter to take a spectrum from 6300 – 9000 Å. The standard stars EG 247 and Feige 34 were used for flux calibration of the objects observed at Lowell.

We also include a spectrum of NGC 5273 taken using the GoldCam spectrograph on the 2.1-m telescope at Kitt Peak National Observatory (KPNO). The blue part of the spectrum, from approximately 3300 – 6000 Å, was observed with a grating with a resolution of 3.1 Å (∼1.25 Å/pixel dispersion), and the red part of the spectrum, from approximately 5500 – 7000 Å, was observed with a grating with a resolution of 3.1 Å (∼1.26 Å/pixel dispersion) and a Schott GG 495 filter. The spectrum was flux calibrated using observations of the standard stars BD 28+4211 (blue) and Feige 98 (red).

To correct the AGN emission-line fluxes for contamination by stellar absorption lines in the host galaxy, we removed the host galaxy spectrum from the data by subtracting off a normal galaxy spectrum (from Kinney et al. 1996), scaled to give the optimum fit to the observed object's absorption line features. Although most of our sample reside in spiral galaxies, the galaxies' nuclear spectra are dominated by the bulge, and therefore an elliptical galaxy spectrum with an old stellar population provided a good fit to the continuum of many of the objects. The remaining continuum was fit by a power-law and subtracted off, though this component was usually rather weak. Table 3.2 gives the Hubble type of the host galaxy template spectrum used for each object, and the fraction of the continuum at 5100 Å attributable to the host. The continuum-subtracted spectra are displayed in Appendix A.

Table 3.1: Log of Optical Observations

Object	Observatory	Date (U.T.)	Wavelength Coverage (Å)	Slit Width[a] (arcsec)
IRAS 18325-5926	CTIO	2007 Sep. 3	3658-5416	2.0
IRAS 18325-5926	CTIO	2007 Sep. 10	5630-6943	4.0
Mrk 334	Lowell	2009 Jan. 31	3255-6785	2.0
Mrk 423	Lowell	2009 Jan. 28	3185-6715	2.0
Mrk 471	SDSS	2005 Apr. 12	3800-9200	3.0
Mrk 516	CTIO	2008 May 10	3658-5416	2.0
Mrk 516	CTIO	2008 May 11	5534-6844	2.0
Mrk 609	CTIO	2007 Oct. 8	3658-5416	2.0
Mrk 609	CTIO	2007 Nov. 10	5630-6943	2.0
Mrk 622	SDSS	2001 Dec. 11	3800-9200	3.0
Mrk 728	SDSS	2004 Apr. 24	3800-9200	3.0

Continued on Next Page…

Table 3.1 – Continued

Object	Observatory	Date (U.T.)	Wavelength Coverage (Å)	Slit Width[a] (arcsec)
Mrk 883	SDSS	2004 Aug. 9	3800-9200	3.0
Mrk 915	CTIO	2008 Jun. 27	3658-5416	4.0
Mrk 915	CTIO	2008 Jun. 29	5630-6943	4.0
Mrk 993	Lowell	2009 Jan. 31	3255-6785	2.0
Mrk 1018	CTIO	2007 Oct. 5	3658-5416	2.0
Mrk 1018	CTIO	2007 Oct. 7	5630-6943	2.0
Mrk 1126	CTIO	2007 Oct. 5	3658-5416	2.0
Mrk 1126	CTIO	2007 Oct. 7	5630-6943	2.0
Mrk 1179	Lowell	2009 Jan. 28	3185-6715	2.0
Mrk 1320	Lowell	2009 Jan. 31	3255-6785	2.0
Mrk 1320	Lowell	2009 Feb. 2	6295-9000	2.0
NGC 1365	CTIO	2009 Jan. 8	3658-5416	4.0
NGC 1365	CTIO	2009 Jan. 9	5630-6943	2.0
NGC 1808	CTIO	2008 Sep. 5	5630-6943	4.0
NGC 1808	CTIO	2008 Sep. 13	3658-5416	2.0
NGC 2622	SDSS	2004 Dec. 8	3800-9200	3.0
NGC 2622	SDSS	2004 Dec. 8	3800-9200	3.0
NGC 2639	Lowell	2009 Jan. 31	3255-6785	2.0
NGC 2992	CTIO	average spectrum[b]	–	–
NGC 3786	Lowell	2009 Jan. 28	3185-6715	2.0
NGC 3982	SDSS	2003 Jan. 31	3800-9200	3.0
NGC 4388	SDSS	2004 Jun. 10	3800-9200	3.0
NGC 4639	Lowell	2009 Jan. 28	3185-6715	2.0
NGC 5033	Lowell	2009 Feb. 1	3845-7375	2.0
NGC 5252	SDSS	2002 Apr. 10	3800-9200	3.0
NGC 5273	KPNO	2008 Jul. 2	3300-6000	2.0
NGC 5273	KPNO	2008 Jul. 3	5500-7000	2.0
NGC 5506	SDSS	2002 Apr. 14	3800-9200	3.0
NGC 5674	Lowell	2009 Jan. 31	3255-6785	2.0
NGC 7314	CTIO	2007 Sep. 8	3658-5416	2.0
NGC 7314	CTIO	2008 May 9	5534-6844	2.0
NGC 7479	CTIO	2008 Aug. 5	3658-5416	2.0
NGC 7479	CTIO	2008 Aug. 8	5630-6943	2.0
NGC 7603	CTIO	2007 Oct. 5	3658-5416	2.0
NGC 7603	CTIO	2007 Oct. 7	5630-6943	2.0
UGC 7064	Lowell	2009 Jan. 28	3185-6715	2.0

Continued on Next Page…

Table 3.1 – Continued

Object	Observatory	Date (U.T.)	Wavelength Coverage (Å)	Slit Width^a (arcsec)
UGC 12138	CTIO	2008 Aug. 5	3658-5416	2.0
UGC 12138	CTIO	2008 Aug. 2	5630-6943	2.0
UM 146	CTIO	2007 Oct. 5	3658-5416	2.0
UM 146	CTIO	2007 Oct. 7	5630-6943	2.0

[a] The SDSS spectra were taken with a 3″-diameter circular aperture. [b] The spectrum of NGC 2992 is the average of ten spectra taken from 2006 January to 2007 June (see Chapter 2).

Table 3.2: Continuum Fits

Object	Template^a	Cont. Fraction^b
IRAS 18325-5926	S0	0.72
Mrk 334	E1	0.90
Mrk 423	E2	0.81
Mrk 471	Sa	0.92
Mrk 516	E1	0.72
Mrk 609	E1	0.85
Mrk 622	E1	0.91
Mrk 728	E1	0.97
Mrk 883	E1	0.95
Mrk 915	E2	0.86
Mrk 993	Sa	0.93
Mrk 1018	S0	0.62
Mrk 1126	Sb	0.78
Mrk 1179	Sa	0.76
Mrk 1320	E2	0.61
NGC 1365	Sb	1.00
NGC 1808	E2	0.92
NGC 2622	Sb	0.82
NGC 2639	E4	0.95
NGC 2992	Sa	0.94
NGC 3786	E2	0.96
NGC 3982	Sb	0.82
NGC 4388	Sb	0.88
NGC 4639	Sa	0.95
NGC 5033	Sa	0.83
NGC 5252	S0	0.93

Continued on Next Page…

Table 3.2 – Continued

Object	Template[a]	Cont. Fraction[b]
NGC 5273	E2	0.80
NGC 5506	Sb	0.88
NGC 5674	E2	0.95
NGC 7314	E4	1.00
NGC 7479	E3	0.74
NGC 7603	E3	0.27
UGC 7064	E2	0.96
UGC 12138	E2	0.70
UM 146	E2	0.90

[a] The classification of the inactive galaxy template spectrum used to subtract off the underlying host galaxy spectrum from the AGN's spectrum, from Kinney et al. (1996). [b] The fraction of the observed continuum at 5,100 Å due to starlight from the host galaxy.

3.3 Analysis of Optical Spectra

3.3.1 Classification of Putative 1.8/1.9s Based on Optical Spectra

The optical spectra were first used to verify the type classification of the objects in our sample. The conventional definition of Seyfert 1.8 galaxies is that they are Seyferts whose optical spectra show only weak broad Hα and Hβ components, while Seyfert 1.9 galaxies are defined by just weak broad Hα. However, this definition is ambiguous about what constitutes a "broad" component, and has led to confusion about which objects should be designated as these types. To keep our classifications self-consistent, we decided to employ the following definition: "broad" emission is line emission that is significantly wider than the [O III] λ5007 line, at least in the wings of the profiles, indicating that the emission is not from the inner NLR, but is generated in a distinct high-density region where [O III] emission is collisionally suppressed (i.e., the BLR).

Detecting faint broad lines is a non-trivial process. The first major source of concern is the contamination of the AGN spectrum by starlight. Weak broad emission from the AGN can be hidden by pressure-broadened stellar absorption lines (e.g., from a population of A stars) in the host galaxy. Or, the reverse may happen, as the continuum features due to K and M giants may lead to a false detection of broad Hα (Filippenko & Sargent 1985). Our subtraction of the host galaxy continuum, described in the last section, is adequate to remove the worst of these problems.

Secondly, Hα must be very carefully disentangled from the [N II] $\lambda\lambda$6548, 6583 lines on its sides in order to detect a weak broad component. The [N II] lines, along with the other narrow lines in the spectrum, are not usually simple Gaussians; they are often asymmetric and frequently have faint extended wings at their bases, and these features must be taken into account to avoid confusing their emission with that of broad Hα. We used the following procedure as our best attempt to de-blend the complex, adapted from Crenshaw & Peterson (1986). First, we created a template profile from one of the other optical narrow lines, usually [O III] λ5007 because it is the strongest and cleanest forbidden line in most of our spectra. In a couple of cases, the [O III] λ5007 line was unsuitable to use as a template, because the structure of this high ionization line was obviously quite different than the the lower-ionization [N II] lines. For these objects, the template was constructed instead from the [S II] λ6716 and λ6731 lines, using the blue half of the λ6716 line and the red half of the λ6731 line of this usually mildly blended pair, in the manner of Ho et al. (1997b). A copy of the template line was then centered at the wavelengths of each of the [N II] lines, scaled in width and height (both lines were assumed to have the same width, and the flux of the line at 6583 Å was set to 3 times that of the line at 6548 Å in accordance with the ratio of their transition probabilities (Osterbrock & Ferland 2006)) and subtracted off the spectrum.

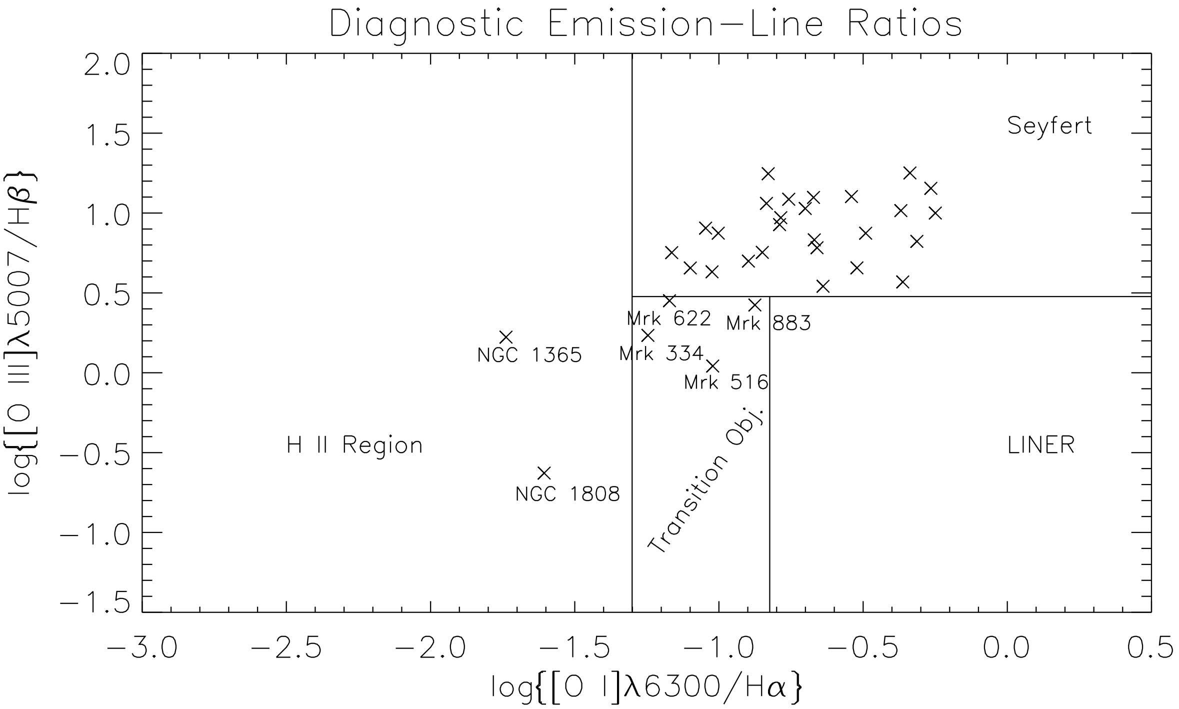

Figure 3.2 A diagnostic diagram in the manner of Veilleux & Osterbrock (1987) of the line ratios of the objects in our sample. Most of our objects fall into the Seyfert regime of this diagram, indicating they have high levels of ionization and large partially-ionized zones. Mrk 334, Mrk 516, Mrk 622 and Mrk 883 fall into the transition object/LINER region, indicating their less powerful continua and lower ionization states, while the positions of NGC 1365 and NGC 1808 indicate their emission includes a strong starburst component.

This process was repeated with different template scale factors until the smoothest broad profile or continuum was attained. A caveat of this method is that forbidden lines with different critical densities or ionization potentials may have different profiles (De Robertis & Osterbrock 1984). However, it was the most practical method we could find, and worked well overall. The Hα profile of each Seyfert after [N II] subtraction is shown in Appendix B, with the [O III] λ5007 line scaled to match the peak flux of Hα over-plotted as a dashed line for comparison of their widths.

From the plots in Appendix B, we find that many of the Seyferts in our sample, at least at the time when observed by us, do not fit our criteria for classification as 1.8s/1.9s. Our new type classifications for our 35 targets are given in Table 3.3. Ten objects lack any sign of broad Hα, and are thus Seyfert 2s. Seven are type 1.0, 1.2, or 1.5, based upon the definitions of these subclasses by Maiolino & Rieke (1995), which rely on the strength of the ratio of broad Hβ to [O III] λ5007 flux (see Appendix B). There are eight 1.9s: Mrk 471, Mrk 915, NGC 2622, NGC 3786, NGC 5252, NGC 7314, UGC 7064, and perhaps NGC 1365, though the broad Hα is very faint in this object. Seyferts 1.8s are much scarcer than 1.9s in our sample; we found only three true Seyfert 1.8s (Mrk 334, Mrk 1126, and UM 146).

The remainder of the objects in our sample are LINERS or starburst galaxies. These classifications were checked by plotting the position of these objects on a diagnostic diagram in the manner of Veilleux & Osterbrock (1987), as shown in Fig. 3.2. The abscissa on this diagram is the ratio of the flux of the [O I] λ6300 line to the flux of narrow Hα, a measure of the extent of the "partially-ionized zone" created by high-energy photons. The ordinate is the ratio of the flux of the [O III] λ5007 line to the flux of narrow Hβ, a proxy for the level of ionization. Most of our objects do indeed fall into the Seyfert region of this diagram, indicating they have the high levels of ionization and large partially-ionized zones characteristic of Seyfert nuclei. Mrk 334, Mrk 516, Mrk 622, and Mrk 883 fall into the "transition object" region, indicating their less powerful continua and thus lower ionization states. However, because the errors in the line ratios are large enough that these objects (with the exception of Mrk 516) could still be classified as Seyferts, we retain the Seyfert classification for these objects. Though it is not plotted in Fig. 3.2 because it does not have measurable Hβ, we also classify NGC 2639 as a LINER on the strength of [O II] λ3727 relative to [O III] λ4959 and λ5007. NGC 1365 has a very strong starburst component, yet shows strong X-ray emission and evidence for weak broad Hα emission, and we therefore classify it as a Seyfert 1.9. NGC 1808 appears to be an H II (starburst) galaxy in this diagram.

Interestingly, the plots in Appendix B show several objects for which the core of the narrow Hα line is narrower than the [O III] λ5007 line core: Mrk 334, Mrk 516, Mrk 609, Mrk 622, NGC 1808, and NGC 7479. This may be due to the addition of a starburst component to the Hα profile, as evidenced by the position of most of these objects below the "Seyfert region" in Fig. 3.2. In this case, a larger fraction of the Hα emission is coming from the lower ionization gas compared to the [O III] emission, resulting in a narrower Hα profile.

3.3.2 Reddening of the NLR and BLR

In order to measure the broad and narrow Balmer decrements, the narrow emission lines must be separated from the broad lines. We used the same template profile created to subtract the [N II] lines, scaled in width and height by trial and error until its subtraction from the total blend left a smooth broad-line profile, to remove the narrow Balmer emission. Unfortunately, in objects with strong and irregularly-shaped broad Hα (mostly Seyfert 1-1.5s), it is particularly difficult to discern which scale factors give the best fit, and the flux of the template line used to fit the narrow component could be scaled by up to $\pm 40\%$ and still give a reasonable-looking broad profile. While this led to some error in the measurement of the fluxes of the broad components, it led to a much larger percentage uncertainty in the fluxes of the narrow components of these objects. However, this method worked much better in the 1.8/1.9s where the broad lines are reduced in strength, making the broad and narrow components easier to separate.

We determined the reddening of the NLR and the BLR (when possible) using the method described in Section 3.1.4, i.e.,

$$E(B-V) = \frac{2.5}{R_{H\alpha} - R_{H\beta}} \log \frac{\left(\frac{f_{H\alpha}}{f_{H\beta}}\right)_{intrinsic}}{\left(\frac{f_{H\alpha}}{f_{H\beta}}\right)_{observed}} \tag{3.2}$$

with $R_{H\alpha}$, $R_{H\beta}$ from the Galactic reddening curve, and assuming $(f_{H\alpha}/f_{H\beta})_{intrinsic} = 2.9$ for the NLR and $(f_{H\alpha}/f_{H\beta})_{intrinsic} = 3.1$ for the BLR.

For the 1.9s, which show only weak broad Hα, only a lower limit to the reddening of the BLR can be derived. To determine if Hβ should be visible based on the strength of Hα if the BLR is unreddened, we performed the following simple test. The broad component of the Hα line was cut from the spectrum, scaled in width to keep the profile width constant in velocity space, and its flux divided by 3.1, to make a template representing the intrinsic Hβ emission line. This template was then added to the spectrum at the position of Hβ. In Mrk 915, NGC 3786, and NGC 7314, this made a visible Hβ line, and the template was then multiplied by progressively smaller scale factors until the line became indistinguishable from the surrounding continuum. This scale factor times the intrinsic expected Hβ flux was then taken as an upper limit to the amount of Hβ present in these galaxies, and used to find a lower limit to the broad Balmer decrement and $E(B-V)_{BLR}$. However, this procedure revealed that for most of the 1.9s broad Hβ would not be visible even if the BLR were totally unreddened; the expected intrinsic Hβ is indiscernible against the noise and the residuals of the host galaxy subtraction in Mrk 471, NGC 1365, NGC 2622, NGC 5252, and UGC 7064. Thus, for the majority of 1.9s we could not determine if the BLR is reddened based on an optical spectrum alone. We give the NLR and BLR reddening values in Table 3.3. The negative reddening values in this table are consistent with zero within their errors.

Table 3.3: Measured $E(B-V)$ Values

Object	Our Type	$E(B-V)^a_{NLR}$	$E(B-V)^b_{BLR}$
IRAS 18325-5926	2	1.63±0.07	–
Mrk 334	1.8	0.20±0.06	-0.13±0.19
Mrk 423	1.5	-0.13±0.17	0.36±0.22
Mrk 471	1.9	0.89±0.23	–
Mrk 516	LINER 2+HII	0.48±0.08	–
Mrk 609	2	0.98±0.11	–
Mrk 622	2	1.03±0.05	–
Mrk 728	1.2	0.03±0.12	0.45±0.14
Mrk 883	2	0.40±0.07	–
Mrk 915	1.9	0.27±0.06	>0.33
Mrk 993	1.5	0.47±0.36	-0.27±0.38
Mrk 1018	1	0	0.25±0.08
Mrk 1126	1.8	0.51±0.23	0.38±0.20
Mrk 1179	1	-0.06±0.26	0.24±0.12
Mrk 1320	1.5	0.38±0.32	-0.07±0.22
NGC 1365	1.9	1.30±0.04	–
NGC 1808	HII	–	–
NGC 2622	1.9	0.36±0.09	–
NGC 2639	2?[c]	–	–
NGC 2992	2	0.71±0.11	–
NGC 3786	1.9	0.45±0.09	>0.16
NGC 3982	2	0.68±0.11	–
NGC 4388	2	0.67±0.09	–
NGC 4639	1[d]	–	–
NGC 5033	1.2	-0.04±0.43	0.19±0.05
NGC 5252	1.9	0.71±0.09	–
NGC 5273	1.5	-0.07±0.27	-0.10±0.17
NGC 5506	2	0.78±0.06	–
NGC 5674	2	0.14±0.08	–
NGC 7314	1.9	0.52±0.02	>0.02
NGC 7479	2?[c]	–	–
NGC 7603	1	-0.03±0.23	0.19±0.36

Continued on Next Page. . .

Table 3.3 – Continued

Object	Our Type	$E(B-V)^{a}_{NLR}$	$E(B-V)^{b}_{BLR}$
UGC 7064	1.9	0.23±0.13	–
UGC 12138	1.5	0.33±0.25	-0.13±0.08
UM 146	1.8	0.42±0.24	0.03±0.19

[a] derived from the ratio of the integrated flux of the narrow component of Hα to integrated flux of the narrow component of Hβ, assuming the intrinsic value of this ratio to be 2.90, and using the reddening curve of Savage & Mathis (1979). [b] derived from the ratio of the integrated flux of the broad component of Hα to the integrated flux of the broad component of Hβ, assuming the intrinsic value of this ratio to be 3.10, and using the reddening curve of Savage & Mathis (1979). [c] Uncertain classification because no Hβ is present in the spectrum, but the spectrum is otherwise characteristic of a type 2 AGN. [d] low-luminosity Seyfert 1 (Ho et al. 1999).

For the objects that show broad Hβ and Hα, Fig. 3.3 shows the reddening of the NLR plotted against the reddening of the BLR. The Seyferts with types <1.8 have points with very large error bars, mostly due to the difficulty of separating out the narrow components from the strong broad emission in these objects. It is interesting to note that none of the three Seyfert 1.8s shows evidence for BLR reddening above that of the NLR. Also rather surprisingly, there is not much correlation between the values in Fig. 3.3. About half of the objects are seen to have larger NLR reddening than BLR reddening. We suggest that this is due to the structure of the dust lanes/spirals in the vicinity of the NLR. The values of reddening being plotted are averages over the entire emitting regions, and if one of these dusty structures does not happen to pass in front of the BLR, the NLR can have a larger average reddening than the BLR. Further, the fact that the points are distributed equally above and below the dashed line representing $E(B-V)_{BLR} = E(B-V)_{NLR}$ argues against the reddening of the BLR in these objects being in general due to a central dusty torus, but suggests instead that their reddening is due to the chance obscuration by a dust lane in the NLR which crosses the nucleus.

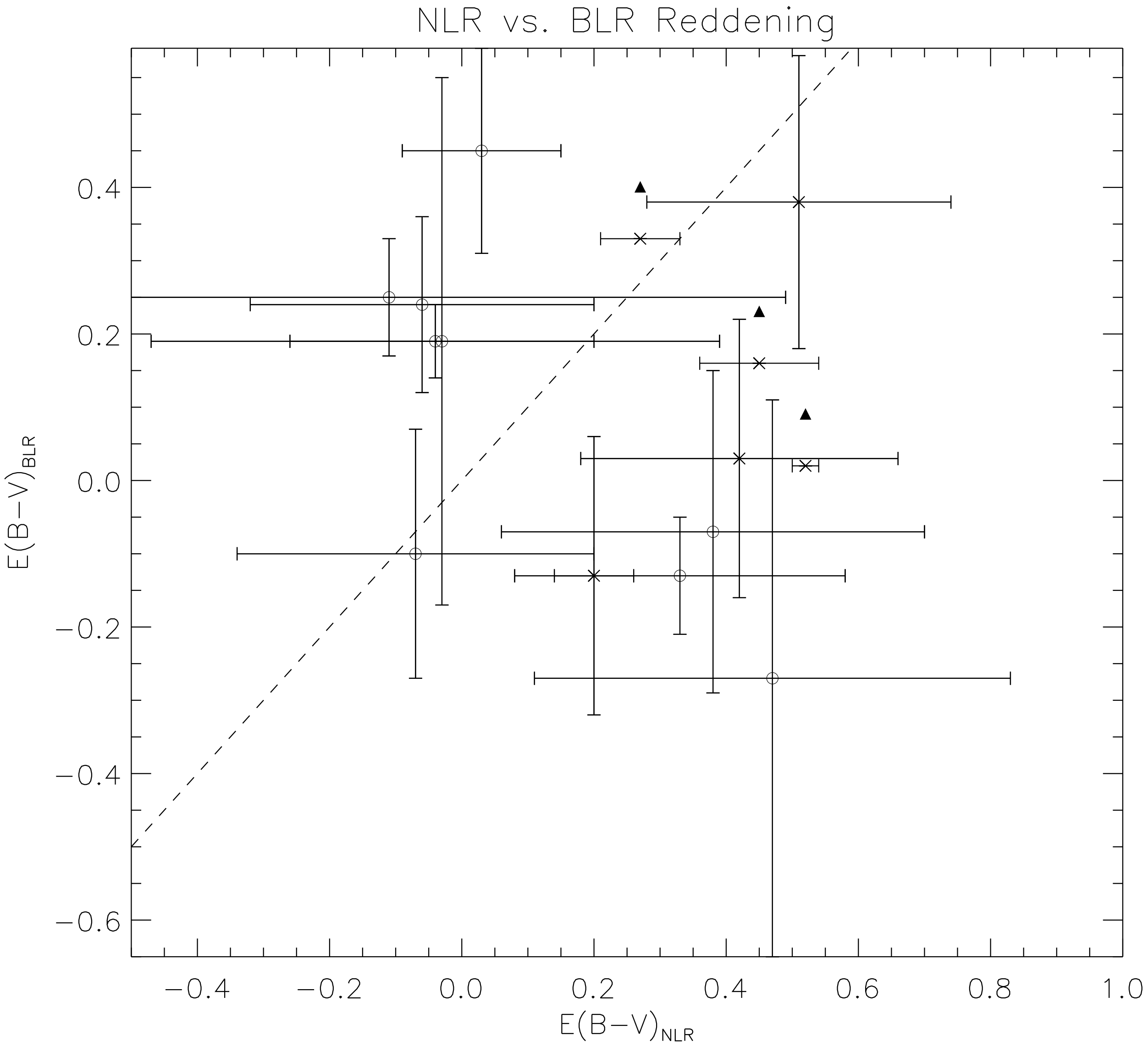

Figure 3.3 The reddening of the BLR vs. the reddening of the NLR for the objects in our sample with both broad Hα and Hβ, derived assuming an intrinsic flux ratio of Hα to Hβ of 2.9 in the NLR and 3.1 in the BLR, and the standard Galactic reddening curve of Savage & Mathis (1979). For the 1.9s, the BLR reddening plotted is the lower limit estimated by the method described in Section 3.3.2. Points: Seyfert 1.8/1.9s represented by crosses, Seyfert 1.0/1.2/1.5s represented by open circles. Dashed line: $E(B-V)_{BLR} = E(B-V)_{NLR}$.

– 4 –

X-ray Spectroscopy

4.1 Introduction to X-ray Spectroscopy of Seyferts

4.1.1 The Origin of the X-rays

X-ray emission is a common feature of Seyferts (Mushotzky et al. 1993). For this study, X-ray spectra are useful to determine the total amount of material in the line of sight all the way to the accretion disk at the center of the AGN. Comparing this with the amount of obscuration derived from $E(B-V)_{NLR}$ and $E(B-V)_{BLR}$ gives information about the location of the absorbing gas.

The X-ray continuum in Seyferts is thought to come from the inverse Compton scattering of UV seed photons emitted by the accretion disk by a population of hot or relativistic electrons hovering above and below the disk in a coronal region (Wang & Netzer 2003). This process predicts the $\Gamma \approx 2$ powerlaw X-ray continuum often observed in unobscured AGN. The corona is thought to exist on size scales less than a few tens of gravitational radii from the black hole, and thus the X-ray continuum can experience reprocessing and pick up signatures of the material from very close to the black hole and outwards.

The energy at which the AGN's X-ray continuum is directly observable is a function of the ionization state and amount of intervening material between the observer and the source. In neutral ("cold") matter, the main source of opacity in the $0.5-10$ keV range is the photoelectric absorption of X-rays by hydrogen, although there is also absorption by heavier elements. Because the hydrogen absorption cross section decreases with photon energy as $(h\nu)^{-3}$, the lowest energy "soft" X-rays have a much higher probability of being absorbed

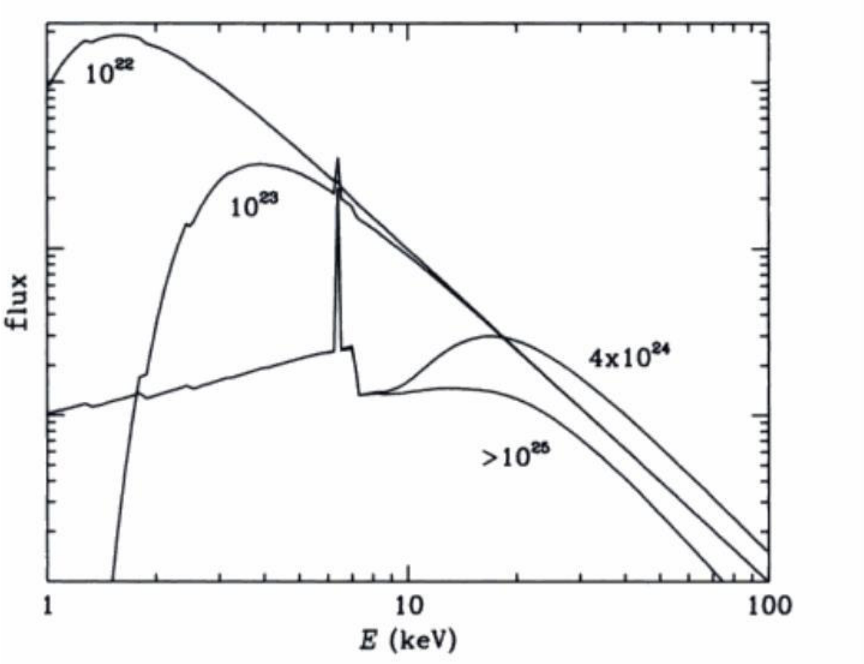

Figure 4.1 The X-ray spectrum of an AGN obscured by $N_H = 10^{22}$, 10^{23}, 4×10^{24}, and $N_H > 10^{25}$ cm^{-2}, assuming a $\Gamma = 2$ powerlaw input spectrum. In the Compton-thick cases ($N_H > 1.5 \times 10^{24}$ cm^{-2}), the spectrum below 10 keV is dominated by the reflection component. The narrow line at 6.4 keV is Fe Kα. Figure from Fabian et al. (2004).

than the higher energy “hard” X-rays, and as the amount of intervening material increases, fewer and fewer soft X-rays are able to penetrate. A frequently used measure of the amount of line of sight material is the equivalent column density of neutral hydrogen atoms, N_H, in hydrogen atoms cm^{-2}, with solar abundances of the other elements assumed. The X-ray spectrum of an obscured AGN is shown for different column densities of neutral gas with solar abundances in Fig. 4.1.

As the ionization state of the absorbing gas increases and the number of neutral hydrogen atoms becomes fewer, the opacity due to hydrogen absorption decreases. Fig. 4.2 shows the transmitted spectrum through a cloud with $N_H = 5 \times 10^{23}$ cm^{-2}. In high-ionization gas, the opacity is dominated by photoelectric absorption by heavier ions, and the bound-free

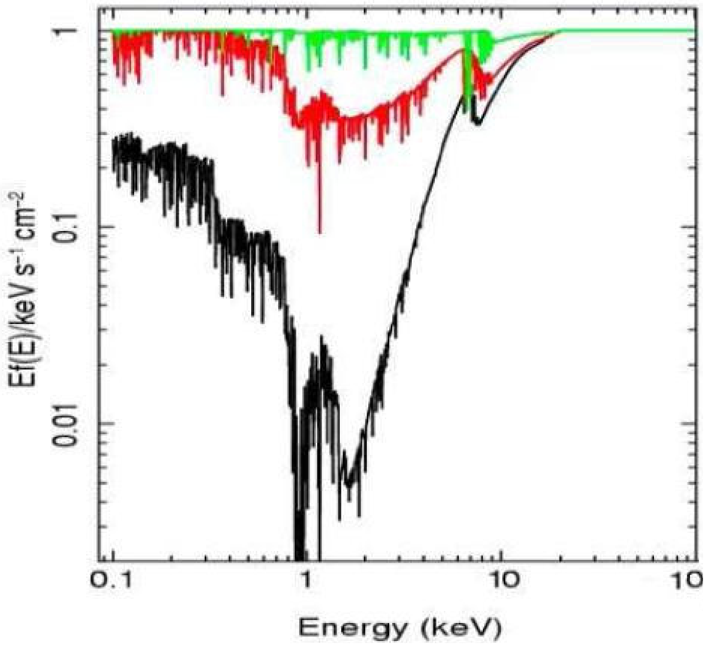

Figure 4.2 The X-ray spectrum of an AGN obscured by $N_H = 5 \times 10^{23}$ cm^{-2}, with $log(\xi) =$ 2 (bottom), 3 (middle), and 4(top), where ξ is the ionization parameter ξ ($= L/nr^2$ where L is the ionizing luminosity, n is the proton density, and r is the distance from the source)in units of ergs s^{-1}. Figure from Turner & Miller (2009).

absorption edges of these ions are apparent in the spectrum.

Absorbing gas is also expected to produce line emission. In particular, Kα lines may be emitted by fluorescence (relaxation after a K-shell photoionization), with a high fraction of photoionizations ultimately producing a Kα photon (Osterbrock & Ferland 2006). For ionized material, the binding edges of the inner shells generally increase with ionization and so the energies of the K edges and emission and absorption lines generally increase with the ionization state. In neutral material the Fe Kα fluorescence line comprises a doublet at energies 6.404 and 6.391 keV, these being indistinguishable by current X-ray spectrometers. The Fe Kβ line at 7.06 keV is expected at about 13.5% of the flux of Kα. In ionized gas, the lines become a complex of permitted, intercombination and forbidden transitions, that cannot be resolved with current instruments (Turner & Miller 2009).

Below ~ 2 keV, the spectra of X-ray absorbed Seyferts also commonly show excess emission above the extrapolation of the absorbed nuclear emission in the hard X-rays. This "soft excess" is thought to be unresolved emission lines from an extended region of photoionized circumnuclear gas within the NLR; high resolution spectra from Chandra have shown the signatures of photoionized gas, and there is an overall coincidence between the soft X-ray emitting regions and the [O III] emitting regions on *HST* maps, on scales as large as a few hundred parsecs (Bianchi et al. 2006).

4.1.2 Models of X-ray Spectra

The detection of X-rays by CCDs is slightly different than the detection of optical light. In the optical, an incident photon liberates a single photoelectron within the semiconductor lattice, which moves from the valence to the conduction band and is then held there by a potential. Many optical photons must be collected to produce a measurable signal (i.e., the signal is integrated over a certain exposure time). An X-ray photon, on the other hand, ejects a photoelectron with energy equal to that of the energy of the incident X-ray minus the binding energy of the electron. This free electron therefore has sufficient energy to produce a trail of secondary ionizations as it moves through the semiconductor lattice, each requiring an average of 3.65 eV to be produced in silicon (Howell 2000). By counting the number of ADUs produced within the CCD pixels, one can determine the energy of each incident photon; thus, X-ray imaging by a CCD provides not only an image but the ability to produce a spectrum from the image.

An X-ray imaging spectrometer measures the number of photon counts within individual instrument channels. The actual spectrum $f(E)$ of the source is related to the observed spectrum $C(I)$ by the relation

$$C(I) = \int_0^\infty f(E)R(I,E)\,dE \tag{4.1}$$

where $R(I,E)$ is the instrumental response function, the probability that an incoming photon with energy E will be detected in channel I. Unfortunately, inverting this equation to find $f(E)$ is problematic; such inversions tend to be non-unique and unstable to small changes in $C(I)$ (Arnaud 1996).

The usual solution to this problem is to work backwards. One tries create a model spectrum $f(E)$, based upon a few parameters that describe the physical conditions of the source, such that the count spectrum of the model determined by the known instrumental response matches the observed data. A fit statistic, such as χ^2 is computed from the comparison, and used to judge how well the model spectrum fits the data. The model parameters are then varied to find the combination of parameter values that provides the best fit (usually, the lowest χ^2).

4.2 X-ray Data and Analysis

The *XMM-Newton* spacecraft (hereafter referred to as just *XMM*) has three X-ray telescopes on board. There is a detector at the focus of each, and these three X-ray imaging spectrometers comprise the European Photon Imaging Camera (EPIC). Two of the cameras are MOS (metal oxide semiconductor) detectors; the third uses a pn CCD. The pn camera is the most sensitive, and can detect photons with high efficiency up to 15 keV (the MOS detectors are limited by their low quantum efficiency in this regime).

To investigate the X-ray properties and determine the total obscuring columns of the nuclei in our sample, we retrieved the available archived EPIC pn observations of the objects previously observed by *XMM*. Observations were available for 23 of our 35 objects. Two of these, Mrk 883 and NGC 2622 were observed by us through the *XMM* Guest Observer program (P.I.: Crenshaw). If the object was observed multiple times, we retrieved the spectra taken closest in time to our optical observations, but none of the observations were simultaneous. The observation date and ID number of each spectrum used is given in Table 4.1.

The *XMM* data were reduced using the standard EPCHAIN processing script included in version 7.1.0 of the XMM-SAS (Science Analysis System) software. The data were filtered to exclude times of high background, and the source spectra were then extracted from circles $32''$ in radius. Background spectra were extracted from an area free of any background sources on the same chip as the source, also from $32''$-circles. Response matrices and ancillary response matrices were generated using the XMM-SAS tasks $rmfgen$ and $arfgen$.

To determine the absorbing hydrogen columns of the objects in our sample (N_H), the X-ray spectra of the source minus the background in the 0.5 to 10 keV range were fit using XSPEC version 12.3.1. Three models were initially fit to each data set and then compared to determine the best fit. The first was a simple powerlaw modified by Galactic absorption only (*wabs*powerlaw* in XSPEC, with *wabs* set to the Galactic column), the second a powerlaw absorbed by a variable cold column (*wabs*powerlaw*, with *wabs* free), and the third a partial covering model (*wabs*pcfabs*powerlaw*, with *wabs* again set to the Galactic column density). By utilizing the *wabs* and *pcfabs* model components, the absorber was assumed to

Table 4.1. Log of *XMM* Observations

Object	Obs. Date	Obs. ID#
IRAS 18325-5926	5 Mar. 2001	0022940101
Mrk 609	13 Aug. 2002	0103861001
Mrk 609	27 Jan. 2007	0402110201
Mrk 622	2 Apr. 2003	0138951401
Mrk 728	23 May 2002	0103861801
Mrk 883	13 Aug. 2006	0302260101
Mrk 883	15 Aug. 2006	0302260701
Mrk 883	21 Aug. 2006	0302261001
Mrk 993	23 Jan. 2004	0201090401
Mrk 1018	15 Jan. 2005	0201090201
NGC 1365	17 Jan. 2004	0205590301
NGC 1365	24 Jul. 2004	0205590401
NGC 1808	6 Apr. 2002	0110980801
NGC 2622	9 Apr. 2005	0302260201
NGC 2992	19 May 2003	0147920301
NGC 3786	24 May 2004	0204650301
NGC 3982	15 Jun. 2004	0204651201
NGC 4388	12 Dec. 2002	0110930701
NGC 4639	16 Dec. 2001	0112551001
NGC 5033	18 Dec. 2002	0094360501
NGC 5252	18 Jul. 2003	0152940101
NGC 5273	14 Jun. 2002	0112551701
NGC 5506	2 Feb. 2001	0013140101
NGC 5506	9 Jan. 2002	0013140201
NGC 5506	7 Aug. 2004	0201830501
NGC 7314	2 May 2001	0111790101
NGC 7479	19 Jun. 2001	0025541001
NGC 7603	14 Jun. 2006	0305600601
UGC 12138	3 Jun. 2001	0103860301

be cold. We initially attempted to fit the spectra with ionized absorbers, but found that the data quality was not high enough to be able to distinguish the spectral signatures of ionized absorption.

Though one of these simple models usually provided a good fit to the data above 2 keV, many objects show an upturn in emission below ~2 keV not taken into account by these preliminary models. As mentioned in the last section, this "soft excess" is a commonly observed feature in the spectra of X-ray obscured AGN and is thought to be due to unresolved emission lines from an extended region of photoionized gas (Guainazzi & Bianchi 2007). We did not attempt detailed models of the soft excess; our main goal was to determine the column density to the central source, and without more information about its source it is impossible to create a physically meaningful model anyway. We therefore modeled the soft excess with an additional powerlaw component of the same spectral index as fit the hard X-rays (to represent reflection/partial covering of the source), and included Gaussian components to provide a reasonable fit to the data in this range. We do not attach any physical significance to these Gaussian;, they were merely included to ensure that the trough of the absorption was well-fit. We also fit Fe Kα with a Gaussian profile whenever it was apparent in the spectrum. The final model was selected as the model with the lowest reduced χ^2, and its components and the total column density are presented in Table 4.2. Plots of this final model, the unfolded spectrum, and the individual components are presented in Appendix C.

Overall, the columns range from values of a a few times 10^{20} cm^{-2}, attributable to material in our Galaxy, to $N_H \approx 10^{24}$ cm^{-2}. The implications of the columns in individual objects are discussed later, in the notes presented in Chapter 6.

Figure 4.3 presents a comparison of the X-ray column densities with the NLR column densities. The NLR column densities were estimated from the reddening of the NLR, assuming the relation $N_H = 5.2 \times 10^{21} E(B-V)$ cm^{-2} derived by Shull & van Steenberg (1985) for the local interstellar medium. As one would expect based on the simplest form of the unified model, most of the objects have greater X-ray columns than NLR columns.

However, two Seyfert 2s in Fig. 4.3 are surprisingly placed: Mrk 609 and Mrk 883 have NLR columns significantly *larger* than their X-ray columns suggest (see Fig. C.2, C.3, C.6, C.7, and C.8 in Appendix C for their *XMM* spectra). Both these objects are Seyfert 2s (although we note that they both have a starburst component), and for them to have bright, apparently unabsorbed X-ray spectra without strong narrow Fe Kα indicating reflection is completely contradictory to the expectations of the simplest form of the unified model. These appear to be "true" Seyfert 2s, which lack discernible broad lines but have strong, unabsorbed X-ray spectra like Seyfert 1s. These objects are discussed more in Section 6.4.

Figure 4.4 shows the X-ray column vs. the BLR column of those objects with broad Hβ, with the BLR columns again estimated by assuming the galactic gas/dust ratio of Shull & van Steenberg (1985). In three of the Seyfert 1s (Mrk 728, Mrk 1018, and NGC 5033) the BLR-obscuring columns are larger than the X-ray columns. This may indicate that their intrinsic Balmer decrements are greater than the assumed value of 3.1, causing their derived BLR reddenings to be too high, or it may indicate that for some reason the broad lines are more absorbed than the continuum, perhaps by self-absorption. In the rest of the objects, the X-ray columns are consistent with or greater than the BLR columns, in accordance with the expectation there may be a component of X-ray absorbing material inside or originating from within the dust sublimation radius, which does not add to the extinction in the optical (see Weingartner & Murray 2002).

In general, the plots of Fig. 4.3, 4.4, and 3.3 show that there is not much correlation between the X-ray, BLR, and NLR columns. This could be due a number of different factors: non-Galactic dust/gas ratios, dust-free absorbers, and complicated absorbing structures could all be playing a role.

Finally, we compare the log of the observed [O III] luminosity in each object with log of its observed $2-10$ keV luminosity in Fig. 4.5. The overplotted solid line is the linear regression fit to the data points (slope=0.67, intercept=12.2). The fit and correlation (Spearman correlation coefficient=0.76) agree fairly well with earlier results from Meléndez et al. (2008) for a sample of 40 nearby X-ray selected Seyferts (slope=0.83, intercept=5.6, Spearman coefficient=0.79). Meléndez et al. (2008) point out that the good correlation between observed [O III] luminosity and observed 2-10 keV luminosity could be due in large part to the fact that these are both absorbed quantities, especially in Seyfert 2s. To test this idea, Fig. 4.6 again plots [O III] luminosity vs. $2-10$ keV luminosity, but with the data corrected for absorption; the [O III] fluxes were de-reddened by the reddening of the NLR, and the unabsorbed X-ray fluxes were calculated from the model fits with the hydrogen column densities set to zero (see Table 4.3 for these values). The liner regression fit is slightly flattened (slope=0.73, intercept=10.5), but the correlation is significantly reduced (Spearman correlation coefficient=0.56) in Fig. 4.6, supporting the idea of Meléndez et al. (2008).

Table 1: X-ray Model Parameters

Object	XSPEC Model Components	wabs $(N_H)^a$	Soft Pwrlaw Norm	1^{st} Soft Gaussian Energy/σ^b	2^{nd} Soft Gaussian Energy/σ^c	pcfabs (CF)^d	Fe Kα Line Energy^e	Hard Pwrlaw Norm	Hard Pwrlaw Γ^f	$(N_H)^g$	Reduced χ^2(dof)
IRAS 18325-5926	wabs*pcfabs*powerlaw	3.38	–	–	–	–	–	6.3e-4	2.17	$2.87^{+0.12}_{-0.11}$	1.31(284)
Mrk 609 (1)	wabs*po	2.91	–	–	–	–	–	3.0e-4	1.77	0.0291^h	0.91(162)
Mrk 609 (2)	wabs*po	2.91	–	–	–	–	–	2.6e-4	1.60	0.0291^h	0.98(291)
Mrk 622	po+(wabs*po)+gauss	2.65	2.0e-5	–	–	–	6.4	9.8e-4	2.0	$112.6^{+37.0}_{-20.8}$	2.58(10)
Mrk 728	wabs*po	1.04	–	–	–	–	–	9.5e-4	1.71	0.0104^h	0.99(347)
Mrk 883 (1)	wabs*po	2.39	–	–	–	–	–	3.5e-4	1.65	$0.080^{+0.009}_{-0.009}$	1.21(188)
Mrk 883 (2)	wabs*po	2.39	–	–	–	–	–	3.5e-4	1.68	$0.079^{+0.008}_{-0.007}$	1.18(231)
Mrk 883 (3)	wabs*po	2.39	–	–	–	–	–	5.0e-4	1.74	$0.107^{+0.008}_{-0.007}$	0.80(262)
Mrk 993	wabs*po	3.12	–	–	–	–	–	2.6e-4	1.62	$0.093^{+0.008}_{-0.008}$	1.13(225)
Mrk 1018	wabs*po	1.46	–	–	–	–	–	2.9e-3	1.98	0.0146^h	1.15(100)
NGC 1365 (1)	wabs*(po+wabs*po+gauss+gauss)	1.04	2.3e-4	0.84/0.13	–	–	6.35	6.2e-3	1.8	$9.77^{+0.10}_{-0.10}$	1.97(1547)
NGC 1365 (2)	wabs*(po+wabs*po+gauss+gauss+gauss)	1.04	1.8e-4	0.83/0.13	1.83/0.02	–	6.32	6.2e-3	1.95	$24.07^{+0.33}_{-0.32}$	1.44(1068)
NGC 1808	wabs*(po+wabs*vmekal)^i	1.56	–	–	–	–	–	5.9e-5	0.79	$0.20^{+0.01}_{-0.01}$	1.13(384)
NGC 2622	wabs*pcfabs*po	2.18	–	–	–	0.88	–	4.5e-4	2.0	$0.70^{+0.08}_{-0.07}$	0.93(166)
NGC 2992	wabs*pcfabs*po	3.12	–	–	–	0.95	6.4	1.6e-2	1.5	$0.49^{+0.003}_{-0.003}$	1.17(1795)
NGC 3786	wabs*pcfabs*po	1.24	–	–	–	0.985	–	2.4e-3	1.8	$3.25^{+0.13}_{-0.12}$	1.03(266)
NGC 3982	wabs*(gauss+gauss+po+wabs*po+gauss)	0.73	1.6e-5	0.53/0.03	0.70/0.20	–	6.4	1.2e-4	2.0	$20.22^{+11.8}_{-6.4}$	0.84(33)
NGC 4388	wabs*(po+wabs*po+gauss+gauss)	1.71	7.0e-5	0.70/0.25	–	–	6.4	1.7e-2	1.8	$31.84^{+0.55}_{-0.53}$	1.18(444)
NGC 4639	wabs*po	1.35	–	–	–	–	–	1.3e-4	1.8	0.014^h	0.97(91)
NGC 5033	wabs*(po+gauss)	0.57	–	–	–	–	6.43	1.1e-3	1.8	0.036^h	0.99(469)
NGC 5252	wabs*(po+wabs*po+gauss)	1.77	6.0e-5	–	–	–	–	3.4e-3	1.8	$4.03^{+0.05}_{-0.04}$	1.48(1438)
NGC 5273	wabs*(gauss+po+wabs*po+gauss)	0.52	3.1e-4	0.58/0.07	–	–	6.45	1.5e-3	1.8	$1.51^{+0.06}_{-0.06}$	1.23(457)
NGC 5506 (1)	wabs*(po+wabs*po+gauss)	3.12	4.8e-4	–	–	–	6.4	2.0e-2	1.8	$2.96^{+0.02}_{-0.02}$	1.04(1576)
NGC 5506 (2)	wabs*(po+wabs*po+gauss)	3.12	5.4e-4	–	–	–	6.4	3.45e-2	1.8	$3.04^{+0.02}_{-0.02}$	1.06(1615)
NGC 5506 (3)	wabs*(po+wabs*po+gauss)	3.12	5.6e-4	–	–	–	6.38	3.34e-2	1.8	$2.89^{+0.02}_{-0.02}$	1.03(1703)
NGC 7314	wabs*(pcfabs*po+gauss)	1.09	–	–	–	0.99	6.39	1.2e-2	1.8	$0.621^{+0.003}_{-0.003}$	1.39(1639)
NGC 7479	wabs*(gauss+po+wabs*po +gauss)	5.82	1.5e-5	0.76/0.10	–	1.0	6.4	2.8e-4	1.8	$62.81^{+29.3}_{-14.9}$	0.75(16)
NGC 7603	wabs*po+po	2.39	3.4e-3	–	–	–	–	4.3e-3	1.8	0.024^h	1.07(1012)
UGC 12138	wabs*po	4.42	–	–	–	–	–	2.3e-3	1.82	0.042^h	1.21(439)

[a] Galactic column estimated from the Galactic reddening values of Schlegel et al. (1988) using the standard Galactic dust/gas ratio of Shull & van Steenberg (1985), in units 10^{20} cm^{-2}. These values were used in the first *wabs* model component. [b,c] The centroid and σ values of Gaussian components used to fit the soft excess, in keV. [d] Covering fraction of partial-covering absorber. [e] Energy (keV) centroid of Gaussian used to represent Fe Kα. [f] If both soft and hard powerlaw components were used, the same photon index Γ was taken for both. [g] Total column to central source from the model, in units 10^{22} cm^{-2}. [h] Column frozen to Galactic value in model. [i] This model is from Jiménez-Bailón et al. (2005). The *vmekal* (Mewe-Kaastra-Liedahl model of thermal emission) component has a temperature kT=0.580 keV.

Table 4.3. Observed and Absorption Corrected [O III] and X-Ray Luminosities

Name	Observed $log(L_{[O\ III]})$	Observed $log(L_{2-10keV})$	Corrected $log(L_{[O\ III]})$	Corrected $log(L_{2-10keV})$
IRAS 18325-5926	41.35	42.96	43.68	43.07
Mrk 609	41.46	42.55	42.86	42.54
Mrk 622	40.51	41.44	41.98	42.50
Mrk 728	40.94	42.99	40.98	42.99
Mrk 883	41.22	42.71	41.79	42.71
Mrk 993	40.19	41.82	40.86	41.82
Mrk 1018	41.02	43.50	41.02	43.50
NGC 1365	40.27	41.81	42.13	42.12
NGC 1808	39.22	40.42	40.26	40.43
NGC 2622	41.24	42.65	41.76	42.67
NGC 2992	40.65	43.05	41.67	43.06
NGC 3786	40.24	42.06	40.89	42.18
NGC 3982	39.48	39.70	40.44	40.01
NGC 4388	40.80	42.49	41.76	43.00
NGC 5033	38.70	40.89	38.70	40.89
NGC 5252	40.91	43.03	41.92	43.16
NGC 5273	39.04	41.22	39.04	41.26
NGC 5506	40.38	42.85	41.50	42.94
NGC 7314	39.79	42.31	40.53	42.34
NGC 7603	41.27	43.58	41.27	43.58
UGC 12138	41.68	43.01	42.15	43.01

*log of luminosities in ergs s^{-1}, calculated from the fluxes using $H_0 = 71$ km s^{-1}, $\Omega_M = 0.3$, and $\Omega_\Lambda = 0.7$, and the redshifts from NED given in Table 6.1.

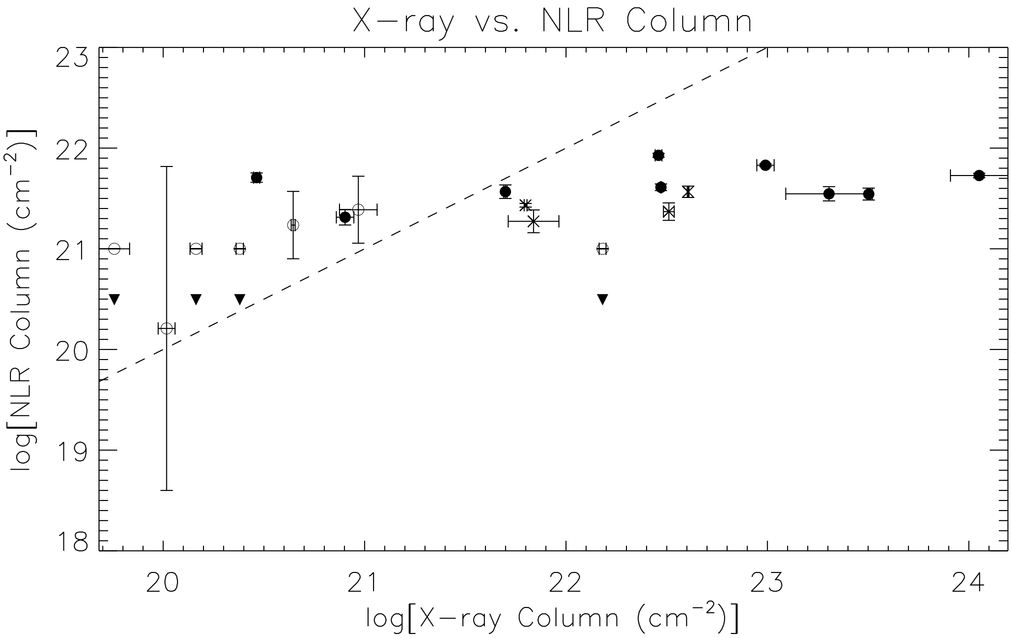

Figure 4.3 The X-ray column versus the column to the NLR, estimated from the reddening assuming the standard Galactic dust/gas ratio. The objects with measured NLR reddenings < 0 are plotted as having an upper NLR column of 1×10^{21} cm^{-2}, based upon the typical measurement error in $E(B-V)$ of ±0.2. Points: Seyfert 2s represented by filled circles, Seyfert 1.8/1.9s represented by crosses, Seyfert 1.0/1.2/1.5s represented by open circles. Dashed line: $N_{H,NLR} = N_{H,X-ray}$.

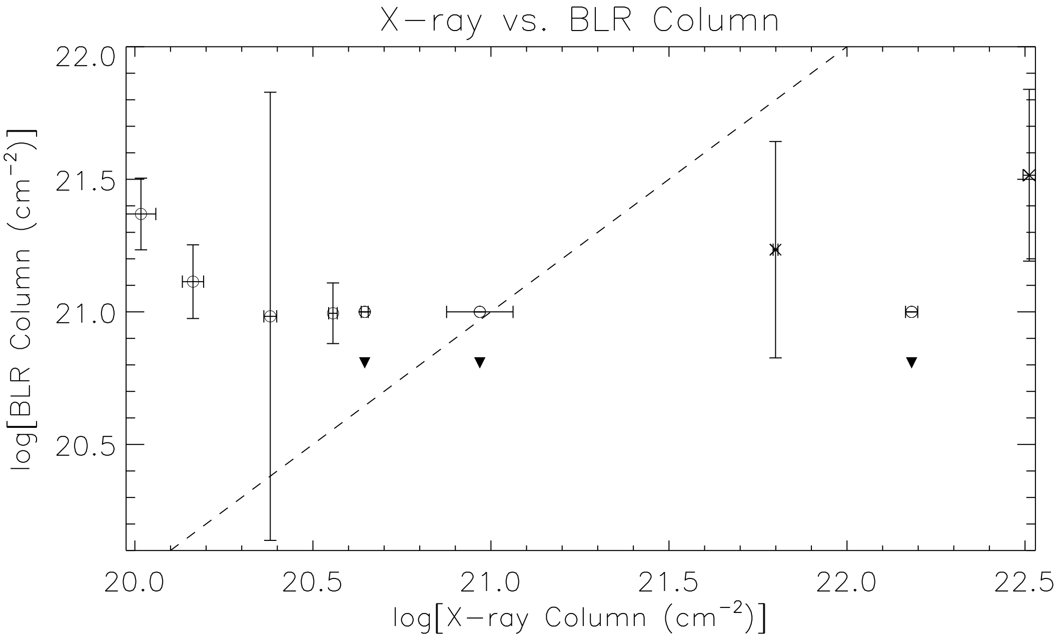

Figure 4.4 The X-ray column versus the column to the BLR, estimated from the reddening assuming the standard Galactic dust/gas ratio. The objects with measured BLR reddenings < 0 are plotted as having an upper NLR column of 1×10^{21} cm^{-2}, based upon the typical measurement error in $E(B-V)$ of ±0.2. Points: Seyfert 1.8/1.9s represented by crosses, Seyfert 1.0/1.2/1.5s represented by open circles. Dashed line: $N_{H,BLR} = N_{H,X-ray}$.

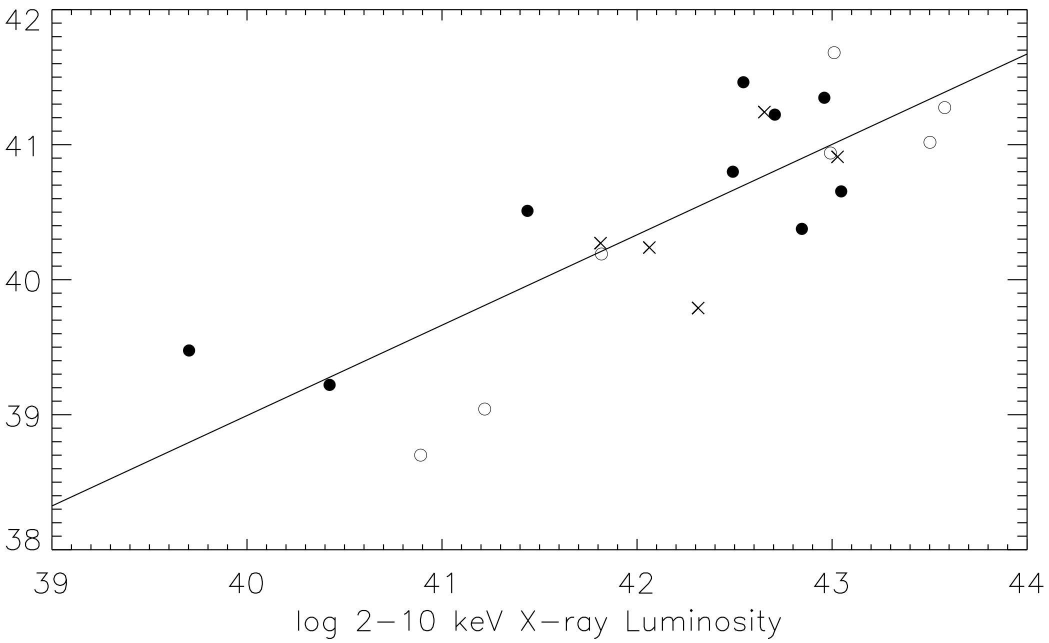

Figure 4.5 X-ray luminosity versus [O III] luminosity. Points: Seyfert 2s represented by filled circles, Seyfert 1.8/1.9s represented by crosses, Seyfert 1.0/1.2/1.5s represented by open circles. Solid line: least-squares linear regression line (slope=0.67, intercept=12.2, Spearman correlation coefficient=0.76).

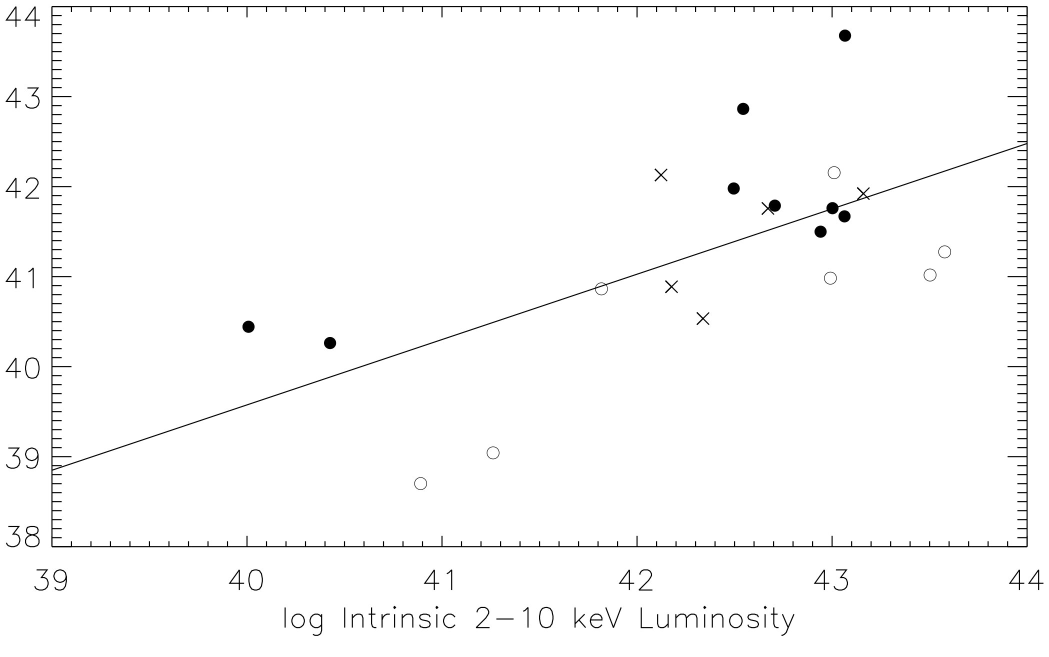

Figure 4.6 Absorption-corrected X-ray luminosity versus dereddened [O III] luminosity. Points: Seyfert 2s represented by filled circles, Seyfert 1.8/1.9s represented by crosses, Seyfert 1.0/1.2/1.5s represented by open circles. Solid line: least-squares linear regression line (slope=0.73, intercept=10.5, Spearman correlation coefficient=0.56).

– 5 –

Other Data

5.1 Optical *HST* Structure Maps

Dust lanes and spirals may play an important role in the reddening of the BLR in intermediate types. In their *HST* broadband WFPC2 imaging survey of nearby Seyferts, Malkan et al. (1998) show that Seyfert 2 nuclei in their sample are more frequently blocked by lanes/patches of host galaxy dust than Seyfert 1 nuclei, and propose these galactic dust structures on scales of hundreds of parsecs could be a viable alternative to the classical parsec-scale torus model. Pogge & Martini (2002), using the technique of "structure mapping" to enhance image contrast and draw out fine dust structures in the circumnuclear environment, show that essentially all of the Seyferts in the CfA Redshift Survey Sample have circumnuclear dust structures on scales of $100-1000$ pc scales (i.e. the scale size of the NLR). However, they find very few Seyfert 2 nuclei obscured by large-scale (> 1 kpc) dust structures, and do not see any significant differences in the circumnuclear dust morphologies of Seyfert 1s and 2s. In any case, both these studies highlight the prevalence of dust structures on the size scale of the NLR, and emphasize that they are important sources of reddening to consider.

To identify hundred-parsec scale or larger sources of obscuration and determine their effect on a Seyfert's 1.8/1.9 status, we downloaded any available WFPC2 broadband images of the galaxies in our sample. Twenty-nine galaxies in our sample had images taken with the F606W filter available, many of these observed for the snapshot survey of Malkan et al. (1998). The F606W filter is wide enough to cover several bright emission lines from high surface brightness regions, and provide sufficient depth to reveal structure at subarcsecond resolution. For NGC 4639, no F606W data was available, so we downloaded and include an image taken with the F547M filter instead. Only five objects had no WFPC2 images available: Mrk 728, Mrk 883, Mrk 1018, Mrk 1179, and Mrk 1320. Those objects that were observed were taken using the PC1 camera (0.″046 resolution), with the exception of UGC 7064, whose nucleus slid off onto the WF 4 chip (0.″1 resolution).

The downloaded images were already reduced by the standard STScI processing pipeline. The only further processing necessary was the removal of cosmic ray hits, which we performed using the IDL procedure IMGCLEAN to flag pixels with values 6 σ above the sky value, and replace them with the average value of the surrounding 10 pixels.

To increase the contrast of these images and draw out dusty structures in the nucleus, we employed the "structure mapping" method of Pogge & Martini (2002). This method, based upon the Richardson-Lucy image restoration, removes most of the large-scale, smooth background light to bring out marginally resolved structures (i.e., structures on the same scale as the PSF). A copy of the original image is convolved with a model of the PSF, and the original image is then divided by this PSF-smoothed image. This ratio is then further convolved with the transpose of the model PSF. Mathematically, the structure map is produced by the procedure

$$\text{Structure Map} = \frac{\text{Image}}{\text{Image} \otimes \text{PSF}} \otimes \ \text{PSF}^t \tag{5.1}$$

where $\otimes$ is the convolution operator and PSF^t indicates the transpose of the PSF.

We used IMEXAMINE routine in IRAF to fit 2-D Gaussians the point sources at the centers of the galaxies, to determine the location of the central source on the detector, and then generated the PSF at each of these locations using the TinyTim software. These PSFs were then used in the above convolutions to generate the final structure map.

The final processed structure maps are shown in Appendix D. The dark regions show the location of dust obscuration, while the bright regions show areas of concentrated stellar light or emission line regions of the AGN.

The 1.8 galaxies Mrk 334 and UM 146 both show an unobscured central nucleus, but have surrounding dark dust spirals on the same scale as the NLR, in agreement with the higher NLR reddening compared to BLR reddening in these objects. Such sources of dust are also apparent in all the other objects in which the reddening of the NLR is greater than that of the BLR (Mrk 993, NGC 7314, UGC 12138, and UM 146).

For the cases where the reddening of the BLR is greater than the reddening of the NLR, we checked the images for sources of reddening in the NLR. In Mrk 423 (type 1.5), although lanes of dust can be traced into the central 500 pc, there is no obvious dust structure crossing the nucleus. In Mrk 915 (type 1.9), there is a dark lane/bar that runs across the nucleus, and could be the source of the higher reddening of the BLR. NGC 5033 (type 1.2) is in a highly inclined host, and the dust near the central point source may partially cover it.

NGC 3786 and have NGC 7314 (both 1.9s) have NLR/BLR reddening estimates consistent to within their (large) errors. In NGC 7314, the reddening of the BLR must be due, at least in part, to the dark lane that crosses over the nucleus seen in Fig. D.24. There is no obvious dust structure crossing the nucleus of NGC 3786.

To summarize, none of the 1.8s have dark lanes crossing their nuclei, although they all show signs of circumnuclear dust. Of the 1.9s, Mrk 915 and NGC 7314 have dark lanes that cross their nuclei, but in Mrk 471, NGC 1365, NGC 2622, NGC 3786, NGC 5252, and UGC

7064 there is no obvious dust structure crossing the nucleus. NGC 2622, NGC 5252 and UGC 7064 are classified as "internally reddened", (see Chapter 6); if they are are internally reddened, it must be on a smaller size scale than the $100 - 1000$ pc structures seen in these images (possibly the torus).

5.2 Spitzer IRS Spectra

Observations in the mid-IR give further insight into the dust properties of these galaxies, and to this end we retrieved and processed the available low-resolution Spitzer IRS spectra from the Spitzer archives (see Deo et al. 2007 for details) for these objects. These spectra are presented in Appendix E. Seyferts optically classified as type 1 typically show much stronger mid-IR continua in the 5-8 μm region than those classified as type 2. These two continuum shapes are modified by two processes: silicate dust emission or absorption and PAH emission from star forming regions. Thus, mid-IR spectra give information on the temperature of the dust from the shape of the continuum and the amount of extinction due to cold dust in the host galaxy from the depth of the silicate 9.7 μm feature (Deo et al. 2007). In our current study, in which we wish to pin down the location of the dust responsible for the reddening in Seyfert 1.8/1.9s, we wanted to compare the reddening from host galaxy from the mid-IR with the $E(B-V)$ values of the NLR and BLR. To this end, we measured the optical depth at the center of the absorption line($\tau_{9.7\mu m}$), and used this to estimate the intrinsic dust extinction of the host galaxy via the relationship for diffuse ISM clouds derived by Roche & Aitken (1984), $A_V = 18.5\tau_{9.7\mu m}$. The column densities corresponding to the reddening values determined in this way are listed in Table 6.1.

Unfortunately, the 9.7 μm line may be surrounded by strong PAH emission lines, which can make placement of the local continuum uncertain and affect line measurement, and we found these measures to be too unreliable to be helpful to our study. The spectra were still useful, however, in determining which Seyferts contain a strong starburst component, as noted in the information on individual objects in the next chapter. It was also interesting to note the apparent mismatch in optical and IR types for NGC 2639 and NGC 7314 (a LINER 2 and a 1.9, respectively) that show the strong rise to short wavelengths most typical of type 1 objects.

– 6 –

Data Summaries of Individual Objects

In this chapter, we give our type classification of the galaxies in our sample, discuss their observation histories, and give our interpretation of the 1.8/1.9s as low-flux or internally reddened objects, or note if the evidence is inconclusive. Table 6.1 at the end of the chapter is a summary of the data collected for each object.

1. **IRAS 18325-5926–Type 2, internal reddening**

Our optical spectra from CTIO show Hα to have about the same width as [O III] λ5007 (FWHM$\approx$850 km s^{-1}), and thus we classify IRAS 18325-5926 as a Seyfert 2. It has a heavily reddened NLR, but its *XMM* spectrum shows it to have a total hydrogen column of $N_H \approx 2.9 \times 10^{22}$ cm^{-2}, several times larger than the equivalent gas column to the NLR, consistent with a Seyfert 2 classification.

There is no real evidence for variability in this object. Although Iwasawa et al. (1995) classified it as a 1.9, their use of Gaussians to fit the [N II] lines on the side of Hα does not seem to be justified based on the structure of the other forbidden lines in the spectrum, and probably led to a false detection of a broad Hα component.

2. **Mrk 334–Type 1.8, low flux**

The spectrum of Mrk 334 taken at Lowell Observatory in January 2009 shows weak broad Hα and very weak broad Hβ after subtraction of the host galaxy spectrum, and thus we classify it as a type 1.8. The weakness of the broad components makes the broad Balmer decrement difficult to measure, but it seems that the BLR is essentially unreddened. The Spitzer IRS spectrum of Mrk 334 shows strong PAH emission features due to the star-forming ring in its central kiloparsec (Deo 2007).

Mrk 334 was originally classified as a 1.8 by Dahari & De Robertis (1988), and does not seem to have undergone any type variability since. It was again classified as a 1.8 by Osterbrock & Martel (1993) from a spectrum taken in September 1991, and appears no different in Gallego et al. (1996).

Because the BLR appears to be essentially unreddened and because its position in Fig. 3.2 is slightly below the Seyfert regime, indicating a history of low ionizing flux, we classify Mrk 334 as a low-flux AGN.

3. **Mrk 423–Type 1.5, internally reddened**

Mrk 423's optical spectrum from Lowell Observatory in January 2009 shows that the AGN's emission spectrum is heavily contaminated by the underlying stellar absorption spectrum of the host galaxy. Although broad Hα is clearly visible, a telluric absorption line cuts into its red side and makes measuring this component more uncertain. The unusual continuum shape was difficult to fit, and the spectrum is choppy and noisy even after the subtraction of a host galaxy template, making Mrk 423 difficult to classify. Though we formally classify Mrk 423 as a 1.5, based on the definition of this class by Maiolino & Rieke (1995), it is close in appearance to a 1.8, and its BLR seems to be affected by slight internal reddening. The NLR is essentially unreddened, and the broad Hα component is fairly strong, yet broad Hβ is weak and no broad Lyα is seen in its *HST* GHRS (Goddard High Resolution Spectrograph) spectrum, taken in May 1996.

This galaxy was originally classified as a 1.8 by Osterbrock (1981), but using slightly different classification criteria than ours, so there is no reason to suspect Mrk 423 of variability. The spectrum presented by Rafanelli et al. (1993) looks similar to ours, as does that of Rudy et al. (1985). Rudy et al. (1985) also present a UV spectrum by IUE, which shows the Lyα line to be of unresolved width.

4. **Mrk 471–Type 1.9, inconclusive cause**

This object's SDSS spectrum from 2005 shows it to be a Seyfert 1.9. From this spectrum, we find the NLR to be highly reddened by $E(B-V)_{NLR} = 0.89$. The Spitzer spectrum of Mrk 471 is heavily contaminated by PAH emission features, making measurement of the 9.7 μm absorption trough uncertain, but it seems to indicate a reddening of $E(B-V)_{NLR} \approx 0.88$, very similar to that of the NLR.

There is no evidence for variable broad components in Mrk 471.

5. **Mrk 516–Transition Object (LINER 2+starburst), low flux**

The CTIO spectrum of Mrk 516 shows it is a "transition object"; the ratio of [O III]/Hβ is only about 1.2 (see Fig. 3.2). No broad components are visible. Both the [O III] lines and [N II] lines have wide, asymmetric profiles. This structure is due to the double nucleus found by Gorjian (1995) in *HST* images; one is thought to be the AGN and the other is thought to be either the nucleus of another galaxy in the final stages of merging with Mrk 516, or an H II region triggered by such a merger.

There is some evidence that this object has shown weak broad-line variability. Osterbrock (1981) classified it as a 1.8 based on a spectrum from 1978 which shows a weak broad $H\beta$

component. Goodrich (1990) noted that in his August 1986 spectra Mrk 516 had no broad $H\beta$ component and that broad $H\alpha$ also seemed weaker than that reported by Osterbrock. We therefore conclude that this object is probably in a low-flux state: in its normal low state it appears as a LINER 2, but during a continuum flare-up the slight broad components observed by Osterbrock appeared, and it appeared as a LINER 1.

6. **Mrk 609–Type 2, low flux**

The CTIO spectrum of Mrk 609 shows it to be a Seyfert 2. It also shows wide [O III] $\lambda\lambda$4959, 5007 lines relative to the other forbidden lines in the spectrum. Although we classify it as a Seyfert 2, data from other wavebands supports the idea that Mrk 609 is a low-flux object. Its Spitzer IRS spectrum shows strong PAH emission features, but little if any 9.7 μm absorption. More unusually, its *XMM-Newton* $0.5 - 10$ keV spectrum taken in January 2007 shows a powerlaw absorbed by only a very small column, consistent with Galactic absorption. This makes Mrk 609 what is known as "true" Seyfert 2 candidate, because it appears that we have a clear view to its nucleus, but there is no sign of the broad-line region in the optical, in apparent contradiction of the orientation-dependent unified model. See Section 7.1.3 for a further discussion of these objects.

Previously published data on Mrk 609 also points to it being a low-flux object at the time of our observations. Mrk 609 was originally classified as a 1.8 by Osterbrock (1981) from spectra taken in 1975 and 1976, but he later revised the type to be a 1.5 with better spectra. Goodrich observed it again in November 1986 and also classified it as a 1.5, but noted that it had a large Balmer decrement. Rudy et al. (1988) present a groundbased optical spectrum made simultaneously with an IUE observation. Broad Balmer components are visible in the optical spectrum, and the IUE spectrum also shows broad Lyα. Interestingly, they found that the ratio $Ly\alpha/H\beta/H\alpha = 16/1.0/5.0$ and infer that the BLR is basically unreddened.

7. **Mrk 622–Type 2**

The SDSS spectrum of Mrk 622 shows its [O III] lines are stumpy with a double peaked structure, much wider than Hβ or [N II]. By our criteria, this is a Seyfert 2 galaxy. In line with this optical classification, the Spitzer IRS spectrum shows it to have a typical Seyfert 2 mid-IR spectrum, with the continuum weakening in the 5-15 micron range (Deo et al. 2007) and strong PAH emission features. Furthermore, its *XMM* X-ray spectrum is also heavily absorbed, by a column of 112.6×10^{22} cm^{-2}.

Goodrich (1995) includes Mrk 622 in his list of Seyfert 1.8/1.9s, but we have no confirmatory evidence of this classification, and so do not expect that its type has varied since it was first observed.

8. **Mrk 728–Type 1.2, formerly a 1.9, due to low flux**

The SDSS spectrum from 2004 of Mrk 728 shows it to be a type 1 Seyfert, or, based on the flux ratio requirements of [O III]λ5007/Hβ of Maiolino & Rieke (1995), a type 1.2. The strong broad Lyα line in its GHRS spectrum is consistent with this classification. Interestingly, its estimated BLR-obscuring column (0.23×10^{22} cm^{-2}) is greater than the X-ray column from *XMM* (0.01×10^{22} cm^{-2}), and its NLR-obscuring column (0.02×10^{22} cm^{-2}).

Mrk 728 was originally discovered as a Seyfert 1.9, but underwent a change in type. Osterbrock & Dahari (1983) first classified it as a Seyfert 1.9, and it was also classified as a 1.9 when observed by Goodrich in 1986 (Goodrich 1989). When it was observed by Goodrich again in March 1993 its Balmer lines were much stronger(Goodrich 1995), and the spectrum looks much as it does in our SDSS spectrum. Goodrich found the changes in $H\alpha$ and $H\beta$ to be consistent with the same change in reddening, but because $H\beta$ is quite weak to nonexistent in the earlier spectrum (it was classed as a 1.9), this measurement is quite uncertain. Furthermore, Goodrich saw no change in the continuum flux or shape, and therefore states that "if the lines brightened due to a dust cloud moving out of our line of sight, then the cloud must still cover the continuum source", which seems unlikely. In short, somewhere between 1986 and 1993 Mrk 728 changed type from a 1.9 to a 1.2 and has been the same ever since, and this is probably due to the fact that it was in a low flux state when it was initially identified as a 1.9 and is now back up.

9. **Mrk 883–Type 2, formerly Type 1.9 due to low flux**

The optical spectrum of Mrk 883 from SDSS show it to be a Seyfert 2. However, its NLR is only reddened by $E(B-V) = 0.4\pm0.1$, and its *XMM* spectrum shows only a small amount of absorption by a column only slightly in excess of Galactic and possibly attributable to Mrk 883's host galaxy. This makes Mrk 883 another "pure" Seyfert 2 candidate, an object that does not show broad lines although it appears that we have a clear view to the nucleus (see Section 7.1.3 for a discussion of these objects). Its Spitzer spectrum is typical of a Seyfert 2 with a significant starburst component.

There are a few small pieces of evidence that Mrk 883 has undergone broad-line variation. Shuder & Osterbrock (1981) claimed to see a broad component of $H\alpha$ in early spectra taken between 1975 and 1980. Osterbrock and Dahari later dubbed it a "marginal 1.9", due to the weakness of the broad component of $H\alpha$ seen after the subtraction of narrow $H\alpha$ and [N II]

(Osterbrock & Dahari 1983). Goodrich (1995) saw weak variations in its broad components between 1978 and 1993, inconsistent with a simple change in reddening, although the continuum did not appear to have changed.

This object appears to be another case like NGC 2992 (Trippe et al. 2008), where it is currently in a low flux state. This is deduced from the evidence for weak intrinsic continuum variations, as well as the its low X-ray column and matching low NLR reddening. As in the case of NGC 2992, it appears that Mrk 883 is currently in a low state, with no broad components visible.

10. **Mrk 915– Type 1.9, internally reddened**

Our CTIO spectra from June 2008 show this to be a Seyfert 1.9 galaxy. It is possible that Hβ shows an extremely weak broad component, at the limit of detectability, but not significant enough to classify this as a 1.8. The lower limit of the reddening of the BLR ($E(B-V)_{BLR} \geq 0.84 \pm 0.51$), derived from the strength of Hα, is still larger than the reddening of the NLR ($E(B-V)_{NLR} = 0.27$). The source of the higher BLR reddening could be the large-scale dust lane that runs directly across the nucleus, seen in its WFPC2 image.

Goodrich reports variability between 1984 and 1993, when it appeared to go from a 1.5 to a 1.9, with evidence that this change was due to a change in reddening $\Delta E(B-V) = 0.38$ (Goodrich 1995), from an estimation of the continuum change between observations. However, due to the uncertainties in flux calibration, the measurements that lead to this claim are highly uncertain.

11. **Mrk 993–Type 1.5, low flux**

The optical spectrum of Mrk 993 from Lowell Observatory in January 2009 shows it to be a type 1.5 Seyfert. From the measured Balmer decrements of this spectrum, the BLR appears to be largely unreddened, while the reddening of the NLR is slightly higher ($E(B-V) = 0.47$), although we note that both these measurements have large errors due to heavy contamination by the underlying host galaxy spectrum. Mrk 993's *XMM-Newton* spectrum shows absorption by only a small column, $\mathrm{N}_H = 9.3 \pm 2.0^{20}$ cm^{-2}, attributable to Galactic absorption and likely absorption by its inclined host galaxy (b/a=0.32). The WFPC2 structure map presented in Pogge & Martini (2002) allows us to visualize these findings. The image shows an unobscured central nucleus and dust spirals on the scale of the NLR, particularly just to the east of the nucleus, in agreement with the higher NLR column compared with the BLR and X-rays.

Mrk 993 appears to currently be a low-flux object. It has a history of variability, and its transition from its original classification as a 1.9 to a 1.5 has been attributed to variable reddening (Tran et al. 1992), but it does not appear to be internally reddened in its current state as a 1.5. Its BLR is essentially unreddened in our spectrum, and this lack of reddening confirmed by its low X-ray column. A paper by Corral et al. (2005) presents an optical spectrum taken simultaneously with the *XMM* observation, and this spectrum confirms that it was in the same optical state as in our Lowell observation. However, Corral et al. (2005) conclude that it has a BLR Balmer decrement of ∼9 (i.e. reddened), while we found it to be 2.3 (i.e. unreddened). The difference in these measurements is probably due to the low signal-to-noise of the spectrum used by Corral et al.

Although the BLR of Mrk 993 isn't reddened in its current state, it is difficult to say if it was reddened as a 1.9. It is possible that the broad line changes seen by Tran et al. (1992) are due to both changes in the intrinsic continuum flux and changes in extinction. However, because Tran et al. (1992) report a reddening of $E(B-V)_{BLR} > 0.76$, it is possible that it was internally reddened when it appeared as a 1.9.

12. **Mrk 1018–Type 1, formerly 1.9, low flux**

The SDSS spectrum of Mrk 1018 shows it to have been a Seyfert 1 in September 2000. A clear rise in the blue end of the SDSS spectrum not seen in the previous optical spectra from the 1980's indicates that the continuum has gained in apparent brightness since then.

This object was a 1.9 when observed by Osterbrock (1981). However, it transitioned to a type 1 between this observation and its observation by Cohen et al. in January 1984 (Cohen et al. 1986), and has apparently remained as a type 1 since. Cohen et al. (1986) attribute the observed change in type to an increase in the brightness of the non-stellar continuum, but note that the increase in flux of broad $H\alpha$ and in broad $H\beta$ are consistent with the same change in reddening, $\Delta E_{B-V} \approx 0.55$. Comparing our spectrum with their "high-state" spectrum from yields $\Delta E(B-V)_{H\alpha} = 0.12$ and $\Delta E(B-V)_{H\beta} = 0.04$, and provides further minor evidence that this object is probably undergoing changes in its intrinsic continuum flux.

13. **Mrk 1126–Type 1.8, low flux, external reddening**

In our spectrum from CTIO in October 2007, both weak broad $H\alpha$ and very weak broad $H\beta$ are apparent after subtraction of the host galaxy spectrum. From measurements of these broad components, we find the reddening of the BLR and the reddening of the NLR to be consistent within their errors, indicating the low-flux scenario for this object. The WFPC2 image of Mrk 1126 shows it to reside in an almost circular face-on spiral galaxy.

Our literature search did not provide any evidence for variability; past authors consistently classify it as a 1.8 (Botte et al. 2004; Schachter et al. 1990), with the exception of Osterbrock & Pogge (1985) who classified it as a narrow-line Seyfert 1 (NLS1) on the basis that high-ionization iron lines such as [Fe VII] and [Fe X] are present in its spectrum. However, because its Balmer lines are clearly a composite of broad and narrow components, and there there is no measurable [Fe II] emission, we believe that it was wrongly classified at that time, and that 1.8 would have been a better designation.

14. **Mrk 1179–Type 1, formerly type 1.9**

Our spectrum of Mrk 1179 from Lowell Observatory in January 2009 shows this to be a type 1 Seyfert galaxy; very strong broad components with FHWM $\approx$ 6,000 km s^{-1} are visible in all of the Balmer lines. Although deconvolution of the components is uncertain due to the overwhelming strength of the broad lines, both the BLR and NLR appear to be essentially unreddened.

Interestingly, this object has changed type quite dramatically since it was previously observed, providing our only new case of type variability. It was classified in the 1980s as a type 1.9 (see Osterbrock & Dahari 1983; Rudy & Rodriguez-Espinosa 1985; Goodrich 1989). Unfortunately, these authors give only the classification without any further information about the spectrum, and so the cause of the change, possibly either variable flux or variable reddening, cannot be determined.

15. Mrk 1320–Type 1.5, low flux

Our Lowell spectrum of Mrk 1320 from January 2009 shows this to be a Seyfert 1.5 object, according to the definition by Maiolino & Rieke (1995), although it is close in appearance to a Seyfert 1.8.

Mrk 1320 was classified by Osterbrock & Dahari (1983) as a Seyfert 1.5. He notes that the broad components of the Balmer lines are slightly weaker than other 1.5s, but still easily visible. A blue spectrum displayed in Marziani et al. (2003) shows it to have what seems to be a larger broad Hβ line than that visible in either our spectrum or that described by Osterbrock.

Because the reddening of the BLR appears to be zero, we classify this as a low-flux object.

16. NGC 1365–marginal Type 1.9, unknown cause

We classify NGC 1365 as a 1.9, though we note that the broad component of Hα is extremely faint in our 2009 January spectrum of this object. Hβ appears to be enhanced relative to [O III], as reflected by its unusual position on the BPT diagram (Fig. 3.2), indicating a very strong starburst component. Its Spitzer spectrum is also indicative of a very strong starburst component, displaying strong PAH emission features. Its *XMM* spectra indicate its nucleus is being absorbed by a column in excess of that in the NLR, but because it is not known how much of this material contains dust, we do not know if this absorber contributes to the optical extinction of the BLR.

There is some evidence of optical type variability in this object. Schulz et al. (1994) comment on the "conspicuous" broad component of Hα observed in October 1988, and in Schulz et al. (1999) the authors show a figure of the Hβ profile which appears to have a quite substantial broad component. Regardless, there is not enough information to establish the cause of this possible variation over time. It seems feasible that, as suggested by Edmunds & Pagel (1982), most of the BLR absorption occurs in the dust lane which just barely covers the nucleus (NGC 1365 looks like a 1.8 in their spectrum from 1979).

There is extensive X-ray data on NGC 1365. Risaliti et al. (2000) reports that the X-ray spectrum is composed of both directly observed and reflected components. It is highly variable in the X-ray; several Compton-thick to Compton-thin transitions have been observed (Risaliti et al. 2005, 2007). Furthermore, Risaliti et al. (2009) observed a change in X-ray flux, which they attribute to an occultation event during a 5-days continuous monitoring campaign with *XMM*, and they infer that the X-ray absorption and reflection originates in the BLR clouds. If so, these clouds are well within the dust sublimation radius and the changes are therefore probably not related to any changes seen in the optical spectrum.

17. **NGC 1808–HII (starburst)**

Our spectrum of NGC 1808 from CTIO in October 2007 shows no broad components and only very weak [O III] lines. We classify it as a starburst galaxy based on the measured line ratios from this optical spectrum (see Fig. 3.2).

NGC 1808's status as an AGN has been the subject of debate for many years (Jiménez-Bailón et al. 2005). It does not, however, seem that it has ever been a Seyfert 1.8/1.9.

18. **NGC 2622–Type 1.9, internally reddened**

This object is classified as a Type 1.9 based on its SDSS spectrum from 2004. Its *XMM* spectrum is well fit by powerlaw with $\Gamma = 2$ attenuated by a column density of 1.3×10^{22}

cm^{-2}. The available *HST* GHRS spectrum shows narrow, but no broad Lyα. Conversely, this object's Spitzer IRS spectrum looks like that of a type 1 AGN, with a continuum rise to lower wavelengths, indicating emission from a hot component.

This object has undergone classification changes in the past. Osterbrock & Dahari (1983) classed it as a 1.8, but Goodrich (1989) observed it to be a Seyfert 1, and that the changes in flux of the broad lines and the continuum near Hα and Hβ were consistent with changes in reddening in all cases. He also later noted that Paβ measurements of this object are also consistent with reddening theory (Goodrich 1990). However, when NGC 2622 was later seen to have faded again in 1993 (Goodrich 1995) it did so in a manner inconsistent with a change in reddening.

This object is most likely being affected by internal reddening, as evidenced from the lack of broad Lα in the GHRS spectrum. Further, the dust column to the NLR from the reddening $E(B-V) = 0.36$ is $N_H = 1.87 \times 10^{21}$ cm^{-2}, while the X-ray column is greater by a factor of ∼7. While this does not prove the BLR to be obscured by dust in the torus, because the column could be from a dust-free absorber, it does give evidence that there is a component of absorption in the inner nucleus. NGC 2622 may be a case of a reddened object that also has an intrinsically variable continuum, as evidenced by the observations of Goodrich (1995) and the mismatch between its optical and IR spectra.

19. **NGC 2639–LINER**

NGC 2639's nuclear spectrum from Lowell Observatory in January 2009 is heavily diluted by the underlying host galaxy spectrum; it does not show any Hβ emission, broad or narrow, and [O III] λ5007 is barely visible even in the host-galaxy subtracted spectrum. Because there is no Hβ, we resort to an alternate system for classification than that of Maiolino & Rieke (1995) used for the other objects in this study, which relies on the ratio of [O III] to Hβ. We classify it as a LINER based instead upon the criteria of Heckman (1980) ([O II] 3727 $\geq$ [O III] 5007 and [O I] 6300 $\geq$ (1/3) [O III] 5007). De-blending the [N II] lines on the sides of Hα proved difficult, due to NGC 2639's irregular forbidden-line profiles. The template that best matched the observed [N II] profiles was a template constructed from the blended [S II] lines: the blue side of the [S II] λ6716 line and the red side of the λ6731 line. While this template fit most of the [N II] profile exactly, the outermost part of the red wing of the λ6583 line still showed excess flux over the template, leading to the spike of leftover emission seen in the [N II]-subtracted spectrum of Appendix B. In spite of this imperfection, it still seems apparent that there is not a broad Hα component. The Spitzer IRS spectrum of NGC 2639 shows strong PAH emission features, 9.7 μm absorption, and a strong rise in the continuum towards short wavelengths. NGC 2639 was observed by *XMM* in April 2005, but due to a very high background level during the observation, the data is poor quality and we did not attempt to model it.

Several authors in the past have claimed there to be a broad component to Hα, leading to its initial classification as a type 1.9 (see Keel 1983; Huchra et al. 1982). However, noting (as do Ho et al. 1997b) the extended wings of the [N II] lines are mostly responsible for the seeming appearance of a broad component to Hα, we suspect that past decomposition of this blend assuming Gaussian line profiles seriously overestimated the flux of this component.

20. **NGC 2992–Type 2, low flux/externally reddened**

We have observed NGC 2992 many times over the past few years, and because the spectra do not show any evidence for variability, the spectrum presented in Appendix A is the average of these spectra. NGC 2992's *XMM* spectrum shows absorption by a column density of $\approx 0.49 \times 10^{22}$ cm^{-2}. Its Spitzer spectrum shows strong PAH emission features, and 9.7 μm absorption corresponding to a reddening of $E(B-V) \approx 2.1$.

As mentioned in the introduction, NGC 2992 has a history of variability, both in the optical and X-ray regimes (see Chapter 2 for details). Because the changes in its optical classification seem to be correlated with its X-ray brightness, but with the column density remaining constant, it seems that this object was classified as a 1.9 because it was in a low continuum state. Because the NLR and BLR have similar reddening, the high Balmer decrement observed at the time it appeared as a 1.9 was most likely due to dust in the plane of the host galaxy.

21. **NGC 3786–Type 1.9**

We classify NGC 3786 as a Seyfert 1.9 in our Lowell spectrum of this object from January 2009. It is possible that a very faint component to Hβ is also present, but it is at the limit of detectability, even after the spectrum correction for the host galaxy contamination. We were not able to tell whether the BLR is more reddened than the NLR; the large uncertainty in the lower limit of reddening of the BLR, $E(B-V)_{BLR} \geq 0.63 \pm 0.47$, puts it within the range derived for the reddening to the NLR ($E(B-V)_{NLR} = 0.45 \pm 0.09$). Its Spitzer IRS spectrum displays the strong PAH emission features indicative of a large starburst, and 9.7 μm absorption corresponding to a reddening of E(B-V)=1.74±0.22. NGC 3786's *XMM* X-ray spectrum is well-fit by a partial covering model, with a covering factor of 0.985 and N_H=3.3± 0.1×10^{22} cm^{-2}.

It is difficult to tell if the broad lines have undergone any variation over time. Past spectra of NGC 3786 certainly look very similar to our own (see Huchra et al. 1982; Goodrich & Osterbrock 1983), with any differences attributable to observing conditions. Goodrich & Osterbrock (1983) classify it as a Seyfert 1.8, and measure the broad Balmer decrement to be ∼8.4. Komossa & Fink (1997) point out that this amount of reddening corresponds to a column of 5.5×10^{21} cm^{-2} to the BLR, which closely matches the column they derived by fitting a warm absorber model to its X-ray spectrum from ROSAT. The *XMM* spectrum from 2004 is not high enough quality to provide information about the ionization state of the absorber to test this claim.

22. **NGC 3982–Type 2**

The SDSS spectrum of this object shows no trace of broad $H\alpha$, showing that this object was a Seyfert 2 when observed in January 2003. In line with this classification, its *XMM-Newton* spectrum is heavily attenuated by a column of $N_H \approx 20.2 \times 10^{22}$ cm^{-2}, and its Spitzer spectrum is also typical of a Seyfert 2.

There is no convincing evidence that this object has ever changed type from past classifications in the literature. Although we included it in our study because Quillen et al. (2001) give its classification as 1.9/2, it has apparently always been a Seyfert 2.

23. **NGC 4388–Type 2**

The SDSS spectrum of NGC 4388 shows no trace of broad Hα, and thus we classify it as a Seyfert 2. Its *XMM* spectrum shows absorption by a column of $31.8 \pm 0.6 \times 10^{22}$ cm^{-2}, also typical of a Seyfert 2, and an excess of soft emission in the 0.5-2 keV range.

There is no evidence from the literature for variability from a previous 1.8/1.9 state. Again, this object was included in our study because of its classification in Quillen et al. (2001) as a type 1.9/2, but appears to have really always been a Seyfert 2.

24. **NGC 4639–low-luminosity Seyfert 1**

Our optical spectrum on NGC 4639 from Lowell Observatory in January 2009 shows that the host galaxy dominates the spectrum. It shows what looks like a broad Hα line, but it is impossible to deblend the [N II] because there are no other forbidden lines in the spectrum to use for comparison. Its *XMM* spectrum is faint, but appears unabsorbed. Both the *XMM* spectrum and the optical spectrum are consistent with its classification by Ho et al. (1999) as a low-luminosity Seyfert 1.

Ho et al. (1995) display a spectrum in which broad Hα looks much more clear than in our data. Though Ho et al. (1999) suggest that the BLR is significantly reddened, and estimate the reddening of the BLR using the ratio of Hγ/Hβ to be ∼0.4, this measurement is very uncertain due to the faintness of these lines.

25. **NGC 5033–Seyfert 1.2, low flux**

The optical spectrum from Lowell Observatory in January 2009 shows NGC 5033 to have the spectrum of a Seyfert 1.2 (according to the definition of this class by Maiolino & Rieke (1995)), heavily contaminated by underlying stellar absorption spectrum from the host galaxy. The Hβ line is apparent only after the subtraction of a host-galaxy template. The BLR seems to be only slightly reddened with $E(B-V)_{BLR} = 0.19 \pm 0.05$, while the NLR seems to be totally unreddened, $E(B-V)_{NLR} = -0.04 \pm 0.43$. NGC 5033's *XMM* spectrum is well-fit with an unabsorbed powerlaw, and a narrow Fe Kα line is also present, indicating a reflected component to the spectrum.

Broad Hα was noted in early spectra of NGC 5033 (see Shuder 1980; Stauffer 1982; Filippenko & Sargent 1985), and Filippenko & Sargent (1985) note that this broad component of Hα seems to be variable from their observations in July 1982 and February 1984. Dahari & De Robertis (1988) classify it as a 1.9, as do Osterbrock & Martel (1993). Koratkar et al. (1995) note the presence of both broad Hα and broad Hβ in their spectrum of NGC 5033 from January 1993. We note, however, that many of these seeming differences in classification are probably due to the difficulty in picking the Hβ line out from the contamination by the host galaxy, and that in spite of the weak variations in the broad Hα noted by Ho et al. (1995), it has probably not undergone changes large enough for it to change its type classification. Because this is known to be a low-luminosity Seyfert, heavily contaminated by the host galaxy, with an unabsorbed X-ray spectrum, it is most likely a low-broad-line-flux object, not an internally reddened object.

26. **NGC 5252–Type 1.9, reddened**

The SDSS spectrum from April 2002 shows the spectrum of a Seyfert 1.9 object. Based on the weakness of Hα, Hβ is below the level of detectability in our spectrum, even if the BLR is completely unreddened. Its *XMM* spectrum shows absorption by a column density $\approx 4 \times 10^{22}$ cm^{-2}, about 10 times that as the column to the NLR indicated from the reddening $E(B-V)_{NLR} \approx 0.71$.

There is no evidence for variability in NGC 5252's past observations. However, it is known from polarization studies (Young et al. 1996) that this object has a hidden BLR, and we therefore classify it as a reddened object.

27. **NGC 5273–Type 1.5, low flux**

Our spectrum from KPNO in June 2008 is rather noisy due to poor seeing conditions, but both broad Hα and Hβ are apparent after subtraction of the host galaxy. Neither the NLR or BLR appears to be significantly reddened in this face-on (b/a=0.89) galaxy. However, its X-ray spectrum does show absorption by a large column, $N_H=1.50\times10^{22}$ cm^{-2}, which may indicate the absorption occurs in a dust-free warm absorber, and that the column density may in fact be even higher than this value, derived assuming cold absorption.

Previous classifications of NGC 5273 are consistent with our current classification (Ho et al. 1995; Dahari & De Robertis 1988), except Osterbrock & Martel (1993), who classify it as a 1.9. We suspect that the subtraction of the host galaxy spectrum may be the cause of this difference, and hence there is no reason to suspect this object of strong variability.

28. **NGC 5506–Type 2**

From the optical SDSS spectrum of NGC 5506 taken April 2002, we classify this as a Seyfert 2. Nagar et al. (2002) have a near-IR spectrum with permitted lines from the BLR with FWHM $<$ 2,000 km/s, and therefore claim it to be an “optically obscured” NLS1. Some part of the reddening of the nucleus must be due to the dust in a lane that crosses over the nucleus, seen in its WFPC2 image.

29. **NGC 5674–Type 2**

NGC 5674 is a Seyfert 2 in our January 2009 spectrum from Lowell.

There is no evidence for variability in NGC 5674; it appears it has always been a Seyfert 2. It was first identified as a Seyfert galaxy by Huchra et al. (1982), who labeled it a type 2. A hard X-ray spectrum from Ginga was found to have a column density of 7.0×10^{22} cm^{-2} by Smith & Done (1996), consistent with its type 2 classification. Osterbrock & Martel (1993) list it as a type 1.9, but this was based upon only one unpublished spectrum and is therefore not substantial evidence for broad-line change.

30. **NGC 7314–Type 1.9, internally reddened**

Our CTIO spectra show broad Hα but no Hβ. We note that though Hα is wider than [O III] λ5007 (and thus "broad" by our definition), it is still relatively narrow, with a FWHM of only $\approx$1600 km s^{-1}, similar to NLS1s. Our *XMM* spectrum shows it to have a column of 0.62×10^{22} cm^{-2}. Interestingly, its Spitzer IRS spectrum (Deo 2007) looks like a Seyfert 1.

NGC 7314 is shown to have a hidden BLR by Lumsden et al. (2004). And, based on the rapid variability in its X-ray spectrum, Dewangan & Griffiths (2005) classify it as another "obscured NLS1". From this evidence, we expect that NGC 7314 is another case of an internally reddened Seyfert.

31. **NGC 7479–Type 2**

NGC 7479's spectrum from CTIO in August 2008 is dominated by the starlight of the host galaxy. [O III] $\lambda\lambda$4959, 5007 lines are weak, and only Hβ absorption is seen. Only narrow Hα is present. The narrow lines show an unusual triple-peaked structure. Its *XMM* spectrum supports a type 2 classification, displaying a heavily absorbed powerlaw of $N_H=56.6\times10^{22}$ cm^{-2}.

Our literature search did not find any evidence for variability of NGC 7479. It has had different classifications by different authors, but this is due to the differences in the criteria for each type by these different authors. For example, it was classified as a LINER by Ho et al. (1993) because [O II] 3727 $\geq$ [O III] 5007 and [O I] 6300 $\geq$ (1/3) [O III] 5007, but as a Seyfert 2 by Maiolino & Rieke (1995) because of their definition ([O III] $\geq 3\mathrm{H}\beta$). It was classified as a 1.9/2 by Quillen et al. (2001), and as a 1.9 by Ho et al. (1997b) who mention that it might have an extremely faint broad component to Hα, but they also note that the complex velocity structure of the narrow lines could have played a role in an inaccurate subtraction of the [N II].

32. **NGC 7603–Seyfert 1**

Our spectrum of NGC 7603 shows a type 1 spectrum with strong broad components. Its *XMM* spectrum is faint, but doesn't appear absorbed. Its Spitzer spectrum is also consistent with classification of type 1, showing a strong rise towards shorter wavelengths typical of that class.

NGC 7603 appeared as a 1.9 in the past, but changed to a type 1. A paper by Tohline & Osterbrock (1976) documents dramatic spectral variability of NGC 7603, where it went from possessing very strong broad lines in November 1974, the broad lines reduced to almost nothing by November 1975, and then regained in brightness a bit by February 1976. Other campaigns that studied its variability are Goodrich (1989), Rosenblatt et al. (1994), and Kollatschny et al. (2000). There are no firm conclusions drawn about the cause of the variability, but it seems to be undergoing intrinsic changes in its continuum strength (Kollatschny et al. 2000).

33. **UGC 7064–Type 1.9, reddened**

There is a very faint broad Hα component in our optical spectrum of UGC 7064 from Lowell, and no broad Hβ, and thus we classify it as a type 1.9. The reddening of the NLR was found to be $E(B-V) = 0.23$ from this spectrum. It's GHRS spectrum shows only narrow Lyα. Its Spitzer IRS spectrum shows a rise in its continuum towards short wavelengths, typical of type 1 AGN.

There does not seem to be any evidence for variability in the observed history of UGC 7064. Osterbrock & Shaw (1988) and Goodrich (1989) classify it as a 1.9, and a blue spectrum from Salzer et al. (1995) shows Hβ that looks the same as in our spectrum. Goodrich (1995) claims there to have been small variations in broad Hα, and that the Hα line weakened in 1993 compared with its previous observations, and that the change did not seem to be consistent with a change in reddening change. However, because a broad Hα component was seen in spectropolarimetric observations of UGC 7064 (Smith et al. 2004), we classify it as a reddened object.

34. **UGC 12138–Type 1.5**

Our spectra from CTIO in August 2008 indicate it to be a Seyfert 1.5. Its BLR is essentially unreddened, but its NLR is reddened by $E(B-V) = 0.33 \pm 0.25$, apparently due to the dust spirals in the NLR seen in the the WFPC2 structure map of Pogge & Martini (2002). In agreement with its optical appearance as a 1.5, UGC 12138 has an unabsorbed power-law *XMM* spectrum.

Previous spectra of UGC 12138 are scarce, but spectra published by de Grijp et al. (1992) and Cruz-Gonzalez et al. (1994) look very similar to ours. UGC 12138 was also classed as a type 1 in Huchra et al. (1982), but they do not show the spectrum.

35. **UM 146–Type 1.8, low flux**

Our blue CTIO spectrum of this object shows a very weak broad component to Hβ after the subtraction of the host galaxy spectrum, and thus we classify UM 146 as a type 1.8. The weakness of these components makes measuring the BLR Balmer decrement somewhat uncertain, but it seems that the BLR is not significantly reddened ($E(B-V)_{BLR} = 0.03\pm0.19$), while the NLR is reddened by $E(B-V)_{NLR} = 0.42 \pm 0.24$, with the higher reddening of the NLR possibly due to dust spirals/lanes within the NLR. Its Spitzer IRS spectrum shows clear silicate absorption, indicating that dust in the host galaxy could be playing a role in the reddening of the NLR.

Osterbrock & Dahari (1983) classed UM 146 as a 1.5, as do Dahari & De Robertis (1988). However, neither publication shows the actual spectrum that lead to this classification, and thus we are unable to confirm if the broad components weakened enough for it to have changed type. Because of the low reddening of the BLR, we classify UM 146 as a low-flux object.

Table 6.1. Summary of Basic Data

Object	z^a	Our Type	b/a^b	Spitzer $N_H{}^c$	NLR $N_H{}^d$	BLR $N_H{}^e$	X-ray $N_H{}^f$
IRAS 18325-5926	0.020231	2	–	–	0.85±0.04	–	$2.87^{+0.12}_{-0.11}$
Mrk 334	0.021945	1.8	0.70	0.57±0.16	0.10±0.03	-0.07±0.10	–
Mrk 423	0.032268	1.5	0.56	–	-0.07±0.09	0.19±0.11	–
Mrk 471	0.0340	1.9	0.67	0.46±0.09	0.46±0.12	–	–
Mrk 516	0.028416	LINER 2+HII	0.83	–	0.25±0.04	–	–
Mrk 609	0.034488	2	0.90	0.33±0.05	0.51±0.06	–	0.0291
Mrk 622	0.0230	2	0.95	0.44±0.07	0.54±0.03	–	$112.6^{+37.0}_{-20.8}$
Mrk 728	0.0350	1.2	0.65	–	0.02±0.06	0.23±0.07	0.0104
Mrk 883	0.0370	2	0.61	0.66±0.11	0.21±0.04	–	$0.09^{+0.008}_{-0.008}{}^g$
Mrk 915	0.024109	1.9	0.30	–	0.14±0.03	≥0.44±0.27	–
Mrk 993	0.015537	1.5	0.32	–	0.24±0.19	-0.14±0.20	$0.0931^{+0.008}_{-0.008}$
Mrk 1018	0.042436	1	0.52	–	-0.06±0.31	0.13±0.04	0.0146
Mrk 1126	0.010624	1.8	1.0	–	0.27±0.12	0.20±0.10	–
Mrk 1179	0.03760	1	1.0	–	-0.03±0.14	0.13±0.06	–
Mrk 1320	0.1030	1.2	0.88	–	0.20±0.17	-0.04±0.11	–
NGC 1365	0.005457	1.9	0.55	1.21±0.15	0.68±0.02	–	$9.77^{+0.10}_{-0.10}/24.07^{+0.33}_{-0.32}$
NGC 1808	0.003319	HII	0.60	–	–	–	$0.20^{+0.01}_{-0.01}$
NGC 2622	0.0280	1.9	0.68	0.58±0.08	0.19±0.05	–	$0.70^{+0.08}_{-0.07}$
NGC 2639	0.011128	LINER	0.61	1.09±0.34	–	–	–
NGC 2992	0.007710	2	0.31	1.09±0.31	0.37±0.06	–	$0.49^{+0.003}_{-0.003}$
NGC 3786	0.008933	1.9	0.59	0.91±0.11	0.23±0.05	≥0.33±0.24	$3.25^{+0.13}_{-0.12}$
NGC 3982	0.003699	2	0.88	0.42±0.15	0.35±0.06	–	$20.22^{+11.8}_{-6.4}$
NGC 4388	0.008419	2	0.19	–	0.35±0.05	–	$31.84^{+0.55}_{-0.53}$
NGC 4639	0.003395	1	0.68	–	–	–	0.014
NGC 5033	0.002919	1.2	0.47	–	-0.02±0.24	0.10±0.03	0.036
NGC 5252	0.022975	1.9	0.56	–	0.37±0.05	–	$4.03^{+0.05}_{-0.04}$
NGC 5273	0.003549	1.5	0.89	–	-0.04±0.14	-0.05±0.09	$1.51^{+0.06}_{-0.06}$
NGC 5506	0.006181	2	0.23	–	0.41±0.03	–	$2.96^{0.02}_{0.02}{}^g$
NGC 5674	0.024931	2	0.91	–	0.07±0.04	–	–
NGC 7314	0.004763	1.9	0.46	≈0	0.27±0.01	≥0.17±0.16	$0.621^{+0.003}_{-0.003}$
NGC 7479	0.007942	2?	0.76	–	–	–	$62.81^{+29.3}_{-14.9}$
NGC 7603	0.029524	1	0.67	≈0	-0.016±0.12	0.10±0.19	0.024
UGC 7064	0.024997	1.9	1.0	0.84±0.28	0.12±0.07	–	–
UGC 12138	0.024974	1.5	0.88	0.63±0.10	0.17±0.13	-0.07±0.04	0.042
UM 146	0.017405	1.8	0.77	0.74±0.18	0.22±0.13	0.02±0.10	–

[a] Redshift, from the NASA Extragalactic Database (NED).

[b] Ratio of host galaxy's major axis length to minor axis length, from NED.

[c] Column density estimated from depth of the silicate 9.7 μm absorption feature in Spitzer IRS spectra, in units of 10^{22} cm^{-2}.

[d] Column density estimated using the reddening of the NLR, assuming the local ISM dust/gas ratio of Shull & van Steenberg (1985), in units of 10^{22} cm^{-2}.

[e] Column density estimated using the reddening of the BLR, assuming the local ISM dust/gas ratio of Shull & van Steenberg (1985), in units of 10^{22} cm^{-2}.

[f] Hydrogen column density measured from *XMM* spectra, in units of 10^{22} cm^{-2}.

[g] Average column of multiple *XMM* spectra.

– 7 –

Results and Conclusions

7.1 Results

7.1.1 Many “1.8/1.9s” are not 1.8/1.9s

The first important consideration brought to light during this study is that many Seyferts alleged to be intermediate types are misclassified (16 of our sample of 35), and that anyone hoping to study the properties of intermediate type galaxies should be aware that optical classifications as such are frequently unreliable. For instance, in the study of Risaliti et al. (1999), they show the distribution of the column densities of 11 “1.8/1.9s” to be significantly lower than that of Seyfert 2s. However, their sample was actually comprised of two Seyfert 2s, four 1.8/1.9s, and five type 1 objects. With 5 of the 11 objects type 1 AGN, it is no wonder the column densities were low! Based on our literature search of the classification history of each object, the most common reason for previous misclassification seems to be large overestimation of the flux of broad Hα, due to inaccurate or no [N II] subtraction. Spectral variability may account for a couple of the type discrepancies, but again, based on our literature search of previously published spectra, this seems unlikely in most cases.

The classification of 1.8 in particular seems to be often misused. Our sample was originally thought to contain nine 1.8s, but only one of these objects actually turned out to fit our criteria of a 1.8. These misidentifications probably result from the fact that a weak broad component to Hβ is very difficult to discern due to contamination by the spectrum of the host galaxy; in the three 1.8s we found in our study, the weak broad Hβ was apparent only after the subtraction of the underlying host galaxy spectrum. It is important to note that classification as a 1.8 depends on spectra S/N and the amount of galaxy contamination. In the case of infinite signal to noise and perfect starlight subtraction, all 1.9s would be classified as 1.8s, as broad Hβ must be present in any object that shows broad Hα. We further emphasize that because true Seyfert 1.8s seem to be something of a rarity, the 1.8 classification of many objects should be treated warily by those who wish to study intermediate-type AGN. Moreover, because they are so few, it is impossible to make generalizations about them as a class, and previous studies that make such claims (e.g., that 1.8s have unusually large broad Balmer decrements) may be unreliable.

7.1.2 Inventory of 1.8/1.9s

Are Seyfert 1.8/1.9s objects with reddened BLRs, or are they objects temporarily in a low-flux state with weakened broad-line components? From the evidence presented in Chapter 6, we conclude that, of the 19 objects that currently or formerly appeared as a 1.8/1.9, eight received this designation because they were at least temporarily in low flux states, and seven because of internal reddening. Four do not have evidence that favors one scenario over the other. Sixteen of the 35 were other objects misclassified as 1.8/1.9s. Table 7.1 gives a summary of our conclusions about the most probable cause of classification for each 1.8/1.9.

A can be seen from Table 7.1, a total of eight objects appeared as 1.9s in our spectra. Of these, five have evidence for internal BLR reddening, and three are inconclusive. Of those that previously appeared as 1.9s, but changed type such that they were not 1.9s when observed by us (Mrk 609, Mrk 728, Mrk 883, Mrk 993, Mrk 1018 Mrk 1179 NGC 2992), there is evidence that the changes in most of these objects were due to an intrinsic change

Table 7.1. Seyfert Galaxies Currently or Previously Appearing as Type 1.8 or 1.9

Object	Our Type	Past Optical Variation	Reason for Classification
Mrk 334	1.8	no	low flux
Mrk 423	1.5[a]	no	internally reddened
Mrk 471	1.9	no	inconclusive
Mrk 609	2	yes (1.5-1.9)	low flux
Mrk 728	1.2	yes (1.9-1.2)	formerly 1.9, low flux
Mrk 883	2	yes (1.9-2)	formerly 1.9, low flux
Mrk 915	1.9	yes (1.5-1.9)	internally reddened
Mrk 993	1.5	yes (1.9-1.5)	formerly 1.9, internally reddened
Mrk 1018	1	yes (1.9-1)	formerly 1.9, low flux
Mrk 1126	1.8	no	low flux
Mrk 1179	1	yes (1.9-1)	inconclusive
NGC 1365	1.9	?	inconclusive
NGC 2622	1.9	yes (1-1.9)	internally reddened
NGC 2992	2	yes (1-2)	formerly 1.9, low flux
NGC 3786	1.9	?	inconclusive
NGC 5252	1.9	no	reddened
NGC 7314	1.9	no	internally reddened
UGC 7064	1.9	no	reddened
UM 146	1.8	?	low flux

[a] Although Mrk 423 is a type 1.5 based upon the definition of this class by Maiolino & Rieke (1995), it is on the borderline of the classification requirements. Because it is close in appearance to a 1.8 and there is evidence that its BLR is reddened, we include it in this table with the rest of the 1.8/1.9s.

in the amount of ionizing continuum as opposed to variable reddening (Mrk 993 is the only exception). In other words, those objects that were observed to be 1.9s because they were in low flux states have more variable continua, as expected, while those observed to be 1.9s because of BLR reddening did not vary.

All of the 1.8s in our sample seem to be due to low flux states. Our three 1.8s, Mrk 334, Mrk 1126, and UM 146, have broad Balmer decrements of 2.7, 4.7, and 3.2 respectively; in Mrk 334 and UM 146, the reddening of the NLR is actually higher than the reddening of the BLR, while in Mrk 1126 the BLR and NLR reddenings are consistent with each other within their error bars.

If, as our results seem to suggest, most 1.8s and at least half 1.9s have unreddened BLRs, how did these objects gain their reputation for large broad Balmer decrements? The original study by Osterbrock contained only five objects, three 1.9s, Mrk 423, Mrk 1018, and V Zw 317, and two 1.8s, Mrk 516 and Mrk 609. Our study shows Mrk 609 has an unreddened BLR (see Chapter 6). Though we have no way of measuring the BLR reddening in Mrk 516, which appears as a LINER 2 in our spectra, the classification of LINER in itself implies a history of low ionizing flux. This study also seemed to show high Balmer decrements in the 1.9s; Osterbrock presents broad Balmer decrements of 9.9, 8.9, and 15 for Mrk 423, Mrk 1018, and V Zw 317, respectively. However, these measurements are certain to have large errors (after all, the definition of 1.9 is that it has no broad Hβ). Furthermore, Mrk 423's spectrum is heavily contaminated by the spectrum of the underlying host galaxy, and was one of the most difficult continua in our sample to fit with a template host galaxy. The choice and scaling of the template spectrum can lead to large differences in the observed line ratios, and an inaccurate fit may have played a role in their measurement of Mrk 423's steep broad Balmer decrement (we measured $(f_{H\alpha}/f_{H\beta})_{broad}$ ~4.6).

The results presented by Goodrich (1995), in which he shows changes in the broad-line fluxes of Hα and Hβ to be consistent with the same change in reddening in three 1.8/1.9s, may also have been misleading. A change in line ratios inconsistent with reddening essentially proves, for lack of a viable alternative, that intrinsic continuum fluctuations are responsible. However, changes in line ratios consistent with reddening changes *do not* prove that variable reddening is at work; it has been shown that the the Balmer decrement may steepen as luminosity decreases, in a manner that can mimic an increase in reddening (Korista & Goad 2004).

Only two of the nine objects that varied in type in Table 7.1 have undergone changes possibly due to variable reddening: Mrk 915 and Mrk 993. Mrk 915 is labeled as "internally reddened" because of the seemingly higher reddening of the BLR than the NLR of this object. The higher reddening of the BLR in this object can, however, be attributed to the dust lane that passes through its nucleus, seen in its WFPC2 image (Fig. D.8). Dust in this lane is not likely to cause the variations seen over the 9 year period between the observations presented in Goodrich (1995). Furthermore, Goodrich doesn't use line ratio changes to show that this one's variations could be due to reddening (his second spectrum of Mrk 915 doesn't cover Hβ); the claim that its variations were consistent with reddening was based on an estimation of the continuum change, which, given the uncertainties in flux calibration, is questionable. Hence, although it is internally reddened, its variability most likely due to intrinsic continuum changes. Furthermore, though Tran et al. (1992) suggest Mrk 993's variability is likely due to variable line of sight extinction, they do not rule out continuum variability as a possibility.

7.1.3 Pure Seyfert 2s

Over the past few years, interest has increased in objects now called "pure" or "true" Seyfert 2s, AGN in which it it appears we have a clear view to their nuclei from their unabsorbed X-ray spectra, but there is no sign of the broad-line region in the optical, in apparent contradiction of the orientation-dependent unified model. Our study has found two such objects, Mrk 609 and Mrk 883. Both are optically classified as Seyfert 2s, yet both have X-ray spectra that are almost completely unabsorbed. Several suggestions have been proffered to explain these objects in the context of the unified model, but none seems to explain our data for Mrk 609 or Mrk 883.

First, it has been theorized that the objects which appear as pure Seyfert 2s are Compton-thick objects, such that the powerlaw turnover due to absorption occurs beyond 10 keV, and thus out of the energy range observed by most X-ray missions. However, this idea has been ruled out for many true Seyfert 2 candidates on the basis that their spectra do not show Fe Kα lines with high equivalent widths, indicating that their continua are not reflection-dominated, and also because their X-ray to [O III] luminosity ratios are similar to Seyfert 1s, indicating that they are unabsorbed (Panessa & Bassani 2002). This is also the case for Mrk 609 and Mrk 883; neither shows strong Fe Kα in their *XMM* spectra, and their X-ray luminosities do not seem to be under-luminous compared with their [O III] luminosities (both are plotted in the upper left part of Fig. 4.6).

Secondly, it has been proposed that the absorption exists, but has been filled in by soft emission from other sources in the area surrounding the AGN (Ghosh et al. 2007). At least for Mrk 609 or Mrk 883, this explanation also doesn't seem to work as it is unlikely that such soft emission would exactly fill in the lost absorption such that one still observes a smooth power-law in the high-quality *XMM* spectra ($\Gamma = 1.6$ for Mrk 609 and $\Gamma = 1.7$ for Mrk 883).

Finally, it has been suggested that the (for the most part) non-simultaneous X-ray and optical observations can catch a variable AGN in two different states. Again, this explanation seems unlikely for Mrk 609 and Mrk 883. Although we do not have simultaneous observations, we have multiple optical observations of Mrk 609 and Mrk 883 that bracket the X-ray observations, none of which show evidence for variability. For instance, Mrk 609 consistently optically appears as a type 2 in 2001 January (spectrum from SDSS), 2007 November (spectrum from CTIO), and January 2009 (spectrum from Lowell), yet it was observed to be unobscured by *XMM* in August 2002 and January 2007. Variations such that it was always caught in an obscured state when observed in the optical but in an unobscured in the X-ray are certainly unlikely. The same is true for Mrk 883. We have optical observations of Mrk 883 as a type 2 from August 2004 (spectrum from SDSS) and January 2009 (spectrum from Lowell), and it was observed by *XMM* between these observations, in August 2006.

However, because both objects were observed to have broad Balmer lines at some point in the past (Mrk 609 was observed to have broad lines by Rudy et al. (1988) in 1984, and Mrk 883 was observed to have broad lines by Goodrich (1995) in 1993), variability may still provide the answer to this apparent paradox. Further investigation with simultaneous X-ray and optical data is needed to develop a satisfactory explanation for these intriguing objects.

7.2 Conclusions

7.2.1 Summary

We have collected evidence from different wavebands to determine the presence and location of dust in a sample of 35 Seyfert 1.8/1.9s. We used optical spectra to determine the reddening of the NLR and BLR, X-ray data from *XMM* to determine the total hydrogen column to the source, and we determined variability from a literature search. From this, we determined that Seyfert 1.8/1.9s are an almost equal mix of low-flux objects with unreddened BLRs, and objects with BLRs reddened by an internal dust source, either the torus or dust structures in the vicinity of the NLR. Seyfert 1.8s are fewer than their reported numbers, due to the difficulty in detecting a weak broad component of the Hβ line. Because they are so few, generalizations are problematic, but all of our three 1.8s seem be low-flux objects that do not suffer additional reddening of their BLRs. For Seyfert 1.9s, one often cannot tell if they are reddened or not, due to the weakness of their broad components. Because the reddenings of the BLRs of these objects are not consistently higher than the reddenings of their NLRs, our study does not provide evidence that these objects are being viewed along a line of sight that grazes the atmosphere of a central dusty torus. Dust spirals on the same size scale as the NLR may instead be responsible for the BLR reddening, as these features appear to randomly cut across the NLR, sometimes blocking the central AGN, and sometimes not. NGC 2622, NGC 5252 and UGC 7064 are internally reddened 1.9s that do not show obvious dust structure crossing their nuclei in their *HST* WFPC2 images. These objects may be cases where the BLR is reddened by torus dust; additional study is needed to test this.

7.2.2 Future Directions

Many of the ambiguities that plagued our current work could be solved with *HST* STIS observations of 1.8/1.9s. In our groundbased spectra, analysis of the nuclear continuum is out of the question; less than 20% of the observed continuum is attributable to the AGN in most of our spectra. *HST*'s high resolution allows nuclear spectra to be taken without the contamination from the host galaxy. The continuum shape would instantly reveal the reddening of the continuum, and this would be of particular use in determining if reddening affects the BLRs of 1.9s. Furthermore, by comparing the observed continuum with that of an unreddened Seyfert (i.e., a Seyfert 1), the reddening curve of the dust effecting the extinction could be determined (see Crenshaw et al. 2001), giving information about the composition and size distribution of the grains. In those objects found to be internally reddened that do not show nuclear dust lanes/spirals on the scale of the NLR that could account for the BLR/continuum reddening, this could lead to the first observational hints of the dust properties of the torus.

Another very interesting project will be to find an explanation for the apparent lack of broad lines in our two "pure" Seyfert 2 candidates. Simultaneous X-ray and optical data will provide the key evidence for understanding these interesting objects.

REFERENCES

Allen, M. G., Dopita, M. A., Tsvetanov, Z. I., & Sutherland, R. S. 1999, ApJ, 511, 686

Antonucci, R. R. J. 1984, ApJ, 278, 499

Antonucci, R. R. J., & Miller, J. S. 1985, ApJ, 297, 621

Arnaud, K. A. 1996, in Astronomical Society of the Pacific Conference Series, Vol. 101, Astronomical Data Analysis Software and Systems V, ed. G. H. Jacoby & J. Barnes, 17–+

Baade, W., & Minkowski, R. 1954, ApJ, 119, 206

Baldwin, J. A., Phillips, M. M., & Terlevich, R. 1981, PASP, 93, 5

Bianchi, S., Guainazzi, M., & Chiaberge, M. 2006, in ESA Special Publication, Vol. 604, The X-ray Universe 2005, ed. A. Wilson, 521–+

Botte, V., Ciroi, S., Rafanelli, P., & Di Mille, F. 2004, AJ, 127, 3168

Capriotti, E., Foltz, C., & Byard, P. 1980, ApJ, 241, 903

——. 1981, ApJ, 245, 396

Cohen, R. D., Puetter, R. C., Rudy, R. J., Ake, T. B., & Foltz, C. B. 1986, ApJ, 311, 135

Colbert, E. J. M., Strickland, D. K., Veilleux, S., & Weaver, K. A. 2005, ApJ, 628, 113

Corral, A., Barcons, X., Carrera, F. J., Ceballos, M. T., & Mateos, S. 2005, A&A, 431, 97

Crenshaw, D. M., Kraemer, S. B., Bruhweiler, F. C., & Ruiz, J. R. 2001, ApJ, 555, 633

Crenshaw, D. M., & Peterson, B. M. 1986, PASP, 98, 185

Cruz-Gonzalez, I., Carrasco, L., Serrano, A., Guichard, J., Dultzin-Hacyan, D., & Bisiacchi, G. F. 1994, ApJS, 94, 47

Dahari, O., & De Robertis, M. M. 1988, ApJS, 67, 249

Das, V. et al. 2005, AJ, 130, 945

de Grijp, M. H. K., Keel, W. C., Miley, G. K., Goudfrooij, P., & Lub, J. 1992, A&AS, 96, 389

De Robertis, M. M., & Osterbrock, D. E. 1984, ApJ, 286, 171

Deo, R. 2007, PhD thesis, Georgia State University

Deo, R. P., Crenshaw, D. M., Kraemer, S. B., Dietrich, M., Elitzur, M., Teplitz, H., & Turner, T. J. 2007, ApJ, 671, 124

Dewangan, G. C., & Griffiths, R. E. 2005, ApJ, 625, L31

Dong, X., Wang, T., Wang, J., Yuan, W., Zhou, H., Dai, H., & Zhang, K. 2008, MNRAS, 383, 581

Edmunds, M. G., & Pagel, B. E. J. 1982, MNRAS, 198, 1089

Erkens, U., Appenzeller, I., & Wagner, S. 1997, A&A, 323, 707

Fabian, A. C., Pounds, K. A., & Blandford, R. D. 2004, Frontiers of X-Ray Astronomy, ed. A. C. Fabian, K. A. Pounds, & R. D. Blandford

Fath, E. A. 1909, Lick Observatory Bulletin, 5, 71

Filippenko, A. V., & Sargent, W. L. W. 1985, ApJS, 57, 503

Gallego, J., Zamorano, J., Rego, M., Alonso, O., & Vitores, A. G. 1996, A&AS, 120, 323

Ghosh, H., Pogge, R. W., Mathur, S., Martini, P., & Shields, J. C. 2007, ApJ, 656, 105

Gilli, R., Maiolino, R., Marconi, A., Risaliti, G., Dadina, M., Weaver, K. A., & Colbert, E. J. M. 2000, A&A, 355, 485

Goodrich, R. W. 1989, ApJ, 340, 190

——. 1990, ApJ, 355, 88

——. 1995, ApJ, 440, 141

Goodrich, R. W., & Osterbrock, D. E. 1983, ApJ, 269, 416

Gorjian, V. 1995, ApJ, 450, L51+

Guainazzi, M., & Bianchi, S. 2007, MNRAS, 374, 1290

Heckman, T. M. 1978, PASP, 90, 241

——. 1980, A&A, 87, 152

Ho, L. C., Filippenko, A. V., & Sargent, W. L. 1995, ApJS, 98, 477

Ho, L. C., Filippenko, A. V., & Sargent, W. L. W. 1993, ApJ, 417, 63

——. 1997a, ApJS, 112, 315

Ho, L. C., Filippenko, A. V., Sargent, W. L. W., & Peng, C. Y. 1997b, ApJS, 112, 391

Ho, L. C., Ptak, A., Terashima, Y., Kunieda, H., Serlemitsos, P. J., Yaqoob, T., & Koratkar, A. P. 1999, ApJ, 525, 168

Howell, S. B. 2000, Handbook of CCD Astronomy, ed. S. B. Howell

Huchra, J. P., Wyatt, W. F., & Davis, M. 1982, AJ, 87, 1628

Iwasawa, K., Kunieda, H., Tawara, Y., Awaki, H., Koyama, K., Murayama, T., & Taniguchi, Y. 1995, AJ, 110, 551

Jiménez-Bailón, E., Santos-Lleó, M., Dahlem, M., Ehle, M., Mas-Hesse, J. M., Guainazzi, M., Heckman, T. M., & Weaver, K. A. 2005, A&A, 442, 861

Keel, W. C. 1983, ApJ, 269, 466

——. 1996, ApJS, 106, 27

Kewley, L. J., Groves, B., Kauffmann, G., & Heckman, T. 2006, MNRAS, 372, 961

Khachikian, E. E., & Weedman, D. W. 1971, Astrofizika, 7, 389

Kinney, A. L., Calzetti, D., Bohlin, R. C., McQuade, K., Storchi-Bergmann, T., & Schmitt, H. R. 1996, ApJ, 467, 38

Kollatschny, W., Bischoff, K., & Dietrich, M. 2000, A&A, 361, 901

Komossa, S., & Fink, H. 1997, A&A, 327, 555

Koratkar, A., Deustua, S. E., Heckman, T., Filippenko, A. V., Ho, L. C., & Rao, M. 1995, ApJ, 440, 132

Korista, K. T., & Goad, M. R. 2004, ApJ, 606, 749

Kraemer, S. B., & Crenshaw, D. M. 2000, ApJ, 544, 763

Kraemer, S. B., Crenshaw, D. M., Hutchings, J. B., Gull, T. R., Kaiser, M. E., Nelson, C. H., & Weistrop, D. 2000, ApJ, 531, 278

Krolik, J. H., & Begelman, M. C. 1988, ApJ, 329, 702

Kulkarni, V. P., York, D. G., Vladilo, G., & Welty, D. E. 2007, ApJ, 663, L81

Kwan, J., & Krolik, J. H. 1981, ApJ, 250, 478

Lawrence, A., & Elvis, M. 1982, ApJ, 256, 410

Lumsden, S. L., Alexander, D. M., & Hough, J. H. 2004, MNRAS, 348, 1451

Maiolino, R., & Rieke, G. H. 1995, ApJ, 454, 95

Malkan, M. A., Gorjian, V., & Tam, R. 1998, ApJS, 117, 25

Markarian, B. E. 1967, Astrofizika, 3, 55

——. 1969a, Astrofizika, 5, 443

——. 1969b, Astrofizika, 5, 581

Marziani, P., Sulentic, J. W., Zamanov, R., Calvani, M., Dultzin-Hacyan, D., Bachev, R., & Zwitter, T. 2003, ApJS, 145, 199

Meléndez, M. et al. 2008, ApJ, 682, 94

Moore, D., Cohen, R. D., & Marcy, G. W. 1996, ApJ, 470, 280

Murphy, K. D., Yaqoob, T., & Terashima, Y. 2007, ApJ, 666, 96

Mushotzky, R. F., Done, C., & Pounds, K. A. 1993, ARA&A, 31, 717

Nagar, N. M., Oliva, E., Marconi, A., & Maiolino, R. 2002, A&A, 391, L21

Nenkova, M., Ivezić, Ž., & Elitzur, M. 2002, ApJ, 570, L9

Nenkova, M., Sirocky, M. M., Nikutta, R., Ivezić, Ž., & Elitzur, M. 2008, ApJ, 685, 160

Netzer, H. 1975, MNRAS, 171, 395

Osterbrock, D. E. 1977, ApJ, 215, 733

——. 1981, ApJ, 249, 462

——. 1989, Astrophysics of gaseous nebulae and active galactic nuclei, ed. D. E. Osterbrock

Osterbrock, D. E., & Dahari, O. 1983, ApJ, 273, 478

Osterbrock, D. E., & Ferland, G. J. 2006, Astrophysics of gaseous nebulae and active galactic nuclei (Astrophysics of gaseous nebulae and active galactic nuclei, 2nd. ed. by D.E. Osterbrock and G.J. Ferland. Sausalito, CA: University Science Books, 2006)

Osterbrock, D. E., & Martel, A. 1993, ApJ, 414, 552

Osterbrock, D. E., & Pogge, R. W. 1985, ApJ, 297, 166

Osterbrock, D. E., & Shaw, R. A. 1988, ApJ, 327, 89

Panessa, F., & Bassani, L. 2002, A&A, 394, 435

Peterson, B. M. 1993, PASP, 105, 247

——. 1997, An Introduction to Active Galactic Nuclei, ed. A. I. Goméz de Castro & M. Franqueira

Peterson, B. M. et al. 2004, ApJ, 613, 682

Peterson, B. M., & Wandel, A. 1999, ApJ, 521, L95

Pogge, R. W., & Martini, P. 2002, ApJ, 569, 624

Quillen, A. C., McDonald, C., Alonso-Herrero, A., Lee, A., Shaked, S., Rieke, M. J., & Rieke, G. H. 2001, ApJ, 547, 129

Rafanelli, P., Marziani, P., Birkle, K., & Thiele, U. 1993, A&A, 275, 451

Risaliti, G., Elvis, M., Fabbiano, G., Baldi, A., & Zezas, A. 2005, ApJ, 623, L93

Risaliti, G., Elvis, M., Fabbiano, G., Baldi, A., Zezas, A., & Salvati, M. 2007, ApJ, 659, L111

Risaliti, G., Maiolino, R., & Bassani, L. 2000, A&A, 356, 33

Risaliti, G., Maiolino, R., & Salvati, M. 1999, ApJ, 522, 157

Risaliti, G. et al. 2009, MNRAS, 393, L1

Roche, P. F., & Aitken, D. K. 1984, MNRAS, 208, 481

Rosenblatt, E. I., Malkan, M. A., Sargent, W. L. W., & Readhead, A. C. S. 1994, ApJS, 93, 73

Rowan-Robinson, M. 1977, ApJ, 213, 635

Rudy, R. J., Cohen, R. D., & Ake, T. B. 1988, ApJ, 332, 172

Rudy, R. J., Cohen, R. D., & Puetter, R. C. 1985, ApJ, 288, L29

Rudy, R. J., & Rodriguez-Espinosa, J. M. 1985, ApJ, 298, 614

Rudy, R. J., & Willner, S. P. 1983, ApJ, 267, L69

Salzer, J. J., Moody, J. W., Rosenberg, J. L., Gregory, S. A., & Newberry, M. V. 1995, AJ, 109, 2376

Sandage, A., & Tammann, G. A. 1987, A revised Shapley-Ames Catalog of bright galaxies, ed. A. Sandage & G. A. Tammann

Savage, B. D., & Mathis, J. S. 1979, ARA&A, 17, 73

Schachter, J., Filippenko, A. V., & Kahn, S. M. 1990, ApJ, 362, 74

Schlegel, D. J., Finkbeiner, D. P., & Davis, M. 1998, ApJ, 500, 525

Schmidt, M. 1963, Nature, 197, 1040

Schmidt, M., & Green, R. F. 1983, ApJ, 269, 352

Schulz, H., Knake, A., & Schmidt-Kaler, T. 1994, A&A, 288, 425

Schulz, H., Komossa, S., Schmitz, C., & Mücke, A. 1999, A&A, 346, 764

Seyfert, C. K. 1943, ApJ, 97, 28

Shuder, J. M. 1980, ApJ, 240, 32

Shuder, J. M., & Osterbrock, D. E. 1981, ApJ, 250, 55

Shull, J. M., & van Steenberg, M. E. 1985, ApJ, 294, 599

Simkin, S. M., Su, H. J., & Schwarz, M. P. 1980, ApJ, 237, 404

Smith, D. A., & Done, C. 1996, MNRAS, 280, 355

Smith, J. E., Robinson, A., Alexander, D. M., Young, S., Axon, D. J., & Corbett, E. A. 2004, MNRAS, 350, 140

Stauffer, J. R. 1982, ApJ, 262, 66

Tadhunter, C. 2008, New Astronomy Review, 52, 227

Tadhunter, C., & Tsvetanov, Z. 1989, Nature, 341, 422

Tohline, J. E., & Osterbrock, D. E. 1976, ApJ, 210, L117

Tran, H. D., Osterbrock, D. E., & Martel, A. 1992, AJ, 104, 2072

Trippe, M. L., Crenshaw, D. M., Deo, R., & Dietrich, M. 2008, AJ, 135, 2048

Turner, T. J., & Miller, L. 2009, A&A Rev., 17, 47

Urry, C. M., & Padovani, P. 1995, PASP, 107, 803

Veilleux, S., & Osterbrock, D. E. 1987, ApJS, 63, 295

Veron, P., Lindblad, P. O., Zuiderwijk, E. J., Veron, M. P., & Adam, G. 1980, A&A, 87, 245

Wang, J.-M., & Netzer, H. 2003, A&A, 398, 927

Ward, M., Penston, M. V., Blades, J. C., & Turtle, A. J. 1980, MNRAS, 193, 563

Weingartner, J. C., & Murray, N. 2002, ApJ, 580, 88

Whittle, M. 1985a, MNRAS, 216, 817

——. 1985b, MNRAS, 213, 33

Yaqoob, T. et al. 2007, PASJ, 59, 283

Young, S., Hough, J. H., Efstathiou, A., Wills, B. J., Bailey, J. A., Ward, M. J., & Axon, D. J. 1996, MNRAS, 281, 1206

Appendices

– A –

Continuum-Subtracted Optical Spectra

This Appendix presents the continuum-subtracted optical spectra used to measure the reddenings in Table 3.3.

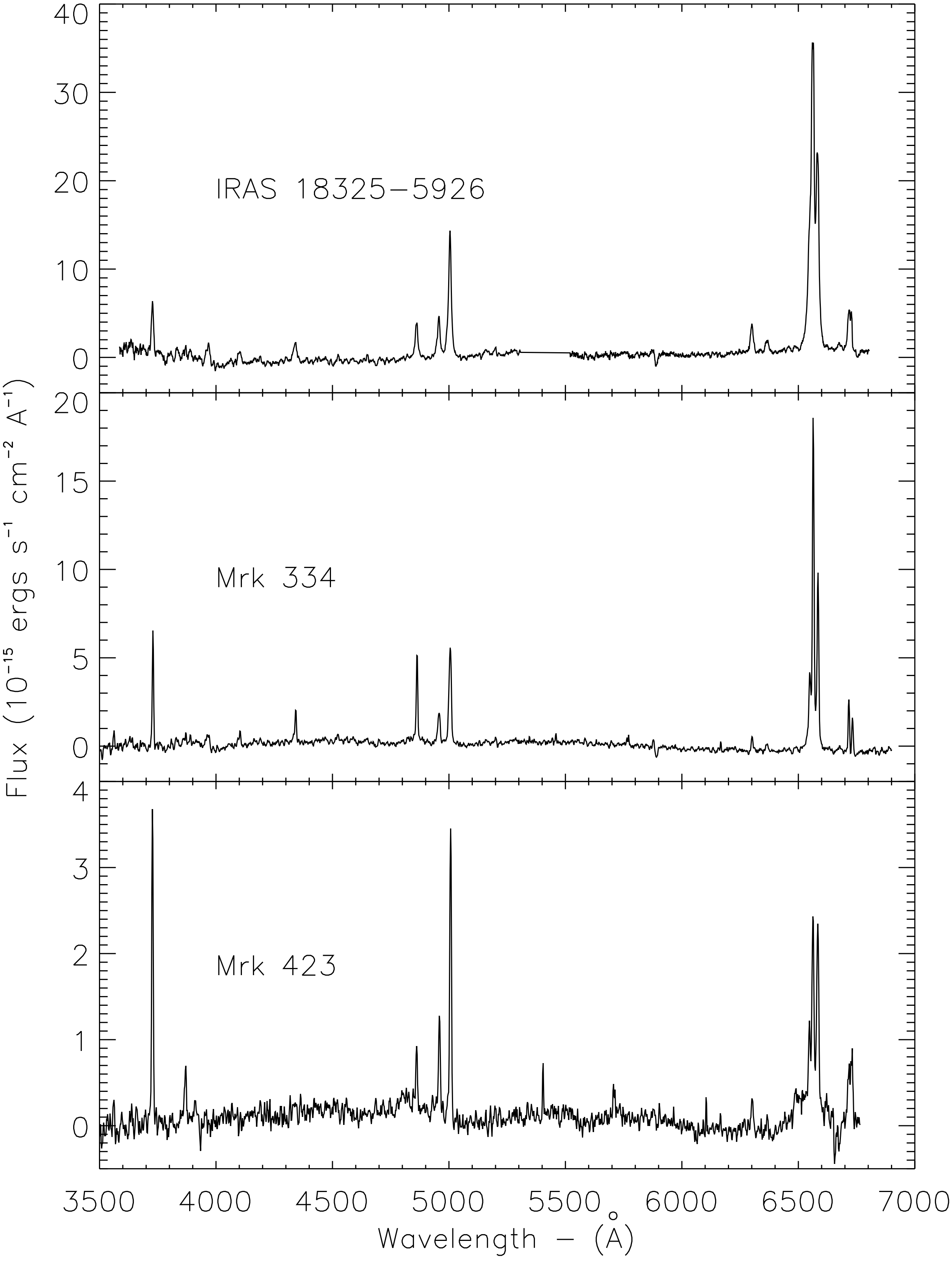

Figure A.1 Continuum-subtracted optical spectra: IRAS 18325-5926, Mrk 334, and Mrk 423

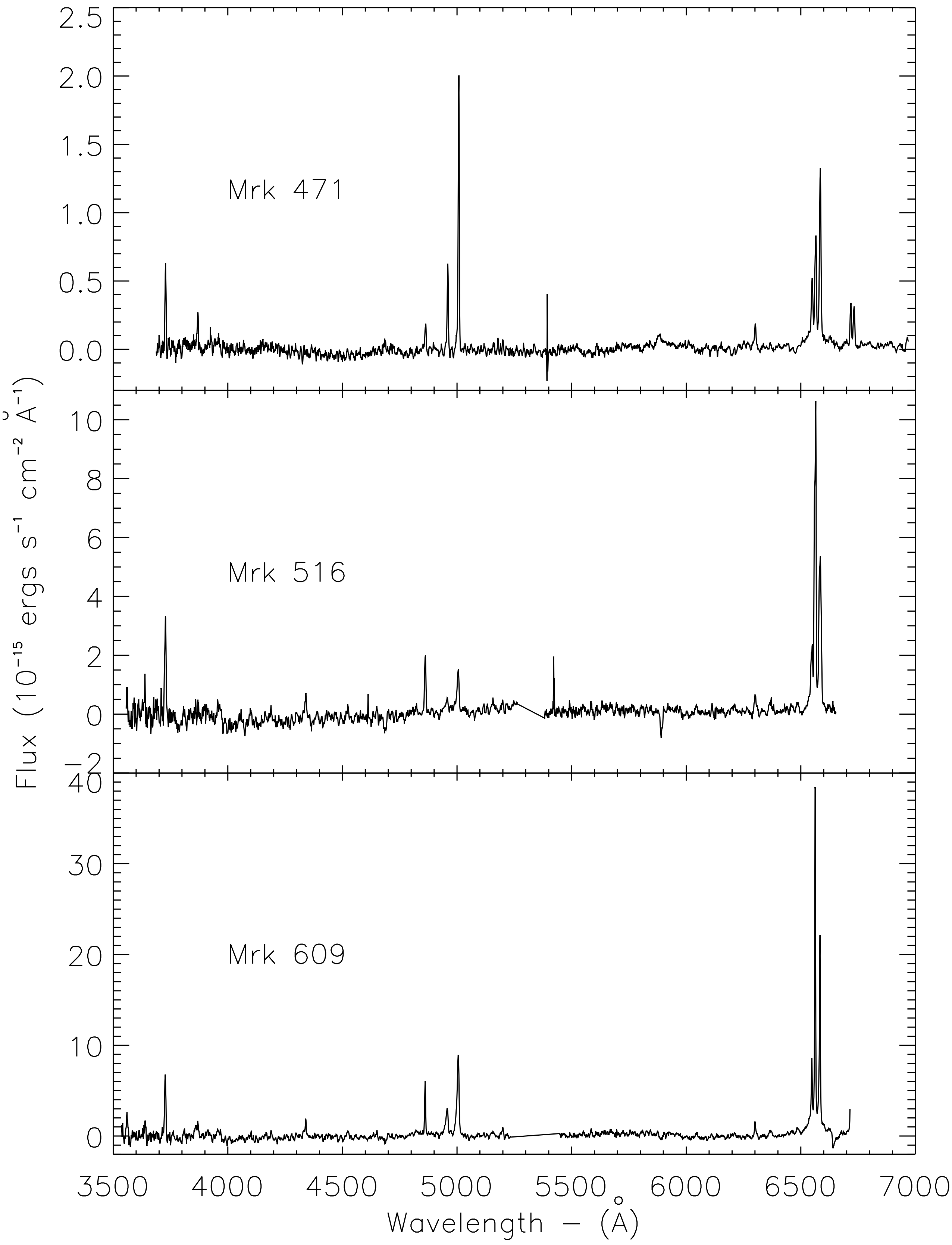

Figure A.2 Continuum-subtracted optical spectra: Mrk 471, Mrk 516, and Mrk 609

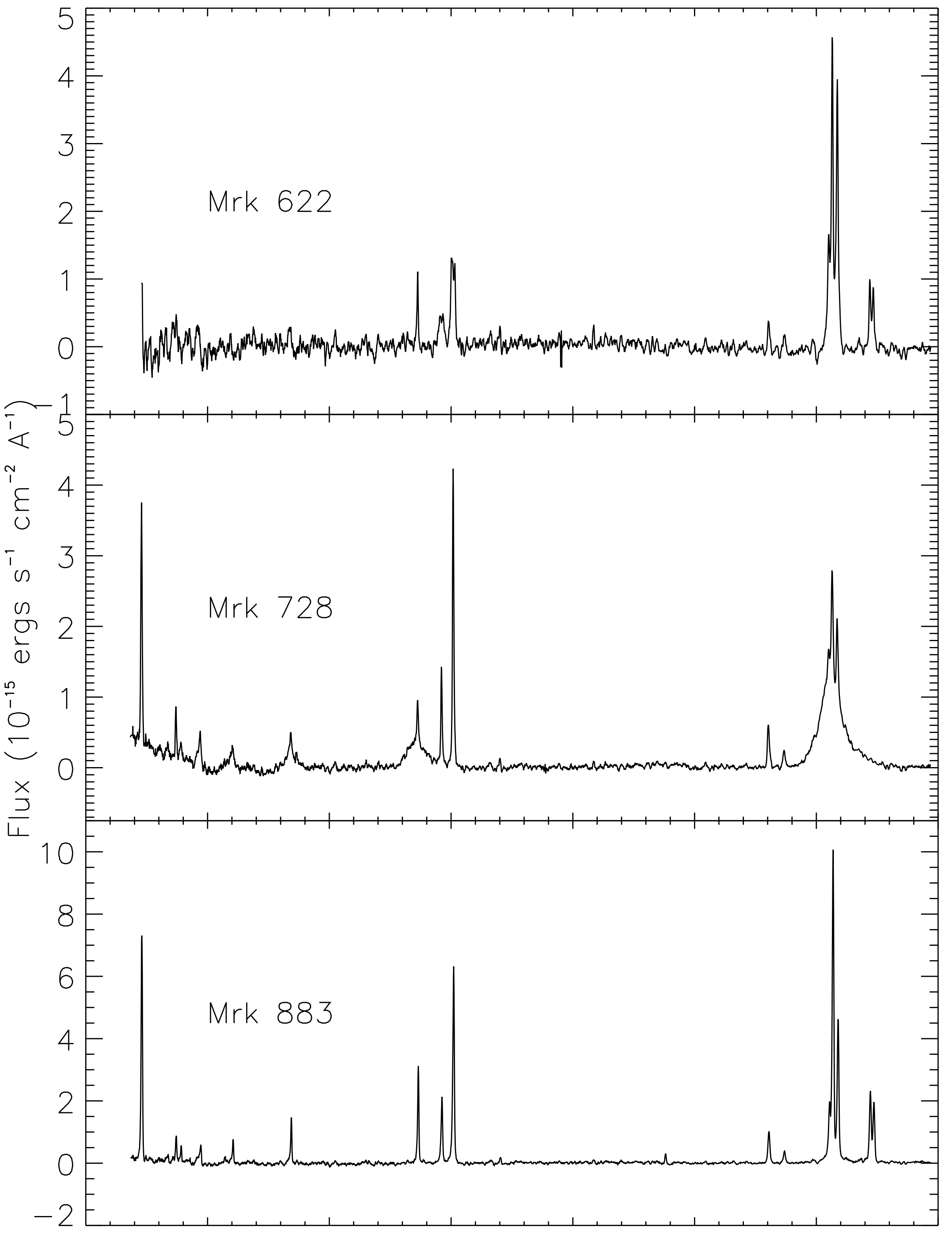

Figure A.3 Continuum-subtracted optical spectra: Mrk 622, Mrk 728, and Mrk 883

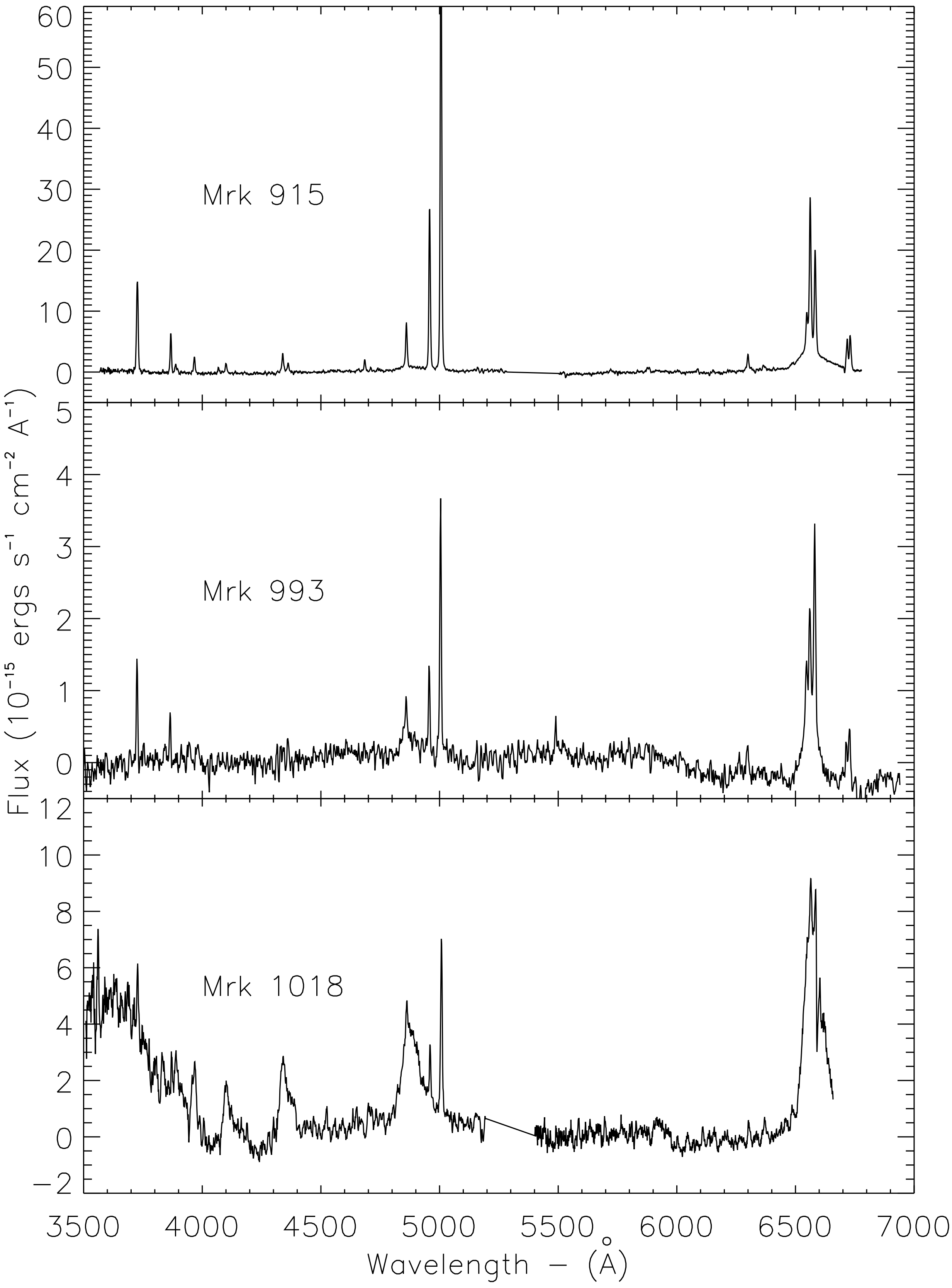

Figure A.4 Continuum-subtracted optical spectra: Mrk 915, Mrk 993, and Mrk 1018

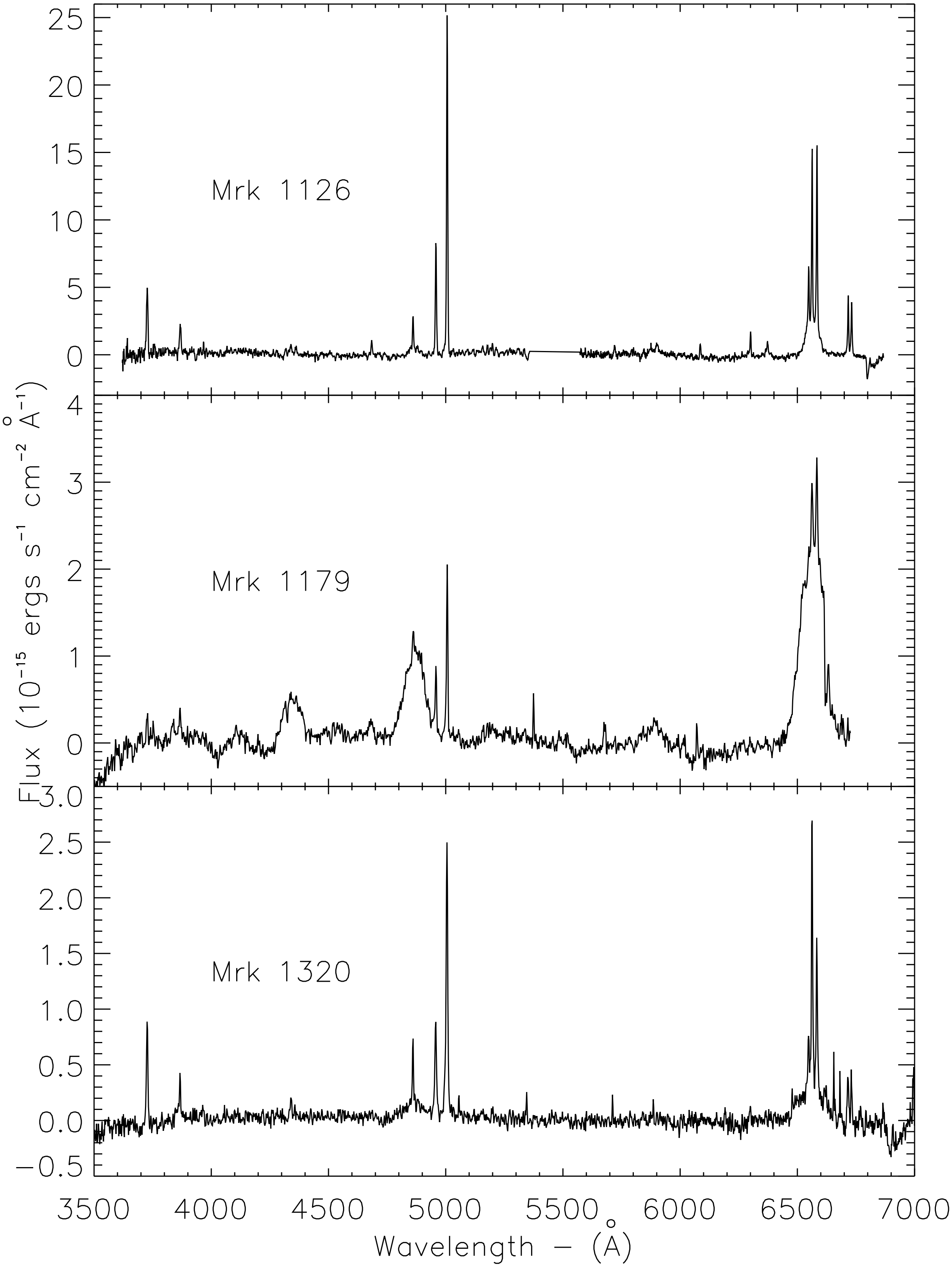

Figure A.5 Continuum-subtracted optical spectra: Mrk 1126, Mrk 1179, and Mrk 1320

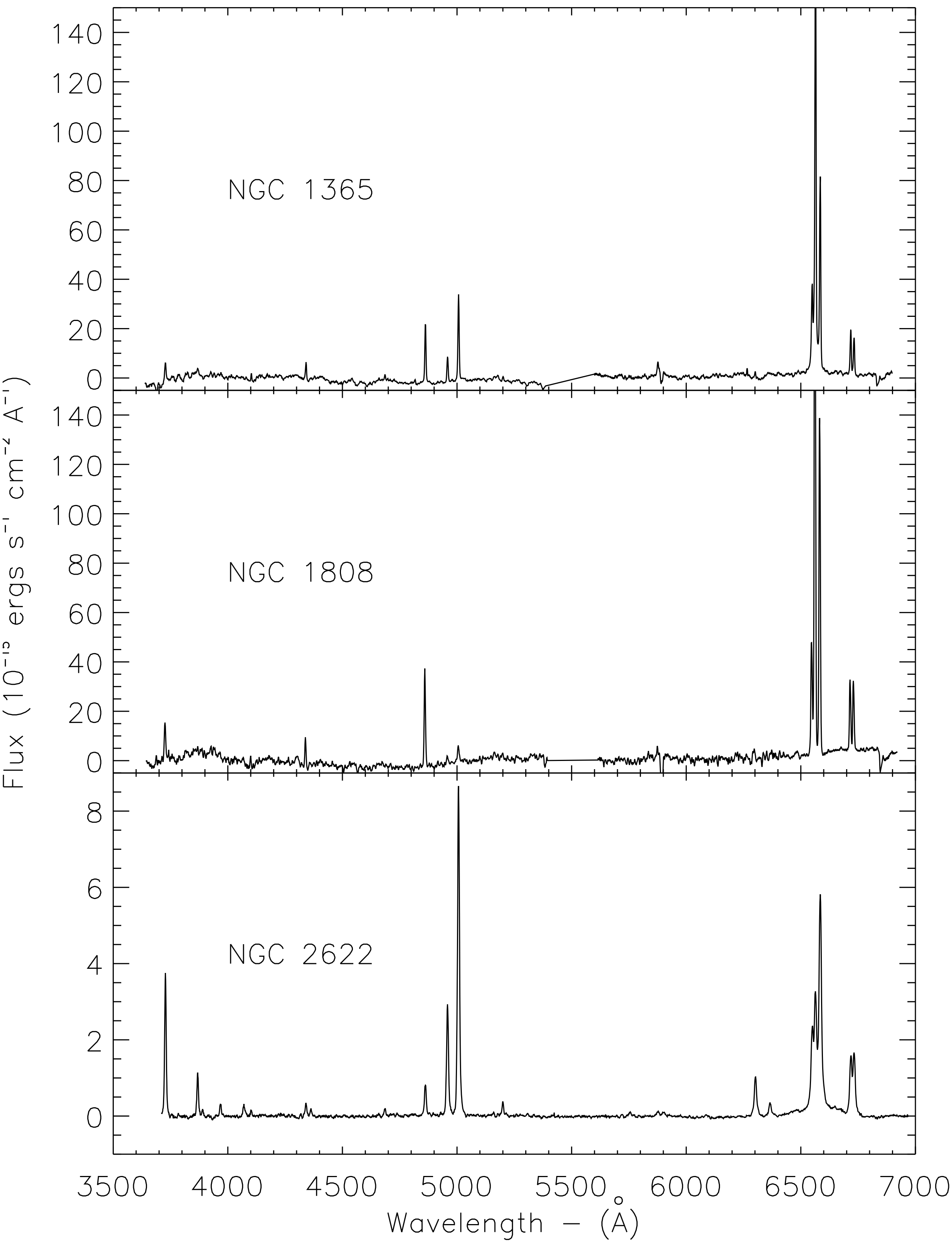

Figure A.6 Continuum-subtracted optical spectra: NGC 1365, NGC 1808, and NGC 2622

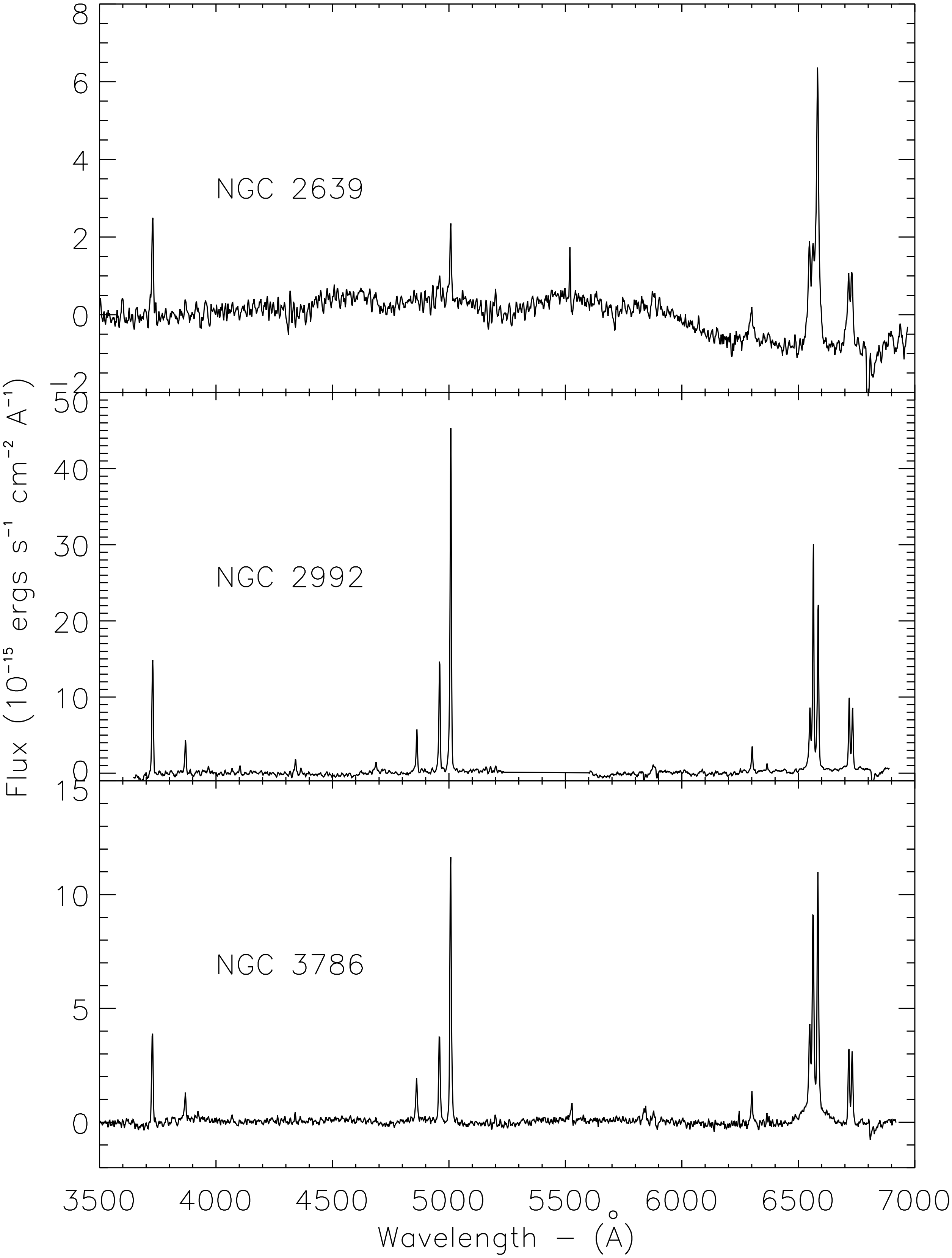

Figure A.7 Continuum-subtracted optical spectra: NGC 2639, NGC 2992, and NGC 3786

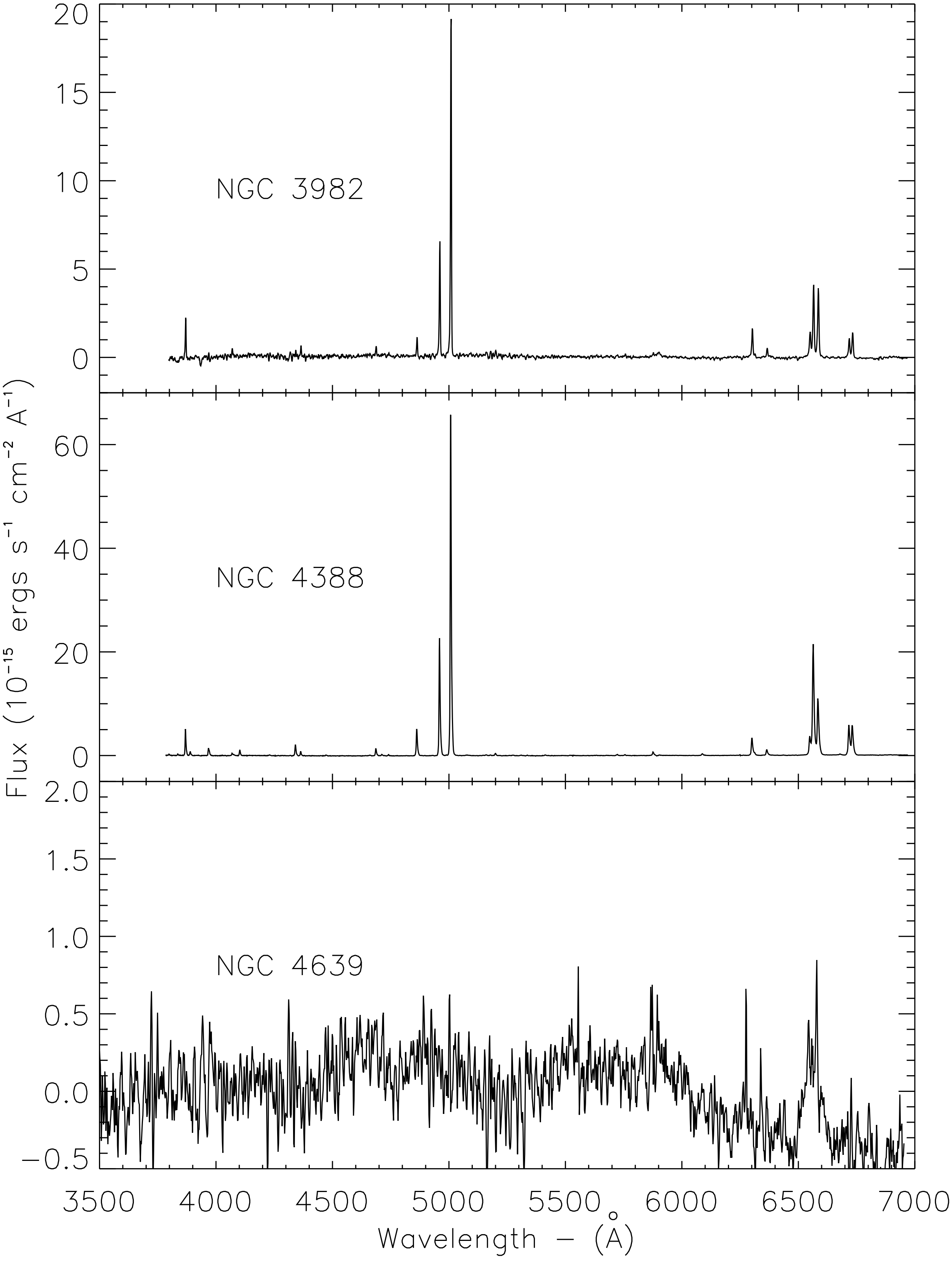

Figure A.8 Continuum-subtracted optical spectra: NGC 3982, NGC 4388, and NGC 4639

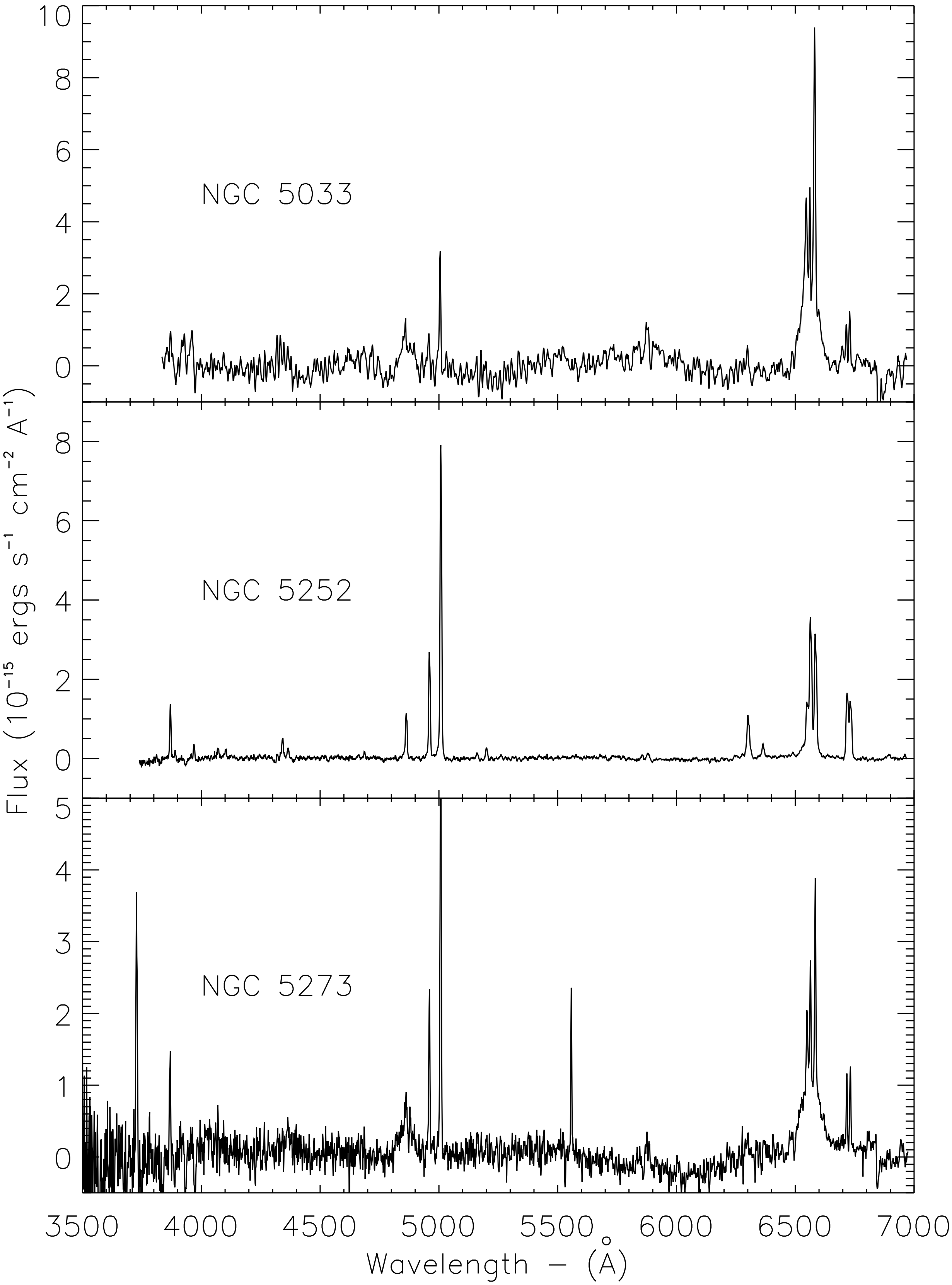

Figure A.9 Continuum-subtracted optical spectra: NGC 5033, NGC 5252, and NGC 5273

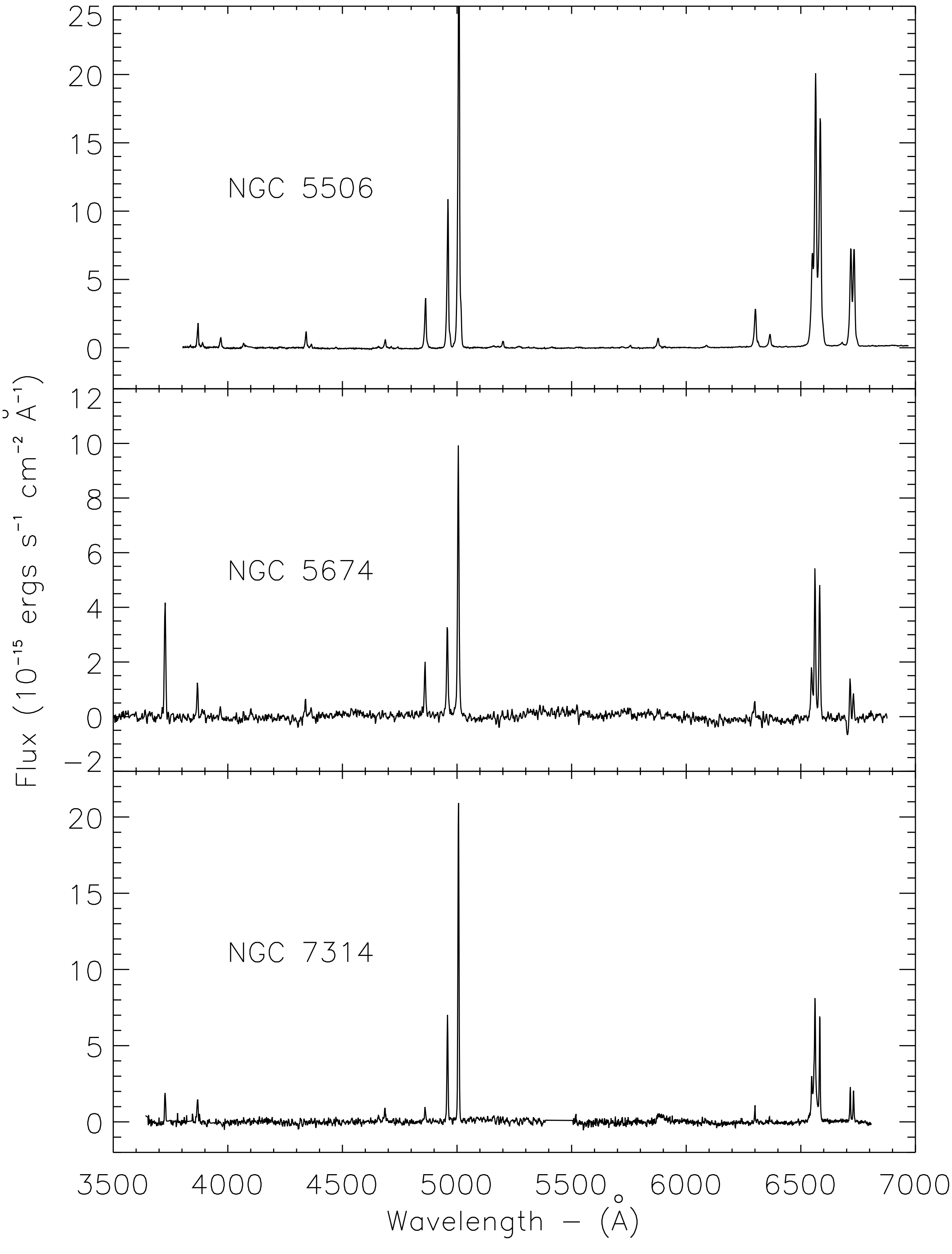

Figure A.10 Continuum-subtracted optical spectra: NGC 5506, NGC 5674, and NGC 7314

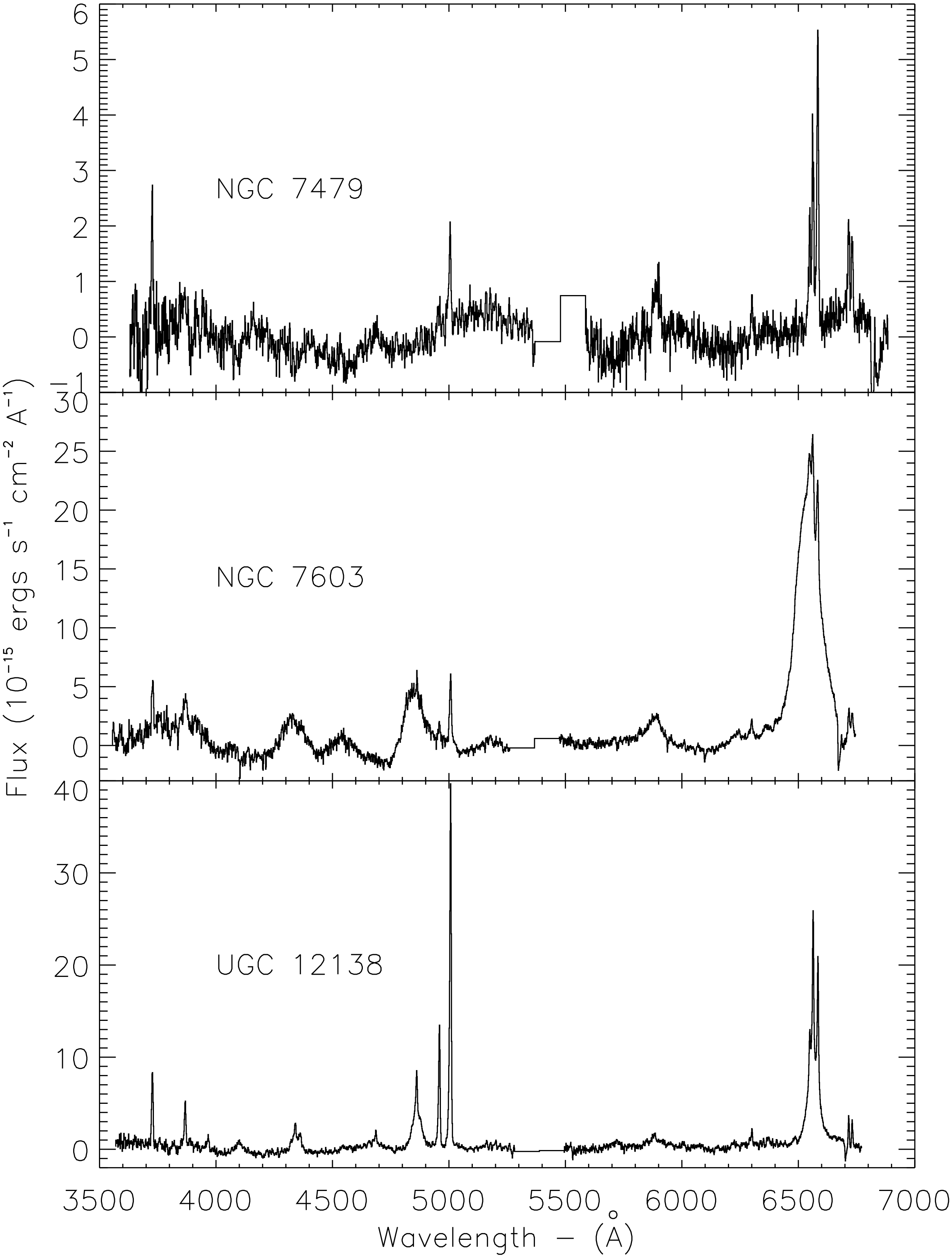

Figure A.11 Continuum-subtracted optical spectra: NGC 7479, UGC 12138, and UGC 7064

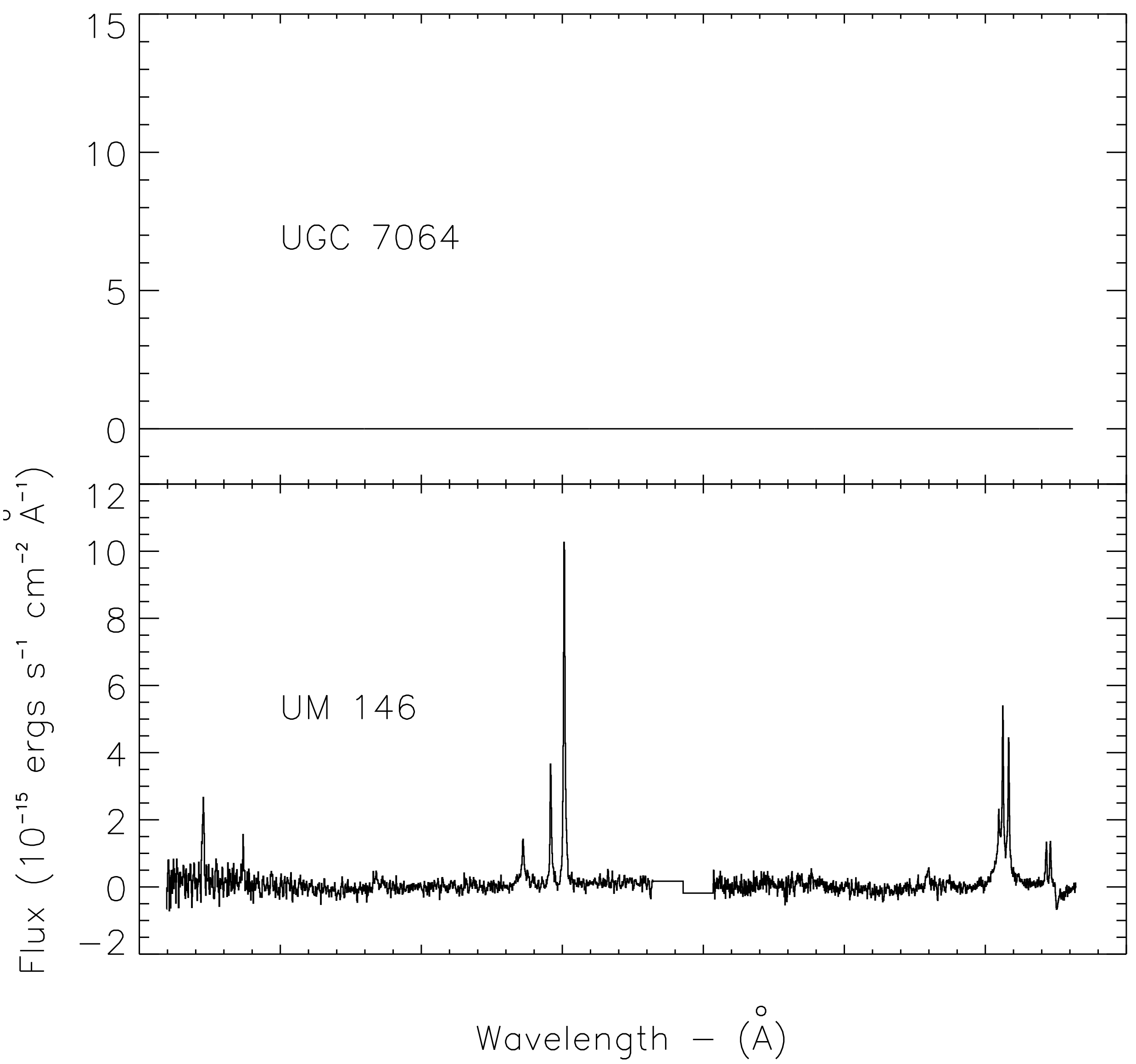

Figure A.12 Continuum-subtracted optical spectra: UM 146

– B –

Hα Profiles

This Appendix presents plots of the Hα profile after [N II] subtraction. The [O III] λ5007 profile, scaled to match the peak of Hα in flux, is overplotted with a dashed line at the centroid of Hα for a comparison of their widths. The Hβ line can be see at the far left end of the plots.

The definitions of the different types are from Maiolino & Rieke (1995) ([O III] refers to the [O III] λ5007 emission line in these definitions):

- Seyfert 1: Objects showing broad Hβ emission line with [O III]/Hβ < 0.3
- Seyfert 1.2: Objects showing broad Hβ with $0.3 <$ [O III]/Hβ < 1
- Seyfert 1.5: Objects showing broad Hβ with $1 <$ [O III]/Hβ < 4
- Seyfert 1.8: Objects showing broad Hβ with $4 <$ [O III]/Hβ
- Seyfert 1.9: Objects not showing broad Hβ, but having broad Hα

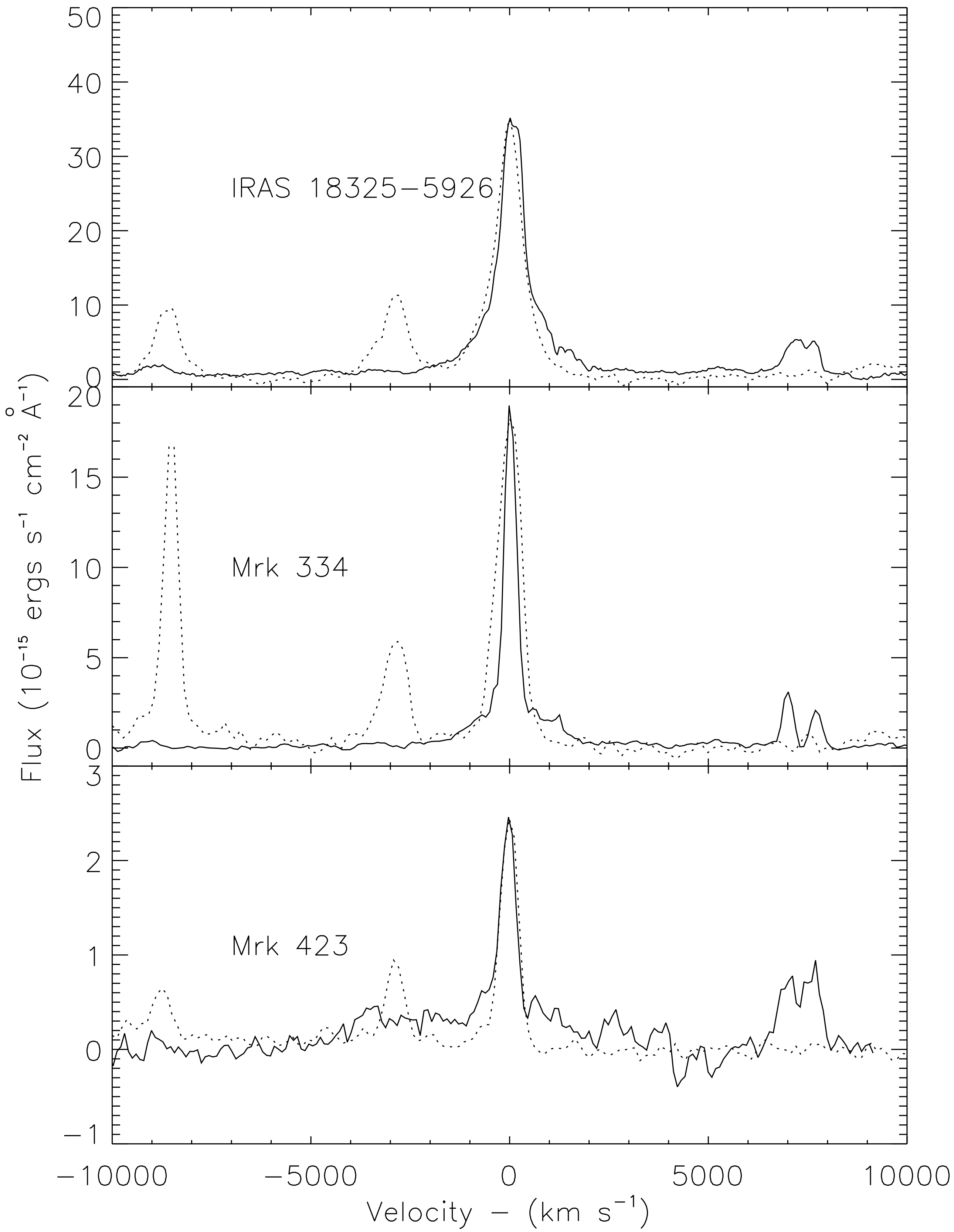

Figure B.1 Hα profiles for IRAS 18325-5926, Mrk 334, and Mrk 423

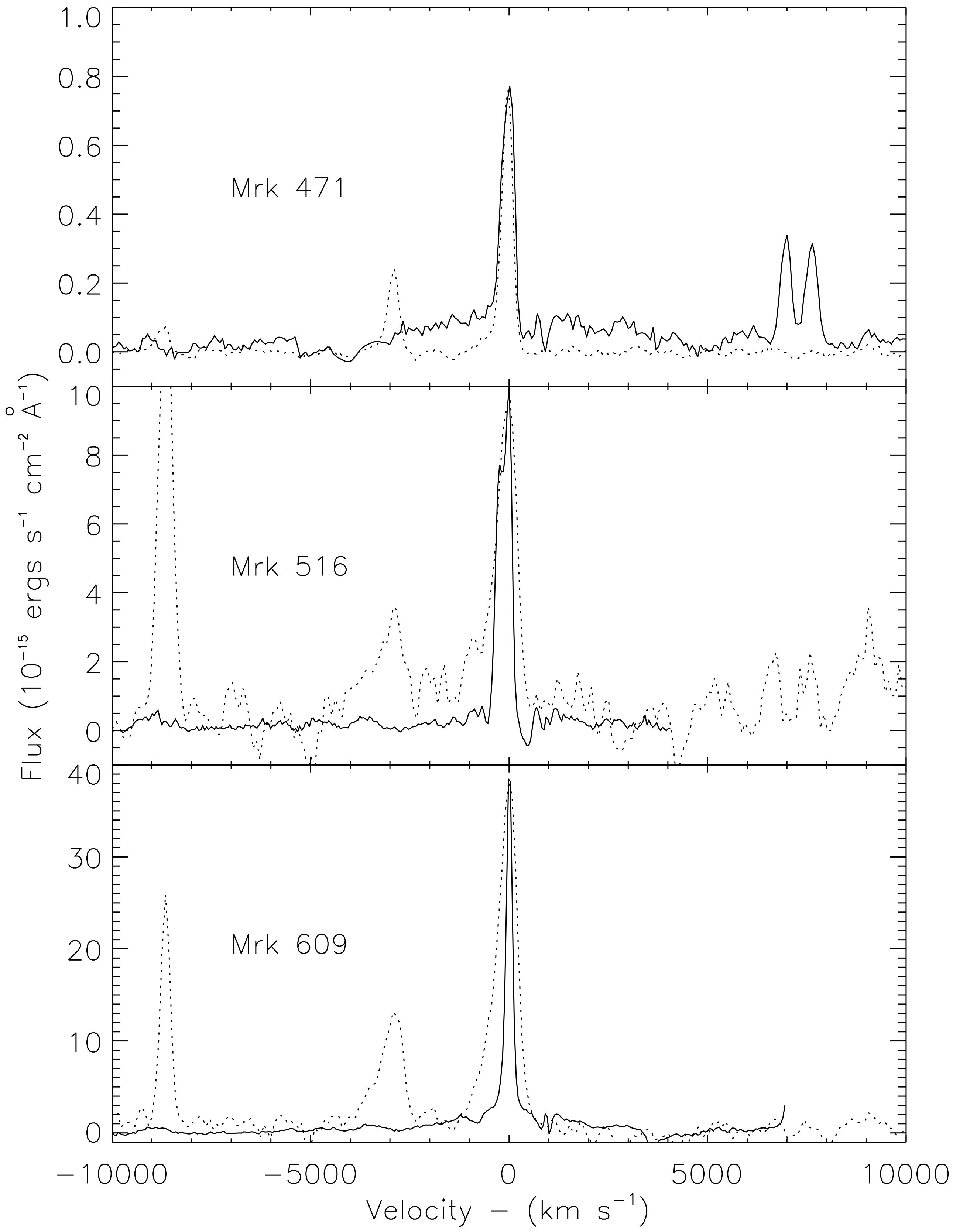

Figure B.2 Hα profiles for Mrk 471, Mrk 516, and Mrk 609

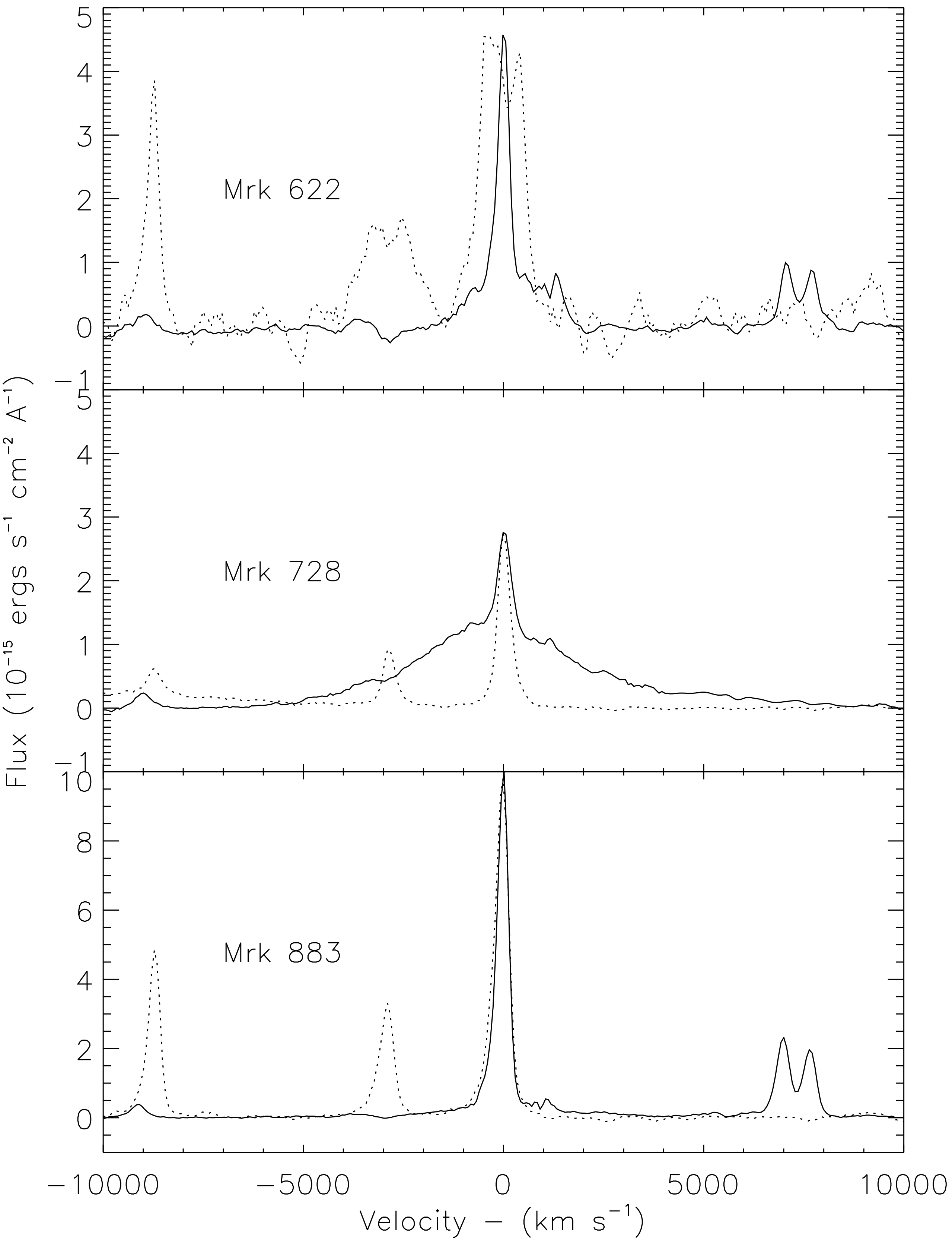

Figure B.3 Hα profiles for Mrk 622, Mrk 728, and Mrk 883

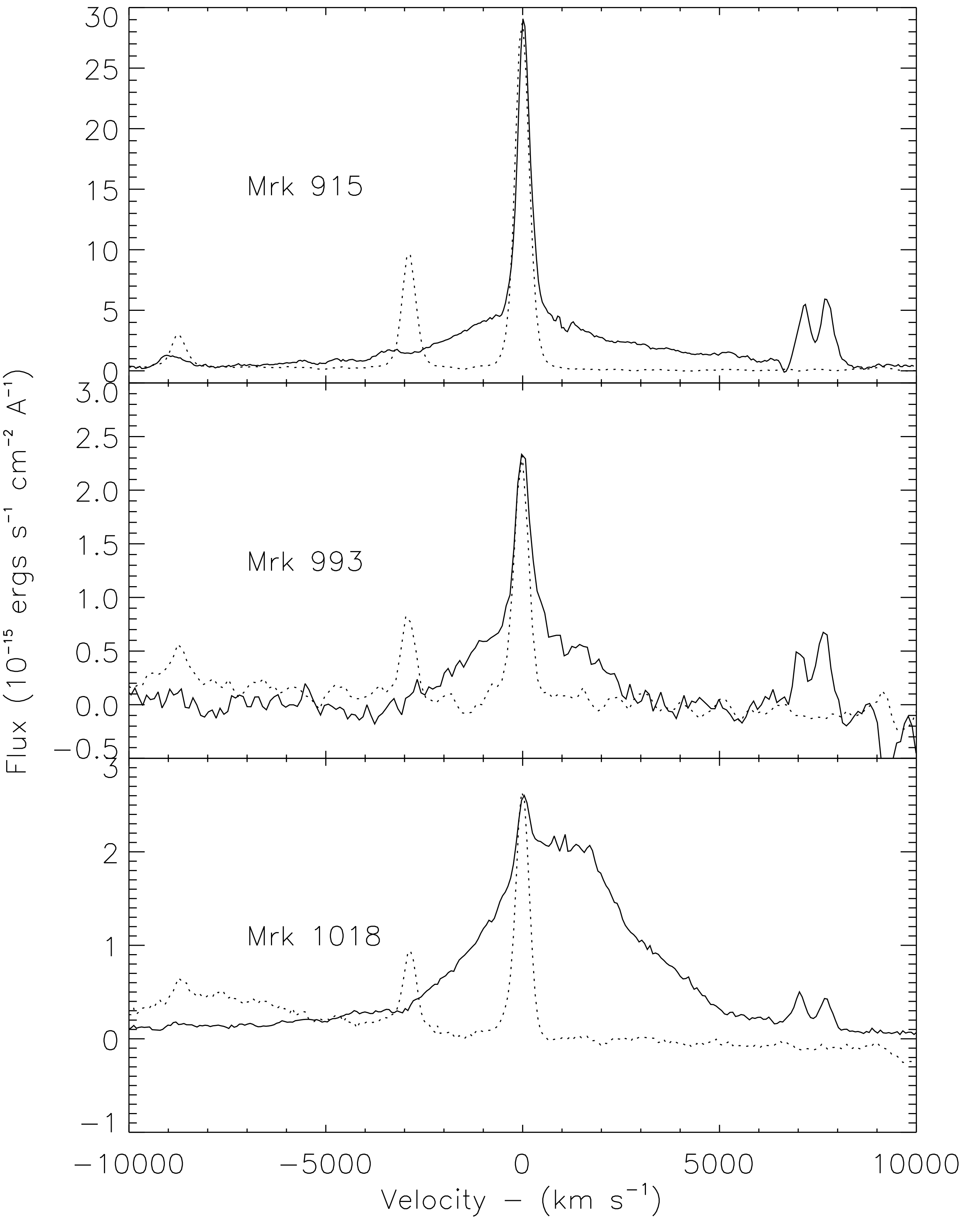

Figure B.4 Hα profiles for Mrk 915, Mrk 993, and Mrk 1018

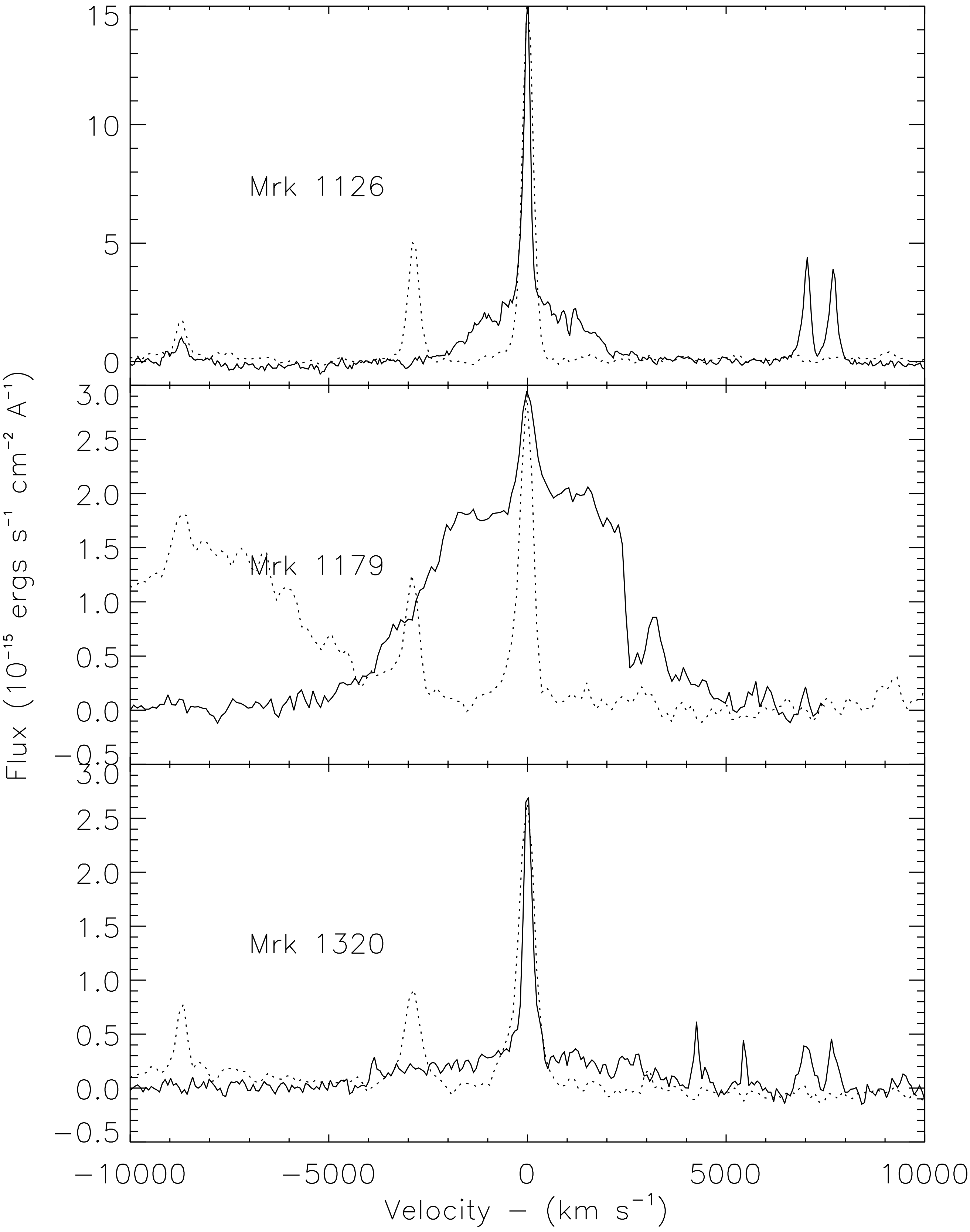

Figure B.5 Hα profiles for Mrk 1126, Mrk 1179, and Mrk 1320

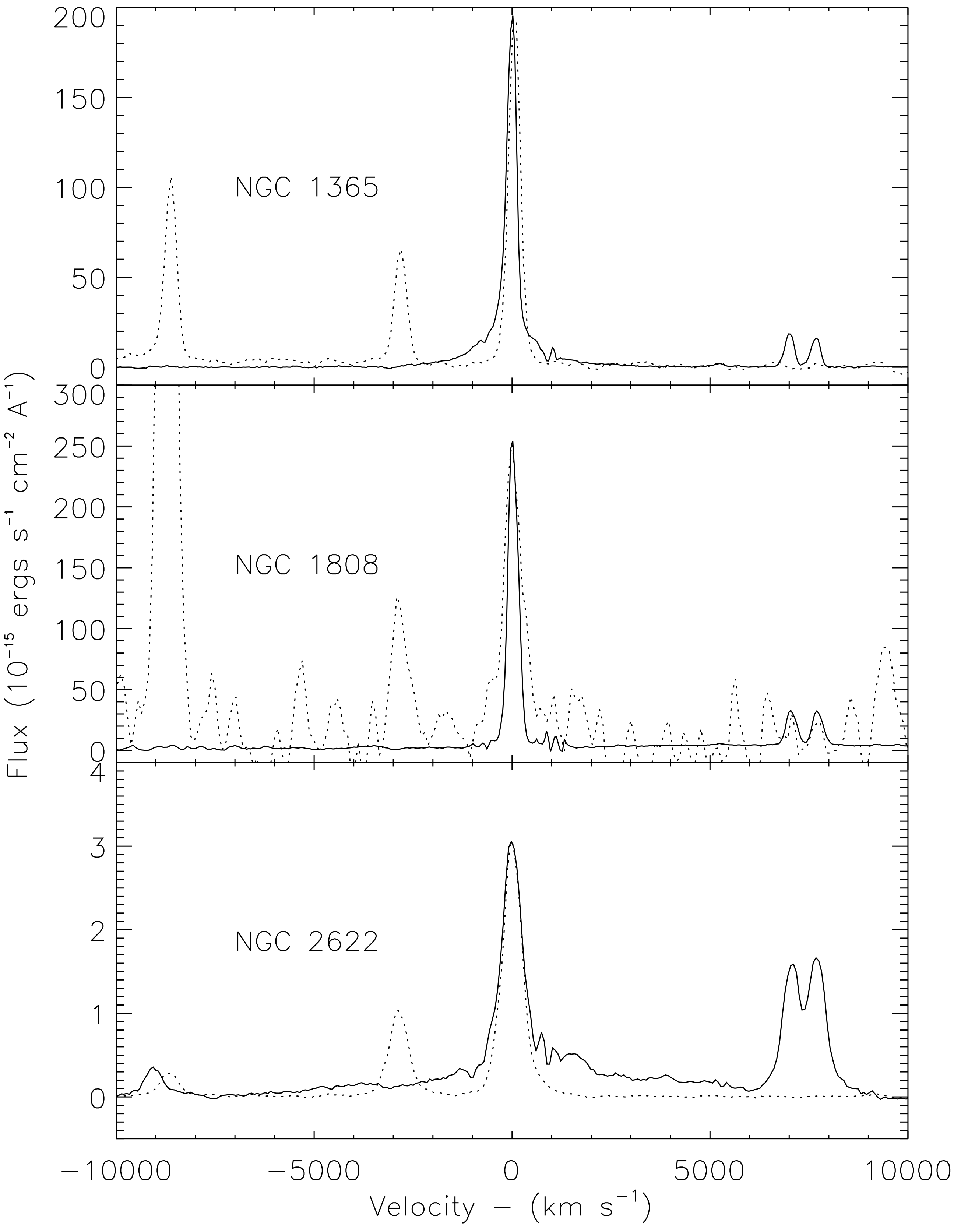

Figure B.6 Hα profiles for NGC 1365, NGC 1808, and NGC 2622

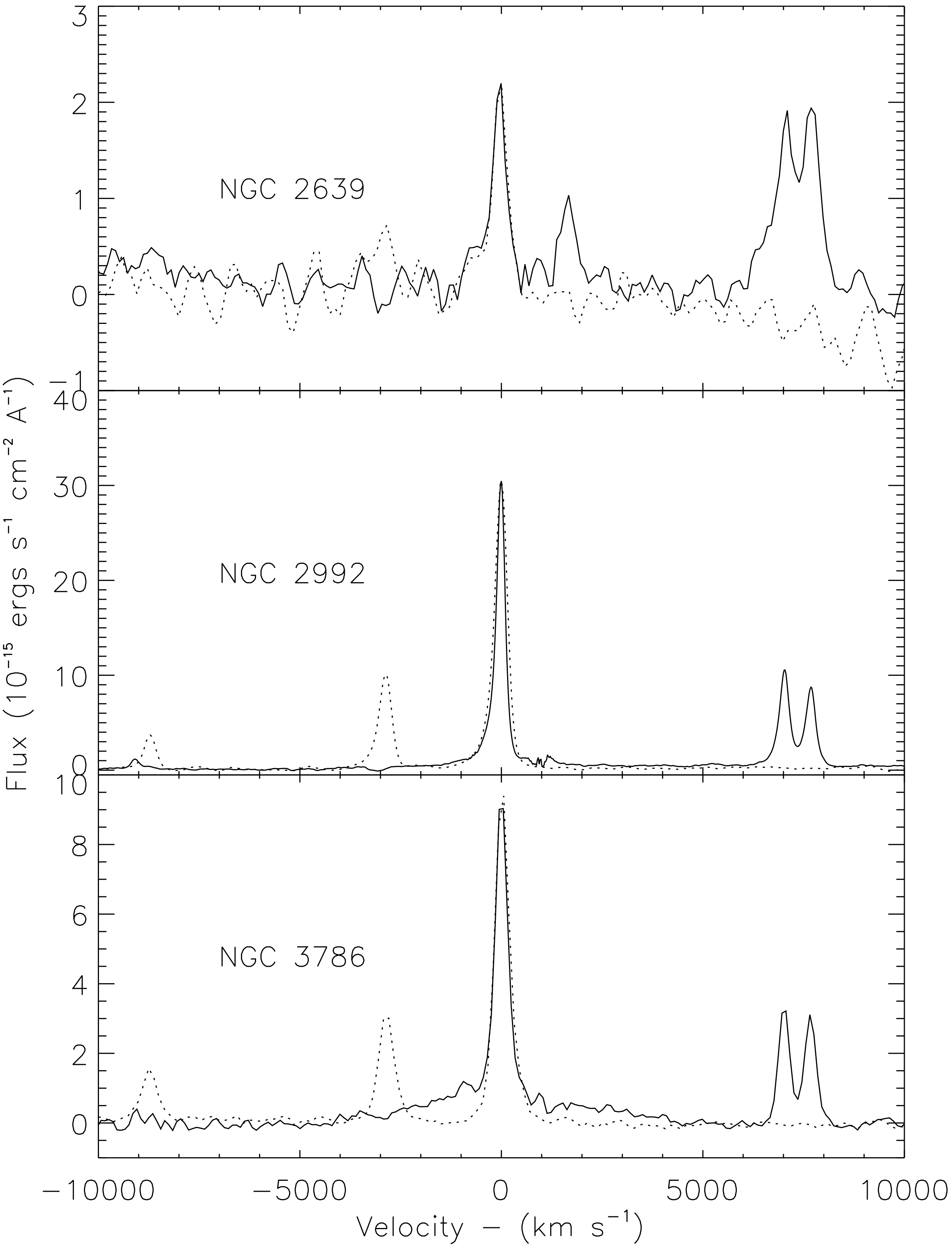

Figure B.7 Hα profiles for NGC 2639, NGC 2992, and NGC 3786

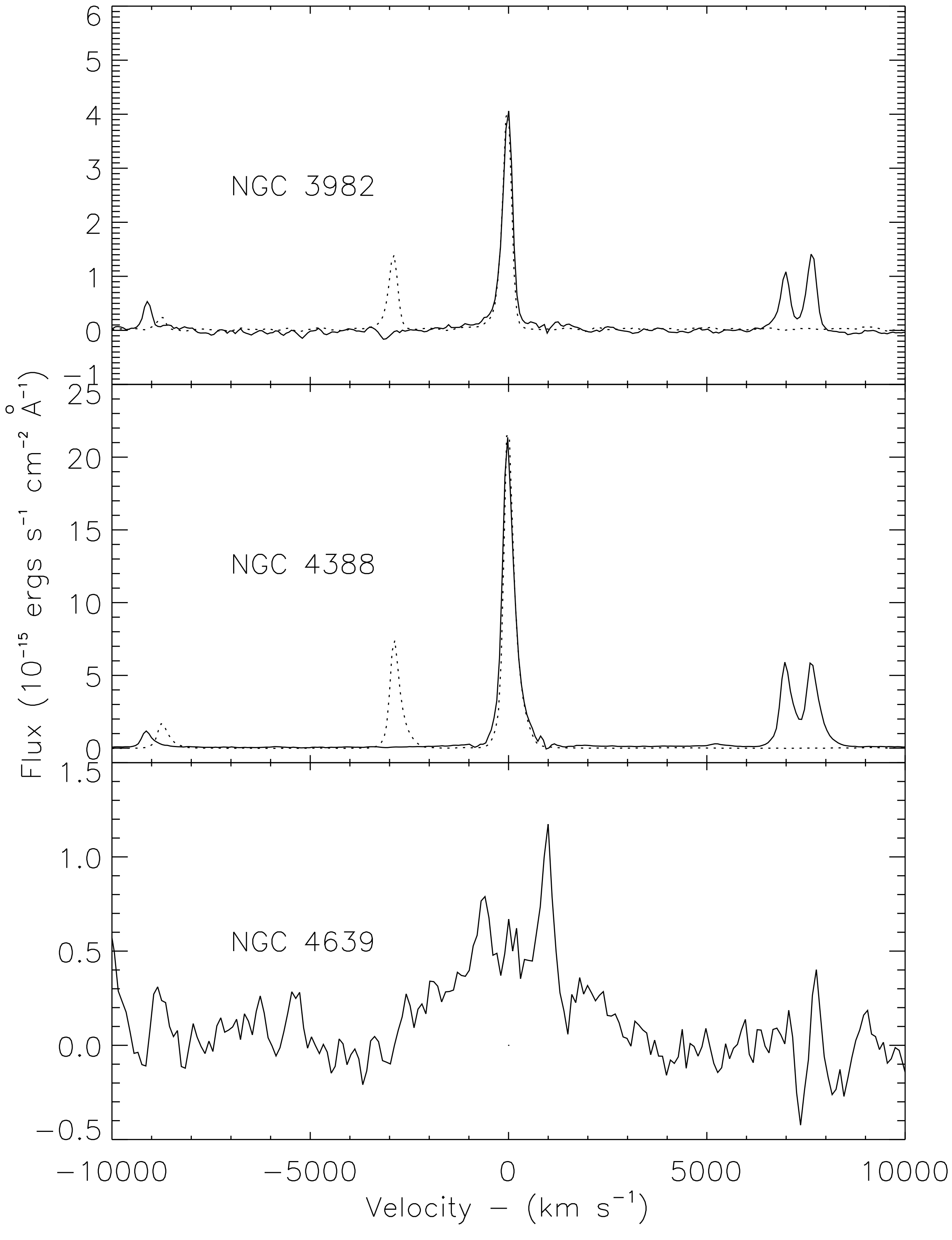

Figure B.8 Hα profiles for NGC 3982, NGC 4388, and NGC 4639

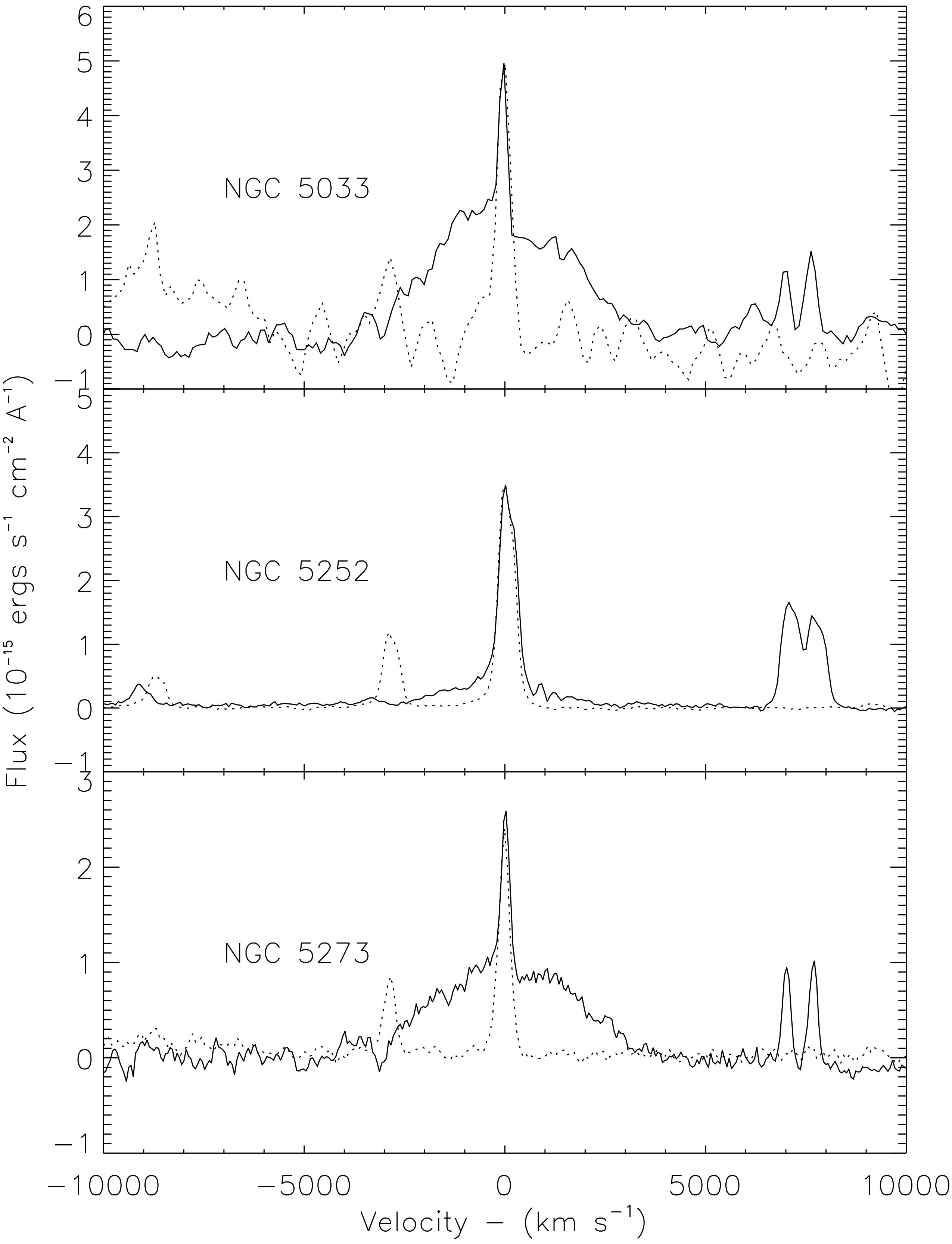

Figure B.9 Hα profiles for NGC 5033, NGC 5252, and NGC 5273

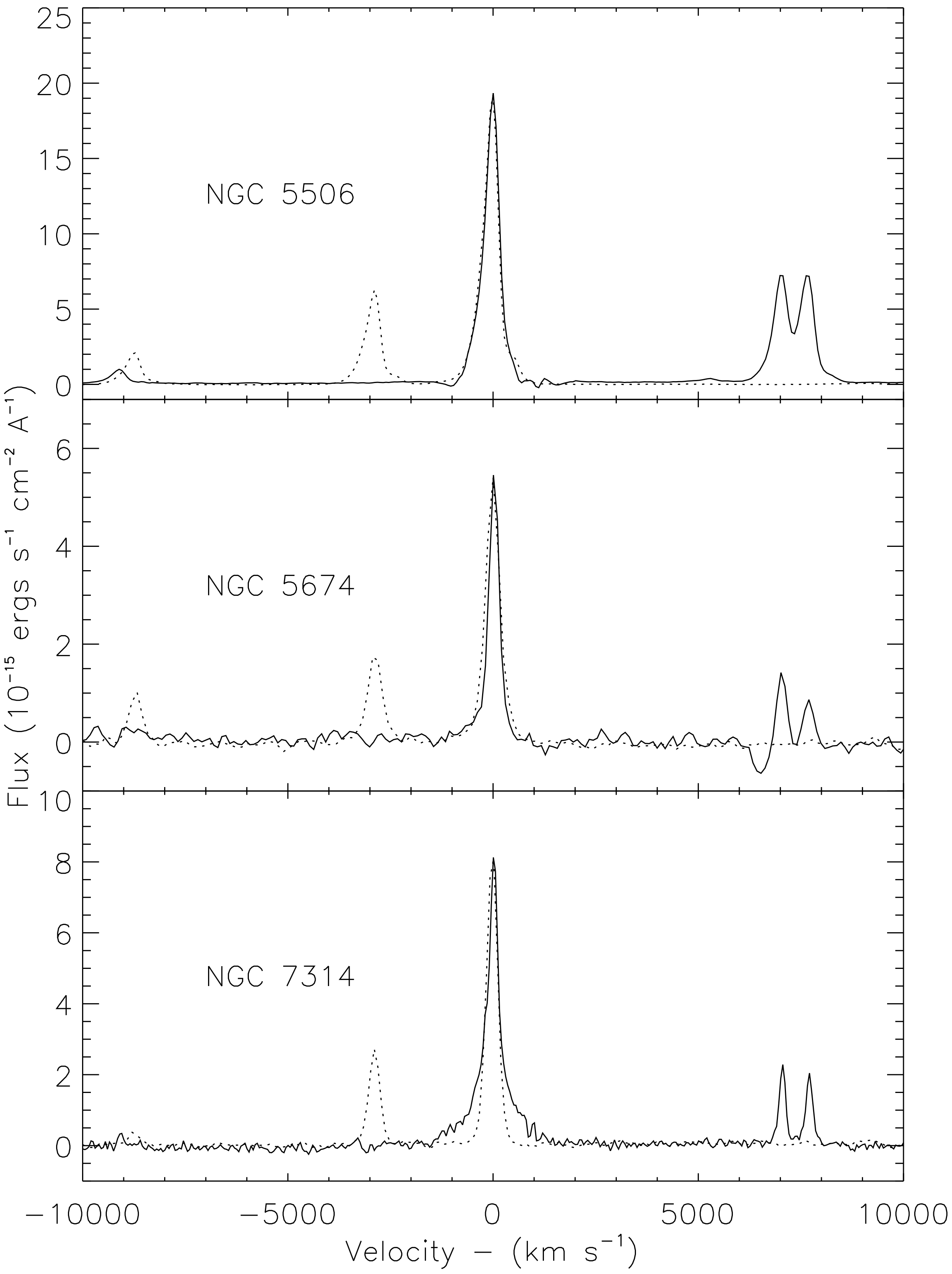

Figure B.10 Hα profiles for NGC 5506, NGC 5674, and NGC 7314

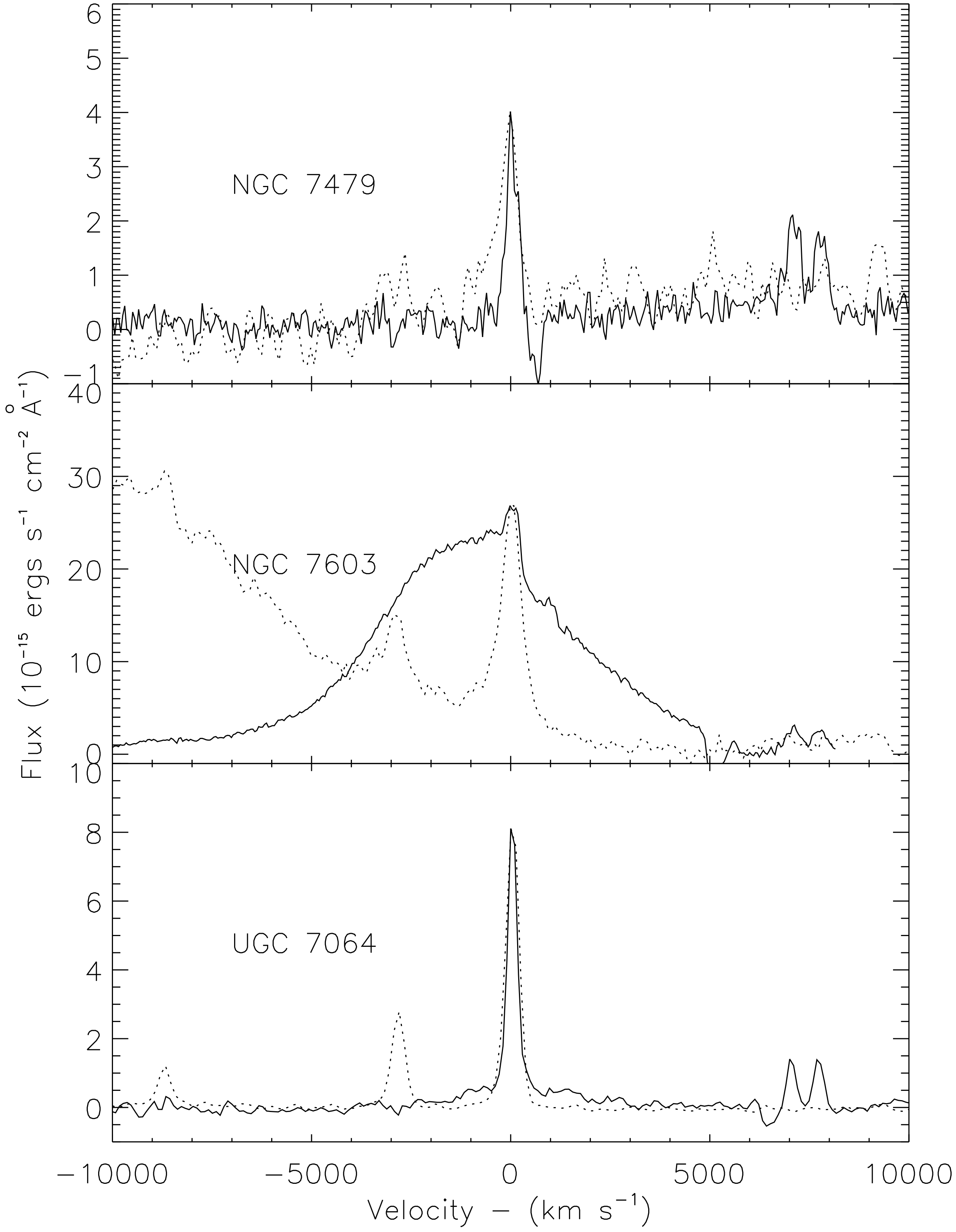

Figure B.11 Hα profiles for NGC 7479, NGC 7603, and UGC 7064

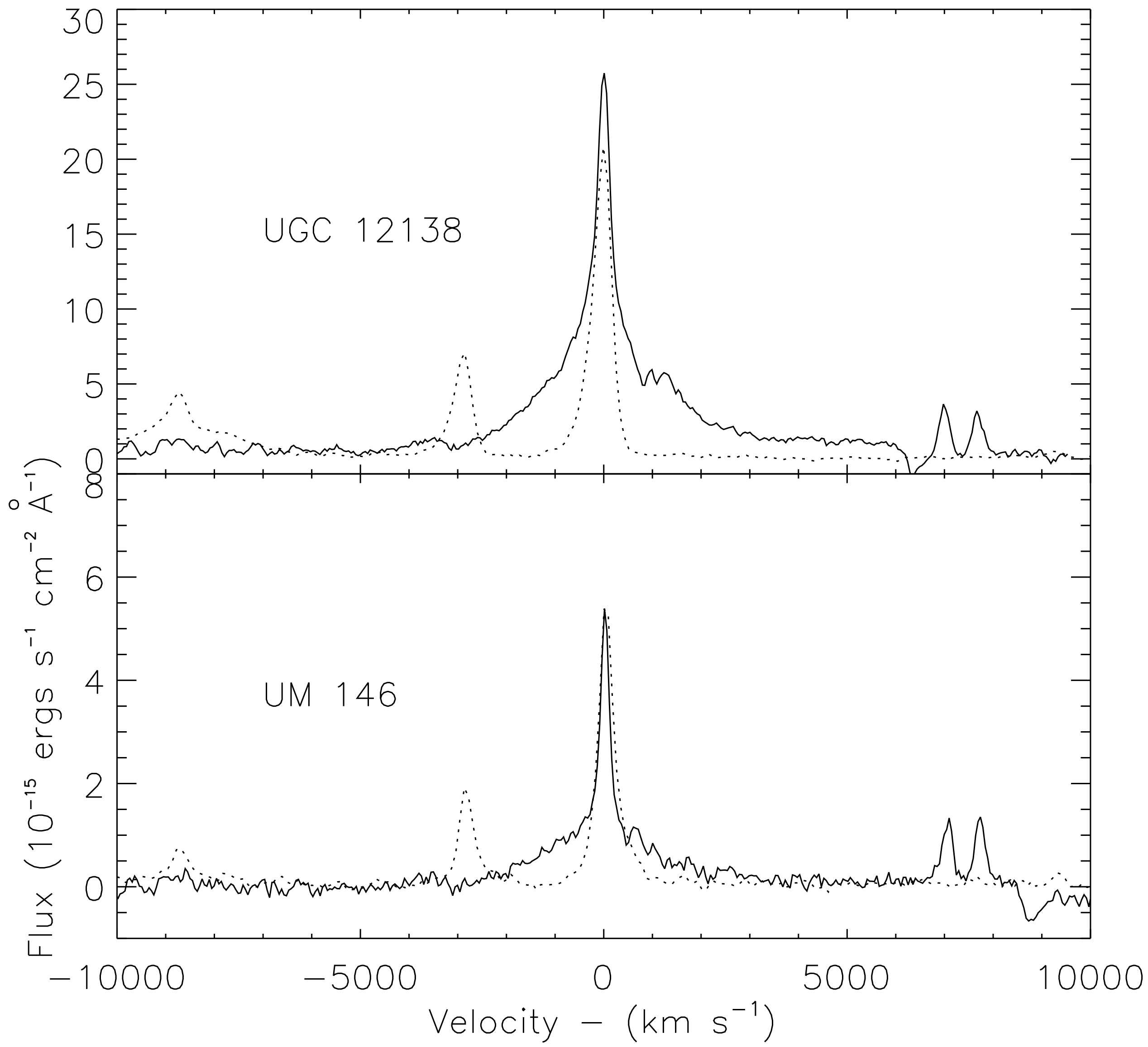

Figure B.12 Hα profiles for UGC 12138 and UM 146

– C –

X-ray Spectra

This Appendix presents the *XMM* EPIC pn 0.5-10 keV spectra discussed in Chapter 4. The total model (solid line) is the sum of its additive components (dotted lines).

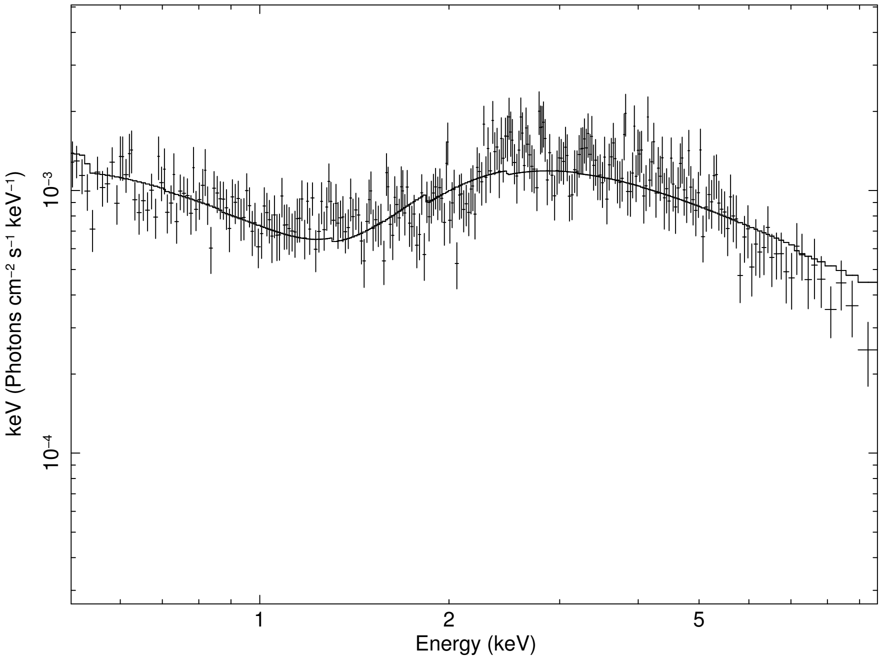

Figure C.1 IRAS 18325-5926, observed 5 March 2001

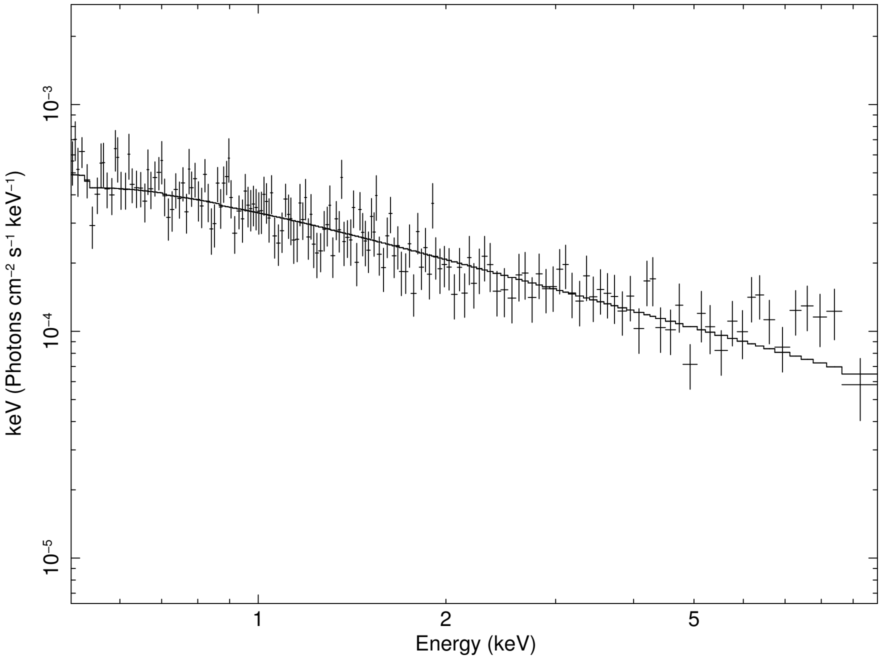

Figure C.2 Mrk 609, observed 13 August 2002

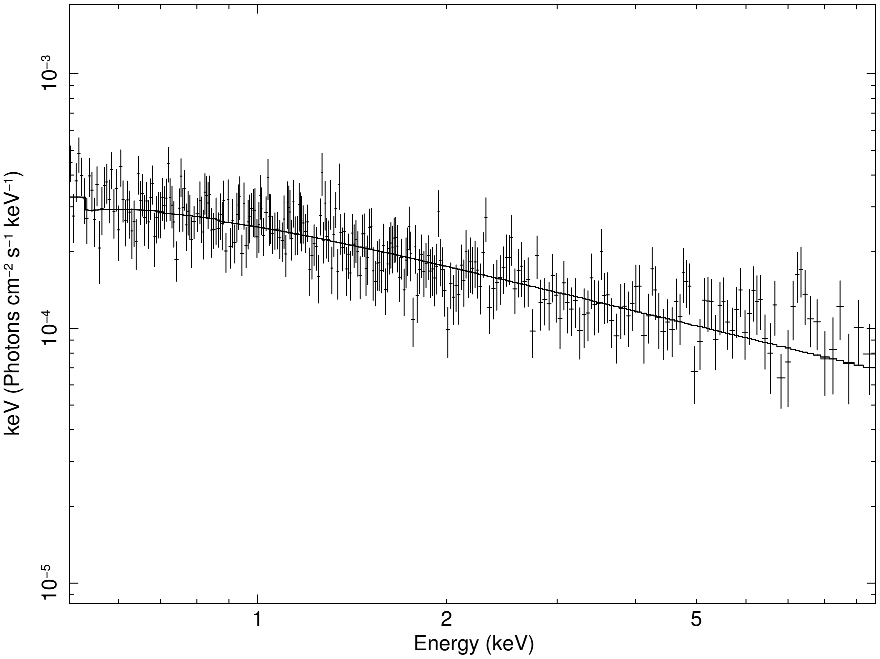

Figure C.3 Mrk 609, observed 27 January 2007

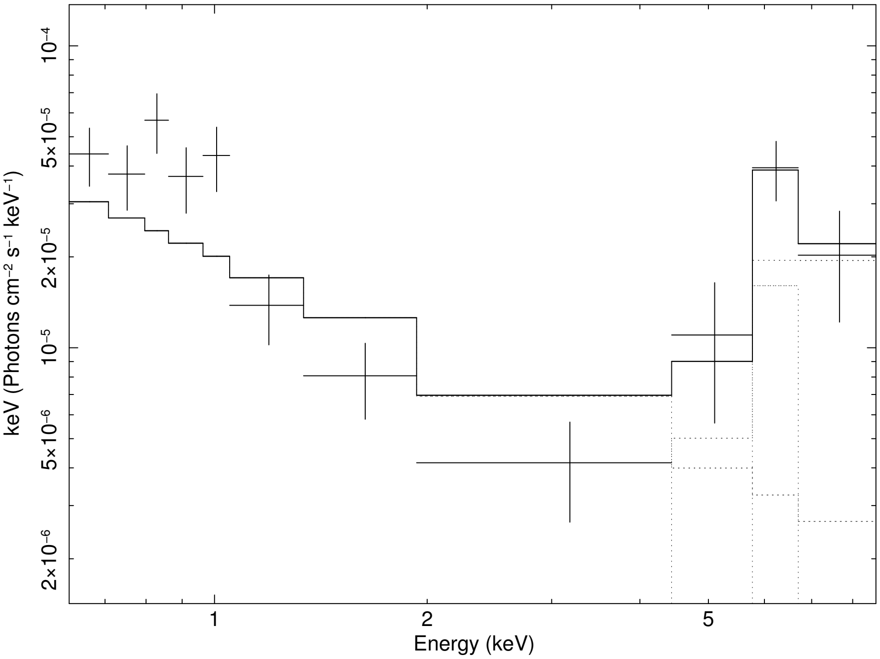

Figure C.4 Mrk 622, observed 2 April 2003

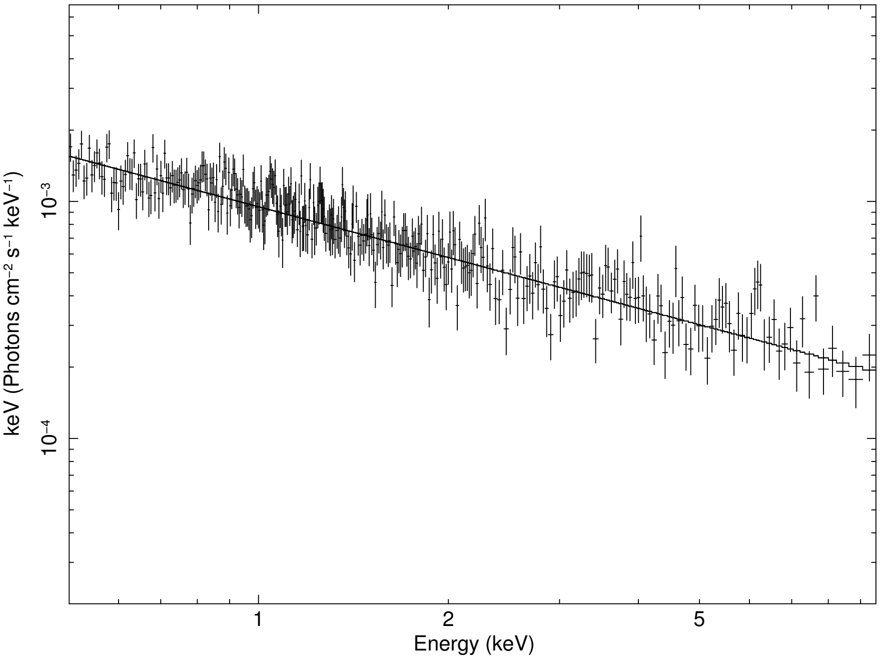

Figure C.5 Mrk 728, observed 23 May 2002

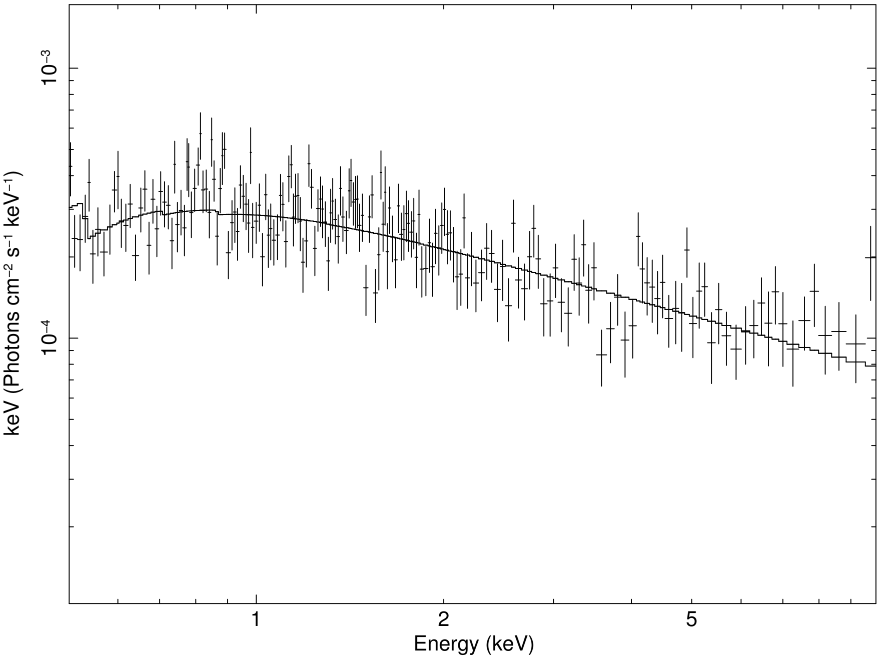

Figure C.6 Mrk 883, observed 13 August 2006

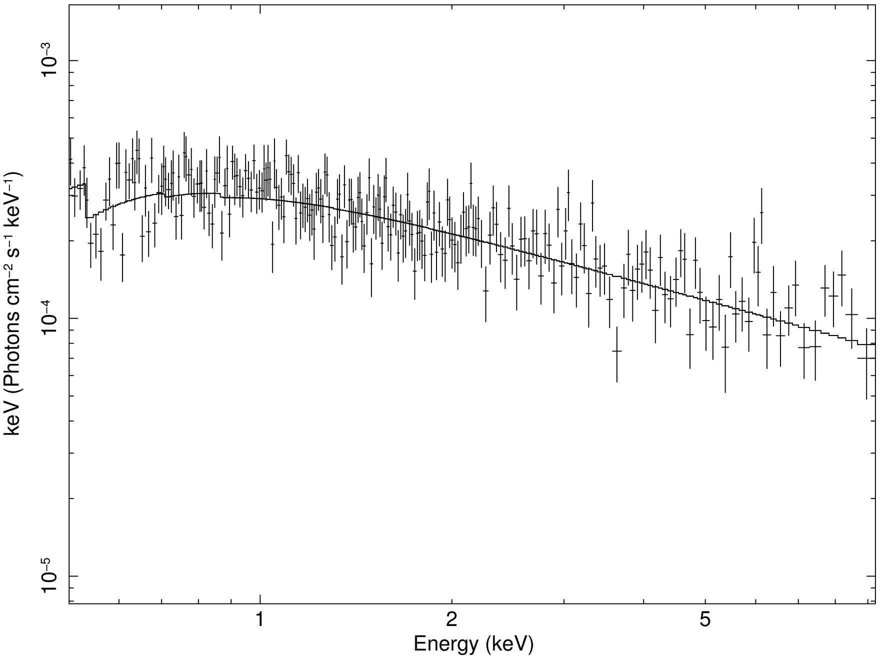

Figure C.7 Mrk 883, observed 15 August 2006

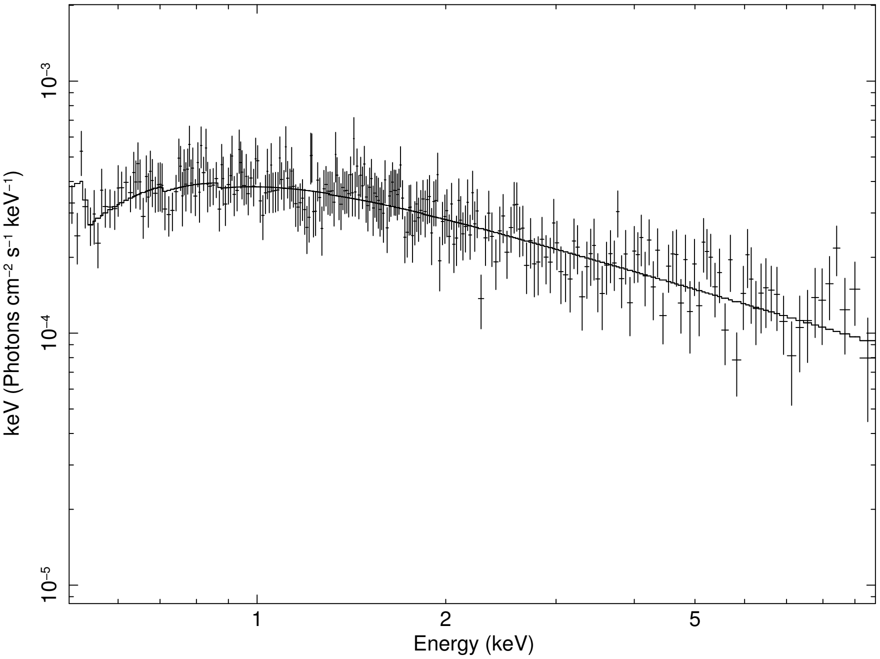

Figure C.8 Mrk 883, observed 21 August 2006

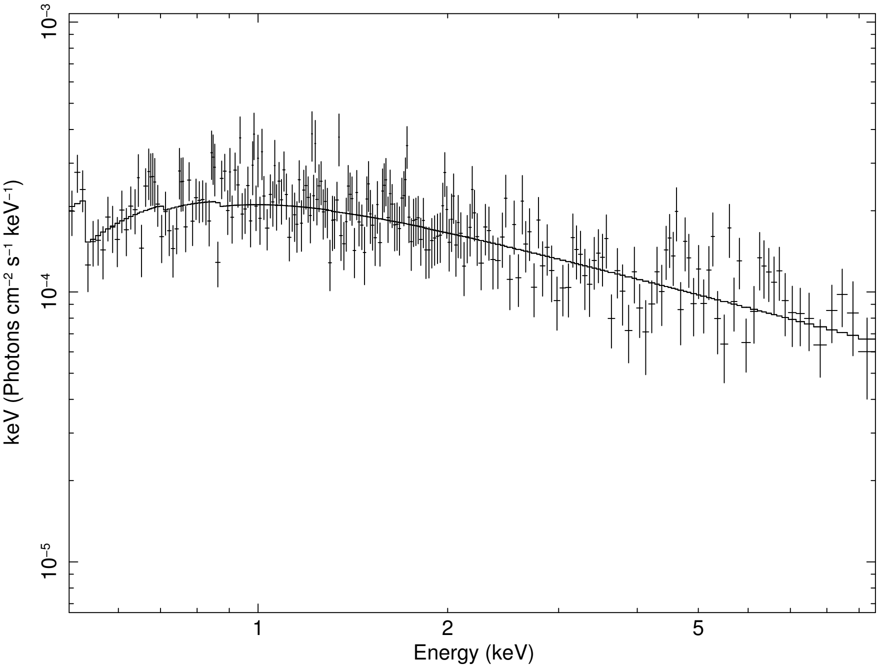

Figure C.9 Mrk 993, observed 23 January 2004

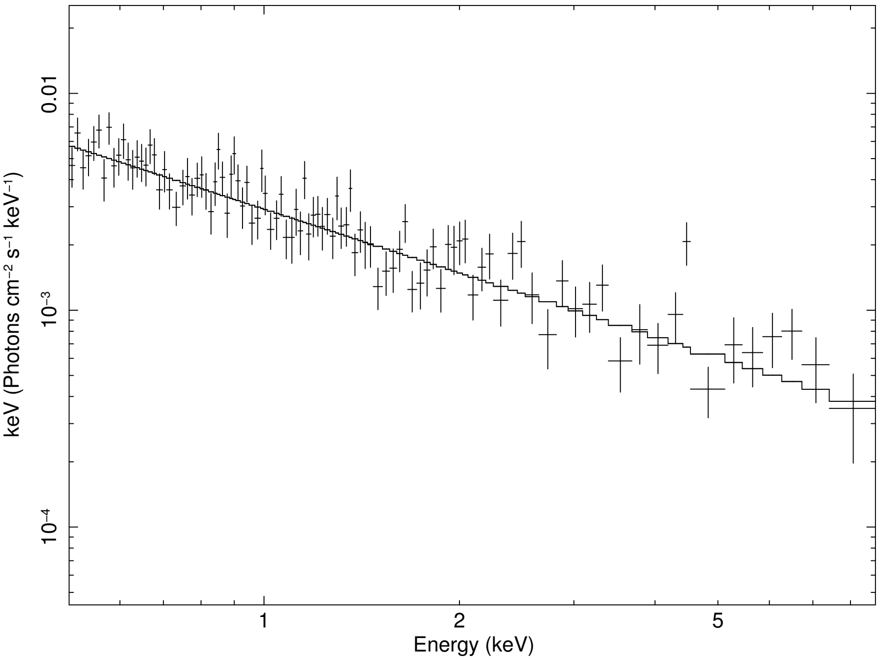

Figure C.10 Mrk 1018, observed 15 January 2005

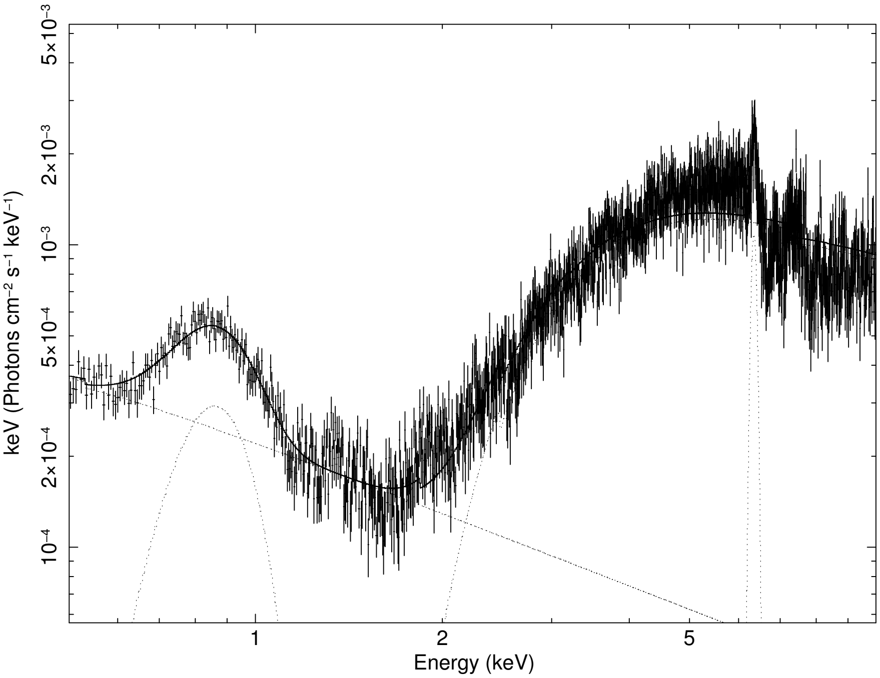

Figure C.11 NGC 1365, observed 17 January 2004

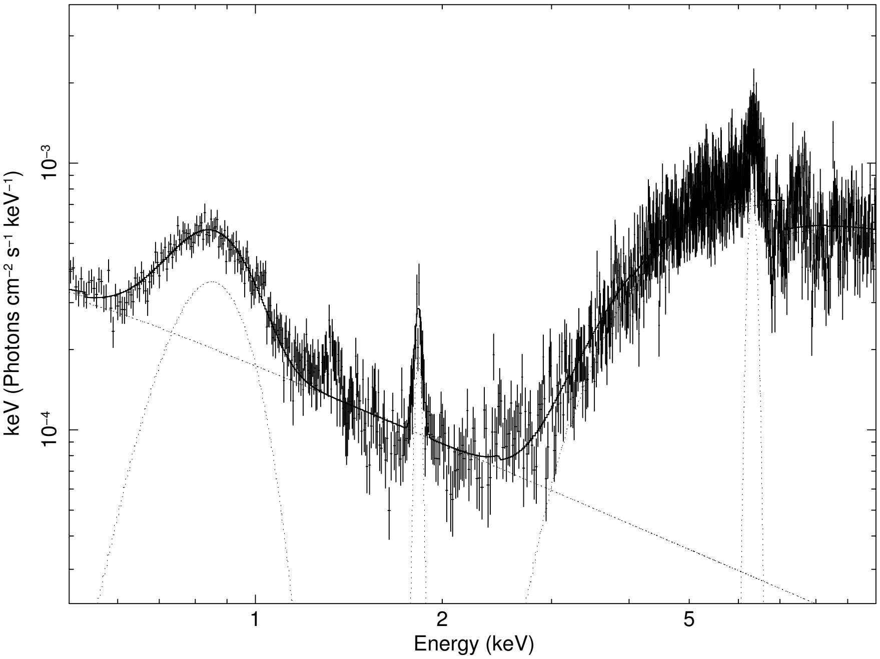

Figure C.12 NGC 1365, observed 24 July 2004

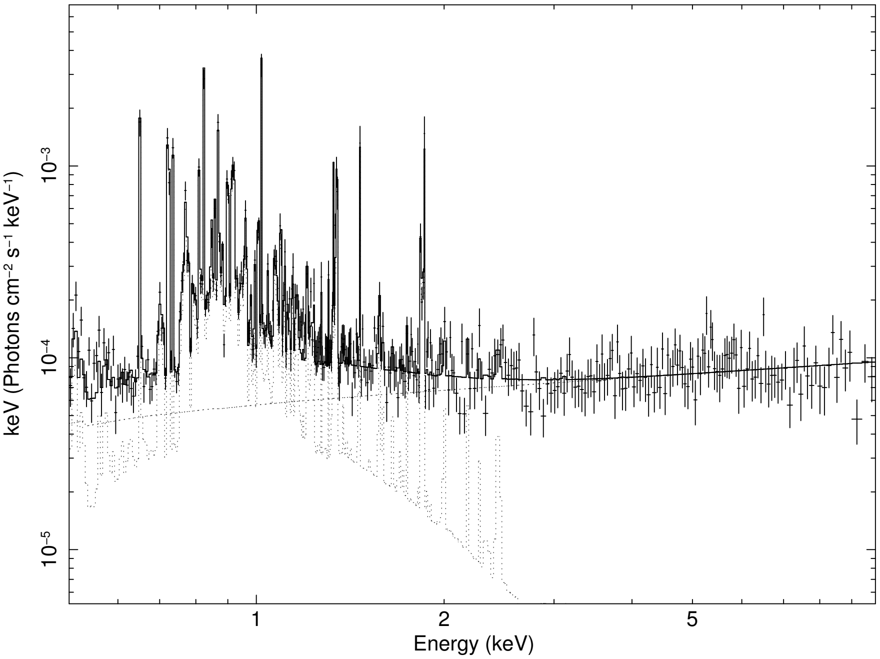

Figure C.13 NGC 1808, observed 6 April 2002

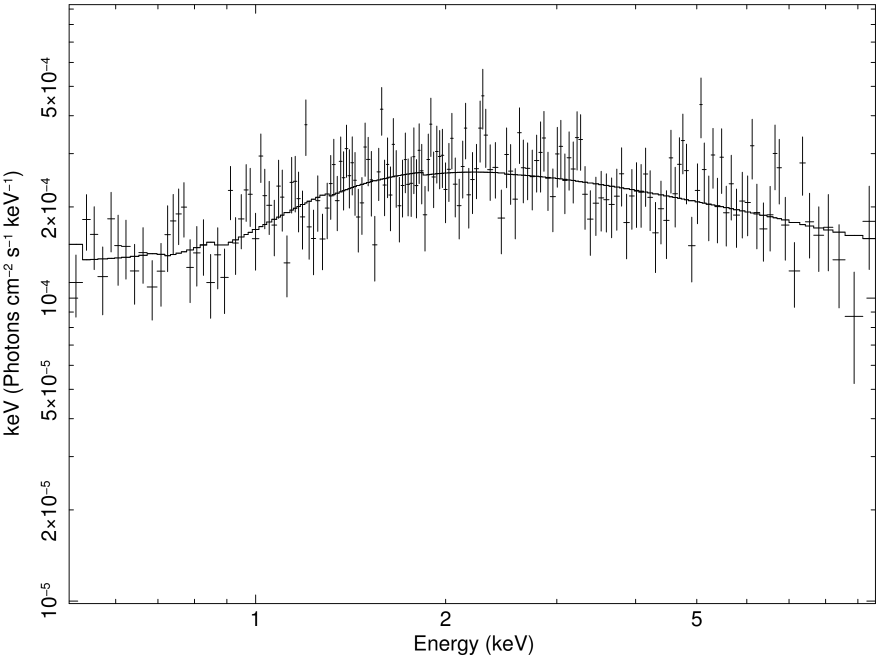

Figure C.14 NGC 2622, observed 9 April 2005

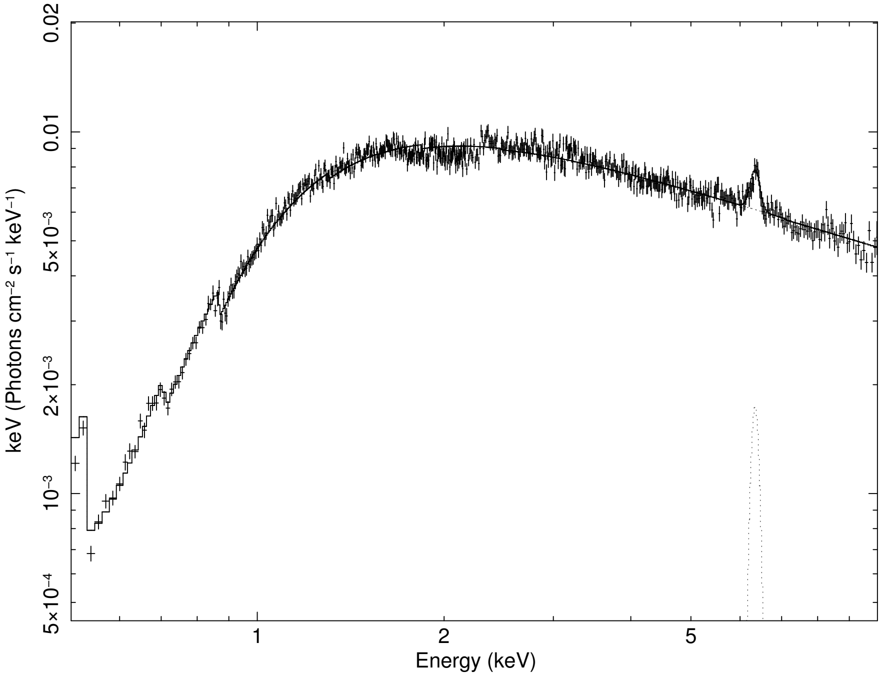

Figure C.15 NGC 2992, observed 19 May 2003

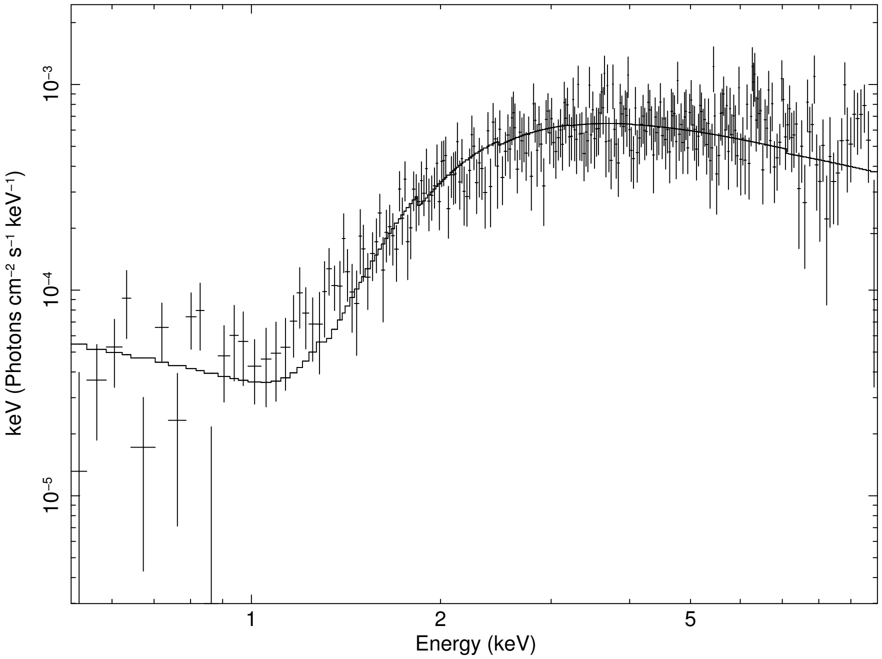

Figure C.16 NGC 3786, observed 24 May 2004

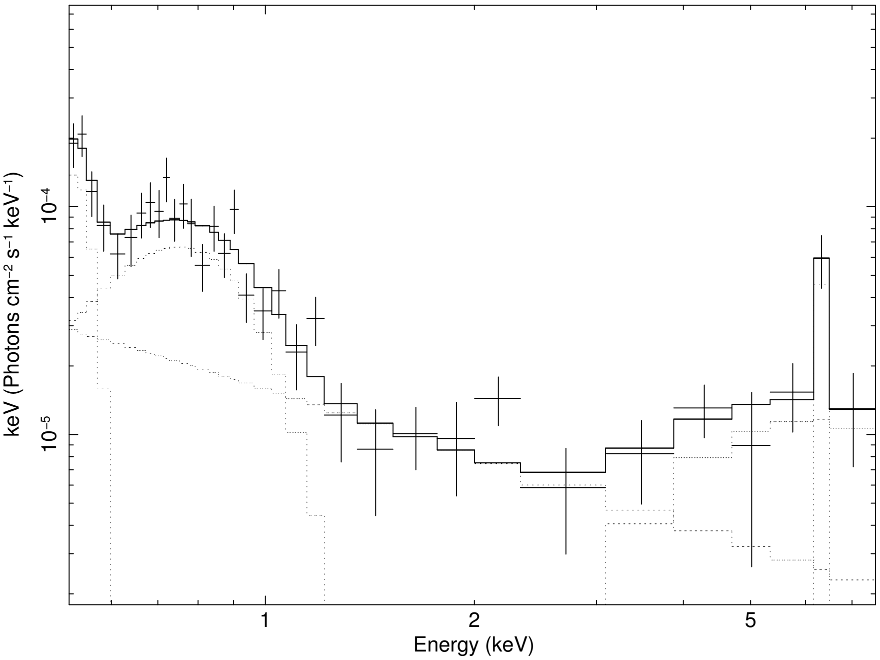

Figure C.17 NGC 3982, observed 15 June 2004

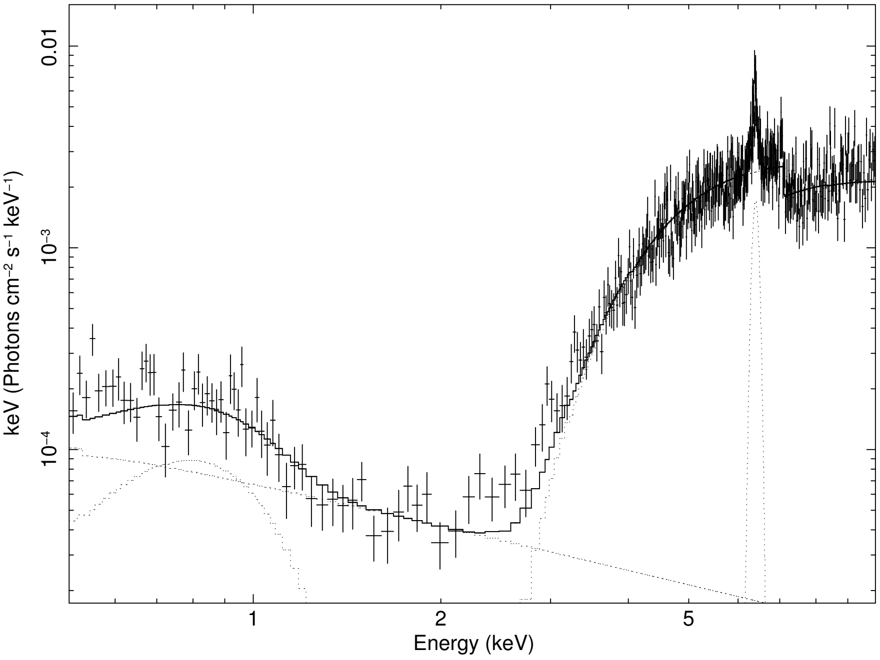

Figure C.18 NGC 4388, observed 12 December 2002

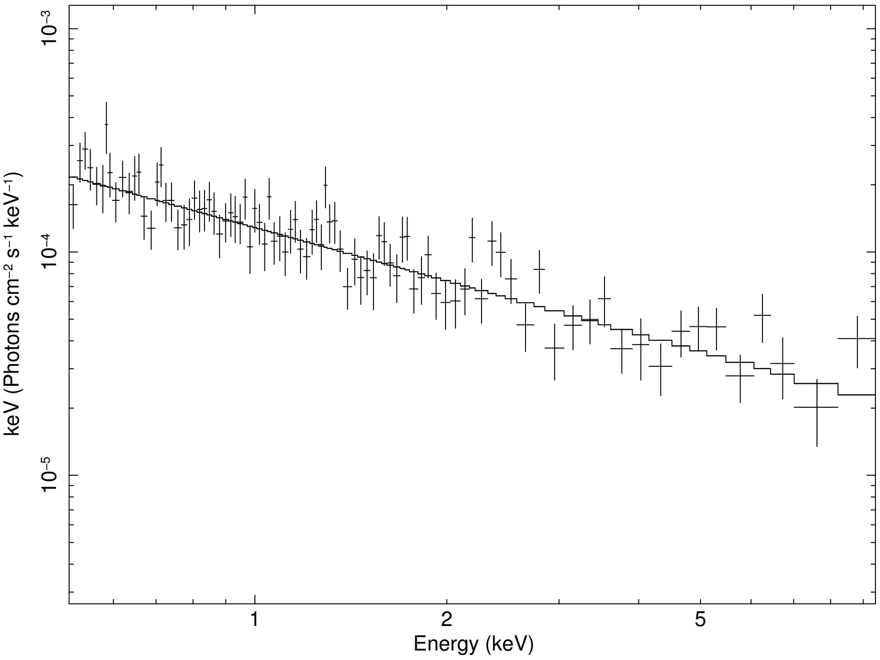

Figure C.19 NGC 4639, observed 16 December 2001

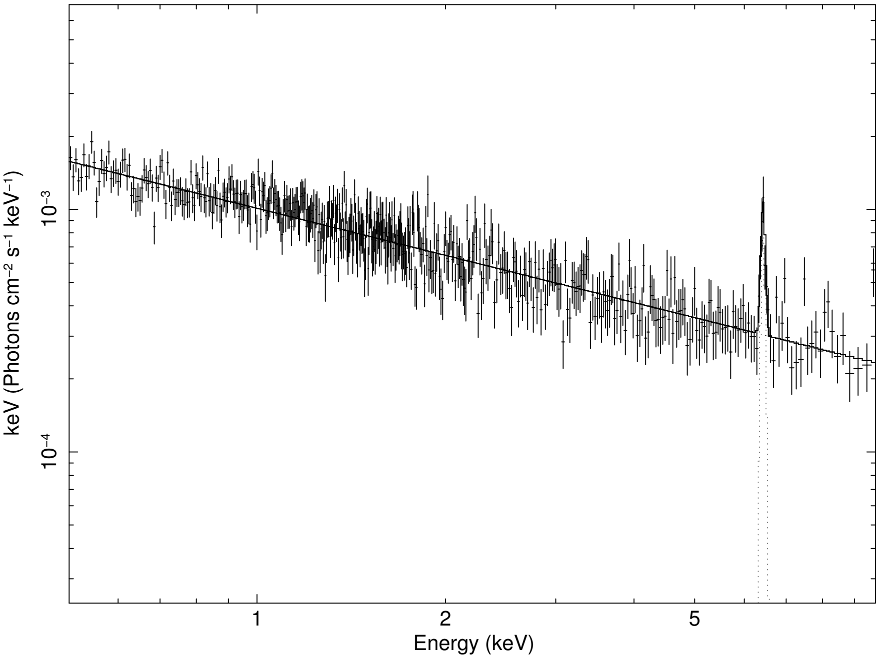

Figure C.20 NGC 5033, observed 18 December 2002

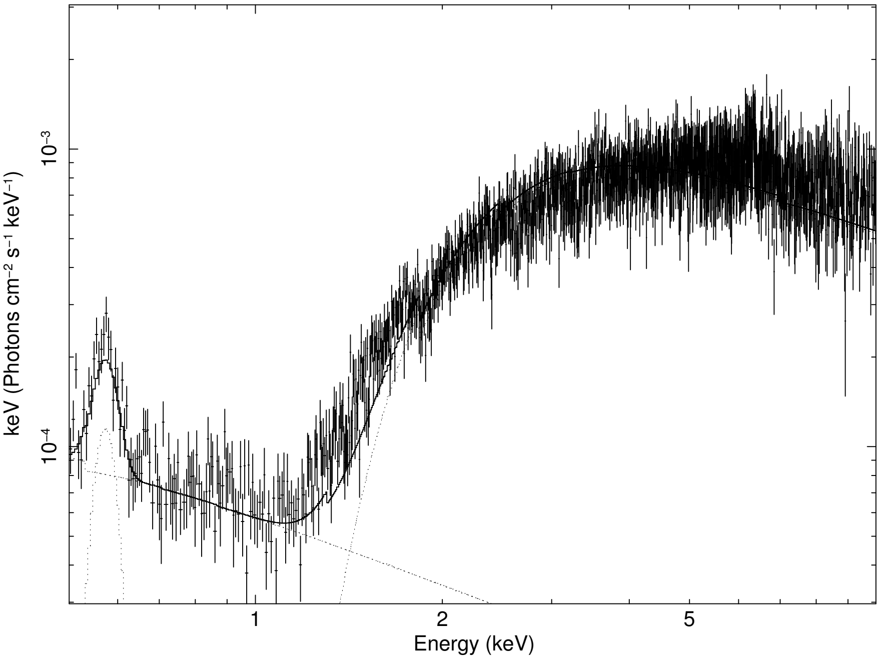

Figure C.21 NGC 5252, observed 18 July 2003

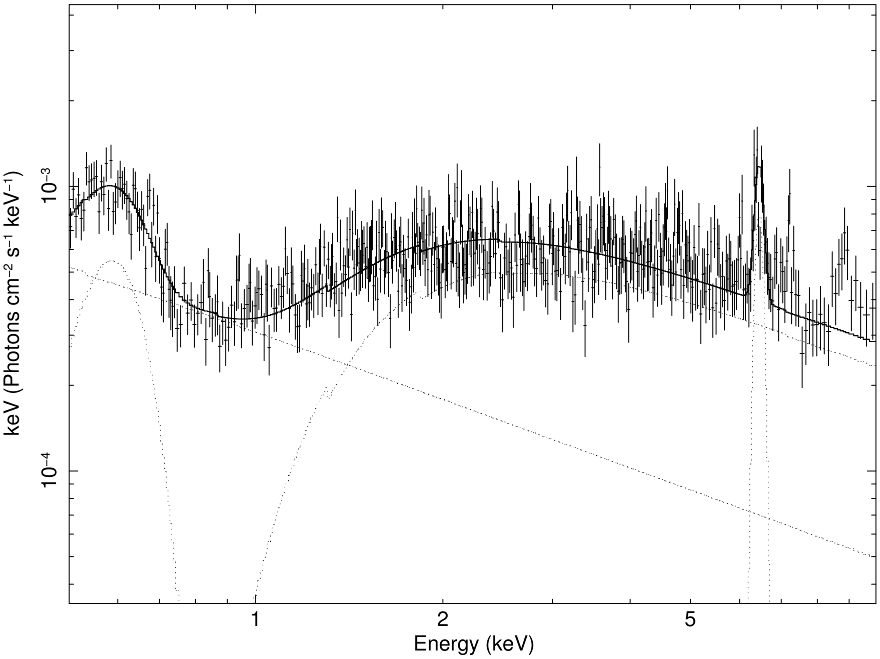

Figure C.22 NGC 5273, observed 14 June 2002

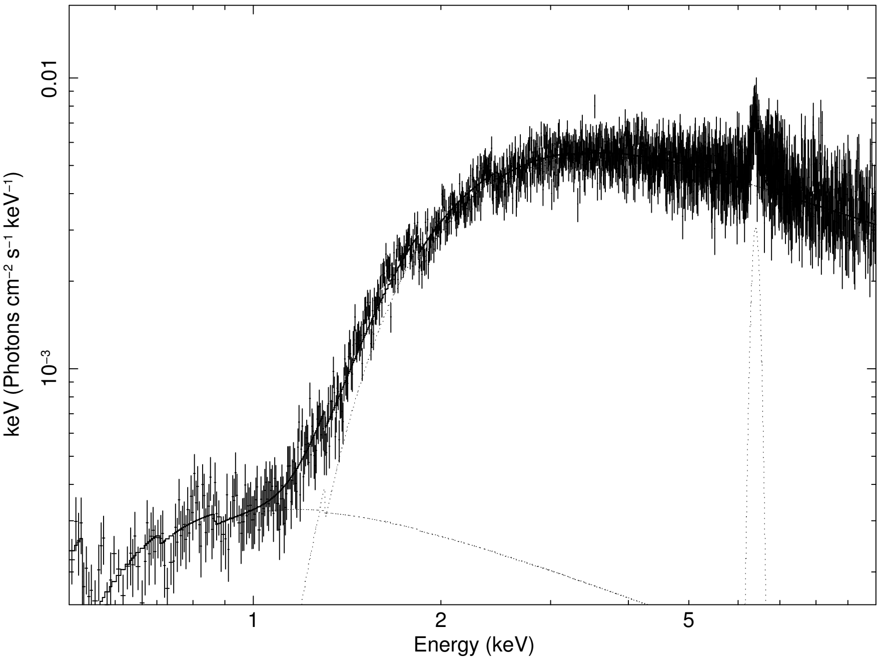

Figure C.23 NGC 5506, observed 2 February 2001

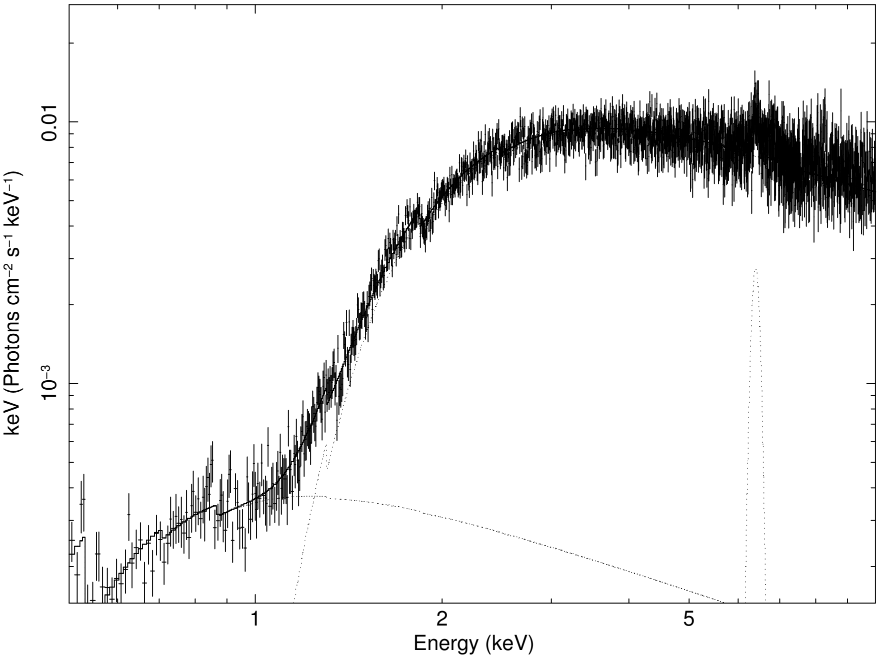

Figure C.24 NGC 5506, observed 9 January 2002

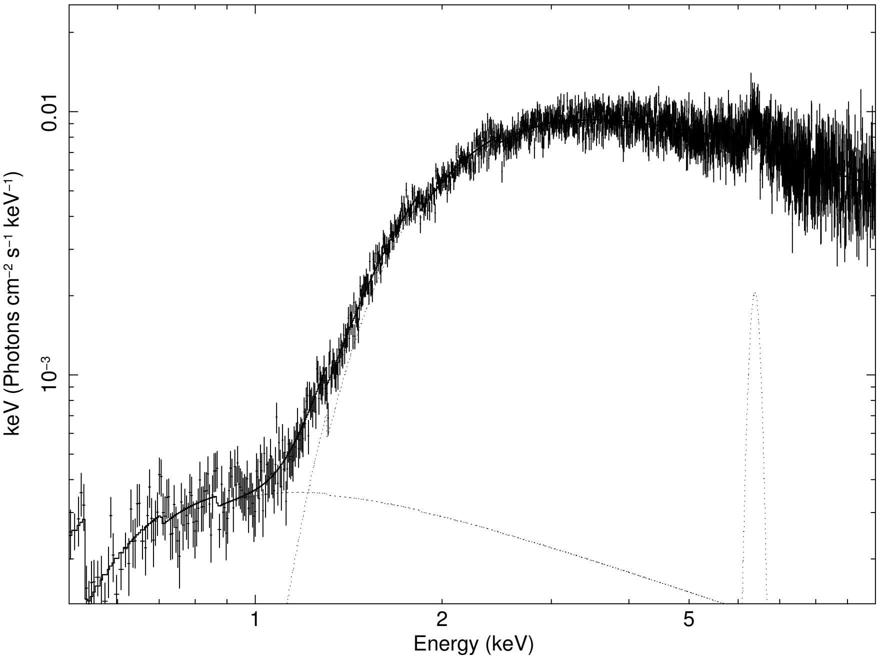

Figure C.25 NGC 5506, observed 7 August 2004

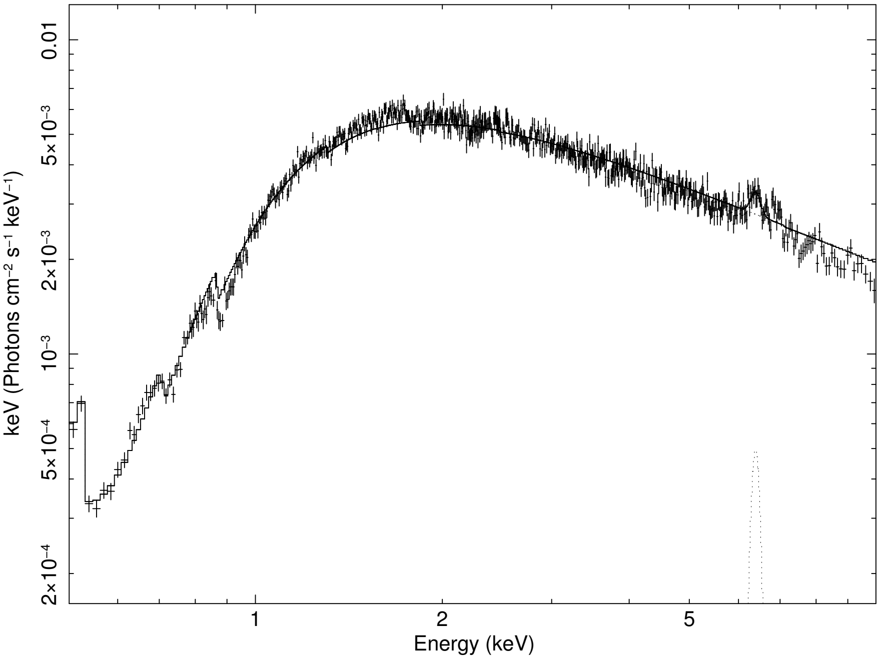

Figure C.26 NGC 7314, observed 2 May 2001

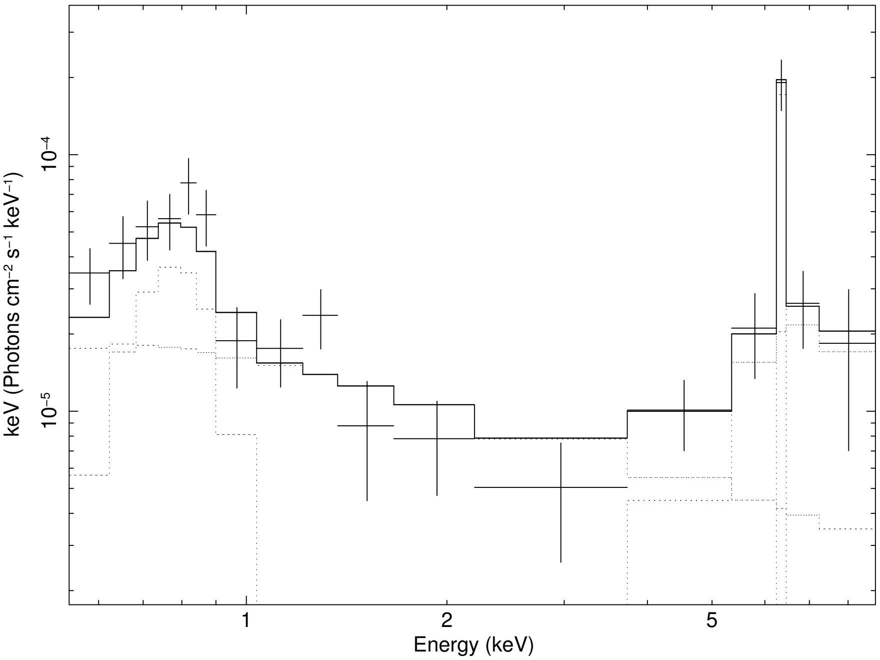

Figure C.27 NGC 7479, observed 19 June 2001

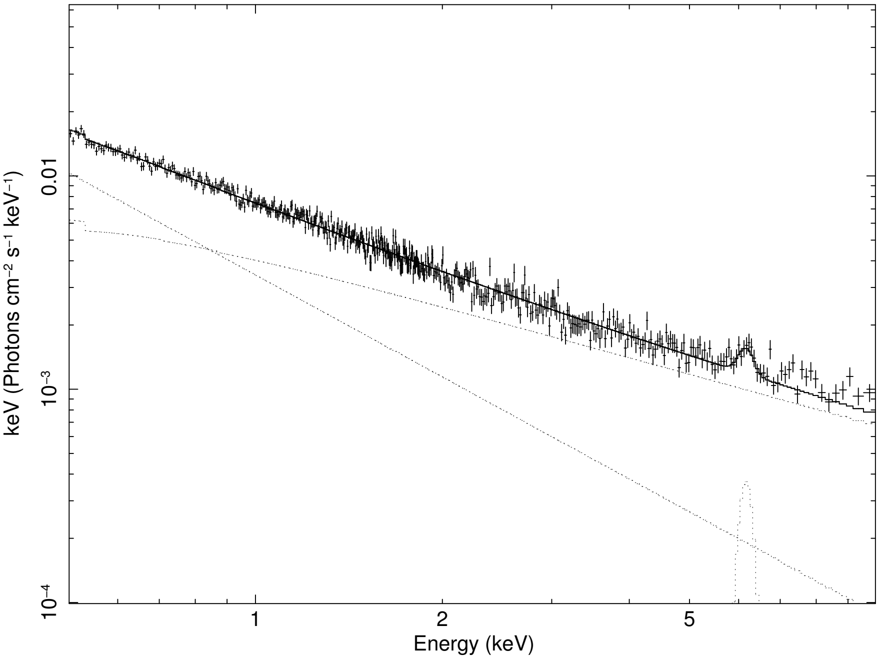

Figure C.28 NGC 7603, observed 14 June 2006

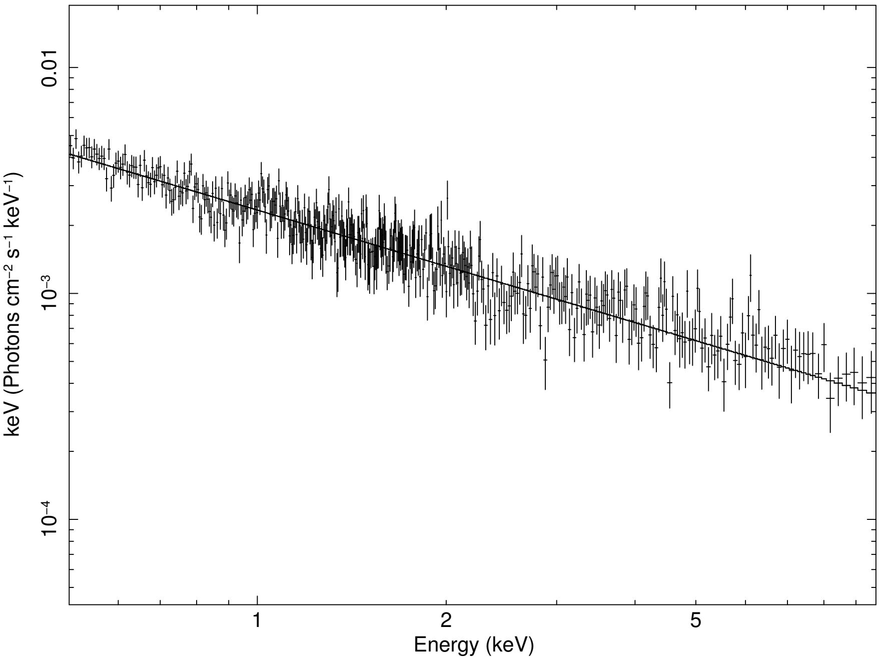

Figure C.29 UGC 12138, observed 3 June 2001

– D –

WFPC2 Structure Maps

This section presents the WFPC2 structure maps discussed in Chapter 5.

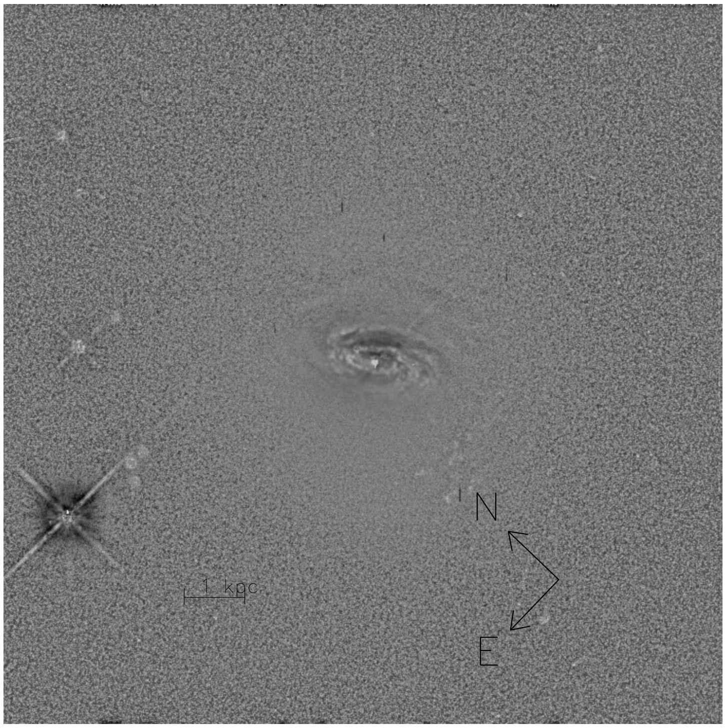

Figure D.1 Structure Map of IRAS 18325-5926

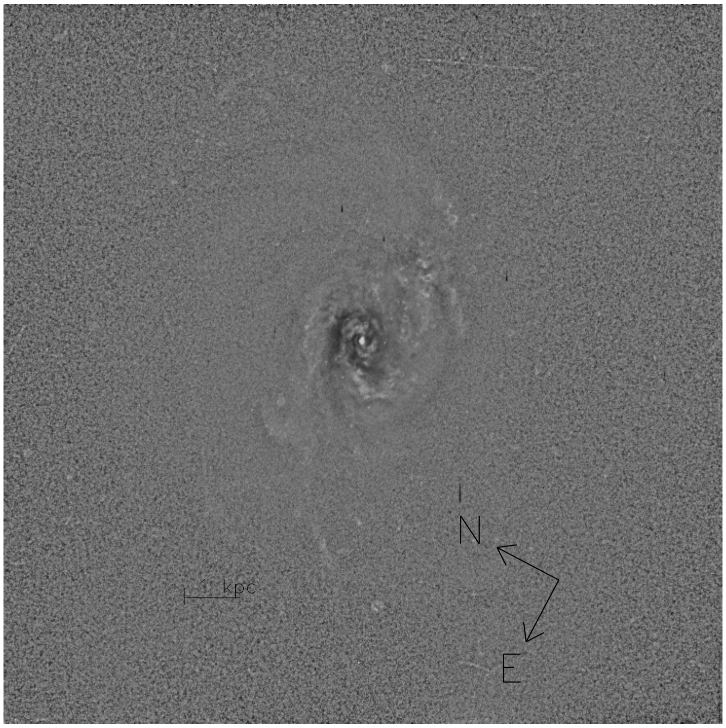

Figure D.2 Structure Map of Mrk 334

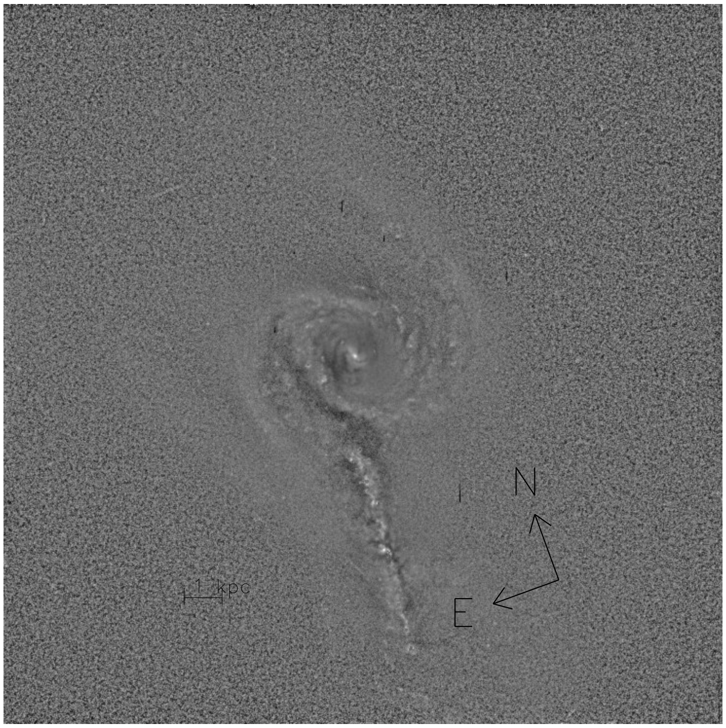

Figure D.3 Structure Map of Mrk 423

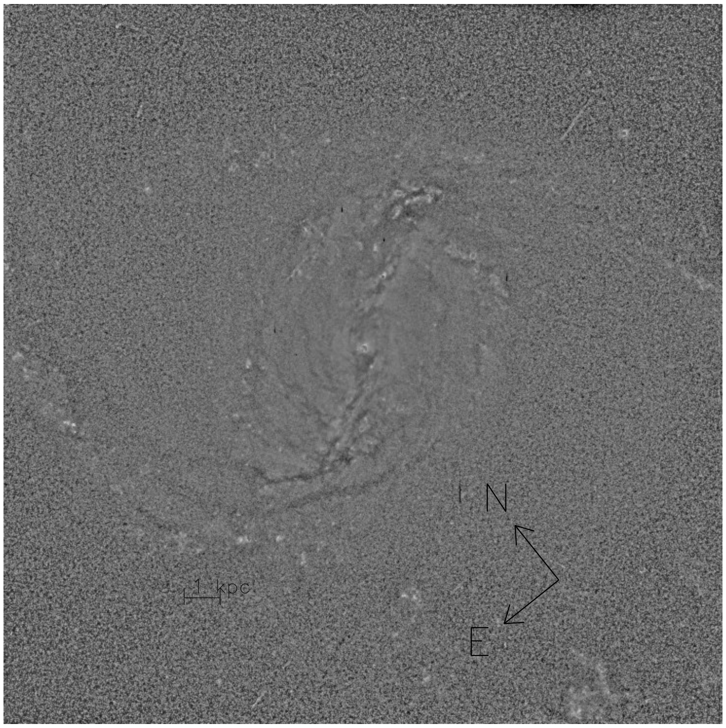

Figure D.4 Structure Map of Mrk 471

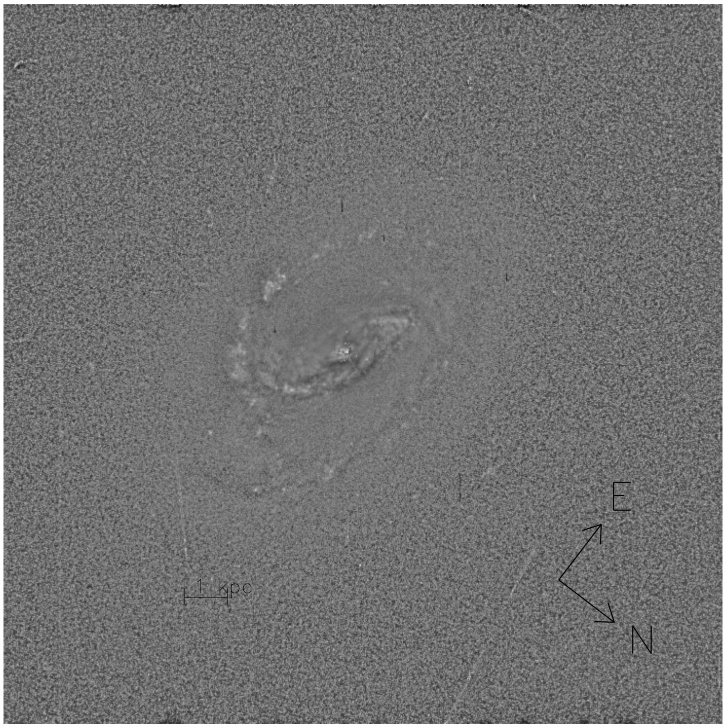

Figure D.5 Structure Map of Mrk 516

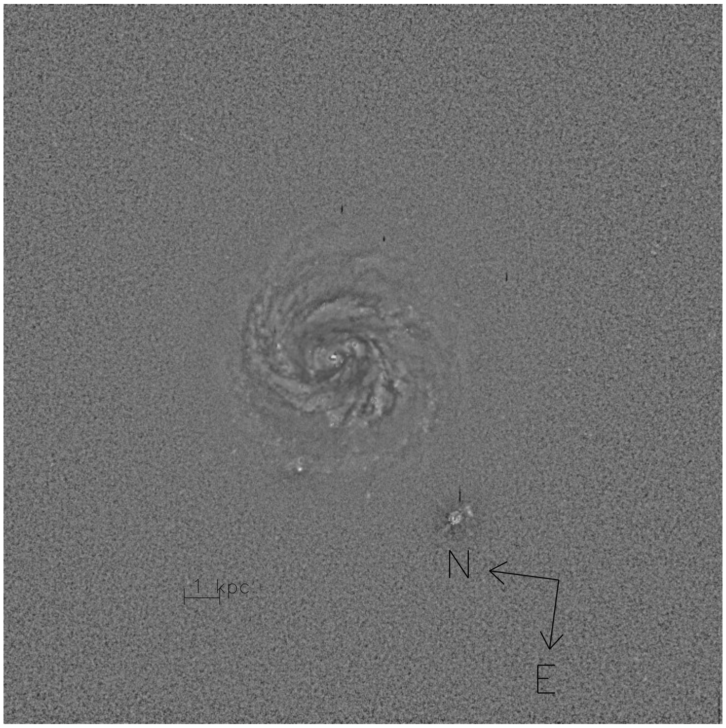

Figure D.6 Structure Map of Mrk 609

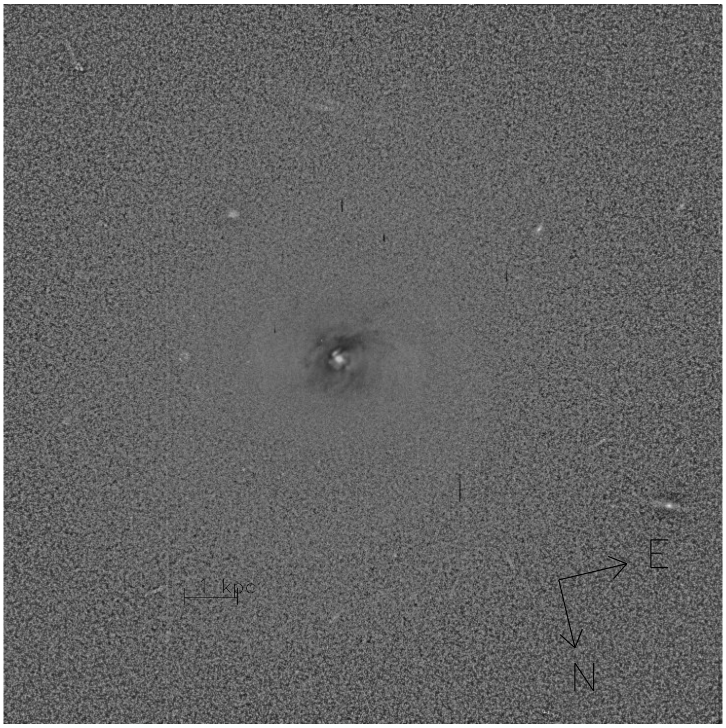

Figure D.7 Structure Map of Mrk 622

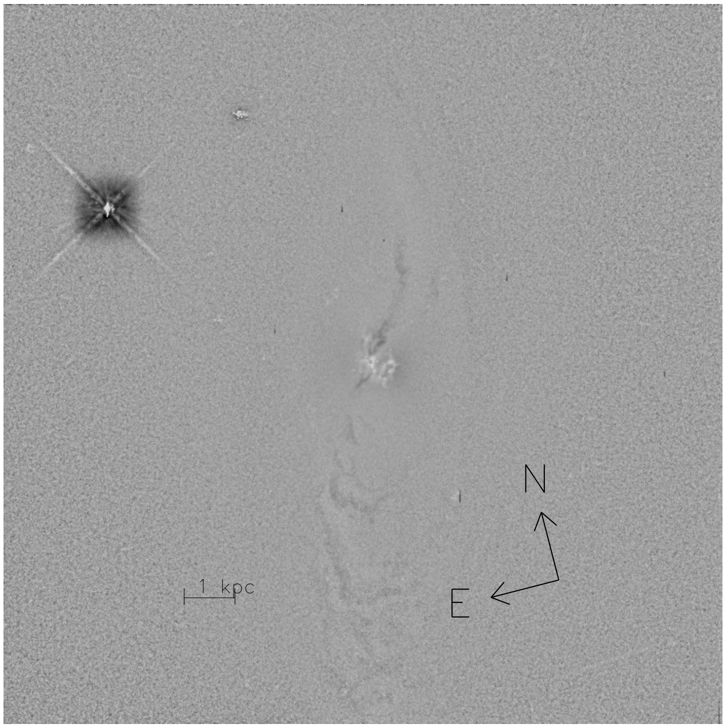

Figure D.8 Structure Map of Mrk 915

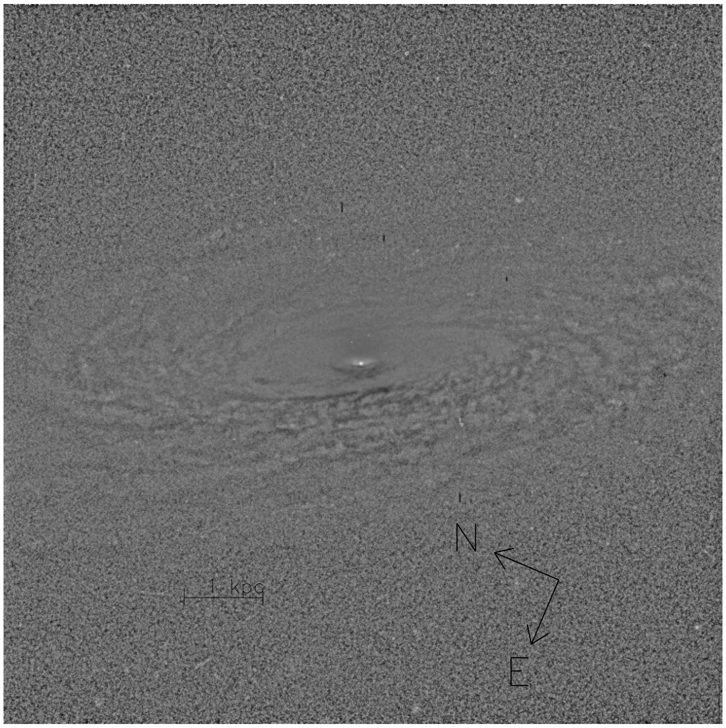

Figure D.9 Structure Map of Mrk 993

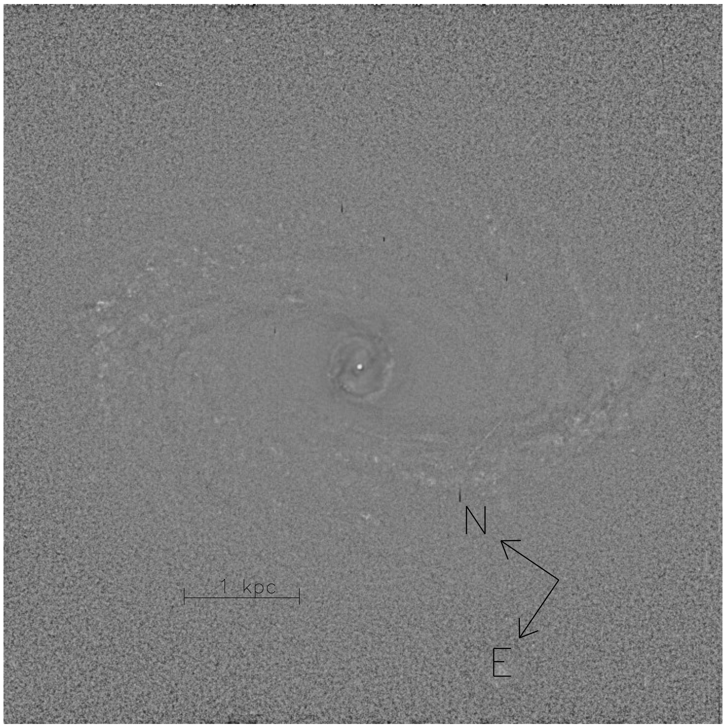

Figure D.10 Structure Map of Mrk 1126

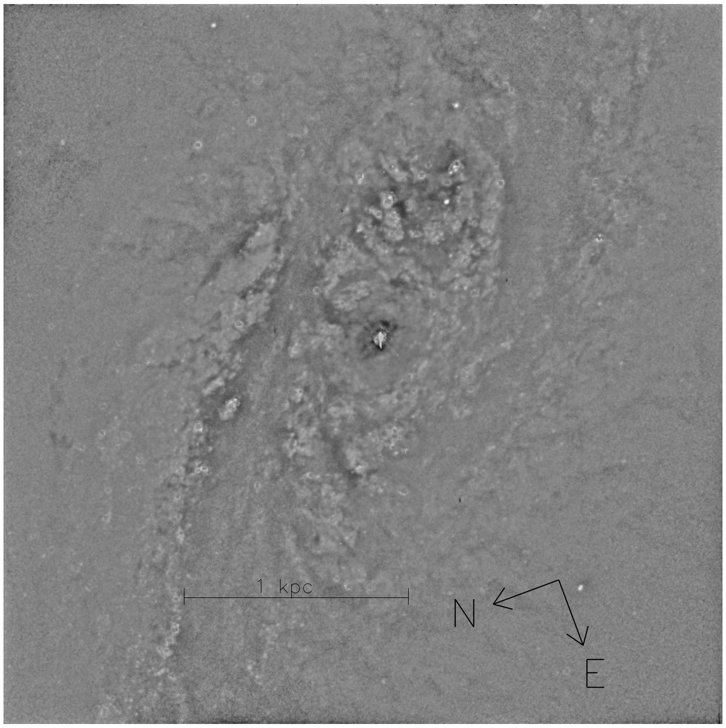

Figure D.11 Structure Map of NGC 1365

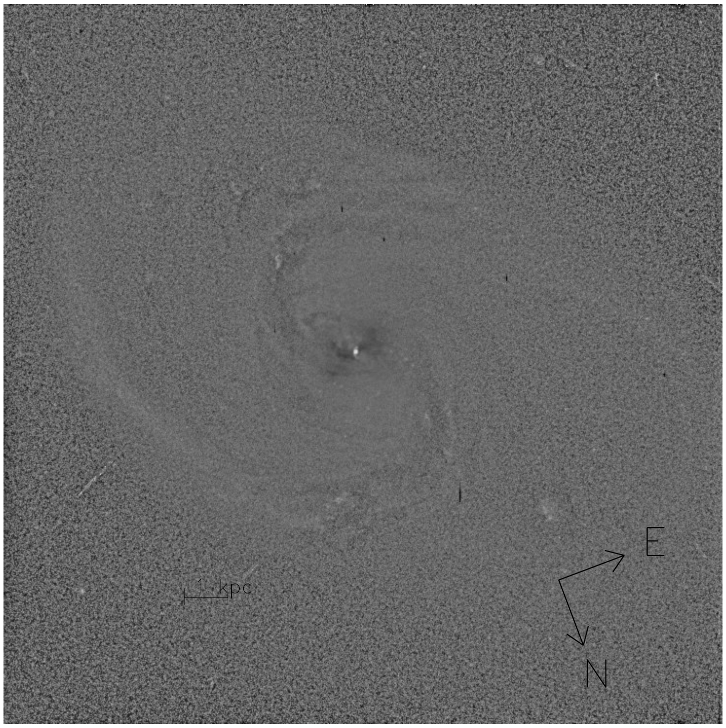

Figure D.12 Structure Map of NGC 2622

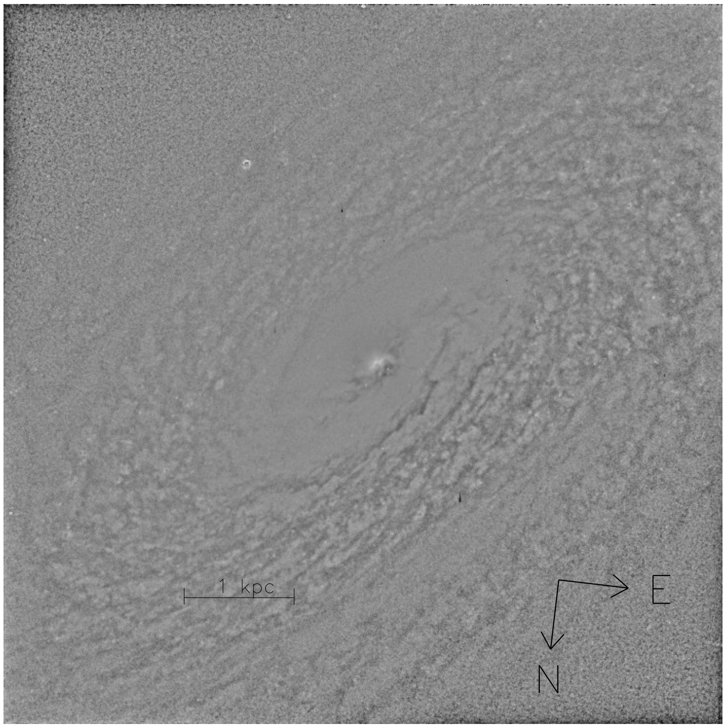

Figure D.13 Structure Map of NGC 2639

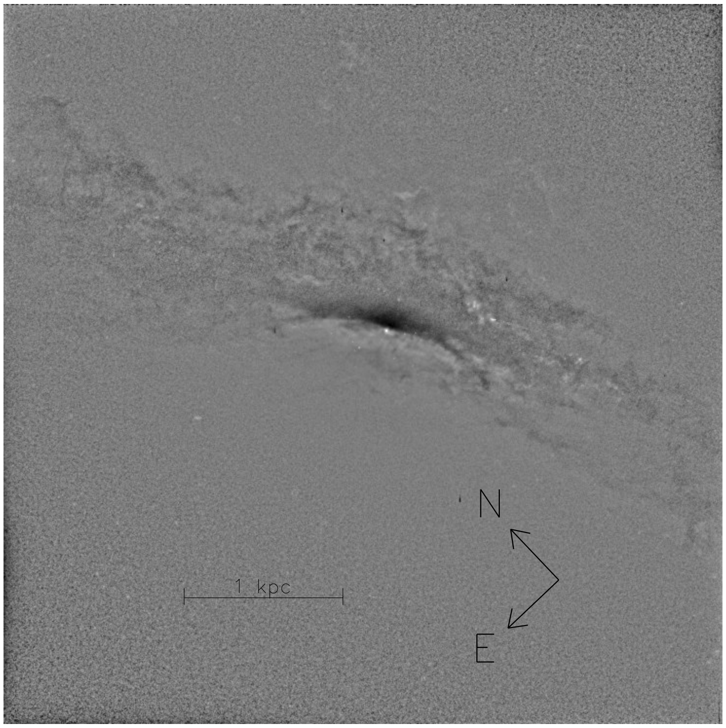

Figure D.14 Structure Map of NGC 2992

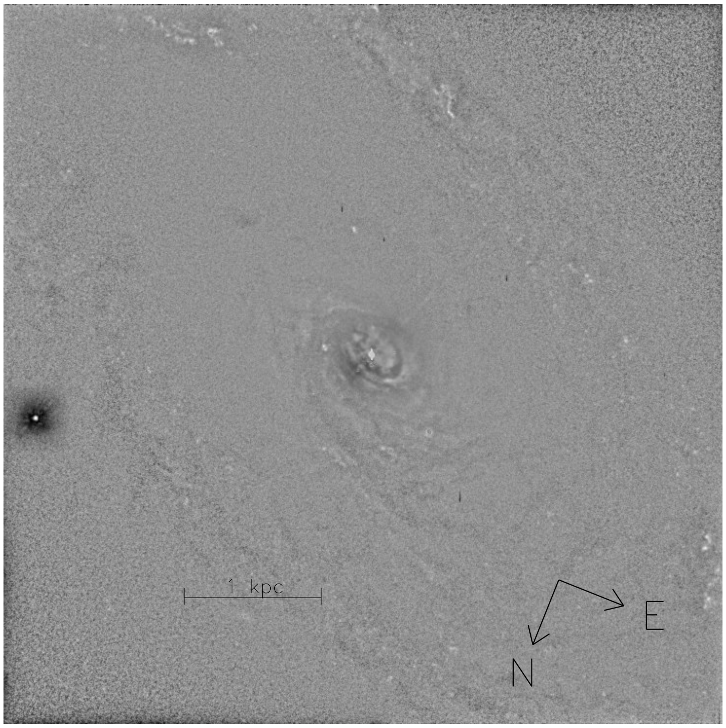

Figure D.15 Structure Map of NGC 3786

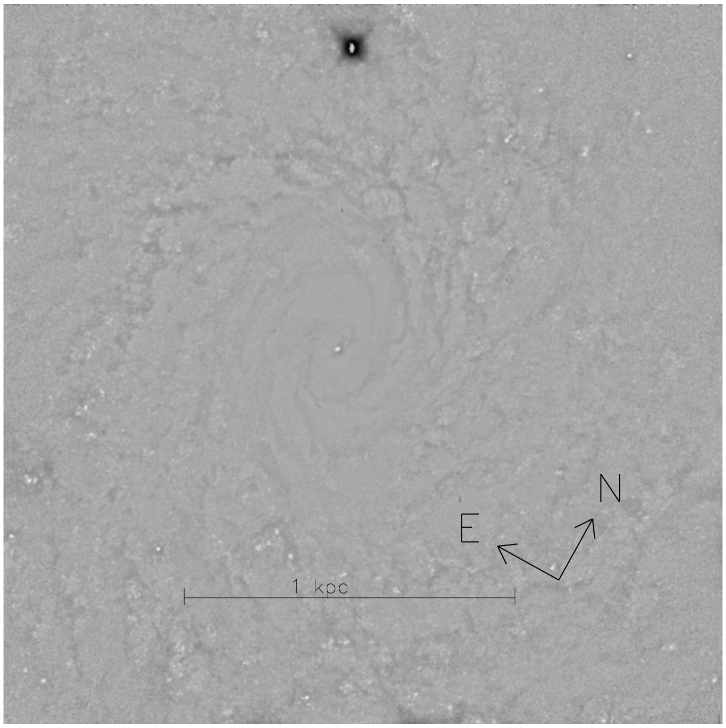

Figure D.16 Structure Map of NGC 3982

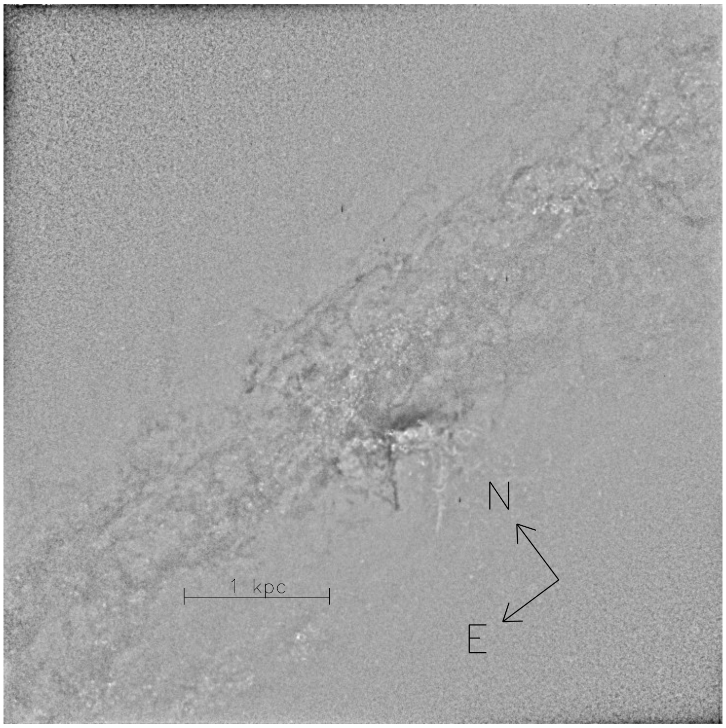

Figure D.17 Structure Map of NGC 4388

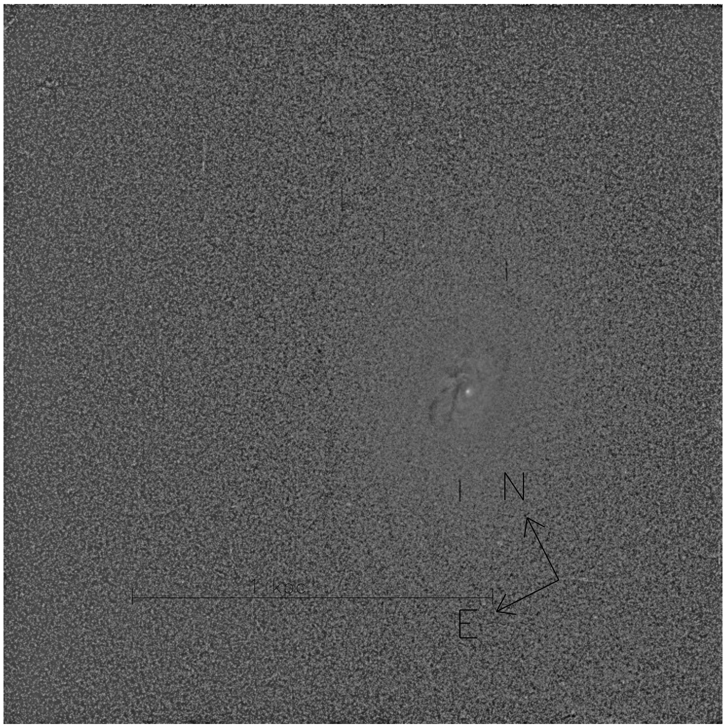

Figure D.18 Structure Map of NGC 4639

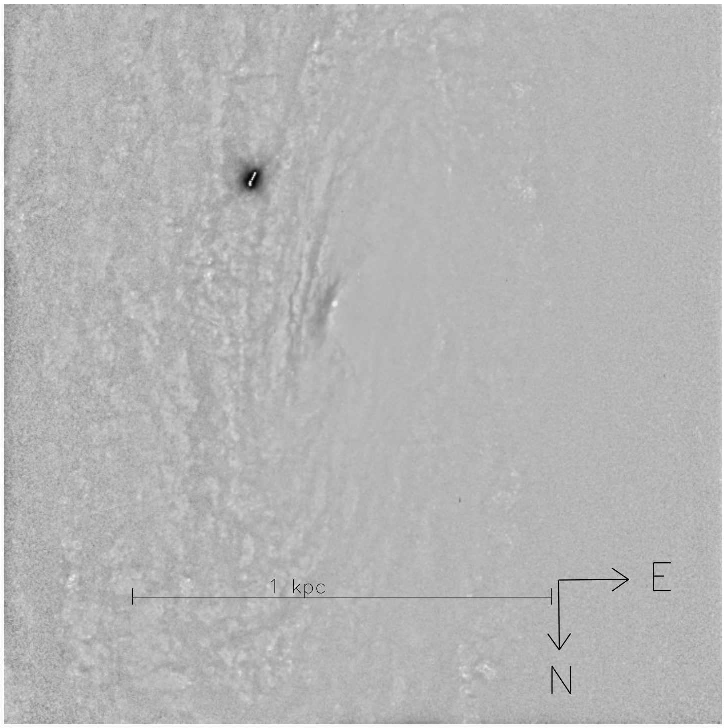

Figure D.19 Structure Map of NGC 5033

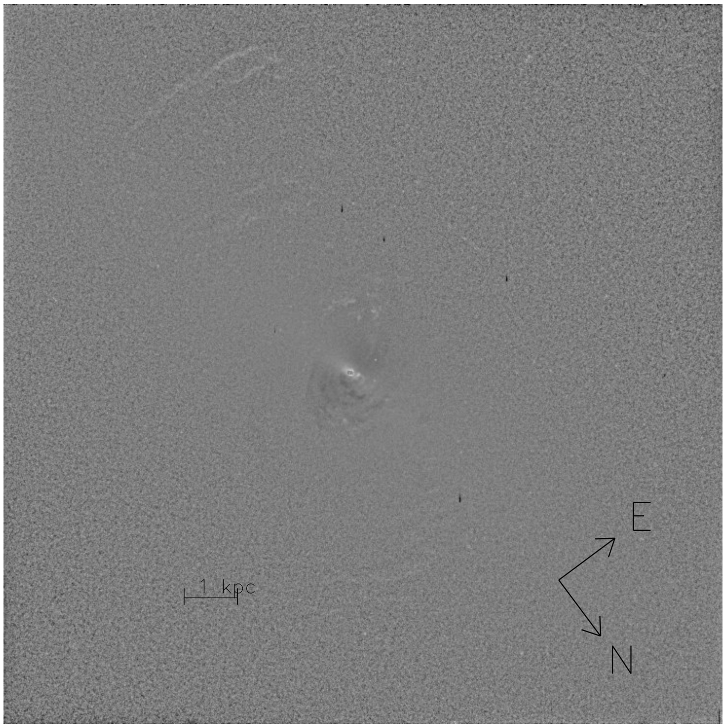

Figure D.20 Structure Map of NGC 5252

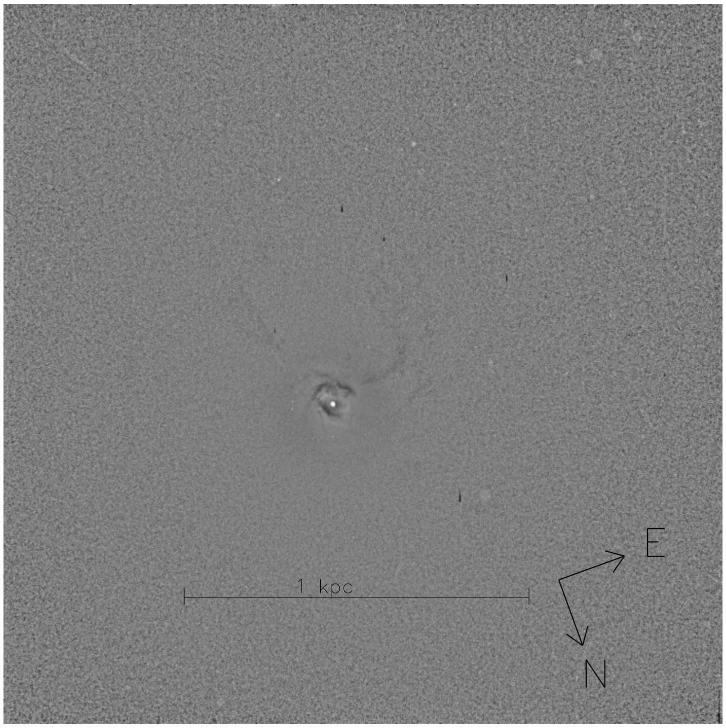

Figure D.21 Structure Map of NGC 5273

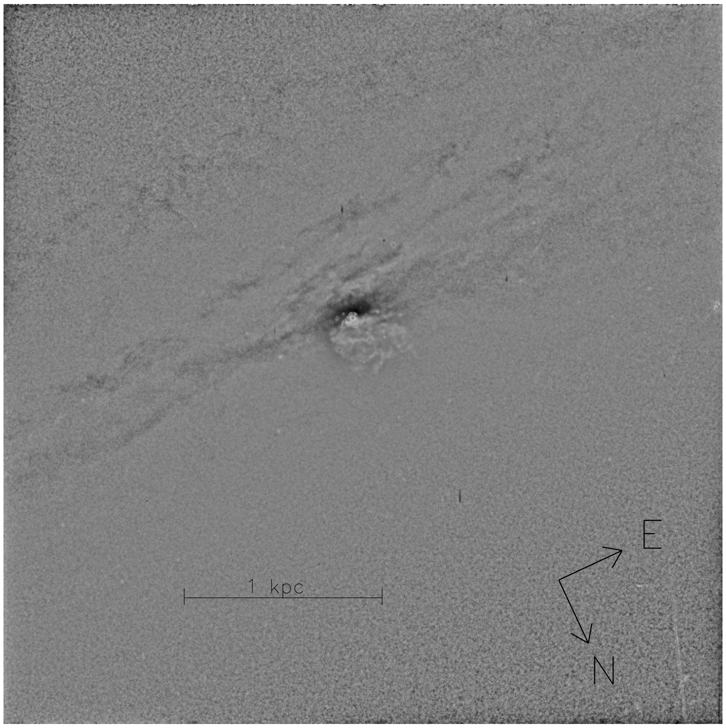

Figure D.22 Structure Map of NGC 5506

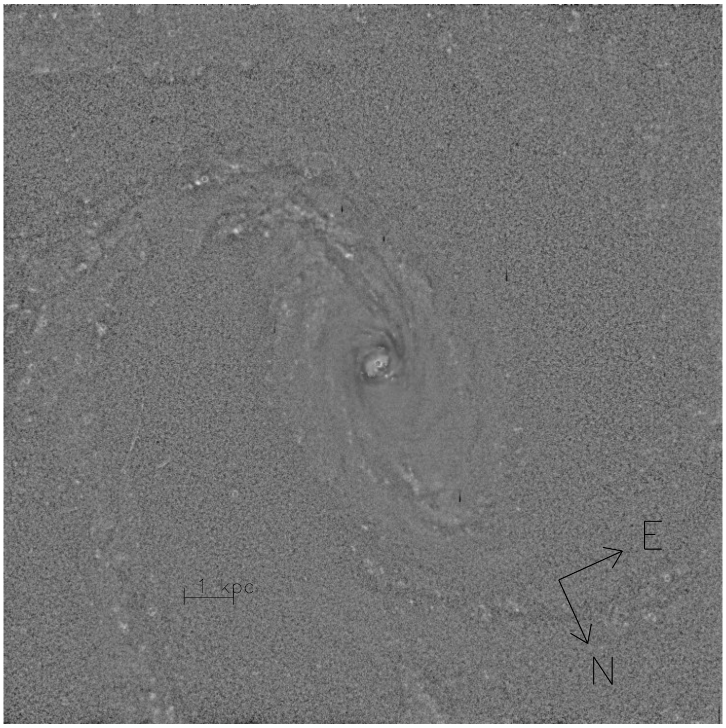

Figure D.23 Structure Map of NGC 5674

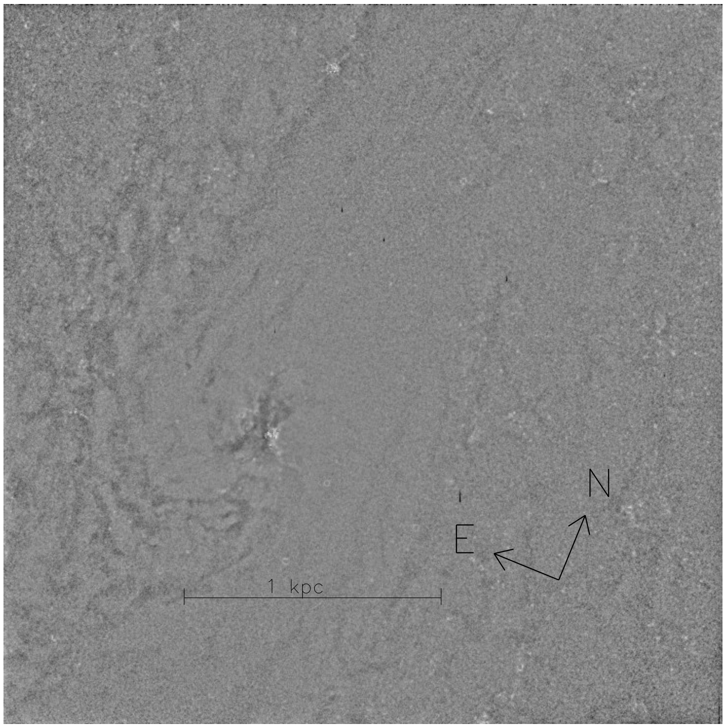

Figure D.24 Structure Map of NGC 7314

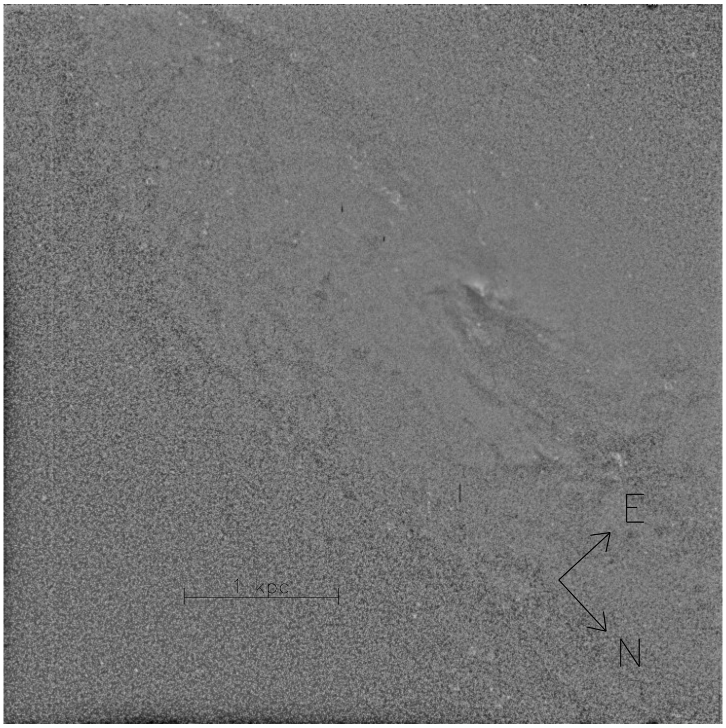

Figure D.25 Structure Map of NGC 7479

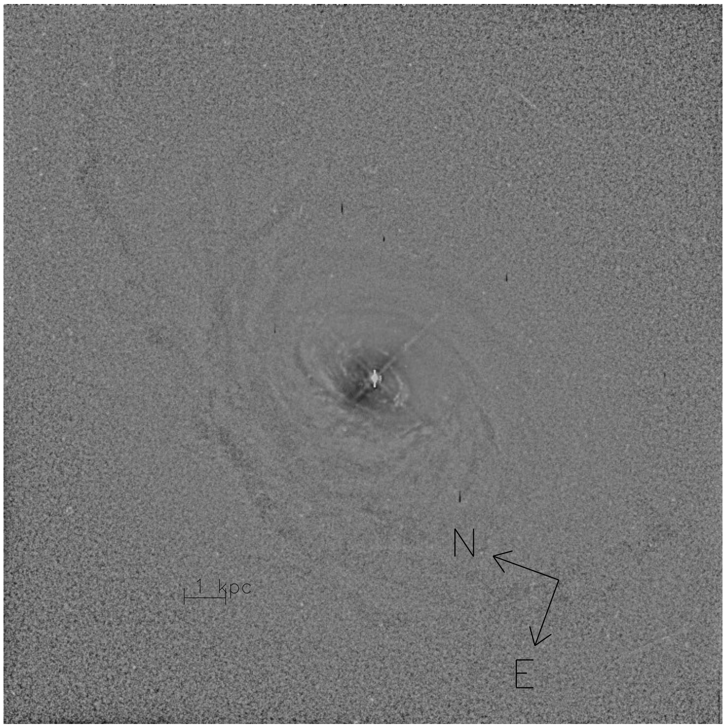

Figure D.26 Structure Map of NGC 7603

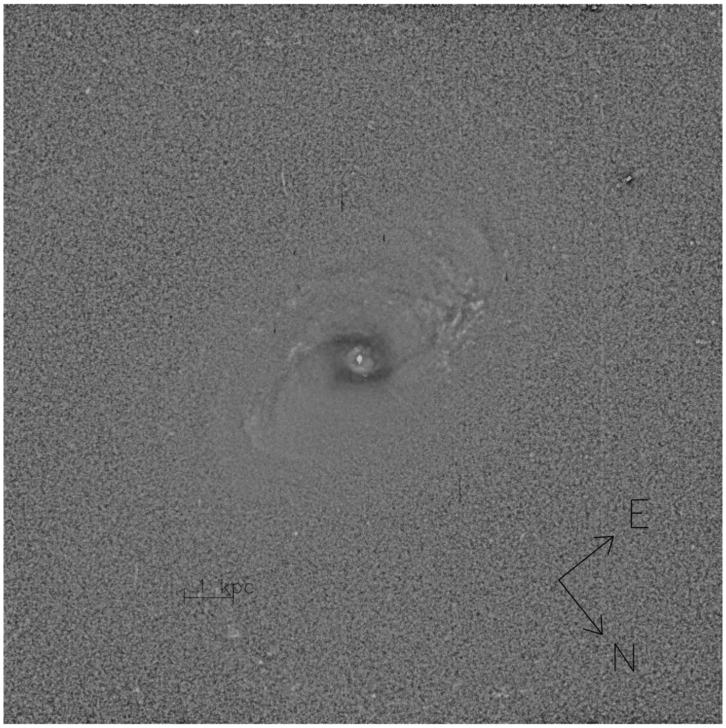

Figure D.27 Structure Map of UGC 12138

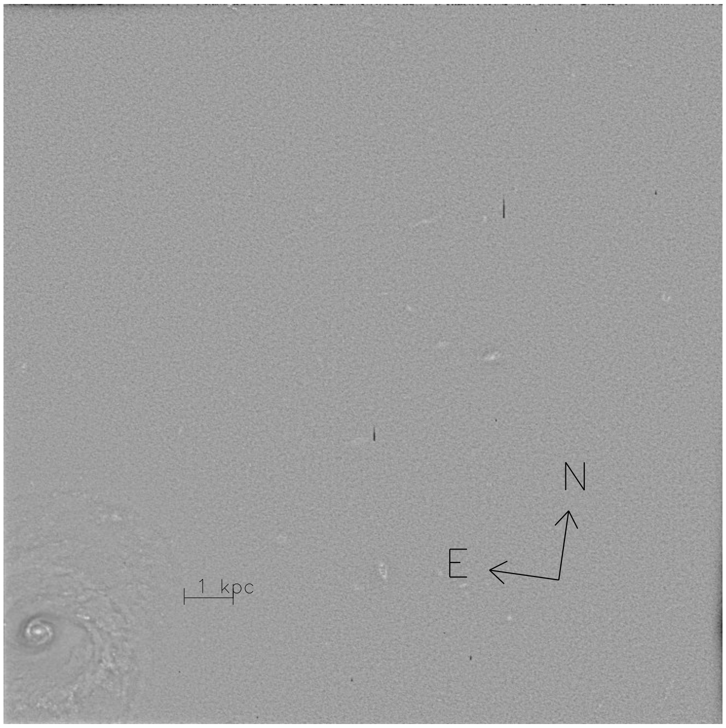

Figure D.28 Structure Map of UGC 7064

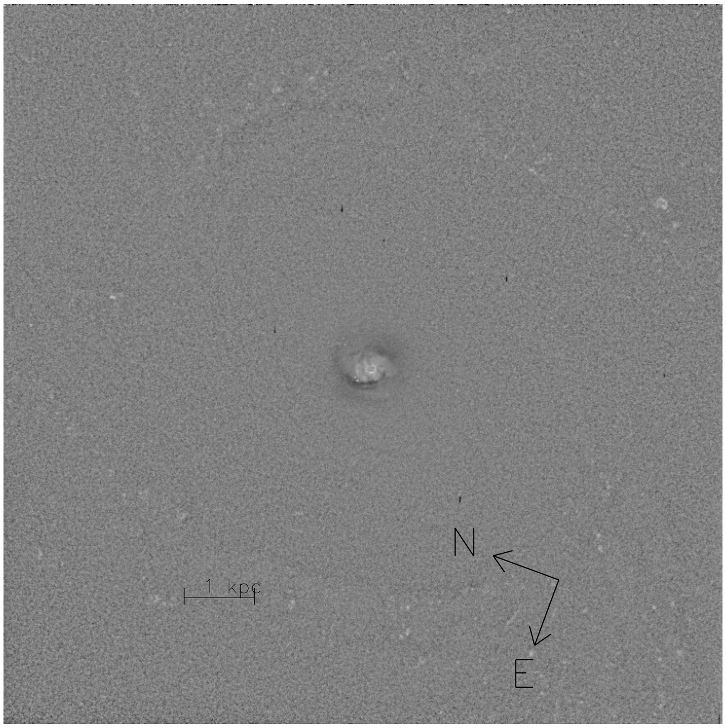

Figure D.29 Structure Map of UM 146

– E –

Spitzer IRS Spectra

This Appendix presents the Spitzer IRS spectra discussed in Chapter 5.

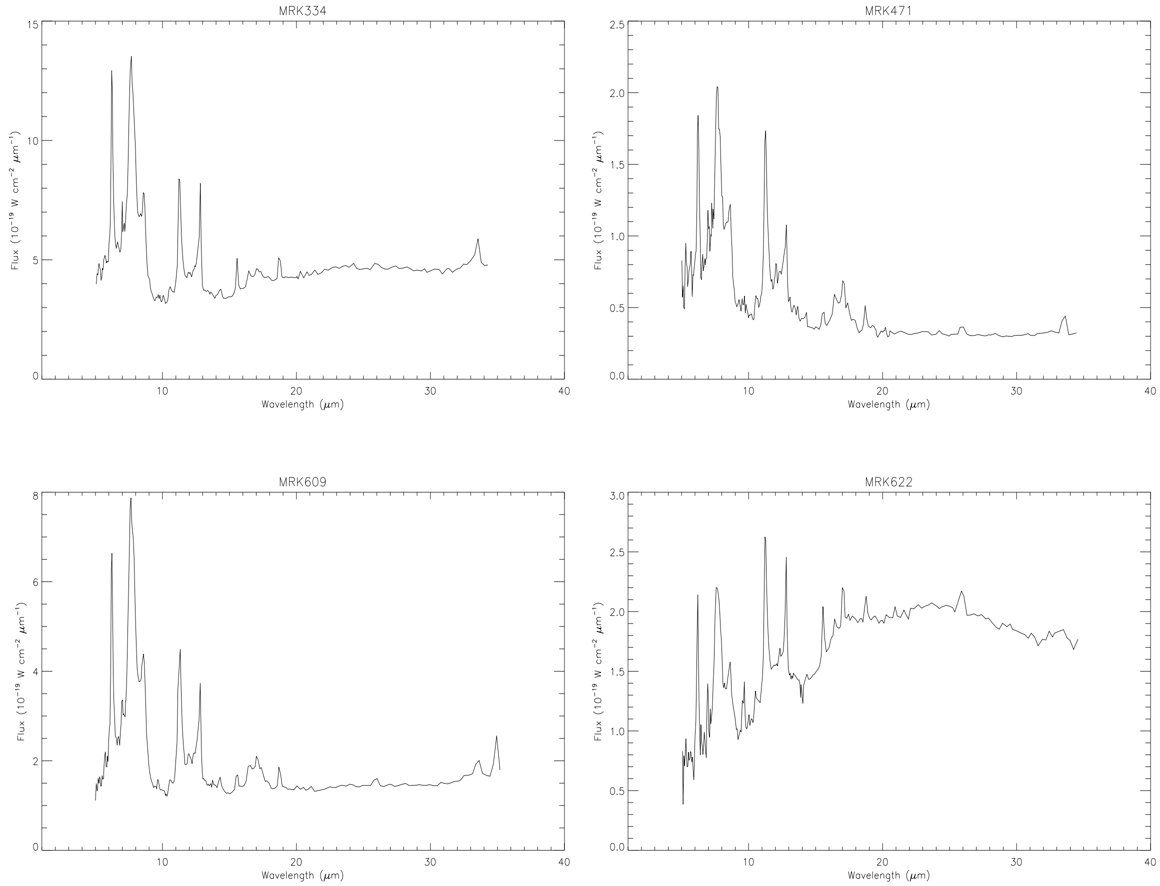

Spitzer IRS spectra of Seyferts: Mrk 334, Mrk 471, Mrk 609, and Mrk 622

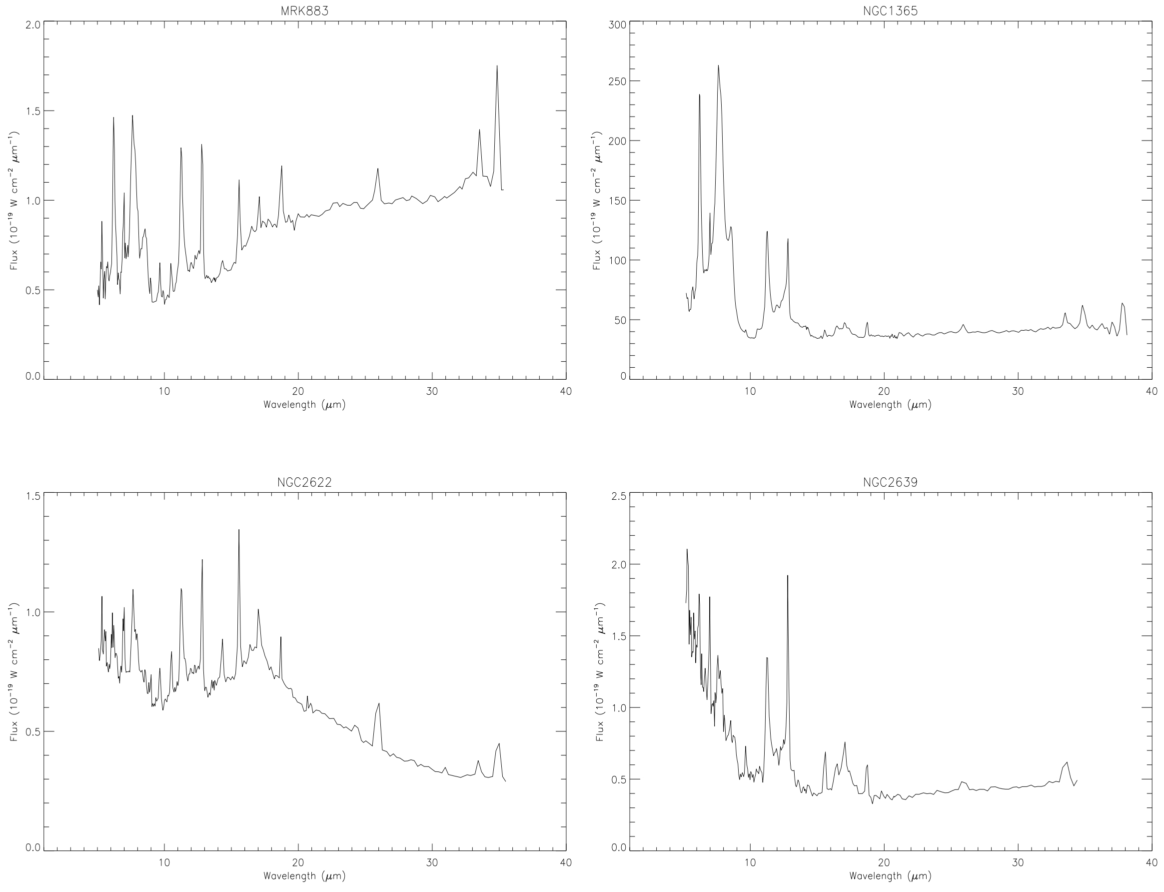

Spitzer IRS spectra of Seyferts: Mrk 883, NGC 1365, NGC 2622, and NGC 2639

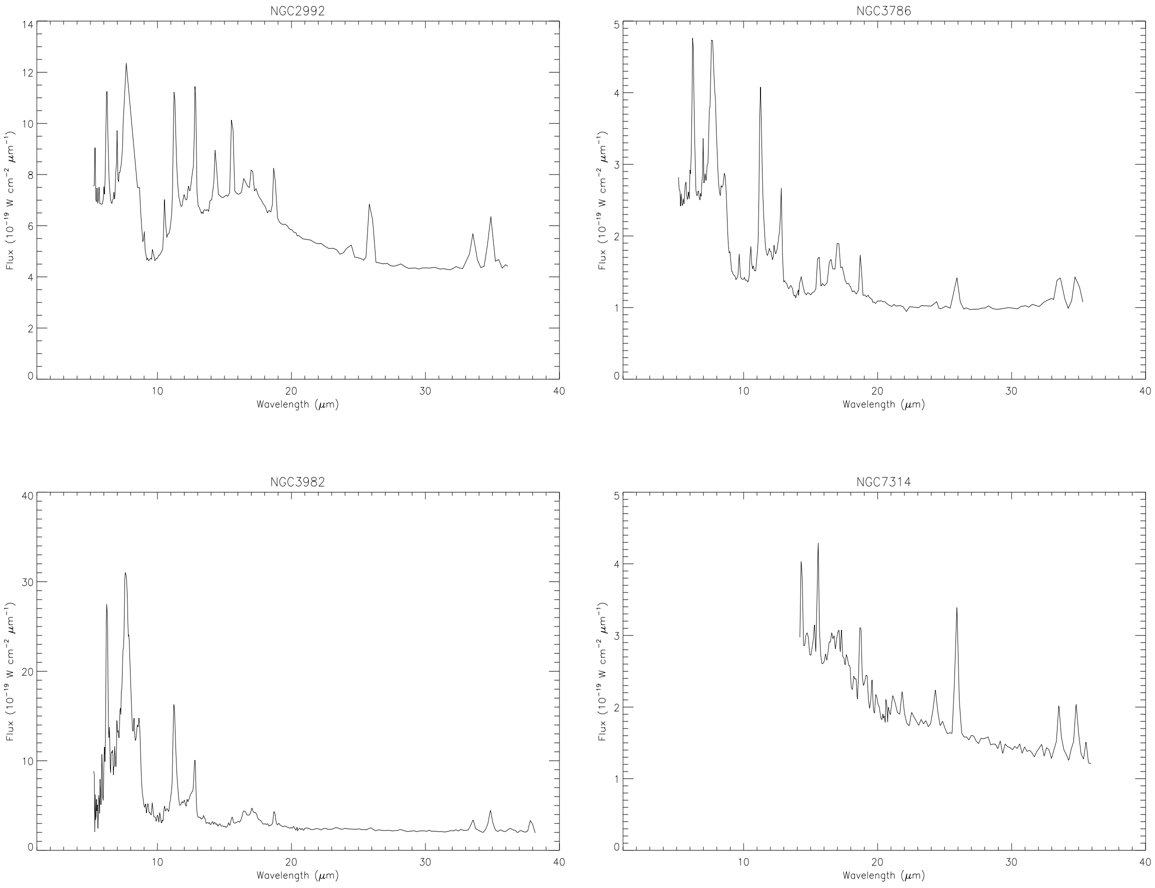

NGC2992

NGC3786

NGC3982

NGC7314

Spitzer IRS spectra of Seyferts: NGC 2992, NGC 3786, NGC 3982, and NGC 7314

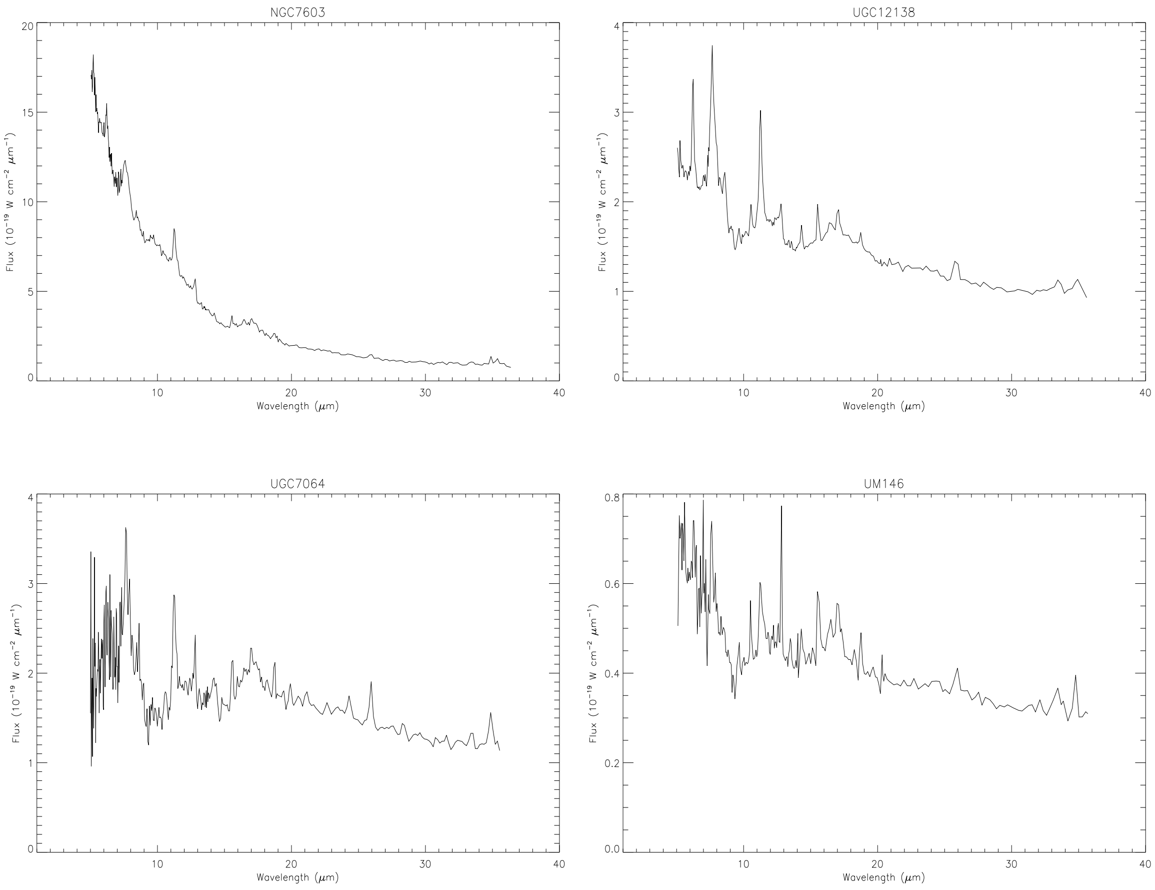

NGC7603

UGC12138

UGC7064

UM146

Spitzer IRS spectra of Seyferts: NGC 7603, UGC 12138, UGC 7064, and UM 146